Dual Characterization of Hydrophobically Modified Polyamidoamine Dendrimers and their Surfactant Aggregate Hosts by Pyrene Excimer Fluorescence

by

Donghan Liu

A thesis

presented to the University of Waterloo

in fulfilment of the

thesis requirement of the degree of

Doctor of Philosophy

in

Chemistry

Waterloo, Ontario, Canada, 2025

© Donghan Liu 2025

Examining Committee Membership

The following served on the Examining Committee for this thesis. The decision of the Examining Committee is by majority vote.

External Examiner	**Dr. Hongbo Zeng** Professor, Department of Chemical and Materials Engineering University of Alberta, Alberta, Canada
Supervisor	**Dr. Jean Duhamel** Professor, Department of Chemistry University of Waterloo, Waterloo, Canada
Internal Member #1	**Dr. Scott Taylor** Professor, Department of Chemistry University of Waterloo, Waterloo, Canada
Internal Member #2	**Dr. Yangju Lin** Professor, Department of Chemistry University of Waterloo, Waterloo, Canada
Internal-External Member	**Dr. Yuning Li** Professor, Department of Chemical Engineering University of Waterloo, Waterloo, Canada

Author's Declaration

This thesis consists of material all of which I authored or co-authored: see Statement of Contributions included in the thesis. This is a true copy of the thesis, including any required final revisions, as accepted by my examiners.

I understand that my thesis may be made electronically available to the public.

Statement of Contributions

Chapter 2: Liu, D.; Patel, S.; Xie, Y.; Zhang, H.; Duhamel, J. Probing Macromolecular Conformation in Restricted Geometry by PEF: Application to Hydrophobically Modified PAMAM Dendrimers Isolated Inside Surfactant Micelles. *J. Phys. Chem. B* **2025**, *129* (3), 1144–1153. DOI: https://doi.org/10.1021/acs.jpcb.4c07737

Chapter 3: Liu, D.; Patel, S.; Duhamel, J. Conformation of Pyrene End-Labeled Polyamidoamine Dendrimers in Catanionic Surfactant Micelles Probed by Pyrene Excimer Formation. *Langmuir* **2025**, *41* (31), 20986-20998. DOI: https://doi.org/10.1021/acs.langmuir.5c02704

Abstract

This thesis explores why the conformational response of generation-0 polyamidoamine dendrimers end-labeled with four identical 1-pyrenealkanoyl groups (PyCX-PAMAM-G0 with X = 4, 6, 8, 10, and 12 for a butyroyl, hexanoyl, octanoyl, decanoyl, and dodecanoyl linker, respectively) to their local environment makes them excellent molecular probes to investigate surfactant aggregates. The conformation of the dendrimers was studied in polar organic solvents, spherical micelles, and non-spherical surfactant aggregates (NSSA) using pyrene excimer formation (PEF) and the model-free analysis (MFA) of the fluorescence decays. In *N*,*N*-dimethylformamide (DMF) and dimethyl sulfoxide (DMSO) and in micelles of sodium dodecyl sulfate (SDS) or dodecyltrimethylammonium bromide (DTAB), the dendrimers with shorter (X = 4, 6, 8) alkanoyl linkers adopted an ideal conformation. In contrast, the PyC10- and PyC12-PAMAM-G0 dendrimers experienced a conformational inversion in pure surfactant micelles driven by the hydrophobicity gradient (HG) generated between the polar surface and the hydrophobic interior of the micelles. The conformational inversion of the PyC10- and PyC12-PAMAM-G0 dendrimers was further investigated with mixed micelles prepared from SDS and DTAB mixtures. The decrease in conformational inversion as the micellar shape evolved from a sphere to an elongated ellipsoid with increasing DTAB content led to the idea of the spatial partitioning theory (SPT). The SPT attributes changes in the average conformation of the dendrimers to the change in the volume fractions of the two regions found inside the mixed micelles, between which the dendrimers partition themselves. These two regions were the polar edge region, which was made of ~ 70 charged SDS molecules, and had a curved surface and a high HG, and a more hydrophobic middle region with a lower surface curvature and a low HG formed by the remaining neutralized surfactants. The SPT provided a robust fundamental framework to predict how the average rate constant ($\langle k \rangle$) for PEF, obtained from the MFA of the fluorescence decays acquired with the PyCX-PAMAM-G0 samples, was

affected by the composition of the NSSA the dendrimers interacted with. The sensitivity of the conformational inversion of the PyC10- and PyC12-PAMAM-G0 dendrimers to their local environment shows the potential of these dendrimers as molecular probes for NSSA formed upon the addition of NaCl or DTAB to aqueous solutions of SDS micelles. Partitioning of the dendrimers with longer C10 and C12 linkers between the edge and middle regions rationalized the changes in $\langle k \rangle$ observed as a function of salt concentration, DTAB content, or both. The generality of the SPT, which applied to all surfactant systems investigated in this thesis, provided strong support for the two regions coexisting in the NSSA, with the edge region being constituted of the same number of charged surfactants as that found in a pure SDS micelle. This insight led to a proposal for the mechanism leading to the formation of NSSA, when salt or oppositely charged surfactants are added to an SDS aqueous solution. Together, the results presented in this thesis suggest that the PyCX-PAMAM-G0 dendrimers constitute outstanding molecular probes to study NSSA in solution.

Acknowledgements

I would like to express my sincere gratitude towards Prof. Duhamel for his continuous trust, guidance, and support throughout my CHEM 494, Master, and Ph.D. research projects. I could not have made it this far in my academic journey without him, not even in my imagination. I also wanted to thank my Ph.D. advisory committee members for all their help over the years, which was critical to the success of my project.

Special thanks to former graduate student Dr. Sanjay Patel for both technical and moral support, and I appreciate the contributions from all former and current lab members from the Duhamel's lab for creating a very friendly and positive working environment together as well as all their help.

Finally, I want to thank my girlfriend Dr. Yutong Liu, my two cats Kiki and Coco, and my dear parents for all their love and support in my life.

Table of Contents

Examining Committee Membership ii

Author's Declaration.....iii

Statement of Contributions iv

Abstract .....v-vi

Acknowledgements vii

List of Figures .....xiii-xvii

List of Tables xviii

List of Abbreviations .....xix-xxiv

Chapter 1 Introduction 1

1.0 Background.....1-5

1.1 Characterization Techniques Used to Probe the Size and Shape of Surfactant Aggregates and the Conformation of Macromolecules.....5

1.1.1 Scattering Techniques.....5-7

1.1.2 Microscopy.....7-9

1.1.3 Viscometry and Rheology.....9-10

1.1.4 Spectroscopy Based Characterization Methods.....11

1.1.4.1 Nuclear Magnetic Resonance (NMR) and Circular Dichroism (CD.....11-12

1.1.4.2 Fluorescence Techniques.....12-18

1.2 Model Free Analysis (MFA).....18-19

1.2.1 Probing the Conformation of Macromolecules with the MFA.....19-22

1.2.2 Determining N_{agg} for surfactant aggregates with the MFA.....22

1.3 Goal of the Thesis.....22-23

1.3.1 PyCX-PAMAM-G0 Dendrimers.....23

1.3.2 SDS Micelles.....23-24

1.3.3 SDS and DTAB Mixed Micelles.....24-25

1.4 Research Objective and Thesis Outline.....25-28

Chapter 2: Application to Hydrophobically Modified PAMAM Dendrimers Isolated Inside Surfactant Micelles.....29

2.1 OVERVIEW.....30

2.2 INTRODUCTION.....31-35

2.3 EXPERIMENTAL 35-39

2.4 RESULTS.....39-48

2.5 DISCUSSION.....48-51

2.6 CONCLUSION.....51-52

Chapter 3: Conformation of Pyrene End-Labeled Polyamidoamine Dendrimers in Catanionic Surfactant Micelles Probed by Pyrene Excimer Formation.....53

3.1 OVERVIEW.....54

3.2 INTRODUCTION.....55-60

3.3 EXPERIMENTAL 60-65

3.4 RESULTS.....66-75

3.5 DISCUSSION.....75-81

3.6 CONCLUSION.....81-82

Chapter 4: Two Distinct Regions in Surfactant Aggregates Identified with Pyrene-Labeled PAMAM Dendrimers.....83

4.1 OVERVIEW.....84

4.2 INTRODUCTION.....85-90

4.3 RESULTS.....90-93

4.4 DISCUSSION.....93-100

4.5 CONCLUSION.....100

Chapter 5: Effect of Salt Concentration on Catanionic Surfactant Aggregates Probed by Pyrene Excimer Formation (PEF) with Pyrene End-Labeled Polyamidoamine (PAMAM) Dendrimers.....101

5.1 OVERVIEW.....102

5.2 INTRODUCTION.....103-108

5.3 EXPERIMENTAL 108-117

5.4 RESULTS AND DISCUSSION.....117-128

5.5 CONCLUSION.....129-130

Chapter 6: Concluding remarks & Future Works.....131

6.1 THESIS CONCLUSION.....132-134

6.2 FUTURE WORK.....134-135

Letters of Copyright Permission.....136

Permission for reproduction of Chapter 2..... 136

Permission for reproduction of Chapter 3..... 136

References.....137

Chapter 1.....137-149

Chapter 2.....150-158

Chapter 3.....159-167

Chapter 4.....168-172

Chapter 5.....173-178

S2-References.....179

S3-References.....179

S4-References.....179-180

S5-References.....180

Appendix: Supporting Information (SI) 181

Appendix A: S2-SI for Chapter 2.....182

A] Characterization of the PyCX-PAMAM-G0 with X = 6 and 10 and NpC2-PAMAM-G0 dendrimers by ^{1}H NMR in d_6-DMSO.....182-184

B] Mass spectra of the PyCX-PAMAM-G0 and NpC2-PAMAM-G0 dendrimers generated by Matrix assisted laser desorption/ionization – time of flight mass spectroscopy (MALDI-ToF MS).....185-187

C] Sample preparation.....188

D] Assessment of the solubility of the PyCX-PAMAM-G0 samples in 50 mM surfactant aqueous solutions based on the analysis of pyrene excimer fluorescence decays and UV-vis absorption spectra.....189-193

E] Fluorescence Resonance Energy Transfer (FRET) study of the PyCX-PAMAM-G0 dendrimers.....194-200

F] Parameters obtained from the model free analysis (MFA) of the PyCX-PAMAM-G0 dendrimers.....201-204

G] Equations used for the end-to-end distance of the dendrimers.....204

Appendix B: S3-SI for Chapter 3.....205

A] Equations used for the global model free analysis of the monomer and excimer fluorescence decays of the PyCX-PAMAM-G0 samples.....205

B] Parameters obtained from the model free analysis (MFA) of the fluorescence decays acquired with the PyCX-PAMAM-G0 samples.....206-209

C] Equation used for the probability of finding two pyrenyl ends in a PyCX-PAMAM-G0 dendrimer within a distance r from each other.....210

Appendix C: S4-SI for Chapter 4.....211

A] Materials, sample preparation, instruments, and analyzing methods.....211-214

B] UV-vis spectra of *PyCX-PAMAM-G0* in NSSA at various NaCl concentration....215

C] Fluorescence spectra of the PyCX-PAMAM-G0 samples in 50 mM SDS aqueous solutions at various NaCl concentrations.....216

D] Parameters obtained from the model free analysis (MFA) of the PyCX-PAMAM-G0 dendrimers.....217-221

E] Equations used to determine the average end-to-end distance of the dendrimers.....222

Appendix D: S5-SI for Chapter 5.....223

A] Global analysis of the monomer and excimer decays of PyCX-PAMAM-G0 using the model free analysis.....223

B] Fluorescence spectra of pyrene in mixed micelles at 50 mM surfactant concentration.....224

C] Fluorescence spectra of 0.45 μM pyrene in surfactant solution.....225-226

D] Change in I_E/I_M(SSF) and I_1/I_3 with total surfactant concentration.....227-228

E] UV-vis spectra of PyCX-PAMAM-G0 in mixed micelles in the presence of NaCl.....229

F] SSF spectra of PyCX-PAMAM-G0 in mixed micelles in the presence of NaCl...230

G] Parameters obtained from the model free analysis (MFA) of molecular pyrene for N_{agg} (NSSA) measurements.....231-232

H] Parameters obtained from the model free analysis (MFA) of the PyCX-PAMAM-G0 dendrimers.....233-234

I] Equations used for the end-to-end distance of the dendrimers.....234

List of Figures

Figure 1.1. Example of a pyrene fluorescence spectrum obtained for an aqueous solution of 0.6 μM pyrene in the presence of 8 mM SDS.....16

Figure 1.2. Example of time resolved decays obtained for pyrene octanoic acid labeled polyamidoamine dendrimers in an aqueous solution of 50 mM SDS and 10 mM NaCl.....21

Figure 1.3. Chemical structure of the PyCX-PAMAM-G0 dendrimers….....23

Figure 1.4. Illustration of a cylindrical NSSA with two edges mainly constituted of charged SDS molecules and a middle region constituted of an SDS/DTAB mixture.....26

Figure 2.1. Chemical structure of the PyCX-PAMAM-G0 dendrimers and their schematic representation with the aromatic pyrenes in blue, the apolar alkoxy linkers with $X = 4$, 6, 8, 10, and 12 in green, and the polar PAMAM core in red.....34

Figure 2.2. Fluorescence spectra of the PyCX-PAMAM-G0 samples normalized at 379 nm in (A) DMF, (B) DMSO, (C) SDS, and (D) DTAB for the PyCX-PAMAM-G0 samples with X equal to (red) 4, (orange) 6, (green) 8, (blue) 10, and (black) 12. Plots of (E) I_E/I_M(TRF) as a function of the local pyrene concentration ($n_{Py}/(L_{Py}/l)^3$) and (F) I_E/I_M(TRF) as a function of I_E/I_M(SSF) for the PyCX-PAMAM-G0 samples in (○) DMF, (Δ) DMSO, (▲) 50 mM SDS, and (●) 50 mM DTAB.....42

Figure 2.3. Plots of (A) the molar fractions (black) f_{diff} and (red) f_{agg} as a function of linker length (X) and $\langle k \rangle$ as a function of $n_{Py}/(L_{Py}/l)^3$ for the PyCX-PAMAM-G0 samples in (B) DMF and DMSO and 50 mM (C) SDS and DTAB aqueous solutions. Symbols: (empty circles) DMF, (empty triangles) DMSO, (filled circles) SDS, and (filled triangles) DTAB.....45

Figure 3.1. Chemical structure of the PyCX-PAMAM-G0 dendrimers with $X = 4$, 6, 8, 10, and 12.....57

Figure 3.2. Schematic representation of the conformation of the PyCX-PAMAM-G0 samples

in SDS micelles (A) with X = 4, 6, and 8 and (B) with X = 10 and 12. The sulfate headgroups of SDS are spread apart resulting in a small packing parameter and a higher surface curvature.....59

Figure 3.3. (A) Schematic representation with values of the a, b, and c semiaxes for the triaxial SDS:DTAB micellar ellipsoid whose capping ends have a surfactant composition expected to approach those of an SDS micelle and (B) plot of f_{Cap} as a function of f_{DTAB}.....66

Figure 3.4. (A) Absorption and (B) fluorescence spectra for the PyCX-PAMAM-G0 samples with X equal to (red) 4, (orange) 6, (green) 8, (blue) 10, and (black) 12 in a 50 mM aqueous solution of the 75:25 SDS:DTAB mixture and (C) plot of I_E/I_M(SSF) as a function of linker length (X) in a 50 mM aqueous solution of the (red) 100:0, (orange) 90:10, (green) 80:20, (blue) 75:25, and (black) 70:30 SDS:DTAB mixtures.....68

Figure 3.5. Fluorescence decays of (A) the pyrene monomer (λ_{em} = 379 nm) and (B) the pyrene excimer (λ_{em} = 510 nm) of the PyC6-PAMAM-G0 sample in the 50 mM 75:25 SDS:DTAB solution. λ_{ex} = 336 nm, χ^2 = 1.03. (C) Plot of I_E/I_M(MFA) as a function of I_E/I_M(SSF) for the PyCX-PAMAM-G0 samples in a 50 mM aqueous solution of the (red) 100:0, (orange) 90:10, (green) 80:20, (blue) 75:25, and (black) 70:30 SDS:DTAB mixtures.....70

Figure 3.6. Plots of I_E/I_M(MFA,f_{free} = 0) as a function of linker length for the PyCX-PAMAM-G0 samples in (A) (hollow circles) DMF and (solid circles) DMSO and (B) in a 50 mM aqueous solution of the (red) 100:0, (orange) 90:10, (green) 80:20, (blue) 75:25, and (black) 70:30 SDS:DTAB mixtures.....71

Figure 3.7. Plots of (A) (solid) f_{diff} and (hollow) f_{agg} and (B) $\langle k \rangle$ for the PyCX-PAMAM-G0 samples in a 50 mM aqueous solution of the (red) 100:0, (orange) 90:10, (green) 80:20, (blue) 75:25, and (black) 70:30 SDS:DTAB mixtures. (C) Plot of the angle θ as a function of the composition of the catanionic surfactant mixture. The vertical dashed line in (C) indicates the

solubility limit of the SDS:DTAB mixture found to equal f_{DTAB} = 0.32.....74

Figure 3.8. (A) Radial distribution function ($r^2 \times W(r)$) for the end-to-end distance of the PyC*X*-PAMAM-G0 samples. From left to right: X = 4, 6, 8, 10, and 12. (B) Plot of $\langle k \rangle$ as a function of the volume fraction (f_{Cap}) of the capping hemispheres in the triaxial ellipsoids for the PyC*X*-PAMAM-G0 samples with X = (blue) 4, (red) 6, and (black) 8. (C) $\langle k \rangle$ values extrapolated to f_{Cap} = 0 in (B) ($\langle k \rangle^{Core}$) plotted as a function of $[Py]_{loc}$ for (solid circles) the PyC*X*-PAMAM-G0 samples with X = 4, 6, and 8 and (hollow circles) predicted $\langle k \rangle^{Core}$ values for the PyC*X*-PAMAM-G0 samples with X = 10 and 12.....77

Figure 3.9. Plots of the (circles) experimental $\langle k \rangle$ and (crosses) theoretical $\langle k \rangle^{th}$ obtained with the PyC*X*-PAMAM-G0 samples as a function of $[Py]_{loc}$ for f_{DTAB} equal to (A) 0.10, (B) 0.20, (C) 0.25, and (D) 0.30.....80

Figure 3.10. Schematic representation of the SDS:DTAB mixed micelles hosting a PyCX-PAMAM-G0 dendrimer with an inverted conformation in the capping hemisphere and with a regular conformation in the core section of the ellipsoidal micellar aggregates.....81

Figure 4.1. A) Chemical structure of the PyCX-PAMAM-G0 dendrimers with X = 4, 6, 8, 10, and 12 and B) illustration of a PyCX-PAMAM-G0 sample in an SDS micelle (top; X = 10, 12) undergoing and (bottom; X = 4, 6, 8) not undergoing a conformational inversion. Depiction of the spatial arrangement of the (blue) charged and (red) partially neutralized SDS molecules in the (C) SDS micelles, (D) elongated NSSA, and (E) extended rod-like NSSA.....87

Figure 4.2. Fluorescence spectra normalized at the 0-0 transition of pyrene for A) PyC12-PAMAM-G0 for [NaCl] increasing from (bottom) 0 to (top) 200 mM, B) PyC12-PAMAM-G0 for [NaCl] increasing from (top) 200 to (bottom) 620 mM, and plots of C) IE/IM, D) <k>, E) fagg, and F) <k>/fdiff as a function of [NaCl] for (green) PyC4-, (blue) PyC6-, (black) PyC8-, (orange) PyC10-, and (red) PyC12-PAMAM-G0. [SDS] = 50 mM, [Py] = 2.4 μM, λ_{ex} = 344 nm.....91

Figure 4.3. A) Plot of A) N_{agg} as a function of [NaCl] for N_{agg} values obtained from references (black triangles) #8 and (red squares) #4, B) (crosses) $[<k>/f_{diff}]^{exp}$ and (hollow circles) $[<k>/f_{diff}]^{th}$ as a function of f_{Mid}, C) $[<k>/f_{diff}]^{exp}(f_{Mid}=1)$ as a function of $[Py]_{loc}$. Colors for the $[<k>/f_{diff}]^{exp}$ and $[<k>/f_{diff}]^{th}$ symbols: (green) PyC4-PAMAM-G0, (blue) PyC6-PAMAM-G0, (black) PyC8-PAMAM-G0, (orange) PyC10-PAMAM-G0, and (red) PyC12-PAMAM-G0. [SDS] = 50 mM, [Py] = 2.4 μM.....96

Figure 4.4. Possible mechanism for the formation of cylindrical NSSA from the encounter between a (blue) SDS micelle and a (red) hydrophobic surfactant aggregate with exposed hydrophobic edges.....99

Figure 5.1. Illustration of A) a cylinder and B) a disk constituted of (red) surfactants with a large *cpp* and whose headgroups are partially neutralized and of (blue) surfactants with a small *cpp* and whose headgroups are fully charged. C) Chemical structure of the PyCX-PAMAM-G0 dendrimers with $X = 4$, 6, 8, 10, and 12. D) Expected conformation of the PyC10- and PyC12-PAMAM-G0 dendrimers in the (left) polar edge and (middle-top) hydrophobic middle regions of the NSSA.....107

Figure 5.2. SSF spectra of 0.45μM pyrene and 100mM NaCl in surfactant solution with total surfactant concentration ranging from A) 5.07mM to 1.01mM, B) 0.51mM to 0.10mM, and C) 0.08mM to 0.01mM. D) I_E/I_M(SSF) and I_1/I_3 retrieved from the fluorescence spectra plotted against total surfactant concentration.....118

Figure 5.3. A) Monomer and B) excimer fluorescence decay of 0.15mM molecular pyrene in mixed micelle solution with 100 mM NaCl. C) I_E/I_M calculated from MFA plotted as a function of I_E/I_M obtained from SSF.....120

Figure 5.4. Plots of A) $<n>$ as a function of pyrene concentration for various NaCl concentrations and B) N_{agg} as a function of NaCl concentration for NSSA made of (red circles) an 80:20 SDS:DTAB mixture and (black disks) pure SDS.....122

Figure 5.5. Plots of A) the number fraction of the NSSA as a function of the hydrodynamic diameter; Traces from left to right for solutions with 10, 20, 50, and 100 NaCl respectively and B) hydrodynamic diameter of NSSA as a function of N_{agg}.....123

Figure 5.6. Plots of A) the $[<k>/f_{diff}]^{exp}$ ratio and B) f_{agg} as a function of NaCl concentration for the PyCX-PAMAM-G0 samples in aqueous solutions of 40 mM SDS and 10 mM DTAB. The red, orange, green, blue, and black crosses are for the PyC4-, PyC6-, PyC8-, PyC10-, and PyC12-PAMAM-G0 samples, respectively.....125

Figure 5.7. Comparison of (crosses) $[<k>/f_{diff}]^{th}$ calculated from Equation 5.8 and (circles) $[<k>/f_{diff}]^{exp}$ obtained from the global MFA of the fluorescence decays plotted as a function of $[Py]_{loc}$ for NaCl concentrations equal to A)10, B) 20, C) 50, and D) 100 mM.....127

Figure 5.8. Plot of $[<k>/f_{diff}]^{exp}$ for the (red) PyC4-, (orange) PyC6-, and (green) PyC8-PAMAM-G0 samples and $[<k>/f_{diff}]^{exp}+f_{\underline{Edge}}\times f_{DTAB}\times[<k>/f_{diff}]^{A\text{-}C}$ for the (blue) PyC10- and (black) PyC12-PAMAM-G0 samples. (+) data obtained for SDS with NaCl, (×) data obtained for SDS:DTAB mixtures without salt, (●) data obtained for an 80:20 SDS:DTAB mixture with NaCl (this study), and (solid lines) trendlines generated by $[<k>/f_{diff}]^{th}$ calculated with Equation 5.8.....128

List of Tables

Table 4.1. $[<k>/f_{diff}]^{Mid}$, $[<k>/f_{diff}]^{Edge,Max}$, and $[<k>/f_{diff}]^{SDS}$ ratios and f_{Mid}^{Max} determined experimentally and used in Eq. 3 to predict the theoretical $[<k>/f_{diff}]^{th}$ ratio.....98

Table 4.2. Mathematical expression of $[< k > / f_{diff}]^{Edge}$ in Eq. 3.....98

Table 5.1. Mathematical expression of $[< k > / f_{diff}]^{Edge}$ used in Equation 5.8 for the PyC10- and PyC12-PAMAM-G0 dendrimers.....117

Table 5.2. $[<k>/f_{diff}]^{Mid}$, $[<k>/f_{diff}]^{Edge,Max}$, and $[<k>/f_{diff}]^{SDS}$ ratios and f_{Mid}^{Max} determined in earlier publication along with $[<k>/f_{diff}]^{A-C}$ calculated with Equation 5.9.....117

Table 5.3. Mixed micelle concentration and their aggregation number at different NaCl concentrations.....121

List of Abbreviations

a	Effective cross-section of a surfactant headgroup or number of carbon atoms in the linker connecting the pyrene moiety to the PAMAM dendrimer
a_i	Pre-exponential factor of the i^{th} exponential
AFM	Atomic force microscopy
CD	Circular dichroism
CMC	Critical micelle concentration
CPC	Cetylpyridinium chloride
cpp	Critical Packing Parameter
Cryo-SEM	Cryogenic scanning electron microscopy
Cryo-TEM	Cryogenic transmission electron microscopy
D	Translational diffusion coefficient
DLS	Dynamic light scattering
DMF	Dimethylformamide
DMSO	Dimethyl sulfoxide
DNA	Deoxyribonucleic acid
DPC	Dodecylpyridinium chloride
DTAB	Dodecyltrimethylammonium bromide
D_h	Number-average hydrodynamic diameter (from DLS)
f_{agg}	Molar fraction of aggregated pyrenyl labels
f_{Cap}	Volume fraction of capping hemispheres of triaxial ellipsoids
f_{Core}	Volume fraction of the ellipsoid core
FCQ	Fluorescence collisional quenching
f_D	Molar fraction of pyrenyl labels in pyrene aggregates forming

	excimer with two poorly stacked pyrene moieties
f_{diff}	Molar fraction of pyrenyl labels forming excimers via diffusive encounters
f_{DTAB}	Molar fraction of DTAB in surfactant mixtures
f_{ED}	Molar fraction of pyrenyl labels in pyrene aggregates detected in the excimer fluorescence decay forming excimer with two poorly stacked pyrene moieties
f_{Edge}	Volume fraction of the polar edge region of NSSA
f_{Ediff}	Molar fraction of pyrenyl labels detected in the excimer fluorescence decay forming excimer via diffusive encounters
f_{EdiffD}	Molar fraction of pyrenyl labels detected in the excimer fluorescence decay forming an excimer with two poorly stacked pyrene moieties via diffusive encounters
$f_{EdiffE0}$	Molar fraction of pyrenyl labels detected in the excimer fluorescence decay forming an excimer with two well-stacked pyrene moieties via diffusive encounters
f_{E0}	Molar fractions of pyrenyl labels in pyrene aggregates forming excimer with two well-stacked pyrene moieties
f_{EE0}	Molar fractions of pyrenyl labels in pyrene aggregates detected in the excimer fluorescence decay forming excimer with two well-stacked pyrene moieties
f_{free}	Molar fraction of free pyrene species
f_{Mdiff}	Molar fraction of pyrenyl moieties detected in the monomer fluorescence decay forming excimers via diffusive encounters
f_{Mfree}	Molar fraction of isolated pyrene monomers

f_{Mid}	Volume fraction of hydrophobic middle region of NSSA
FID	Free induction decay (NMR)
FRET	Fluorescence resonance energy transfer
HM	Hydrophobically modified
HM-PAMAM	Hydrophobically modified polyamidoamine
HMWSM	Hydrophobically modified water-soluble macromolecules
HG	Hydrophobicity gradient
HG^{Edge}	Hydrophobicity gradient in the NSSA edge region
HG^{Mid}	Hydrophobicity gradient in the NSSA middle region
I	Scattering intensity
I_E	Excimer fluorescence intensity
I_M	Monomer fluorescence intensity
I_0	Initial fluorescence intensity
I_1	First vibronic band intensity of pyrene
I_3	Third vibronic band intensity of pyrene
IRF	Instrument response function
k_{diff}	Bimolecular rate constant for diffusive encounters between pyrenyl labels
k_q	Quenching rate constant
$<k>$	Average rate constant of pyrene excimer formation
$[<k>/f_{diff}]^{Edge}$	$<k>/f_{diff}$ ratio in the NSSA Edge region
$[<k>/f_{diff}]^{Edge,Max}$	Maximum $<k>/f_{diff}$ ratio in the NSSA Edge region
$[<k>/f_{diff}]^{exp}$	Experimental $<k>/f_{diff}$ ratio
$[<k>/f_{diff}]^{Mid}$	$<k>/f_{diff}$ ratio in the NSSA Middle region
$[<k>/f_{diff}]^{SDS}$	$<k>/f_{diff}$ ratio in SDS micelles

$[\langle k\rangle/f_{diff}]^{th}$	Theoretical $\langle k\rangle/f_{diff}$ ratio
l	Length of the surfactant tail or length of a C-C bond
L_{Py}	End-to-end distance of pyrene-labeled dendrimers
MALLS	Multiangle laser light scattering
MDS	Molecular dynamics simulations
MFA	Model-free analysis
MHS	Mark-Houwink-Sakurada
$\langle n\rangle$	Average number of pyrene molecules per micelle
N_A	Avogadro number
N_{agg}	Aggregation number
NMR	Nuclear magnetic resonance
n_{Py}	Number of ground-state pyrene labels in a dendrimer
NSSA	Non-spherical surfactant aggregates
PEF	Pyrene excimer formation
PyLM	Pyrene-labeled macromolecule
PyCX-PAMAM-GY	Pyrene-labeled PAMAM dendrimers, X = linker length, Y = generation number
Py_{agg}*	Excited pyrene monomer involved in pyrene aggregates
Py_{diff}*	Excited pyrene monomer forming excimer by diffusive encounters
Py_{free}*	Excited pyrene monomer that does not form excimer
q	Scattering vector
R_0	Förster radius
R_h	Hydrodynamic radius
R_G	Radius of gyration
SANS	Small-angle neutron scattering

SAXS	Small-angle X-ray scattering
SEM	Scanning electron microscopy
SDS	Sodium dodecyl sulfate
SSF	Steady-state fluorescence
TEM	Transmission electron microscopy
THF	Tetrahydrofuran
UV	Ultraviolet
UV–vis	Ultraviolet-visible
V_M	Volume of macromolecule
V_{alkyl}	Volume of the alkyl tail of a surfactant
α	Exponent in the MHS equation
η	Solvent viscosity
$[\eta]$	Intrinsic viscosity
λ	Wavelength of incident irradiation in light scattering
λ_{ex}	Wavelength of excitation
λ_{em}	Wavelength of emission
θ	Angle between the $<k>$-*vs.*-$[Py]_{loc}$ straight lines obtained for dendrimers with a short (X=4,6,8) and a long (X=8,10,12) linker or detection angle in scattering experiments
τ_D	Lifetime of the pyrene excimer formed by two poorly stacked pyrene moieties
τ_{E0}	Lifetime of the pyrene excimer formed by two well-stacked pyrene moieties
τ_i	Decay time of the i^{th} exponential

τ_M	Lifetime of the pyrene monomer
τ_o	Lifetime of a dye without quencher
$<\tau>$	Number average fluorescence lifetime

Chapter 1: Introduction

1.0 Background

Polyamidoamine (PAMAM) dendrimers are a class of monodisperse synthetic macromolecules with a well-defined and highly branched architecture.[1,2] Due to their highly tunable structure and properties, they have seen great potential in a variety of applications for wastewater treatment or energy storage, and in drug delivery vehicle development.[3-5] Since native PAMAM dendrimers are highly water-soluble and possess tunable surface functionalities, their applications in hydrophobic environments can be limited. Moreover, the presence of free amine groups at the periphery of PAMAM dendrimers contributes significantly to their cytotoxicity, likely due to membrane disruption resulting from electrostatic interactions, which has hindered their development for pharmaceutical applications.[6] To address these issues, the hydrophobic modification of PAMAM dendrimers has emerged as a powerful strategy to modulate their physicochemical properties, enhance their self-assembly behavior, and expand their utility in drug delivery, nanoreactors, and supramolecular chemistry.[5,7,8]

Hydrophobic modifications of PAMAM dendrimers are commonly achieved via covalent attachment of (1) straight or branched alkyl chains onto the dendrimer surface to reduce solubility and promote micelle-like self-assembly,[9] (2) aromatic moieties like the pyrene dye for π–π stacking and enhanced encapsulation of aromatic guests like drugs,[10] or (3) biocompatible fatty acids or steroids, to facilitate membrane interactions or drug delivery.[11] These hydrophobically modified PAMAM dendrimers (HM-PAMAM) are especially useful in pharmaceutical applications due to their amphiphilic nature, which enables synergistical interactions with surfactants and penetration through lipid bilayers, enhancing their potential for transdermal or intracellular delivery.[12] The evaluation of their performance typically involves the characterization of their encapsulation efficiency and loading capacity.[13] Cell culture and fluorescence imaging are also common practices to study the cytotoxicity of the HM-PAMAM.[14] Although these characterization methods are the gold standard in identifying

interactions between HM-PAMAM and environments of interests such as a lipid cellular membrane, no molecular level information on the conformation of HM-PAMAM dendrimers within the lipid bilayers is provided. According to the literature, this molecular level understanding can be interpreted to reveal the location of PAMAM dendrimers inside the bilayers, how they interact with cell membranes, and possibly the mechanism of endocytosis.[15] As of today however, this understanding is exclusively obtained through molecular dynamics simulations (MDS) with little experimental backing.[16] Therefore, it is crucial to gain molecular level information about the conformation of HM-PAMAM as they interact with hydrophobic restricted geometries such as lipid bilayers through experimental means to fully understand the interactions between HM-PAMAM and a cellular membrane.

With the importance of HM-PAMAM conformation in bilayers and micelles having been clearly stated, it is also worth noting that their conformation and overall performance can be significantly affected by the nature of the hosting environment, as will be demonstrated in this thesis. Consequently, changes in the conformation of HM-PAMAM dendrimers can be used to describe the properties of its host, which in this thesis, are surfactant aggregates formed by sodium dodecyl sulfate (SDS) molecules or mixtures of SDS and dodecyltrimethylammonium bromide (DTAB). In effect, such studies lead to the dual characterization of both the conformation of HM-PAMAM dendrimers and the properties of their host, providing a synergistic approach to the study of these complex systems.

Surfactants have been used widely for decades due to their ability to lower the surface tension of aqueous solutions and self-assemble into surfactant aggregates such as micelles when present at surfactant concentrations above the critical micelle concentration (CMC).[17] The large number of extensive studies conducted over this long period and the resulting insights gained about these systems support the claim that surfactants serve as suitable candidates for forming simple and idealized restricted domains in water, whose properties mimic those

encountered in cell membranes.[18] Among synthetic surfactants, SDS and DTAB are classic representatives of anionic and cationic surfactants, respectively. Therefore, these surfactants were used in this thesis to study the conformation of HM-PAMAM dendrimers in various surfactant aggregates generated by SDS, DTAB, and their mixtures to provide different types of restricted hydrophobic microdomains in aqueous solution.

The characterization of surfactant aggregates typically involves the determination of their CMC, shape, and size through their aggregation number (N_{agg}), which is the number of surfactants per aggregate. Since the volume occupied by a methyl (49 Å^3) and methylene (28 Å^3) groups is known,[19] the volume (V_{alkyl}) of the alkyl tail of a surfactant can be determined, which yields the volume of the hydrophobic interior of a surfactant aggregate from the product $N_{agg} \times V_{alkyl}$.[20] Information about the size and shape of surfactant aggregates is obtained from scattering and spectroscopy techniques.[21] The good agreement found between the volumes determined from both methods supports their use in the characterization of surfactant aggregates.[20,21]

Despite the importance of the characterization of surfactant aggregates due to their multiple applications, our current understanding about surfactant aggregates is lacking in several aspects due to the limitations of conventional characterization methods. For instance, it is unclear how external parameters such as the addition of salt or oppositely charged surfactants affect the interior of surfactant aggregates as they grow in size in terms of the hydrophobicity gradient (HG) generated between the polar micellar surface and the hydrophobic interior. Therefore, the development of novel molecular probes to better characterize the interior of surfactant aggregates would represent a valuable achievement. In this context, this thesis aims to assess the value of pyrene end-labeled polyamidoamine (PAMAM) dendrimers as possible molecular probes in the study of surfactant aggregates.

The above discussion provides the different elements that will be discussed in the

Introduction of my thesis. First, the conventional characterization techniques used to probe the size and shape of surfactant aggregates and the conformation of macromolecules like HM-PAMAM dendrimers will be reviewed. For each characterization method, the type of information and how that information is obtained will be described, followed by a brief discussion on the reliability of the data and the limitations of these conventional techniques. Then the pyrene end-labeled PAMAM dendrimers used as molecular probes to characterize surfactant aggregates will be introduced followed by a brief review of the type of surfactant aggregates considered in this thesis. Finally, the outline of my thesis will be provided.

1.1 Characterization Techniques Used to Probe the Size and Shape of Surfactant Aggregates and the Conformation of Macromolecules

1.1.1 Scattering Techniques

Often regarded as the classic techniques for structural analysis, scattering techniques continue to play a central role in the characterization of the size and shape of macromolecules and colloids in the nanoscale owing to their non-destructive nature and the extensive methodological expertise, that was developed over many years. All scattering techniques are based on determining the spatial distribution of a radiation (neutron, X-ray, visible light) scattered by a sample of interest expressed as a plot of the scattering intensity I as a function of the scattering vector q. The relation between q and the scattering detection angle θ is given in Equation 1.1, where λ is the wavelength of the incident radiation.[22-24]

$$q = 4\pi \times \sin\theta / \lambda \tag{1.1}$$

One advantage of scattering techniques is that they yield a direct measure of the radius of gyration (R_G) of macromolecules and colloids by applying Guinier's law to the low-q region

of a $Ln[I(q)]$-*vs*-q^2 plot, which is linear with a slope equal to $(-R_G^2/3)$. In turn, R_G provides a measure of the macromolecular or colloidal radius. A common application of the Guinier analysis is found in gel permeation chromatography (GPC), where a polydisperse polymer sample is separated into infinitely thin slices of monodisperse samples, which are passed through a multiangle laser light scattering (MALLS) detector to get R_G for each slice allowing their averaging to obtain $<R_G>$ for the whole polymer sample.[25] Beside R_G obtained at low q values, information about macromolecular conformation or colloidal shape can be obtained by fitting the entire $I(q)$-*vs*-q profile according to an appropriate model by using small angle X-ray (SAXS) or neutron (SANS) scattering.[26] Specifically, SAXS is primarily sensitive to electron density differences, and SANS is sensitive to nuclear contrast, particularly between hydrogen and deuterium, making it ideal for contrast variation experiments and labeling studies.[27] Numerous examples can be found in the literature where the conformation of polymers, dendrimers, proteins, nucleic acids, and self-assembled systems like surfactant aggregates are characterized.[28,29]

Apart from the above-mentioned static scattering techniques, dynamic light scattering (DLS) is also widely applied to characterize the size of macromolecules and colloids due to its simplicity, speed, and sensitivity to size over a wide range of length scales (1 nm – 10 μm). DLS is particularly well-suited for characterizing macromolecules, polymers, proteins, surfactant aggregates, and nanoparticles in dilute to moderately concentrated solutions.[30,31] DLS operates by analyzing the temporal fluctuations in scattered light intensity resulting from the Brownian motion of particles. These fluctuations are mathematically related to the translational diffusion coefficient (D), which in turn yields the hydrodynamic radius R_h using the Stokes–Einstein equation shown as Equation 1.2.[32] η in Equation 1.2 represents the solvent viscosity.

$$R_h = \frac{k_B T}{6\pi\eta D} \tag{1.2}$$

Besides having the advantage of being non-invasive, application of scattering techniques to macromolecular or colloidal characterization has its requirements and limitations. For instance, the entity of interest must have a narrow size distribution, since large entities dominate the scattering signal, and broad or multimodal distributions are difficult to resolve accurately.[33,34] On this issue, SAXS and SANS do show better tolerance, but still suffer from structural blurring and parameters averaging to some extent during the analysis of scattering data obtained with polydisperse samples.[35] More importantly, all scattering techniques typically require sample concentrations above 1 g/L due to poor sensitivity.[26-29] This condition requires larger sample quantities for scattering studies, which can become costly when characterizing biomacromolecules like antibodies. Meanwhile, characterization of isolated macromolecules, that tend to concentrate in restricted domains like those generated by surfactant aggregates, is challenging even with isotope labeling, as the further elevated sample concentrations required in scattering experiments induce intermolecular interactions in the restricted domains, that are likely to alter macromolecular conformations.

1.1.2 Microscopy

Microscopy techniques provide essential insights into the morphology, size, and structure of materials at the micro-to-nanoscale. Among these, Atomic Force Microscopy (AFM),[36,37] Scanning Electron Microscopy (SEM),[38,39] and Transmission Electron Microscopy (TEM)[40,41] are most widely applied in nanoscience, materials science, and biophysics for their ability to resolve features from the micron scale down to the atomic level. Each technique operates on different physical principles. AFM is based on mechanical surface sensing as it measures forces between a sharp tip mounted on a flexible cantilever and the sample surface. As the tip raster-

scans over the surface, interactions induced by van der Waals, electrostatic, or mechanical forces cause deflections in the cantilever, which are monitored by a laser beam reflected onto a position-sensing photodetector.[42] SEM exploits electron-surface interactions by using a focused beam of high-energy electrons that scans across the sample surface. Interactions between electrons and atoms generate secondary electrons, backscattered electrons, and X-rays, which are collected to produce high-resolution images and provide compositional information.[43] Apart from surface interaction, nanoscale objects can also be probed by TEM where a beam of electrons is transmitted through an ultra-thin sample.[44] The transmitted electrons are scattered by the internal structure, producing an image with contrast based on density and atomic number. Modern TEMs also include diffraction and spectroscopy modes designed for different sample types and research goals. Collectively, these methods form a complementary suite of tools for investigating the size, shape, surface texture, and internal architecture of nanomaterials, thin films, polymers, and biological macromolecules.[45,46] However, the different sample preparations applied in these methods can lead to distortions of the macromolecule under study resulting in images that might not reflect the actual conformation of macromolecules in solution. In AFM, such distortions can be induced by the adsorption of the macromolecule onto the substrate, which can lead to flattening, or during the drying of macromolecules on the substrate surface. In SEM and TEM, samples are characterized in vacuum, which represents an even harsher condition that is likely to alter macromolecular conformations as the water molecules that stabilize the macromolecule are evacuated from the apparatus.[47] Other artefacts encountered in SEM and TEM are induced by the heavy metal stains used to enhance contrast, that can potentially interfere with the conformation of the macromolecule of interest.[48] This is especially challenging for colloids and biological samples as they typically provide little contrast. More advanced techniques like Cyro-SEM and Cryo-TEM can be applied to avoid the complications induced by the drying

and staining process.[49,50] However, since both techniques provide 2D projections, overlapping features or particles at different depths can obscure structural details, unless a tilt-series of images are acquired to reconstruct the tomography of the soft material under study.[51] Despite the investigative power of Cyro-TEM, this technique would struggle to characterize the conformation of small organic molecules such as the generation-0 PAMAM (PAMAM-G0) dendrimers investigated in this thesis due to resolution limit and the low contrast of organic molecules on their own and embedded inside surfactant aggregates. Information about the conformation of PAMAM-G0 dendrimers would also be difficult to obtain by SEM since it focuses on surface morphology and provides little information about the interior of restricted domains, such as the surfactant aggregates where the PAMAM-G0 dendrimers investigated in this thesis would reside.

1.1.3 Viscometry and Rheology

While scattering and microscopy methods offer a direct experimental means for measuring the size and shape of macromolecules and colloids, viscosity measurements can provide complementary information about bulk flow behavior, which reflects similar molecular-level features. Like scattering and microscopy, these techniques are non-invasive, scalable, and sensitive to changes in molecular architecture, making them valuable tools for characterizing polymer size and conformation, network formation, and aggregation phenomena. Perhaps the most useful parameter for characterizing size and shapes obtained by viscometry is the intrinsic viscosity ($[\eta]$), which yields the hydrodynamic radius of a macromolecule according to Equation 1.3, where N_A is the Avogadro number and M is the molecular weight of the macromolecule.

$$[\eta]=\frac{10\pi}{3}N_A\frac{R_h^3}{M} \tag{1.3}$$

Furthermore, the parameters K and α obtained for the Mark-Houwink-Sakurada (MHS) relationship given in Equation 1.4 are related to the macromolecular conformation in solution. In Equation 1.4, M_v represents the viscosity-average molecular weight. For instance, α takes a value of 0.50 or 076 for a polymer in a θ– or a good solvent, where the chain takes an ideal or extended conformation, respectively. Moreover, the dependence of $[\eta]$ on the nature of the macromolecule can be used to obtain conformational information such as branching,[52,53] rigidity,[54] or solvent quality reflecting chain extension.[55]

$$[\eta] = K \times M_v^{\alpha} \tag{1.4}$$

As for rheology measurement, entanglements of macromolecules or aggregates in the sample solution can be revealed by the shear-thinning effect.[56] Such behavior is also observed in surfactant solutions as a network form between surfactant aggregates, which can be enabled by the presence of hydrophilic chains like poly(ethylene oxide) modified at both ends with hydrophobic groups.[57,58]

Similar to scattering experiments, viscosity and rheology measurements are non-invasive, but a sample concentration higher than 1 g/L is also typically necessary for the bulk phase to show detectable changes from the solvent. Intermolecular interactions can be an issue at such high concentration. Another major limitation for scattering and viscosity measurements is that the sample characterization is conducted on the bulk phase and is therefore indirect. It requires further modeling to extract the information relevant to study the size and shape of macromolecules and colloids and leads to complications when dealing with heterogeneous samples.

1.1.4 Spectroscopy Based Characterization Methods

Other useful tools for characterizing the size and shape of macromolecules and colloids are based on spectroscopic techniques. Most applied examples include nuclear magnetic resonance (NMR), circular dichroism (CD), and fluorescence spectroscopy.

1.1.4.1 Nuclear Magnetic Resonance (NMR) and Circular Dichroism (CD)

NMR and CD are especially useful for investigating the secondary structures of macromolecules,[59] particularly proteins, peptides, nucleic acids, and synthetic polymers such as polypeptides.[60-62] NMR exploits the magnetic properties of certain atomic nuclei like ^{1}H, ^{13}C, and ^{15}N that possess a non-zero nuclear spin. In a magnetic field, these nuclei absorb energy and transition between states having different spins. The subsequent relaxation and emission of energy by the nuclei generate detectable signals resulting in a free induction decay (FID), which is Fourier-transformed to yield an NMR spectrum.[63] 1D NMR has been the gold standard to probe the chemical environment of nuclei and the chemical structure of small organic molecules, while 2D and 3D NMR can provide further information such as the coupling between non-zero spin nuclei, sequence information for peptides, and through space distances, which can ultimately be translated into the 3D structure of a macromolecule.[64,65]

CD measurements are based on the differential absorption of left-handed and right-handed circularly polarized light by optically active substances. Therefore, molecules that possess chiral centers or adopt asymmetric conformations, which are common in biological macromolecules, can be clearly identified using CD. CD spectra are typically recorded in the far-UV (180–250 nm)[66,67] and near-UV (250–320 nm) regions.[68] CD in the far-UV is sensitive to peptide bond transitions and is used to assess secondary structure (α-helix, β-sheet, random coil). Specifically, α-helices show characteristic double minima at ~208 and 222 nm, β-sheets exhibit a single minimum around 216–218 nm, and random coils show a minimum near 198

nm. Deconvolution of CD spectra using reference datasets yields the relative content of each secondary structure.[69] On the other hand, near-UV CD probes the environment of aromatic side chains and disulfide bonds, providing insights into tertiary structure. It can be used to monitor protein folding, thermal denaturation, and ligand-induced conformational changes.[70,71,72]

NMR and CD measurements bear the advantage of being non-destructive and are performed in aqueous or physiological conditions, which reflects the natural state of the macromolecule under characterization. Nevertheless, NMR requires the sample to tumble reasonably fast in solution while CD measurements have relatively low-resolution.[70] Both techniques can also be affected by the presence of solvent, whose signal can overlap that from the macromolecule of interest in the CD or NMR spectra. This is a particularly challenging problem for CD measurements with solvents that absorb in the far UV region such as DMF or DMSO. The problems associated with the presence of residual solvents in a sample are typically due to the sample purification process with some solvents remaining bound to a macromolecule through strong interactions. Meanwhile, both techniques also require sample concentrations that are typically above 1 g/L, which leads to the same issues encountered with scattering techniques for the determination of macromolecular conformation with potential intermolecular interactions resulting in conformational changes.

1.1.4.2 Fluorescence Techniques

The only meaningful way for preventing intermolecular interactions and probing isolated macromolecules involves lowering the sample concentration and amplifying the signal emanating from the macromolecule. In this context, fluorescence with its high sensitivity and ability to determine intramolecular distances is ideally suited to characterize macromolecular conformations. The most prominent fluorescence technique is fluorescence resonance energy

transfer (FRET) due to its ability to act as a "spectroscopic ruler" and determine distances between 1 and 10 nm, [73] which is ideal for tracking conformational changes in macromolecules.[74] FRET describes a highly distance-dependent transfer of energy from an excited donor to a nearby energy acceptor via dipole-dipole coupling. The transfer requires spectral overlap between the donor emission and the acceptor absorption, and the FRET efficiency is given in Equation 1.5. In Equation 1.5, r is the distance between the donor and acceptor, and R_0 is the Förster radius, which is specific for a given donor/acceptor pair.

$$E = \frac{1}{1 + (r / R_o)^6} \tag{1.5}$$

Analysis of the fluorescence spectrum of a macromolecule doubly labeled with an energy donor and acceptor yields E, whose expression can be rearranged to give r, enabling the study of macromolecular conformation. A representative example can be found in a recent study on DNA aptamers where FRET was applied to detect the ligand and provide structural information about the aptamer.[75] Despite its widespread use, FRET can only be quantitatively applied to obtain intramolecular distances for structured macromolecules that were labeled at two specific positions, typically the chain ends. Since backbone dynamics for unstructured macromolecules affect the donor/acceptor distance and thus E, FRET is mostly applied to probe chain dynamics for linear chains whose conformation is already known. Furthermore, labeling of a macromolecule with multiple donors and acceptors results in an intractable distribution of intramolecular distances greatly complicating the quantitative analysis of the fluorescence signal. The restriction of working with a doubly labeled structured macromolecule seriously limits the applicability of FRET to the study of more complex colloidal systems such as those involving the interactions between HM-PAMAM dendrimers and surfactant aggregates investigated in this thesis.

Beside FRET, fluorescence collisional quenching (FCQ) can also be used for probing macromolecular conformations by labeling a macromolecule with a dye/quencher pair, where quenching of the excited dye occurs strictly upon contact with the quencher instead of over distance as with FRET. Like FRET, early FCQ experiments focused on macromolecules labeled at two specific positions, typically the chain ends of a monodisperse chain, to gain information about macromolecular conformation from the quenching efficiency determined form the intramolecular quenching rate constant (k_q).[76-78] Recognizing the conceptual difficulty of measuring the volume (V_M) of a macromolecule, k_q represented a pseudo-unimolecular rate constant equal to the product $k_{diff}\times(1/V_M)$, where k_{diff} is the bimolecular rate constant for diffusive encounters between the dye and quencher and $(1/V_M)$ is the local quencher concentration equivalent to one quencher molecule inside V_M. In these experiments, a large or small k_q reflected a small or large V_M associated with a compact or expanded macromolecule.

Unfortunately, these early FCQ experiments on macromolecules were plagued by the similar requirement of dealing with well-defined macromolecules labeled at two specific positions as for FRET, without the benefit of determining intramolecular distances like FRET. As for FRET, the multiple labeling of macromolecule with dyes and quenchers would result in an intractable distribution of rate constants preventing quantitative analysis of the fluorescence data.[79] A solution to this problem was recently introduced, when the average rate constant ($\langle k \rangle$) for the quenching of a macromolecule labeled with multiple dyes and quenchers was found to be directly proportional to the product $k_{diff}\times[Q]_{loc}$, where $[Q]_{loc}$ is the local quencher concentration in the fluorescently labeled macromolecule.[80] A mathematical expression for $[Q]_{loc}$ was derived by dividing the known number of quenchers in a macromolecule by the cube of the square root of the squared end-to-end distance between all dyes and quencher calculated by assuming that the oligomeric segments linking every dye/quencher pair in a macromolecule obeyed Gaussian statistics. Using series of pyrene end-labeled monodisperse oligomers and

dendrimers and polydisperse linear chains randomly labeled with pyrene, a 1:1 direct relationship was found between $<k>$ for pyrene excimer formation (PEF), a classic FCQ example, and the local concentration ($[Py]_{loc}$) of ground-state pyrenes in the macromolecules.[80] Since the location of the pyrenyl labels on the macromolecules was known, $[Py]_{loc}$ determined from the observable $<k>$ obtained from the analysis of the fluorescence decays of the pyrene-labeled macromolecules (PyLM) reflected the local density of the macromolecule, which could be used in a quantitative manner to determine its conformation.

Apart from macromolecular conformation, fluorescence is also well suited for the characterization of surfactant assemblies. FCQ experiments can be adapted to measure the critical micelle concentration (CMC),[81,82] above which surfactant micelles start to form, as well as the micelle size from the aggregation number (N_{agg}),[81,83,84] which is the number of surfactant molecules per micelle. The calculation of N_{agg} from FCQ experiments involves the use of a fluorescent probe such as pyrene that preferentially interacts with the surfactant aggregates, and a fluorescence quencher like cetyl- (CPC) or dodecyl- (DPC) pyridinium chloride or dinitrotoluene that similarly associates with the surfactant aggregates. The determination of the CMC is often achieved with a dye whose fluorescence signal changes with the polarity of its environment. The pyrene dye is particularly suitable for N_{agg} and CMC measurements as it acts as its own quencher by forming a pyrene excimer and responds to the polarity of its local environment.[85,86] Figure 1.1 shows the fluorescence spectrum of an 8 mM aqueous solution of SDS with 0.6 μM pyrene, where the pyrene monomer emits sharp bands between 370 and 410 nm and the excimer fluoresces with a broad structureless emission centered at 480 nm.

The fact that pyrene self-quenches to form an excimer is a main advantage for using pyrene as a dye since no additional quencher is required, which simplifies the experimental design and procedure. The determination of the CMC of the surfactant involves the use of a

low pyrene concentration due to its poor solubility in water (0.7 μM)[87] to prevent PEF between excited and ground-state pyrenes. As the surfactant concentration is increased above the CMC and micelles start to form, the pyrene molecules are concentrated in the micellar hydrophobic interior and PEF occurs. As the surfactant concentration is further increased, more micelles form and the pyrene molecules distribute themselves into the micelles, where they are isolated and can no longer undergo PEF resulting in a decrease in excimer fluorescence. An example of this type of experiment can be found in a previous study.[88]

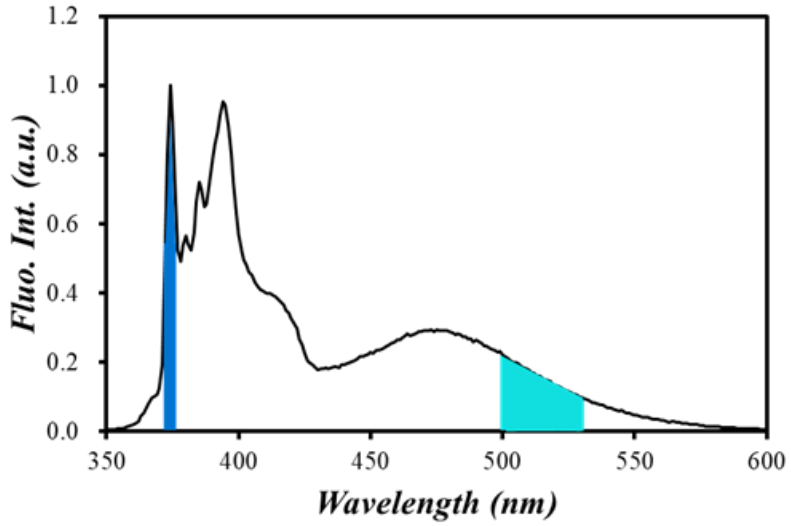


Figure 1.1 Example of a pyrene fluorescence spectrum obtained for an aqueous solution of 0.6 μM pyrene in the presence of 8 mM SDS.

Since the transfer of a pyrene molecule from the polar water phase to the hydrophobic interior of surfactant micelles is accompanied by a change in the polarity of the local environment probed by an excited pyrene molecule, it is accompanied by changes in the pyrene fluorescence spectrum. The partitioning of pyrene between water and micelles can be monitored from changes in the relative fluorescence intensity of the first (I_1) and third (I_3) in the pyrene fluorescence spectrum.[85,86] The I_1/I_3 ratio has been reported to take a value of 1.87[86] and 1.04[85] for pyrene in water and inside SDS micelles, respectively, with a I_1/I_3-*vs*-[Surfactant]

plot showing a sharp transition at a surfactant concentration equal to the CMC.[88] Consequently, changes in the I_1/I_3 and I_E/I_M ratios can be used effectively to determine the CMC of surfactants.

FCQ experiments have also been used extensively to determine N_{agg}. These experiments are conducted with a dye and quencher having a strong affinity for the surfactant micelles induced by hydrophobicity or electrostatic attraction. A very low dye concentration is used to ensure that the probability of having more than one dye per surfactant aggregate is negligible. The surfactant aggregates are then populated by the quenchers, which distribute themselves among the surfactant aggregates according to a Poisson distribution. The quenching of the dye is then described by Equation 1.6 derived by Tachiya,[89] which is used to fit the fluorescence decays.[83,84]

$$I(t) = I_o \times \exp(-t/\tau_o - < n > [1 - \exp(-k_q t)]) \tag{1.6}$$

In Equation 1.6, I_0 and I(t) are the fluorescence intensities at time 0 and t, respectively, while τ_o is the lifetime of the unquenched dye, k_q is the quenching rate constant, and $<n>$ represents the average number of quenchers per micelle. A mathematical expression of $<n>$ is given in Equation 1.7. Since the CMC is determined earlier, $<n>$ can be obtained from the decay fit with Equation 1.6, and since the quencher and surfactant concentrations are known, Equation 1.7 can be rearranged to yield N_{agg}.[83,84,90] While Equation 1.7 works extremely well to determine N_{agg} for many surfactant micelles, it failed for surfactant aggregates and vesicles.[83] The high viscosity found in surfactant aggregates and vesicles results in a time dependent quenching rate constant ($k_q(t)$), which is not accounted for by Tachiya's equation.[89] Furthermore, isolation of dyes without quencher would be impossible to achieve with the much larger vesicles, which would prevent application of the Poisson distribution of quenchers associated with the failure of Equation 1.6.

$$< n > = N_{agg} \times \frac{[Q]}{[\text{Surfactant}] - CMC} \tag{1.7}$$

For the many surfactant micelles where the micellar volume is small, k_q is large, so that for long-lived dyes like ruthenium complexes,[90] Equation 1.6 simplifies to $I_o \times \exp(-t/\tau_o)\exp(-<n>)$, which can be used to calculate the fluorescence intensity ratio $I([Q]=0)/I([Q])$ of a micellar solution without and with quencher, whose expression is given in Equation 1.8. According to Equation 1.8, a plot of $Ln[(I([Q]=0)/I([Q])]$ as a function of quencher concentration gives a straight line whose slope equals $N_{agg}/([\text{Surfactant}] - CMC)$ according to Equation 1.7 and can be used to determine N_{agg}.[90]

$$\frac{I([Q]=0)}{I([Q])} = \frac{\int_{t=0}^{\infty} I_o \times \exp(-t/\tau_o)dt}{\int_{t=0}^{\infty} I_o \times \exp(-t/\tau_o)\exp(-<n>)dt} = \exp(<n>) \tag{1.8}$$

1.2 Model Free Analysis (MFA)

The phenomenological analysis of FCQ experiments conducted with dyes and quenchers interacting within confined microdomains such as the interior of surfactant micelles[89,90] or when attached to a macromolecule[76-78] have led to the application of physical models leading to the derivation of equations, that can be applied to fit fluorescence decays. The equations derived by Tachiya[90] or Birks[91] to describe FCQ in surfactant micelles[81,82] or linear monodisperse chains end-labeled with two pyrenyl dyes[76-78] are classic illustrations of such theoretical investigations. The problem with this modus operandi however is that slight changes to the original conditions for which those phenomenological equations were derived typically

blocks their usage, which is a major scientific hurdle. The introduction of the model free analysis (MFA) was meant to circumvent these deficiencies by providing an analytical method that would always provide some quantitative information about the system under study.[92] The MFA is designed for FCQ experiments involving PEF with the pyrene dye, whereby the fluorescence decays of the pyrene monomer and excimer are fitted globally to enhance the accuracy on the kinetic parameters retrieved from the analysis.[7979] Moreover, the versatility of the MFA enables its application to problems as varied as the determination of N_{agg} for surfactant aggregates or characterization of macromolecular conformation.[93-95]

1.2.1 Probing the Conformation of Macromolecules with the MFA

Application of the MFA for the characterization of macromolecular conformations requires that the macromolecule be labeled with a pyrene derivative, and the fluorescence decays of the pyrene monomer and excimer obtained for the pyrene-labeled macromolecule (PyLM) be fitted globally with Equations 1.9 and 1.10, respectively.[96,97] The sum of exponentials used in Equation 1.9 to fit the pyrene monomer fluorescence decay reflects the fact that any fluorescence decay can be fitted with a sum of exponentials. An example of global fit according to the MFA can be found in Figure 2.

$$[Py^*]_{(t)} = [Py^*_{diff}]_{(t=0)} \times \sum_{i=1}^{n} a_i \times \exp(-t/\tau_i) + [Py^*_{free}]_{(t=0)} \times \exp(-t/\tau_M) \tag{1.9}$$

$$[E^*]_{(t)} = -[Py^*_{diff}]_{(t=0)} \times \sum_{i=1}^{n} a_i \frac{\frac{1}{\tau_i} - \frac{1}{\tau_M}}{\frac{1}{\tau_i} - \frac{1}{\tau_{E0}}} \exp(-t/\tau_i) + \left([E0^*]_{(t=0)} + [Py^*_{diff}]_{(t=0)} \times \sum_{i=1}^{n} a_i \frac{\frac{1}{\tau_i} - \frac{1}{\tau_M}}{\frac{1}{\tau_i} - \frac{1}{\tau_{E0}}} \right) \times \exp(-t/\tau_{E0})$$

$$-[Py^*_{diff}]_{(t=0)} \times \sum_{i=1}^{n} a_i \frac{\frac{1}{\tau_i} - \frac{1}{\tau_M}}{\frac{1}{\tau_i} - \frac{1}{\tau_D}} \exp(-t/\tau_i) + \left([D^*]_{(t=0)} + [Py^*_{diff}]_{(t=0)} \times \sum_{i=1}^{n} a_i \frac{\frac{1}{\tau_i} - \frac{1}{\tau_M}}{\frac{1}{\tau_i} - \frac{1}{\tau_D}} \right) \times \exp(-t/\tau_D)$$

$$+ [ES^*]_{(t=0)} \times \exp(-t/\tau_{ES}) \tag{1.10}$$

In Equations 1.9 and 1.10, τ_M represents the lifetime of the pyrene monomer, and it is fixed during the MFA of fluorescence decays. Equation 1.9 is split into two contributions depending on whether an excited pyrene forms (Py_{diff}*) or does not form (Py_{free}*) an excimer by diffusive encounter with a ground-state pyrene. The pre-exponential factors (a_i) and decay times (τ_i) can be used to derive Equation 1.10 providing a mathematical expression for the fluorescence decay of the pyrene excimer assuming that an encounter between an excited and a ground-state pyrene results into an excimer *E*0* or *D** where the two pyrenyl moieties are well or poorly stacked, respectively. The pyrene moieties involved in an excimer *E*0* or *D** emit with the excimer lifetimes τ_{E0} or τ_D, respectively. An excimer *E0** or *D** can also be generated through the direct excitation of a pyrene aggregate. In some cases, the presence of short-lived pyrene excimer (*ES**) has been detected but their contribution to the excimer fluorescence decays is typically ignored due to their short decay time (~ 3-4 ns).[98]

The pre-exponential factors (a_i) and decay times (τ_i) in Equation 1.9 can be combined in Equation 1.11 to yield the average decay time ($<\tau>$), which is then used to determine the average rate constant ($<k>$) for PEF. $<k>$ has been shown to be directly proportional to the local concentration ($[Py]_{loc}$) of ground-state pyrenyl labels experienced by an excited pyrenyl label in a PyLM.[80] Since $[Py]_{loc}$ is proportional to the local density of a macromolecule, which reflects its conformation, $<k>$ is an observable determined experimentally that can be used to probe macromolecular conformations.

$$< k >= \frac{\sum_{i=1}^{n} a_i}{\sum_{i=1}^{n} a_i \tau_i} - \frac{1}{\tau_M} = \frac{1}{< \tau >} - \frac{1}{\tau_M} = k_{diff} \times [Py]_{loc} \qquad (1.11)$$

The pre-exponential factors retrieved from the global MFA of the fluorescence decays yield the molar fractions f_{free}, f_{diffE0}, f_{diffD}, f_{E0}, and f_D of the pyrene species Py_{free}*, the pyrene species Py_{diffE0}* and Py_{diffD}* producing the excimers $E0$* and D* by diffusive encounters, and the pyrene species involved in the formation of the excimers $E0$* and D* by direct excitation of a pyrene aggregate, respectively. Summing f_{diffE0} and f_{diffD} on the one hand and f_{E0} and f_D on the other hand yields the molar fractions f_{diff} and f_{agg} of pyrene species forming excimer by diffusive encounters or direct excitation of a pyrene aggregate, respectively.

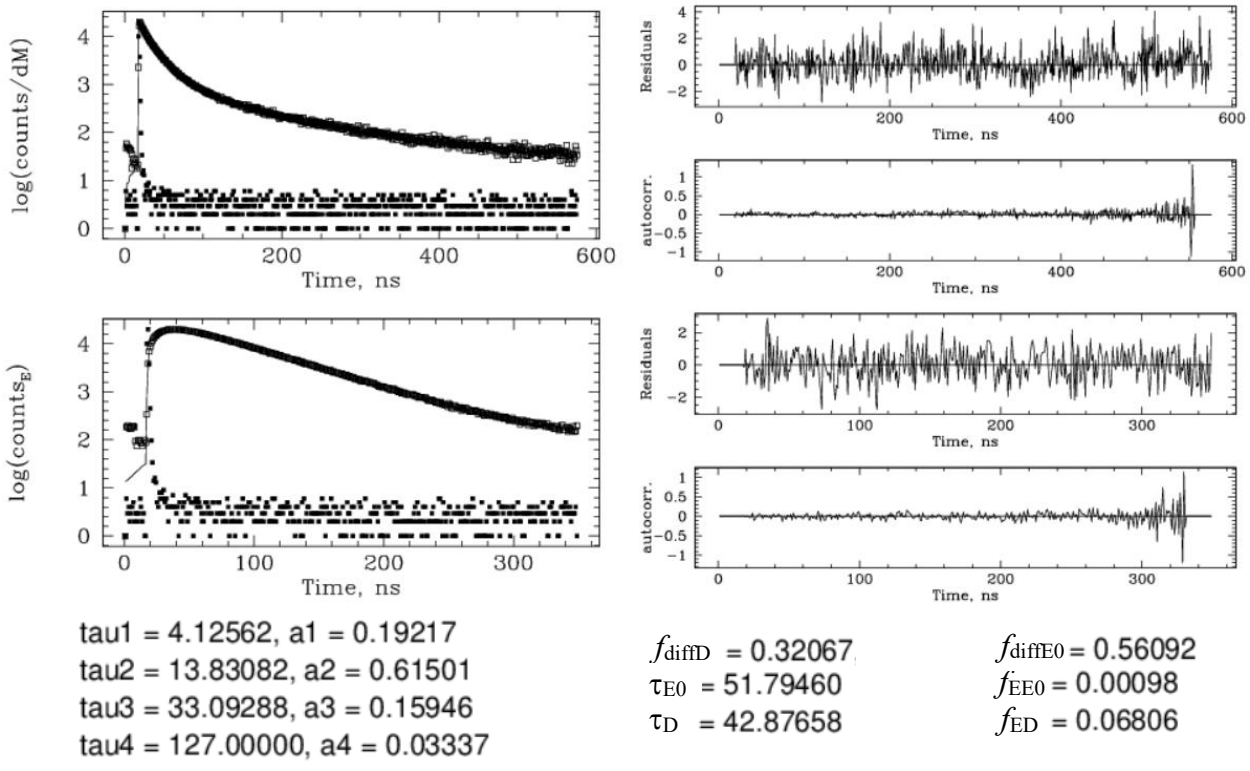


Figure 1.2. Monomer (top left) and excimer decay (bottom left) obtained from polyamidoamine dendrimers labeled with pyrene octanoic acid in an aqueous solution of 50 mM SDS and 10 mM NaCl. Residuals and autocorrelation of the residuals are shown in the right panels. They are randomly distributed around zero indicating that the quality of the fit is satisfactory. Fluorescence decay times τ_i and their pre-exponential factors a_i are listed at the bottom left. Excimer lifetimes and molar fractions of the pyrene species are presented in the

bottom right. $\chi^2 = 1.11$.

The parameters retrieved from the MFA can be rearranged into Equation 1.12 to yield the absolute I_E/I_M(MFA) ratio which is expected to be proportional to the relative I_E/I_M ratio obtained through the analysis of the fluorescence spectrum of a system undergoing PEF (see Figure 1.1).[99,100]

$$I_E / I_M(MFA) = \frac{(f_{diffE0}\tau_{E0} + f_{diffD}\tau_D) < k > < \tau > + f_{E0}\tau_{E0} + f_D\tau_D}{(f_{diffE0} + f_{diffD}) < \tau > + f_{free}\tau_M} \quad (1.12)$$

1.2.2 Determining N_{agg} for Surfactant Aggregates with the MFA

One advantage of the MFA is that it can use the ratio $[Py_{free}^*]_o/([Py_{diff}^*]_o + [Py_{free}^*]_o)$ retrieved from the monomer fluorescence decays (see Equation 1.9) to yield the molar fraction (f_{Mfree}) of pyrene moieties that do not form excimer. In the case of pyrene molecules distributed inside surfactant micelles, f_{Mfree} has been shown to be related to the average number ($<n>$) of pyrene molecules per surfactant micelle as shown in Equation 1.13.[101] Equation 1.13 thus provides a means for determining N_{agg} by introducing $<n>$ into Equation 1.7, which was presented earlier.

$$<n> = -Ln(f_{Mfree}) \quad (1.13)$$

1.3 Goal of the Thesis

The ability of the MFA to retrieve $<k>$, which is an experimental observable that reports on the macromolecular conformation of a PyLM in solution, opens the path for taking advantage of the outstanding sensitivity of fluorescence in general and PEF in particular to probe the conformation of PyLM in the nooks and crannies of soft matter. It is applied in my thesis to characterize the conformation of a series of pyrene end-labeled generation-0 polyamidoamine

(PyCX-PAMAM-G0) dendrimers as they interact with surfactant aggregates generated with aqueous solutions of SDS to which NaCl, DTAB, or a mixture of both are added.

1.3.1 PyCX-PAMAM-G0 Dendrimers

A generation 0 PAMAM dendrimer had its four amine terminals modified with either 1-pyrenebutyric acid (PyC4), 1-pyrenehexanoic acid (PyC6), 1-pyreneoctanoic acid (PyC8), 1-pyrenedecanoic acid (PyC10), and 1-pyrenedodecanoic acid (PyC12) to yield the PyCX-PAMAM-G0 dendrimers with *X* equal to 4, 6, 8, 10, and 12, respectively.[94,100] The chemical structure of the PyCX-PAMAM-G0 samples is given in Figure 1.3. The PAMAM dendrimer in red is soluble in water but not in the hydrophobic interior of the surfactant aggregates but the pyrene moiety in blue together with the alkanoyl linker in green is insoluble in water and interacts with the micellar interior. The PyCX-PAMAM-G0 samples are thus macromolecular probes, whose pyrenyl labels will undergo PEF as they interact with surfactant aggregates, and the observable <*k*> will be determined to probe the conformation of the PyCX-PAMAM-G0 dendrimers interacting with surfactant aggregates.

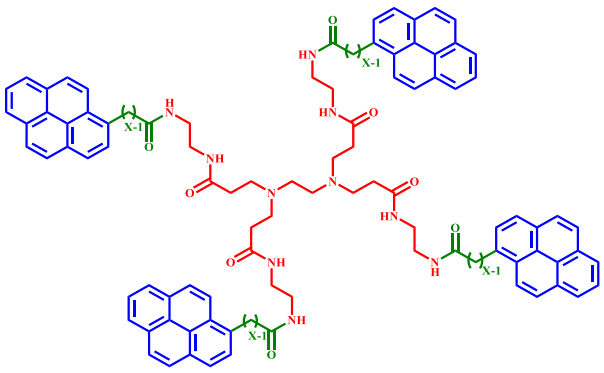


Figure 1.3. Chemical structure of the PyCX-PAMAM-G0 dendrimers. (red) PAMAM-G0 core, (green) alkanoyl linker with *X* = 4, 6, 8, 10, and 12, and (blue) pyrenyl moiety.

1.3.1 SDS Micelles

SDS is probably the most applied, and as such, most studied surfactant. SDS molecules are constituted of a charged sulfate headgroup and a hydrophobic dodecyl tail. In aqueous solutions, their amphiphilic nature induces them to locate themselves at the water/air interface, which lowers the surface tension, and to self-assemble into micelles at concentrations above its CMC in water, which is around 8 mM.[102-104] The formation of SDS micelles has been exploited in the production of food,[105] detergent, pesticides,[106] and numerous other applications, where an homogeneous mixing between an organic or oily phase and water is needed. The numerous studies, that were conducted on SDS micelles using the characterization methods that were reviewed in Section 1.1, have revealed that SDS micelles can be approximated as spheres with a diameter of about 3.6 nm[107,108] made of a number (N_{agg}) of about 70 SDS molecules.[90] Further studies with NaCl suggested that the spherical SDS micelles morphed into non-spherical surfactant aggregates (NSSA) taking a rod-like shape at high NaCl concentrations.[109,110] This conclusion was drawn from the increase in their N_{agg} and hydrodynamic diameter (D_h) and was attributed to the screening effect where the sodium ions partially neutralize the negative charge of the SDS headgroup, and reduce the repulsion between them.[111,112] The headgroup of those partially neutralized SDS will thus have a smaller cross-section a, and a larger critical packing parameter (cpp), which equals $v/(a \times l)$, with v and l being the volume and extended length of the surfactant alkyl tail. Partially neutralized SDS pack more closely due to their larger cpp resulting in smaller surface curvature as well as bigger micelle size.[111]

1.3.2 SDS and DTAB Mixed Micelles

Besides adding NaCl to an SDS aqueous solution, the size of SDS micelles can also be adjusted by introducing a surfactant with an oppositely charged headgroup, which reduces the cross-section of the SDS sulfate headgroup, increases the cpp, and leads to the formation of larger

mixed micelles. In this regard, surfactant aggregates made of SDS/DTAB mixtures have been intensively studied. It has been shown through SAXS,[113] Cryo-TEM,[114] and FCQ,[81,82] that the size of SDS/DTAB mixed micelles increases as the molar fraction of DTAB in the SDS/DTAB mixture increases from 0 to 0.32 and they morph from spheres for pure SDS micelles to elongated triaxial ellipsoids.[115] Moreover, at 0.32 DTAB, the surfactant aggregates transform into much larger structures like vesicles, which can be used as templates to grow nanoparticles or biological membrane mimics for drug delivery studies.[81]

1.4 Research Objective and Thesis Outline

As discussed in the Introduction, the goal of this project is to illustrate how PEF can be applied to probe the conformation of macromolecules in restricted microdomains. This is accomplished with a series of pyrene end-labeled generation-0 PAMAM dendrimers interacting with the surfactant aggregates generated in aqueous solutions of SDS to which NaCl, DTAB, or mixtures of both were added. In the second chapter, the five PyCX-PAMAM-G0 dendrimers were first studied in two homogeneous organic solvents, namely DMF and DMSO, before being probed in pure SDS and pure DTAB micelles to demonstrate the validity of the methodology.[100] The global MFA of the fluorescence decays of the pyrene-labeled dendrimers dissolved in homogeneous solvents or interacting with surfactant micelles yielded $\langle k \rangle$, which was plotted against $[Py]_{loc}$ calculated with the assumption that the internal segments of the dendrimers obeyed Gaussian statistics. The $\langle k \rangle$-*vs*-$[Py]_{loc}$ plots yielded straight lines passing through the origin for all the dendrimers in DMF and DMSO and for the PyC4-, PyC6-, and PyC8-PAMAM-G0 dendrimers with the surfactant micelles. This result demonstrated that the internal segments of PyC4-, PyC6-, and PyC8-PAMAM-G0 obeyed Gaussian statistics in DMF, DMSO and the SDS and DTAB micelles. However, a much larger than expected $\langle k \rangle$ value was obtained for the PyC10- and PyC12-PAMAM-G0 dendrimers in pure SDS and DTAB aqueous

solutions resulting in a characteristic checkmark pattern in the $<k>$-*vs*-$[Py]_{loc}$ plot. This checkmark pattern was attributed to the strong interactions between the decanoyl and dodecanoyl linkers of the PyC10- and PyC12-PAMAM-G0 dendrimers, which induced a conformational inversion in the dendrimers that brought the pyrenyl groups closer resulting in the increased $[Py]_{loc}$ and $<k>$.[100]

To assess whether this conformational inversion experienced by the dendrimers with a decanoyl and dodecanoyl linker would be sensitive to the size of the surfactant aggregates, the interactions of the PyCX-PAMAM-G0 dendrimers with non-spherical surfactant aggregates (NSSA) composed of SDS/DTAB mixtures were studied in Chapter 3.[116] The checkmark pattern became less pronounced as the molar fraction of DTAB in the surfactant mixtures increased from 0 to 0.3 suggesting that the conformational inversion experienced by the dendrimers with a longer linker became weaker with increasing DTAB content. Since adding DTAB to the SDS solution resulted in larger and more elongated cylinders, we tried to relate the weakening of the conformational inversion of the PyC10- and PyC12-PAMAM-G0 dendrimers with the composition of the NSSA, whose prolate shape was approximated as the elongated cylinder shown in Figure 4 assumed to be made of two regions.

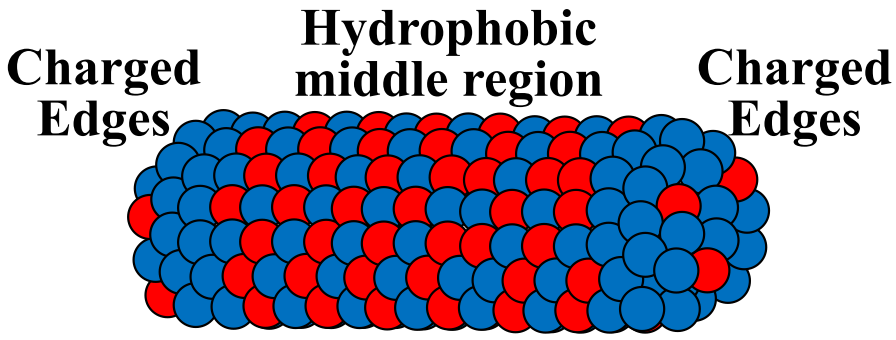


Figure 1.4. Illustration of a cylindrical NSSA with two edges mainly constituted of charged SDS molecules and a middle region constituted of an SDS/DTAB mixture. (blue) SDS, (red) DTAB.

The first region is the edge region representing the two hemispheres capping the elongated body of the NSSA prolate. Brought together, the two hemispheres would be similar to a pure SDS micelle constituted of about 70 SDS molecules, that would be charged and would thus be associated with a large *cpp* resulting in a large surface curvature. In contrast, the middle region would represent the location of the SDS molecules that are partially neutralized by DTAB. The middle region would thus be relatively more hydrophobic and have a lower surface curvature than the edge region. Since the edge region spans from the charged SDS headgroups to the interface with the hydrophobic middle region, the edge region would thus be subjected to a hydrophobicity gradient (HG) induced by the hydrophobicity difference between its surface and the interface with the middle region. In contrast, the more hydrophobic middle region would generate a small HG. Following this line of thoughts, $\langle k \rangle$ should equal the average of $\langle k \rangle^{\text{Edge}}$ and $\langle k \rangle^{\text{Mid}}$, which would be the $\langle k \rangle$ value taken by the dendrimer in the edge and in the middle region of the NSSA, respectively, weighed by the corresponding volume fractions of the edge and the middle regions. This assumption was validated in Chapter 3 which demonstrated that the change in $\langle k \rangle$ with DTAB content was therefore the result of the spatial partitioning of the PAMAM dendrimers between the two regions found in the NSSA. This study led to the introduction of the Spatial Partitioning Theory (SPT) to explain the changes in $\langle k \rangle$.[116]

After illustrating the potential use of the PyCX-PAMAM-G0 dendrimers as molecular probes, the dendrimers were employed in Chapter 4 to characterize the interior of NSSA generated by the addition of NaCl to aqueous solutions of SDS. To account for changes in aggregation experienced by the pyrenyl labels as the dendrimers interacted with the NSSA, the experimentally determined ratio $[\langle k \rangle / f_{\text{diff}}]^{\text{exp}}$ was used. Using the SPT developed in Chapter 3, a theoretical expression of $[\langle k \rangle / f_{\text{diff}}]^{\text{exp}}$ was developed and the excellent agreement found between $[\langle k \rangle / f_{\text{diff}}]^{\text{th}}$ and $[\langle k \rangle / f_{\text{diff}}]^{\text{exp}}$ further validated the heterogeneous nature of NSSA made

of a polar edge and hydrophobic middle regions, where the PyCX-PAMAM-G0 dendrimers would partition. This conclusion also led to the proposal of a general mechanism for the formation of NSSA.

In the fifth chapter, the SPT was extended to all the systems studied in this thesis. The SPT based on the $[<k>/f_{diff}]^{exp}$ ratio appeared to be universal once the correction factor $[<k>/f_{diff}]^{A\text{-}C}$ was included to account for changes in $[<k>/f_{diff}]^{exp}$ due to the cationic-aromatic interactions between DTAB and pyrene. The generality of the SPT suggests that it can be applied to represent the partitioning of pyrene-labeled PAMAM-dendrimers in all types of NSSA prepared from mixtures of oppositely charged surfactants and the addition of salt.

In summary, my thesis has established the feasibility of probing the conformation of macromolecules embedded in surfactant aggregates by using the combination of PEF, global MFA of fluorescence decays, and the direct relationship between $<k>$ and $[Py]_{loc}$. This combination led to the identification of the conformational inversion experienced by the PyCX-PAMAM-G0 dendrimers with the decanoyl and dodecanoyl linkers as they interacted with surfactant micelles. In turn, changes in the conformational inversion for these dendrimers were employed to probe the heterogeneous nature of NSSA resulting in the conclusion that NSSA are composed of a polar edge and hydrophobic middle regions among which the dendrimers partition themselves according to the SPT. In so doing, this thesis lays the path toward using the PyCX-PAMAM-G0 dendrimers as an important family of molecular probes for the study of complex colloidal systems involving surfactants, whereby the conformation of the dendrimers can be monitored with the observable $<k>$ which will report on the nature of the microdomains they interact with.

Chapter 2: Probing Macromolecular Conformation in Restricted Geometry by PEF: Application to Hydrophobically Modified PAMAM Dendrimers Isolated Inside Surfactant Micelles

Reproduced with permission from Liu, D.; Patel, S.; Xie, Y.; Zhang, H.; Duhamel, J. Probing Macromolecular Conformation in Restricted Geometry by PEF: Application to Hydrophobically Modified PAMAM Dendrimers Isolated Inside Surfactant Micelles. *J. Phys. Chem. B* **2025**, *129*, 1144–1153, Copyright 2025 American Chemical Society.

2.1 OVERVIEW

The conformation of a series of zero-generation polyamidoamine dendrimers end-labeled with four 1-pyrene-butyroyl, -hexanoyl, -octanoyl, -decanoyl, and -dodecanoyl derivatives, referred to as the PyCX-PAMAM-G0 samples with X = 4, 6, 8, 10, and 12, respectively, was characterized in *N*,*N*-dimethylformamide (DMF), dimethyl sulfoxide (DMSO), and aqueous solutions of 50 mM sodium dodecyl sulfate (SDS) or 50 mM dodecyltrimethylammonium bromide (DTAB). The conformation of the PyCX-PAMAM-G0 samples was determined from the global model free analysis (MFA) of the fluorescence decays, which yielded the average rate constant (<*k*>) for pyrene excimer formation (PEF) between an excited and a ground-state pyrenyl labels. <*k*> being proportional to the local concentration ($[Py]_{loc}$) of the pyrenyl labels within the macromolecular volume, <*k*>-*vs*.-$[Py]_{loc}$ plots yielded straight lines passing through the origin in DMF and DMSO, demonstrating that the internal segments of the dendrimers obeyed Gaussian statistics in these two solvents. In aqueous surfactant solutions, the hydrophobic pyrenyl labels induced the interactions of the PyCX-PAMAM-G0 dendrimers with the SDS and DTAB micelles. Plots of <*k*> as a function of $[Py]_{loc}$ yielded straight lines passing through the origin for the PyCX-PAMAM-G0 samples with X equal to 4, 6, and 8 indicating that the internal segments of these three dendrimers obeyed Gaussian statistics within the surfactant micelles. However, <*k*> departed from the straight lines for the PyCX-PAMAM-G0 samples with X = 10 and 12 associated with the SDS and DTAB micelles. This behavior indicated that $[Py]_{loc}$ was much larger than expected for the dendrimers prepared with the longer alkanoyl linkers. This behavior was attributed to strong hydrophobic interactions between the longer linkers and the dodecyl tails of the surfactants in the hydrophobic core of the micelles, which induced a conformational change for the dendrimers inside the micelles, which could be probed at the molecular level by PEF.

2.2 INTRODUCTION

Macromolecular conformation is an important element in the molecular-level characterization of a macromolecule as it relates to its macroscopic properties. For instance, flexible polypeptides containing more glycine [1] and alanine [2] yield longer folding times [3] and hydrogels produced from solutions of entangled linear chains yield larger moduli for stiffer polymers. [4 - 6] All experimental techniques aiming to characterize the conformation of macromolecules in solution share the ability to probe their local macromolecular density due to the inherent link existing between the local density of a macromolecule in solution and its conformation. Among the most intensively used techniques in macromolecular science, static light (SLS) and small angle X-ray (SAXS) and neutron (SANS) scattering yield the radius of gyration (R_G) of a macromolecule, [7 - 9] which describes the mass distribution of the macromolecule with respect to its center of gravity; viscometry measurements yield the intrinsic viscosity ($[\eta]$) representing the ratio of the hydrodynamic volume of the macromolecule over its molar mass; [10,11] nuclear magnetic resonance (NMR) experiments employ the nuclear Overhauser effect (NOE) to probe interatomic distances. [12,13] The direct relationship between the local macromolecular density and R_G, $[\eta]$, and NOE explains why scattering, viscometry, and NMR all play a predominant role to characterize the conformation of macromolecules in solution. [7- 13]

In this context, pyrene excimer formation (PEF) between pyrenyl labels covalently attached to a macromolecule provides an appealing alternative to these classic techniques. Since the average rate constant ($\langle k \rangle$) for PEF was recently demonstrated to equal the product $k_{diff} \times [Py]_{loc}$ (see Equation 2.1), [14] where k_{diff} is the bimolecular rate constant for diffusive encounters between dyes and quenchers and $[Py]_{loc}$ is the local quencher concentration experienced by an excited dye, $\langle k \rangle$ is a direct measure of $[Py]_{loc}$ and thus the local density of the macromolecule onto which the pyrenyl labels are attached. Consequently, $\langle k \rangle$ reflects

macromolecular conformation[15] in the same manner as R_G, [η], and NOE do. Like any other techniques used to probe macromolecular conformations, PEF experiments yield the persistence length of linear polymers[16-18] and the end-to-end distance of both monodisperse linear chains,[14] polymeric bottlebrushes,[19] and low generation dendrimers.[20,21] But in contrast to any other techniques, that typically operate with polymer concentrations in the 1 – 50 g/L range, PEF experiments use polymer concentrations that are between 2 and 4 orders of magnitude lower. For instance, the conformation of low generation pyrene end-labeled dendrimers made of a bis(hydroxymethyl)propionic acid (HMPA) and polyamidoamine (PAMAM) backbone was characterized at concentrations as low as 1 mg/L.[20,21] The impressive sensitivity of PEF experiments combined with their recently discovered ability to probe macromolecular conformations[14,15,19-21] unlocks the path toward characterizing the conformation of isolated macromolecules in restricted geometries, conditions requiring extremely low polymer concentrations that traditional techniques cannot meet due to their well-known lack of sensitivity.

$$\langle k \rangle = k_{diff} \times [Py]_{loc} \tag{2.1}$$

These features are captured in the present report where PEF was applied to probe the large conformational changes undergone by hydrophobically modified zero-generation PAMAM dendrimers (HM-PAMAM-G0) as they interacted with surfactant micelles. HM-PAMAM dendrimers have found interesting applications as potential drug delivery vehicles since capping the terminal amines with hydrophobic moieties promotes their interactions with cell membranes while significantly reducing their otherwise cytotoxic response.[22-30] The interactions between HM-PAMAM dendrimers and cell membranes are typically assessed through microscopy images of transfected cells and cell viability measurements but no

experimental technique provides molecular-level conformational information about the hydrophobically modified dendrimers as they interact with cell membranes. Currently, such information can only be obtained from molecular dynamics simulations.[31-33] To address this dearth of experimental studies, this report describes how the length of an alkyl linker connecting the dye pyrene to a PAMAM-G0 dendrimer affects the conformation of these HM-PAMAM-G0 dendrimers as they interact with surfactant micelles selected as micellar membrane models.

The HM-PAMAM-G0 samples investigated in this report were PAMAM-G0 dendrimer end-labeled with four 1-pyrene-butyroyl, hexanoyl, octanoyl, decanoyl, and dodecanoyl derivatives to yield the samples PyCX-PAMAM-G0 with *X* equal to 4, 6, 8, 10, and 12, respectively. To ensure that the surfactant micelles would remain spherical, the PEF experiments were conducted at a low 50 mM surfactant concentration, where the surfactant was either anionic sodium dodecyl sulfate (SDS) or cationic dodecyltrimethylammonium bromide (DTAB). Due to the poor solubility of the PyCX-PAMAM-G0 samples in water, aqueous 50 mM surfactant solutions were prepared with dendrimer concentrations between 0.5 and 1.5 μmol/L, a dendrimer concentration so low as to make it physically impossible to have more than one dendrimer per micelle. As described in Figure 2.1A, the PyCX-PAMAM-G0 samples are constituted of the polar and most likely charged PAMAM dendrimer core, four pyrenyl labels, and the alkyl apolar spacer shown in red, blue, and green, respectively. Earlier reports describing the interactions of PAMAM dendrimers and surfactant membranes have established that the polar polyamidoamine core is located at or near the micellar surface[27,32,33] and that the pyrene moieties prefer to reside in the micellar palisade separating the polar outer shell of the micelle from its apolar aliphatic core.[34-38]

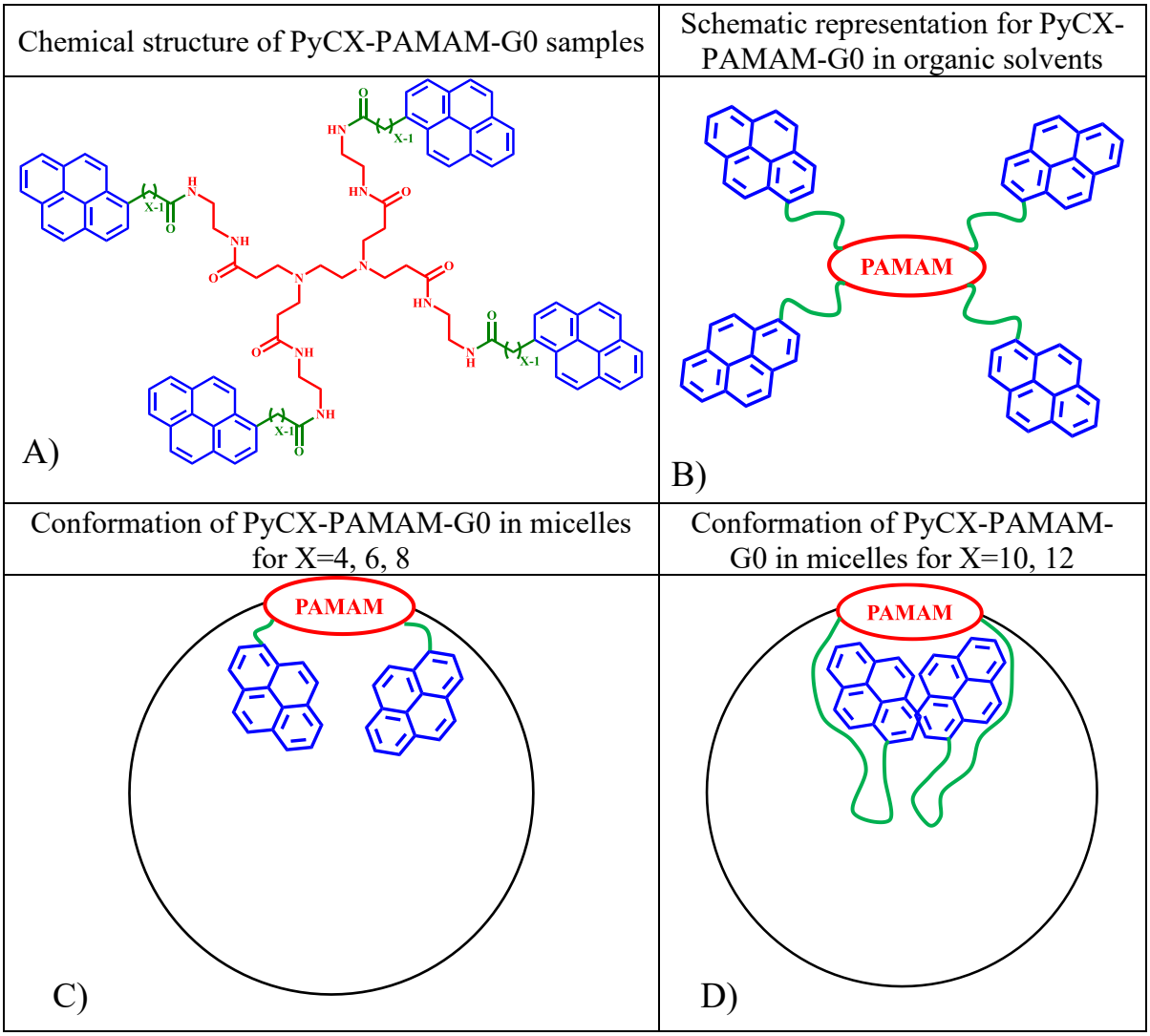


Figure 2.1. Chemical structure of the PyCX-PAMAM-G0 dendrimers and their schematic representation with the aromatic pyrenes in blue, the apolar alkoxy linkers with $X = 4$, 6, 8, 10, and 12 in green, and the polar PAMAM core in red.

The alkyl spacers used to link the pyrenyl moieties to the PAMAM core will interact with the apolar micellar core and the strength of this interaction will increase with increasing alkyl spacer length. The effect that the strength of this hydrophobic interaction had on the conformation of the PyCX-PAMAM-G0 samples, as they interacted with surfactant micelles, was characterized in the present report by using the direct relationship existing between $<k>$ and $[Py]_{loc}$ as defined in Equation 2.1.[14]

The fluorescence results based on the <*k*>-*vs.*-[*Py*]$_{loc}$ relationship[14] indicated that dendrimers with X = 4, 6, and 8 adopted an ideal conformation inside the micelles with the dendrimer internal segments obeying Gaussian statistics, but that the PyC10- and PyC12-PAMAM-G0 samples underwent a significant conformational change. This conformational change was induced by strong interactions between the longer alkyl spacers and the apolar micellar core, which brought the pyrenyl labels closer to each other. Such a conformational rearrangement could only occur if the pyrenyl moieties pointed outwards toward the micellar surface and thus facing the aqueous phase (Figure 2.1D) contrary to their orientation for the shorter alkyl linkers with the pyrenyl moieties pointing inward toward the interior of the micelles (Figure 2.1C).

Considering that many drugs in current use and being developed are hydrophobic and contain aromatic elements,[39-41] control over the spatial arrangements inside surfactant micelles of dendrimer end-groups decorated with hydrophobic and aromatic moieties, represented in this study by the pyrenyl moieties, could guide the design of new drug delivery systems. The PEF experiments described herein also illustrate how their extreme sensitivity can be combined with the newly established <*k*>-*vs.*-[*Py*]$_{loc}$ relationship[14] to offer a new means for probing macromolecular conformations under extremely dilute conditions such as those found in the restricted geometries generated by surfactant micelles.

2.3 EXPERIMENTAL

Chemicals: The surfactants sodium dodecyl sulfate (SDS) and dodecyltrimethylammonium bromide (DTAB) and the solvents *N*,*N*-dimethylformamide (DMF), dimethyl sulfoxide (DMSO), and chloroform were purchased from Sigma-Aldrich and used as received. The synthesis and characterization of the samples PyC4-, PyC8-, and PyC12-PAMAM-G0 were described earlier,[20,21] and the same procedure was employed to prepare the samples PyC6-,

PyC10-PAMAM-G0, and a PAMAM-G0 end-labeled with 1-naphthaleneacetic acid (NpC2-PAMAM-G0), whose ^{1}H NMR and MS spectra are presented in Supporting Information (SI).

UV-Vis absorption measurements: The absorption spectra were acquired on a Cary 100 UV-Visible spectrophotometer with a 5.0 cm pathlength quartz cuvette. Compared to a traditional cuvette with a 1.0 cm pathlength, the longer 5.0 cm pathlength yielded a larger absorbance for the very dilute aqueous PyCX-PAMAM-G0 solutions. The detection of sharp peaks in the absorption spectra was taken as evidence that the highly hydrophobic 1-pyrenealkanoyl derivatives used for the PyCX-PAMAM-G0 dendrimers were solvated inside the surfactant micelles.

Steady-state fluorescence: A HORIBA QM-400 spectrofluorometer equipped with a xenon arc-lamp as an excitation source was used to obtain the fluorescence spectra of the PyCX-PAMAM-G0 solutions. The PyCX-PAMAM-G0 solutions in DMF and DMSO were degassed with a gentle flow of nitrogen for 35 minutes while aerated aqueous solutions were used for the fluorescence measurements. The fluorescence spectra were acquired with a 1 nm slit width for the excitation and emission monochromators. The PEF efficiency was determined from the I_E/I_M fluorescence intensity ratio calculated from the fluorescence intensities of the pyrene monomer (I_M) and excimer (I_E) obtained by integrating the first sharp peak of the pyrene monomer fluorescence spectrum from 376 to 382 nm and the broad structureless emission of the pyrene excimer from 500 to 530 nm in the fluorescence spectra of the PyCX-PAMAM-G0 solutions, respectively.

Time-resolved fluorescence: A FluoroHub time-resolved fluorometer from HORIBA equipped with a 336 nm DeltaDiode laser was used to acquire the fluorescence decays of the PyCX-PAMAM-G0 solutions with a minimum of 20,000 counts at the decay maximum and over 1,024 channels. A 379 and 510 nm wavelength were selected to collect the fluorescence decays of the pyrene monomer and excimer with a time-per-channel of 0.44 and 0.87 ns and a 370 and

495 nm cut off filter, respectively. The cut off filters were inserted between the sample chamber and the emission monochromator to minimize stray light from reaching the detector. The instrument response function (IRF) used in the analysis of the fluorescence decays was obtained from the reflection of a triangular aluminium monolith acquired under the same condition as a fluorescence decay but with the wavelength of the emission monochromator set at 336 nm. Fluorescence decay analysis was conducted globally for both the pyrene monomer and excimer by convoluting the IRF with the sums of exponentials used in the model free analysis (MFA) and comparing the convoluted product with the experimental decays while optimizing the pre-exponential factors and decay times in the sums of exponentials with the Marquardt-Levenberg algorithm.[42] The global fit of the pyrene monomer and excimer fluorescence decays for a given PyCX-PAMAM-G0 solution was deemed satisfactory if the χ^2 was smaller than 1.3 and the residuals and autocorrelation of the residuals were randomly distributed around zero.

Model free analysis of the fluorescence decays: The MFA acknowledges that any fluorescence decay can be fitted with a sum of exponentials, which is used to describe the monomer fluorescence decays as shown in 2.1 in SI.[43,44] One exponential in Equation S2.1 has its decay time fixed to equal τ_M, which is the lifetime of the isolated pyrenyl labels Py_{free}*, that do not form excimer and emit as if they were free in solution. The other exponentials represent the pyrenyl species Py_{diffE0}* and Py_{diffD}*, which form one of the two excimers *E*0* or *D** by diffusive encounters, respectively. The excimer *E*0* and *D** can also be formed instantaneously upon direct excitation and they emit with their lifetime τ_{E0} and τ_D, respectively. For a few pyrene excimer fluorescence decays acquired with the PyCX-PAMAM-G0 samples, a fast decay could be detected, that was attributed to a short-lived excimer species (*ES**) with a τ_{ES} lifetime. Such a short decay time has been reported in the pyrene excimer fluorescence decays for PEF in restricted geometries[45] as observed for the PyCX-PAMAM-G0 samples. The

contributions of the short-lived *ES** species was not included, when calculating the contribution of the different pyrenyl species as done in earlier reports due to its short-lived presence in the fluorescence decay.[20,21] The MFA yielded the molar fractions f_{diffE0}, f_{diffD}, f_{free}, f_{E0}, and f_D representing the pyrenyl species Py_{diffE0}*, Py_{diffD}*, Py_{free}*, $E0$*, and D*, respectively. f_{diffE0} and f_{diffD} were summed to yield the molar fraction (f_{diff}) of pyrenyl species (Py_{diff}*) forming excimer by diffusive encounters and f_{E0} and f_D were similarly summed to yield the molar fraction (f_{agg}) of aggregated pyrenyl labels (Py_{agg}*) that formed excimer instantaneously upon direct excitation. The decay times (τ_i) and pre-exponential factors (a_i) used to represent Py_{diffE0}* and Py_{diffD}* in Equation S1 are conserved in Equation S2 used to fit the excimer decay globally with the monomer decay. This procedure ensures much better accuracy in the recovery of the different parameters retrieved from the global MFA of the pyrene monomer and excimer fluorescence decays. The pre-exponential factors (a_i) and decay times (τ_i) were then combined to determine the number average lifetime ($<\tau>$), which is used in Equation 2.2 to calculate $<k>$. The experimentally determined $<k>$ can then be related to $[Py]_{loc}$ through Equation 2.1.

$$< k >= \frac{\sum_{i=1}^{n} a_i}{\sum_{i=1}^{n} a_i \tau_i} - \frac{1}{\tau_M} = \frac{1}{< \tau >} - \frac{1}{\tau_M} \tag{2.2}$$

The parameters retrieved from the MFA of the fluorescence decays could also be recombined to yield the absolute I_E/I_M(TRF) ratio as presented in Equation 2.3.

$$I_E / I_M (TRF) = \frac{\left(f_{diffE0}\tau_{E0} + f_{diffD}\tau_D\right) \times < k >< \tau > + f_{E0}\tau_{E0} + f_D\tau_D}{(f_{diffE0} + f_{diffD}) \times < \tau > + f_{free}\tau_M} \tag{2.3}$$

Local concentration of pyrenyl labels for a PyCX-PAMAM-G0 sample: The local concentration ($[Py]_{loc}$) of pyrenyl labels within the macromolecular volume defined by the PyCX-PAMAM-G0 samples was obtained by dividing the number (n_{Py}) of ground-state pyrenyl labels by the cube of the average end-to-end distance (L_{Py}) normalized by the bond length (l).[20,21] For the PyCX-PAMAM-G0 samples with four pyrenyl labels, n_{Py} equals 3 since one of the four pyrenyl labels must be excited to be detected for fluorescence measurements and is required for PEF. The expression of L_{Py} has been derived mathematically for low generation PAMAM dendrimers earlier and is given in Equation 2.4.[20,21]

$$L_{Py}^2(N) = \left(2a + \frac{\left[2 - 2^{N+2} + (N+1)\times 2^{N+3}\right] b + 2^{N+1} c + 2^{N+1} - 1}{2^{N+2} - 1} \right) \times l^2 \qquad (2.4)$$

In Equation 2.4, N is the generation number equal to 0 for the PyCX-PAMAM-G0 samples, a is the number of carbon atoms in the linker connecting the pyrene moiety to the PAMAM dendrimer and equals X (= 4, 6, 8, 10, and 12), b (= 7) represents the number of non-hydrogen atoms in the aminoethyl propionamide building block of the PAMAM dendrimer, and c (= 4) is the number of non-hydrogen atoms in the ethylene diamine core of the dendrimer.

2.4 RESULTS

While the dissolution of the PyCX-PAMAM-G0 samples in DMF and DMSO was straightforward, their dissolution in the 50 mM surfactant aqueous solutions required special care. Numerous procedures were tried (see sample preparation section in Supporting Information (SI)). Most procedures resulted in aggregation of the pyrenyl labels with unresolved absorption spectra and no rise time in the fluorescence decays of the pyrene excimer (see Figure S2.7 in SI). These features reflected the presence of pyrene aggregates, which

indicated that the pyrenyl labels were not fully solvated in the surfactant micelles. One procedure resulting in strongly reduced pyrene aggregation consisted in suspending the dendrimers and surfactants in chloroform before evaporating the chloroform under a gentle flow of nitrogen to yield a film, which was dry for the samples with SDS but required that it be kept under vacuum overnight for the samples with DTAB to remove residual chloroform. After adding the required amount of water to the films, clear solutions of the PyCX-PAMAM-G0 samples were obtained in 50 mM surfactant aqueous solutions that yielded the well-resolved absorption bands expected from the pyrenyl labels and a well-defined rise time in the fluorescence decays of the pyrene excimer.[46] Since the surfactant concentration of 50 mM was well above the critical micelle concentration of 8 mM for SDS[47] and 15 mM for DTAB,[48] the surfactants formed micelles that were hosting the PyCX-PAMAM-G0 samples.

The dendrimer concentration in DMF and DMSO equaled 0.6 μM but was adjusted from 0.5 to 1.0 μM in the surfactant solutions for the dendrimers with X decreasing from 12 to 4 because the longer alkyl linkers connecting the pyrene moieties to the PAMAM dendrimers made the PyCX-PAMAM-G0 samples less soluble in water. Since the solubility limit of pyrene in water equals 0.7 μM,[49] pyrene is hardly soluble in water and the PyCX-PAMAM-G0 samples with four pyrenyl labels cannot reside in water and must interact with the surfactant micelles. Since the number (N_{agg}) of surfactants per micelle equals 70 and 51 for SDS[47] and DTAB,[50] respectively, the surfactant micelles hosted an average number ($<n>$) of dendrimers per micelle given by the expression $<n> = N_{agg}\times$[PyCX-PAMAM-G0]/([Surf] – CMC) and equal to ~ 1.0×10^{-3}. Such low $<n>$ values meant that the ratio of the probability (Pr(i>1)) of finding more than one dendrimer per micelle divided by the probability (Pr(i=1)) of finding one dendrimer per micelle was minuscule and equaled $[1 - \exp(-<n>) - <n>\times\exp(-<n>)]/[1-\exp(-<n>)] = 5.0\times10^{-4}$. While the low dendrimer concentration was required to dissolve the hardly soluble PyCX-PAMAM-G0 samples in the aqueous surfactant solutions, it also ensured

that the probability of finding more than two dendrimers per micelle was negligible and that the fluorescence signal was solely due to isolated dendrimers interacting with surfactant micelles.

The fluorescence spectra of the five PyCX-PAMAM-G0 samples were acquired in DMF, DMSO, and 50 mM SDS or DTAB in water as shown in Figure 2.2 after normalization to the first peak at 379 nm corresponding to the 0-0 transition of pyrene. The fluorescence spectra showed the features expected for a pyrene-labeled macromolecule (PyLM), with sharp bands between 370 and 410 nm characteristic of the pyrene monomer and the broad structureless fluorescence of the pyrene excimer centered at 490 nm.[46] Contrary to most PyLM, where an increase in $[Py]_{loc}$ yields stronger PEF, the amount of excimer produced by the series of PyCX-PAMAM-G0 molecules in Figures 2.2A-D showed no trend with increasing $[Py]_{loc}$. Increasing the linker length (X) in the PyCX-PAMAM-G0 samples should reduce $[Py]_{loc}$ (see chemical structure of PyCX-PAMAM-G0 dendrimers in Figure 2.1A), which should yield fewer pyrene-pyrene encounters and weaker PEF for the PyLM. The absence of such a trend is clearly illustrated in Figure 2.2E, where the I_E/I_M ratio is plotted as a function of the number (X) of carbon atoms in the linker connecting the pyrene group to the dendrimer. This effect is a consequence of the outsized contribution of the fluorescence of unattached pyrenyl labels, referred to as Py_{free}*, to the fluorescence signal of the pyrene monomer in PyCX-PAMAM-G0 samples. Residual changes in the amount of Py_{free}* species from sample to sample are known to strongly affect the I_E/I_M(SSF) ratio obtained from the analysis of the fluorescence spectra obtained with PyLM having a large $[Py]_{loc}$ as is the case for the PyCX-PAMAM-G0 samples.[51,52] For quantitative analysis of fluorescence data obtained with such PyLM, the Py_{free}* species must be isolated. This isolation can only be done through the analysis of the fluorescence decays of the pyrene monomer by taking advantage of its long lifetime (τ_M)

ranging from 127 to 132 ns depending on the pyrene derivative used to label the dendrimers in aerated 50 mM SDS and DTAB aqueous solutions.

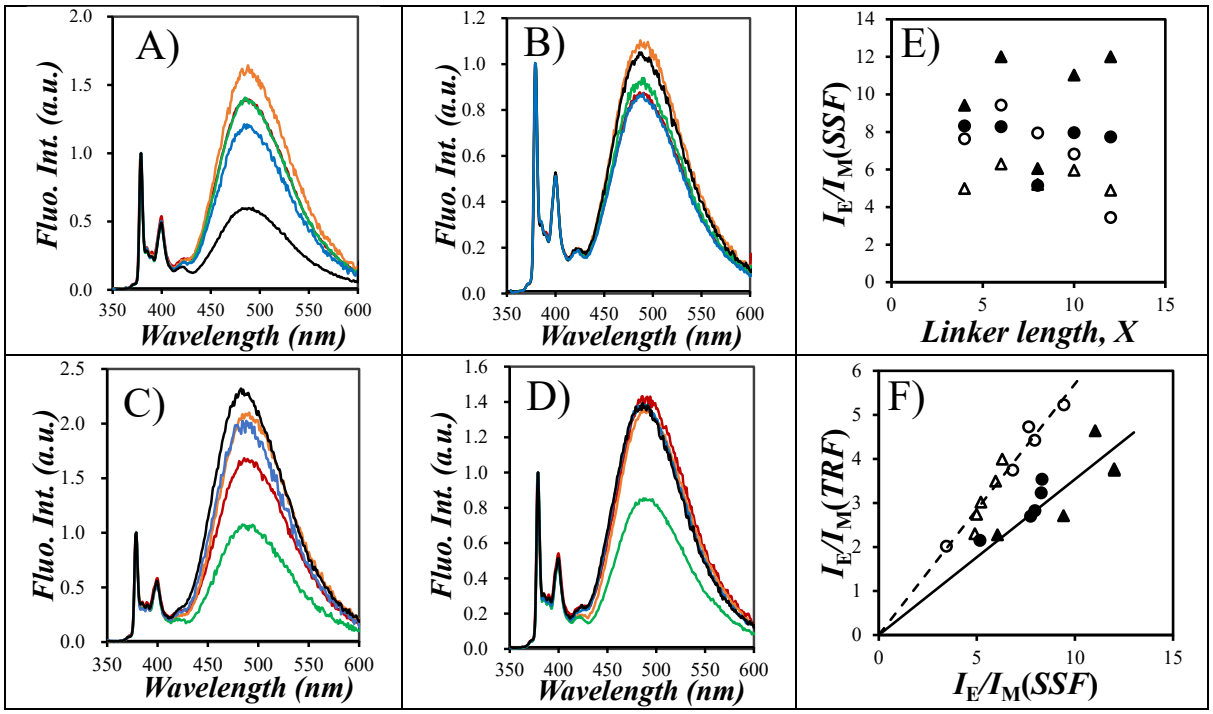


Figure 2.2. Fluorescence spectra of the PyCX-PAMAM-G0 samples normalized at 379 nm in A) DMF, B) DMSO, C) SDS, and D) DTAB for the PyCX-PAMAM-G0 samples with *X* equal to (red) 4, (orange) 6, (green) 8, (blue) 10, and (black) 12. Plots of E) I_E/I_M(TRF) as a function of the local pyrene concentration ($n_{Py}/(L_{Py}/l)^3$) and F) I_E/I_M(TRF) as a function of I_E/I_M(SSF) for the PyCX-PAMAM-G0 samples in (○) DMF, (△) DMSO, (▲) 50 mM SDS, and (●) 50 mM DTAB.

To this end, the fluorescence decays of the pyrene monomer and excimer of the five PyCX-PAMAM-G0 samples were acquired in DMF, DMSO, and 50 mM surfactant aqueous solution and fitted globally according to the Model Free Analysis (MFA) to yield the molar fractions f_{diff}, f_{free}, and f_{agg} of the pyrenyl species Py_{diff}*, Py_{free}*, and Py_{agg}*, respectively, the average rate constant (<*k*>) for PEF with Equation 2.2, and the lifetimes τ_{E0} and τ_D of the excimers *E*0* and *D**, respectively.[43,44] The MFA parameters were introduced into Equation

2.3 to obtain the I_E/I_M(TRF) ratio, which was compared to the I_E/I_M(SSF) ratio obtained from the analysis of the fluorescence spectra in Figure 2.2F. Interestingly, whereas the plot of I_E/I_M(SSF) as a function of linker length in Figure 2.2E showed an evident lack of trend, the data in the I_E/I_M(TRF)-*vs.*-I_E/I_M(SSF) plot shown in Figure 2.2F coalesced around two well defined straight lines, one for the PyCX-PAMAM-G0 samples in DMF and DMSO and another for the PyCX-PAMAM-G0 samples in the 50 mM surfactant aqueous solutions.

The clear-cut correspondence between the I_E/I_M(TRF) and I_E/I_M(SSF) ratios indicated that the parameters retrieved from the global MFA of the pyrene monomer and excimer fluorescence decays were a good representation of the information contained in the fluorescence spectra shown in Figures 2.2A-D. The different slopes obtained for the two straight lines in Figure 2.2F are probably due to the difference in polarity experienced by the excited pyrenyl labels in the polar DMSO and DMF solvents and the less polar interior of the surfactant micelles.[53,54] Solvent polarity is known to affect the intensity of the first peak at 379 nm in the fluorescence spectrum of the pyrene monomer which was used to calculate the I_E/I_M(SSF) ratio.[55-57] While it is strongly reduced for pyrenyl derivatives with an alkyl spacer without a nitrogen or oxygen heteroatom in the position β to the pyrene moiety as used for the PyCX-PAMAM-G0 samples, the pyrene moiety of such pyrene derivatives still retains some sensitivity to solvent polarity.[58,59] In contrast, the I_E/I_M(TRF) ratio is impervious to changes in the polarity of the environment experienced by the pyrenyl labels since it is calculated from the MFA parameters, which only report on the kinetics of PEF and are thus insensitive to the polarity of the environment.

Since f_{free} represented residual pyrene derivatives, that were not successfully removed during the purification of the PyCX-PAMAM-G0 samples but were isolated in the MFA of the decays, the molar fractions f_{diff} and f_{agg} (= 1 – f_{diff}) were calculated after excluding the contribution from the species Py_{free}*. f_{diff} and f_{agg} were plotted in Figure 2.3A as a function of

the linker length (X). They showed that PEF occurred mainly through diffusive encounters with f_{diff} being larger than 0.75 for all but one sample. This conclusion is consistent with the sharp bands in the absorbance spectra (Figures S2.7 and S2.9 in SI) and the rise time in the pyrene excimer fluorescence decays (Figures S2.8 and S2.10) observed in the 50 mM surfactant aqueous solutions of the PyCX-PAMAM samples that both confirmed that the pyrenyl labels were well solvated in the organic solvents and the surfactant aqueous solutions. The average rate constant (<k>) for PEF was then plotted in Figure 2.3B for the PyCX-PAMAM-G0 samples in DMF and DMSO and in Figure 2.3C for the PyCX-PAMAM-G0 samples in the 50 mM SDS and DTAB aqueous solutions as a function of $[Py]_{loc}$ taken as the ratio $n_{Py}/(L_{Py}/l)^3$, where n_{Py} equals 3 and L_{Py}/l is provided in Equation 2.4. Straight lines passing through the origin were obtained for the <k>-*vs.*-$[Py]_{loc}$ plots in Figure 2.3B. The linear trends shown in Figure 2.3B are a consequence of Equation 2.1, which was recently demonstrated experimentally to establish the correspondence between <k> and $[Py]_{loc}$.[14,20,21] This relationship is general and has been demonstrated for other dendrimers with a bishydroxymethylpropionic acid backbone.[60,61] The difference in slopes is a consequence of, in part, k_{diff} in Equation 2.1, which is larger in much less viscous DMF (η = 0.76 mPa·s at 25 °C)[62] than DMSO (η = 1.99 mPa·s at 25 °C),[62] and thus yields larger <k> values in DMF. The difference in solvent viscosity and probability of forming an excimer,[63] which both affect k_{diff} and thus <k> based on Equation 2.1, can be handled by using a pyrene model compound, which leads to the merger of the two trends.[20,21,61] The straight lines passing through the origin shown in Figure 2.3B validate the assumption made in the derivation of L_{Py} in Equation 2.4, namely that the internal segments of the PyCX-PAMAM-G0 samples obey Gaussian statistics in DMF and DMSO.[20,21]

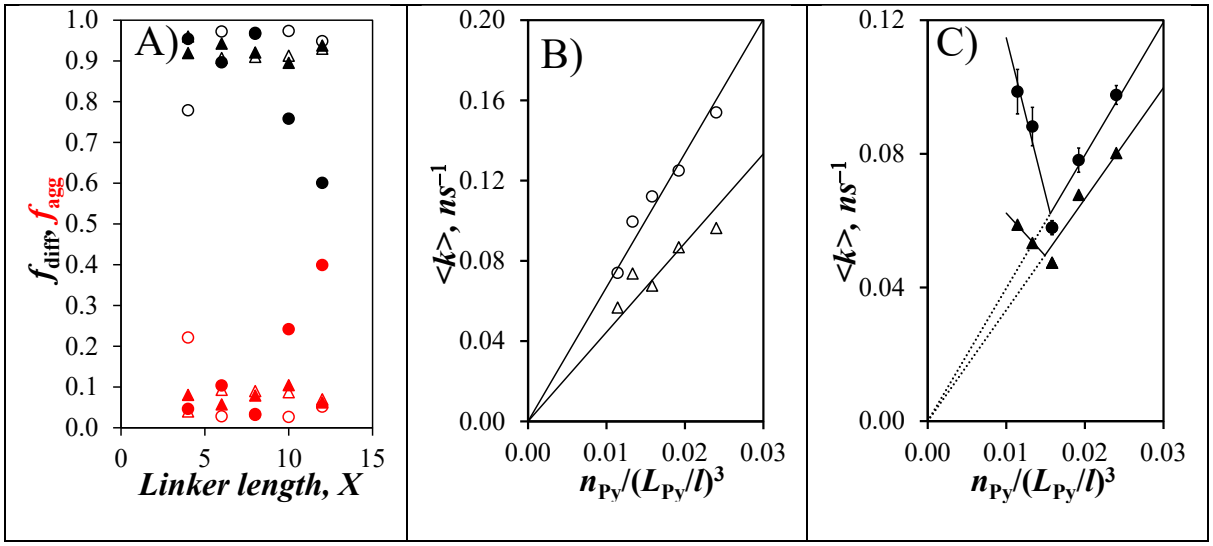


Figure 2.3. Plots of A) the molar fractions (black) f_{diff} and (red) f_{agg} as a function of linker length (X) and <k> for the PyCX-PAMAM-G0 samples in B) DMF and DMSO and 50 mM C) SDS and DTAB aqueous solutions. Symbols: (empty circles) DMF, (empty triangles) DMSO, (filled circles) SDS, (filled triangles) DTAB.

In contrast to the linear <k>-*vs.*-$[Py]_{loc}$ plots obtained for the PyCX-PAMAM-G0 samples in DMF and DMSO, the <k>-*vs.*-$[Py]_{loc}$ plots shown in Figure 2.3C for the PyCX-PAMAM-G0 samples in 50 mM SDS and DTAB aqueous solutions were more intriguing as they showed a clear checkmark pattern. While <k> increased linearly with increasing $[Py]_{loc}$ for the PyCX-PAMAM-G0 samples with X equal to 4, 6, and 8, a clear deviation from linearity was found for the two PyCX-PAMAM-G0 samples with X equal to 10 and 12 in both the SDS and DTAB micelles. Such pronounced breaks in the <k>-*vs.*-$[Py]_{loc}$ plots suggest a significant conformational rearrangement for the PyCX-PAMAM-G0 samples with the longer spacers inside the surfactant micelles.

To investigate if aggregation between the PyCX-PAMAM-G0 samples could be a factor for the unexpected checkmark patterns shown in Figure 2.3C despite the relatively low f_{agg} values reported in Figure 2.3A, fluorescence resonance energy transfer (FRET) experiments were conducted. To this end, PAMAM-G0 was labeled with 1-naphthaleneacetic

acid to yield NpC2-PAMAM-G0. NpC2-PAMAM-G0 was mixed with the PyCX-PAMAM-G0 samples with X = 10 and 12 in an about 80:20 molar ratio in the 50 mM SDS and DTAB aqueous solutions. The fluorescence spectra of the NpC2/PyCX-PAMAM-G0 mixtures were compared to the sum of the fluorescence spectra acquired for the 50 mM SDS and DTAB solutions with NpC2-PAMAM-G0 only and PyCX-PAMAM-G0 only. The identical fluorescence spectra obtained in Figures S2.11 – S2.16 in SI for the NpC2/PyCX-PAMAM-G0 mixtures and the sum of the fluorescence spectra of the individual components of the mixtures ruled out FRET between the naphthalene- and pyrene-labeled dendrimers and confirmed that the surfactant micelles hosted isolated dendrimers.

One reason for the increased <k> values obtained in the surfactant micelles with the longer linkers could simply be due to the larger size of the PyCX-PAMAM-G0 dendrimers with X = 10 and 12, that might not be accommodated inside the surfactant micelles. However, this possibility is highly unlikely considering the size of the dendrimers relative to the interior of the SDS and DTAB micelles. Based on the expression of L_{Py} in Equation 2.4 and the fact that l was determined to equal 0.241 nm for the PAMAM dendrimers,[20] L_{Py} would equal 1.47 and 1.54 nm for the PyCX-PAMAM-G0 dendrimers with X equal to 10 and 12, respectively.[20] These L_{Py} values needed to be compared to the diameter of the hydrophobic interior of the surfactant micelles found to equal 3.7 and 3.3 nm by considering that N_{agg} equals 70 and 51 for SDS and DTAB, respectively, and that the volume of a methylene and methyl groups equals 0.028 and 0.049 nm^3,[64] respectively. Based on this comparison of the respective dimensions of the dendrimers and the interior of the SDS micelles, all PyCX-PAMAM-G0 dendrimers were expected to be well accommodated inside the micelles regardless of their linker length (X).

Having ruled out the effects of dendrimer size and aggregation to rationalize the check mark pattern observed in Figure 2.3C for the PyCX-PAMAM-G0 samples with X equal to 10

and 12, another effect was considered, namely the strength of the hydrophobic interactions that were likely to occur between the longer alkyl segments connecting pyrene to the PAMAM dendrimers and the dodecyl chains constituting the interior of the surfactant micelles. PAMAM dendrimers are highly polar macromolecules that dissolve in polar solvents like water, methanol, DMF, or DMSO but are insoluble in apolar solvents like dodecane and thus, are incapable of penetrating the apolar interior of surfactant micelles. Consequently, the main reason for the PyCX-PAMAM-G0 samples to interact with the surfactant micelles in this study was the four hydrophobic 1-pyrenealkanoyl derivatives used to label the dendrimers that anchored the PAMAM dendrimers among the surfactant headgroups of the micelles. With the PAMAM dendrimers located at the surface of the micelles[27,32,33] and the pyrene moieties located either in the palisade between the hydrophobic core and the polar shell of the SDS micelles[34-38] or closer to the trimethylammonium headgroups due to aromatic-cationic interactions in the DTAB micelles,[65-68] the alkanoyl linker connecting the pyrene groups to the PAMAM dendrimers seem to offer a powerful experimental means for controlling the conformation of the PyCX-PAMAM-G0 samples in the micelles. Based on the checkmark pattern shown in Figure 2.3C, the short linkers with *X* equal to 4, 6, and 8 were not sufficiently hydrophobic to induce significant hydrophobic interactions with the hydrophobic core of the surfactant micelles. Since the linear trends shown in Figure 2.3C passed through the origin for the PyCX-PAMAM-G0 samples with a shorter alkanoyl linker, the internal segments of these dendrimers appeared to adopt a random conformation based on Gaussian statistics, which was used to calculate $[Py]_{loc}$ based on L_{Py} determined with Equation 2.1.[20,21] In contrast, the higher than expected $\langle k \rangle$ values found in the surfactant micelles for the PyCX-PAMAM-G0 samples with *X* equal to 10 and 12 were most likely the result of strong hydrophobic interactions between the decanoyl and dodecanoyl linkers and the dodecyl chains of the surfactants in the micellar core. With the pyrene moieties and the PAMAM-G0 dendrimer located close to the

headgroups, stronger interactions between the longer linkers and the hydrophobic micellar core would bring the pyrenyl labels closer to each other, as described in Figure 2.1D in a manner that would increase $[Py]_{loc}$ and thus $\langle k \rangle$ according to Equation 2.1. Contrary to organic solvents, where increasing the linker length connecting the pyrenyl moieties to the PAMAM dendrimers results in a decrease in $[Py]_{loc}$ (see Figure 2.3B and references 20 and 21), strong hydrophobic interactions between the longer alkanoyl linkers and the dodecyl chains of the surfactant micelles would lead to the opposite outcome with $[Py]_{loc}$ showing a significant increase with longer linkers.

Another interesting feature of Figure 2.3C is the consistently lower $\langle k \rangle$ values obtained for the PyCX-PAMAM-G0 samples interacting with the DTAB compared to the SDS micelles. This effect cannot be due to the difference in size between the smaller DTAB micelles and larger SDS micelles with N_{agg} equal to 50 and 70, respectively, since L_{Py} for the PyCX-PAMAM-G0 dendrimers has been found to be significantly smaller than the micellar diameters. Thus, the size of the micelle cannot influence the conformation of the PyCX-PAMAM-G0 sample. Rather, the well-reported aromatic-cationic interactions between the pyrenyl labels and the trimethylammonium headgroups of the DTAB surfactants[64-68] are probably responsible for this effect. The main outcome would be a slowing down of the diffusive motions of the pyrenyl end groups associated with a decrease in k_{diff} and an interaction holding the pyrenyl labels closer the micellar surface counteracting the hydrophobic pull toward the micellar core, both effects contributing to a reduced change in $[Py]_{loc}$ for the longer alkanoyl linkers in DTAB compared to SDS micelles.

2.5 DISCUSSION

The expression for L_{Py} given in Equation 2.4 assumes that the internal segments constituting the PyCX-PAMAM-G0 dendrimers obey Gaussian statistics.[20,21] L_{Py} could then be used to

calculate $[Py]_{loc}$ taken as $n_{Py}/(L_{Py}/l)^3$ for nine different PyCX-PAMAM-GY, with $X = 4$, 8, and 12, and generation number $Y = 0$, 1, and 2.[20,21] Since plotting $\langle k \rangle$ obtained in DMF and DMSO as a function of $[Py]_{loc}$ in Figure 2.3B yielded a straight line that passed through the origin, it demonstrated the validity of the $\langle k \rangle$-*vs.*-$[Py]_{loc}$ relationship and confirmed that the internal segments of the low generation PyCX-PAMAM-GY dendrimers obeyed Gaussian statistics. The validity of the $\langle k \rangle$-*vs.*-$[Py]_{loc}$ relationship was further extended in this study by adding the PyCX-PAMAM-G0 samples with $X = 6$ and 10 whose $\langle k \rangle$ and $[Py]_{loc}$ data sets nicely aligned with the other data points in DMF and DMSO as shown in Figure 2.3B.

The similar linear relationship obtained between $\langle k \rangle$ and $[Py]_{loc}$ in Figure 2.3C for the PyCX-PAMAM-G0 samples with $X = 4$, 6, and 8 indicates that the internal segments of the dendrimers obey Gaussian statistics as they interact with the surfactant micelles as described in Figure 2.1C. Yet, contrary to the conditions in the organic solvents DMF and DMSO where the pyrenyl moieties can sample the entire macromolecular volume as described in Figure 2.1B, less than half of that space is available to the pyrenyl groups in the surfactant micelles as described in Figure 2.1C since their strong hydrophobicity prevents them from venturing into the aqueous phase. The linear relationship between $\langle k \rangle$ and $[Py]_{loc}$ passing through the origin for the PyCX-PAMAM-G0 samples with a shorter linker is thus interesting as it suggests that despite occupying the restricted volume defined by the intersection between the dendrimer and micellar volumes, the internal segments of these dendrimers appear to retain sufficient randomness for the Gaussian statistics to hold with Equation 2.4. Departure of the $\langle k \rangle$ and $[Py]_{loc}$ values from this linear relationship in Figure 2.3C for the dendrimers with the longer linkers with $X = 10$ and 12 indicates that the pyrenyl end groups are no longer randomly distributed in the macromolecular volume and are located much closer to each other than expected. Analysis of the location of the different constituting parts of the PyCX-PAMAM-G0 dendrimers led to the conclusion that the unexpected $\langle k \rangle$-*vs.*-$[Py]_{loc}$ behavior identified by the

checkmark pattern in Figure 2.3C for the samples with X = 10 and 12 was due to stronger hydrophobic interactions between the alkanoyl linkers and the dodecyl chains constituting the micellar core. The folding of the longer alkyl linkers into the hydrophobic core of the surfactant micelles and the local inversion in the pyrenyl end groups, that would appear to point out toward the aqueous phase as shown in Figure 2.1D, could be important factors in the design of drug delivery vehicles. This effect might facilitate the transduction of a hydrophobically modified water-soluble macromolecule (HM-WSM) across a cell membrane to promote the translocation of a hydrophobic cargo bound to the HM-WSM of interest.

Be it for the transduction of a hydrophobic cargo by amphipathic cell penetrating peptides [69 - 72] or the delivery of hydrophobic drugs with a hydrophobically modified dendrimer,[22-30] the interactions between HM-WSM and a cell membrane are under intense scrutiny. Of particular interest is the development of a molecular level understanding of how HM-WSM adjust their conformation as they transition from the polar water medium to the hydrophobic environment of a lipid bilayer. While such interactions are clearly demonstrated through microscopy or cytotoxicity experiments that show the location of a fluorescently labeled HM-WSM in the different compartments of a cell or how efficient the loaded drug delivery vehicle is at killing targeted cells,[22-30] experimental techniques capable of probing these macromolecular conformational changes at the molecular level are dearly lacking. The main reason for this dearth of experimental techniques is that the classic techniques like NMR, scattering, or viscometry capable of characterizing macromolecular conformations in solution are usually not sensitive enough and require relatively large concentrations (~ g/L) of macromolecules. Such conditions are poorly suited to study isolated macromolecules embedded in dilute nanostructures generated by amphiphilic molecules like lipid bilayers or surfactant micelles. If the formation of such nanostructures requires lipid or surfactant concentrations in the ~ g/L range, macromolecule concentrations must be orders of magnitude

lower, in the ~ mg/L range, to ensure that isolated macromolecules are interacting with these nanostructures. Such conditions impose enhancing the signal from the macromolecule of interest by using isotope labeling for NMR or scattering techniques, but these procedures are often costly and cannot be done routinely. Fluorescence collisional quenching experiments offer an interesting alternative to these other experimental and simulation studies by taking advantage of the inherently high sensitivity of fluorescence and the response of $\langle k \rangle$ to the local quencher concentration.[14] Although fluorescent labels are pricey, the high sensitivity of fluorescence allows the use of little material, which helps keep costs down, while still providing conformational information about fluorescently labeled HM-WSM that are isolated as single macromolecules in a given colloidal entity like SDS and DTAB micelles. These principles were illustrated in the present study with the PyCX-PAMAM-G0 samples.

2.6 CONCLUSION

This study represents the first example in the literature where the conformation of a series of hydrophobically modified PAMAM dendrimers (HM-PAMAM) was characterized experimentally as they interacted with surfactant micelles used as lipid membrane mimics. It was enabled by leveraging the high sensitivity of PEF with its ability to report on $[Py]_{loc}$ and the local density of a pyrene-labeled macromolecule through the parameter $\langle k \rangle$ obtained from the global MFA of the fluorescence decays acquired with the PyCX-PAMAM-G0 samples. While linear trends of $\langle k \rangle$-*vs.*-$[Py]_{loc}$ passing through the origin were obtained for the five PyCX-PAMAM-G0 samples in DMF and DMSO, the same behavior held in aqueous solutions of surfactant micelles for the dendrimers prepared with short linkers with X equal to 4, 6, and 8 but not for the dendrimers prepared with linkers having larger X values of 10 and 12. The checkmark patterns observed for the series of PyCX-PAMAM-G0 dendrimers in Figure 2.3C indicated a significant conformational change reflecting the strong interactions between the

longer alkanoyl linkers and the dodecyl chains constituting the micellar interior. Whether such conformational changes could also be at play for the stretches of hydrophobic amino acids found in the sequence of amphipathic cell penetrating peptides like MPG or transportan-10[68-72] and other HM-WSM as they efficiently translocate through a cell membrane remains to be seen, but the PEF procedure illustrated herein provides a possible experimental means to study these interactions at the molecular level.

Chapter 3: Conformation of Pyrene End-Labeled Polyamidoamine Dendrimers in Catanionic Surfactant Micelles Probed by Pyrene Excimer Formation

Reproduced with permission from Liu, D.; Patel, S.; Duhamel, J. Conformation of Pyrene End-Labeled Polyamidoamine Dendrimers in Catanionic Surfactant Micelles Probed by Pyrene Excimer Formation. *Langmuir* **2025**, *41*, 20986-20998. Copyright 2025 American Chemical Society.

3.1 OVERVIEW

A series of generation-0 polyamidoamine (PAMAM-G0) dendrimers, referred to as the PyCX-PAMAM-G0 samples, were end-labeled with 4 identical 1-pyrenealkanoyl derivatives with either a (*X*=4) butyroyl, (*X*=6) hexanoyl, (*X*=8) octanoyl, (*X*=10) decanoyl, or (*X*=12) dodecanoyl linker. Their conformation was investigated in mixed micelles composed of sodium dodecyl sulfate (SDS) and dodecyltrimethylammonium bromide (DTAB). As the molar fraction (f_{DTAB}) of DTAB in the SDS:DTAB mixtures was increased from 0.0 to 0.3, the micellar aggregates grew in size and changed their shape from spheres to ellipsoids. Global model free analysis of the fluorescence decays yielded the average rate constant (<*k*>) for pyrene excimer formation (PEF) between an excited and a ground-state pyrenyl labels bound to the PyCX-PAMAM-G0 dendrimers. Plots of <*k*> as a function of the local concentration ($[Py]_{loc}$) of ground-state pyrenyl labels indicated that the conformation of the PyCX-PAMAM-G0 dendrimers bearing shorter *X* = 4, 6, and 8 alkanoyl linkers was that expected if the internal segments of these dendrimers obeyed Gaussian statistics. The <*k*>-*vs.*-$[Py]_{loc}$ plots also indicated that the PyCX-PAMAM-G0 samples with the longer linkers underwent a conformational inversion. However, the conformational inversion experienced by the PyCX-PAMAM-G0 samples with longer linkers appeared to become less pronounced with increasing f_{DTAB}. Analysis of the <*k*>-*vs.*-$[Py]_{loc}$ trends obtained with increasing f_{DTAB} led to the conclusion that the PyCX-PAMAM-G0 dendrimers with longer alkanoyl linkers underwent conformational inversion in the SDS-rich capping ends of the ellipsoidal micelles but not in their more hydrophobic central section and that partitioning of the dendrimers between the two regions of the surfactant aggregates resulted in the decrease in conformational inversion identified by PEF. Consequently, these PEF experiments represent an interesting experimental means for probing the conformation of complex hydrophobically modified water-soluble macromolecules as they interact with the microdomains generated by amphiphilic molecules.

3.2 INTRODUCTION

Hydrophobically modified water-soluble macromolecules (HMWSM) such as diblock copolymers with a hydrophobic and hydrophilic block,[1-9] hydrophobically modified dendrimers,[10-18] amphiphilic arborescent and hyperbranched polymers,[19-26] or polymer bottlebrushes[27-29] are under intense scrutiny to assess their potential as vehicles for the delivery of hydrophobic drugs into cells. The function of the HMWSM is to generate hydrophobic microdomains, that are big enough to host large payloads of hydrophobic drugs, and whose stability in water is ensured by the hydrophilic component of the HMWSM. An efficient drug delivery vehicle (DDV) will have a high loading capacity, representing the number of grams of encapsulated drug per gram of DDV, and will transfer its payload across the cell outer and inner membranes to deliver the hydrophobic drug to the desired cell target. Methods based on spectroscopy such as UV-Vis absorption or fluorescence have been established to determine the loading capacity of a drug in a DDV[30-32] and the efficiency of a DDV at delivering its payload to a specific cellular target can be assessed through cytotoxicity studies and fluorescence microscopy.[33,34]

While these studies unambiguously demonstrate the efficacy of a given DDV,[30-34] they offer little molecular level information about the mechanism describing how a DDV interacts with the cell membrane. Yet the development of such an understanding is critical for improving the current design of the next generation of DDV. Currently, molecular dynamics simulations (MDS) appear to be the main tool used to gain insight into the interactions taking place between DDV and a cell membrane.[15-18] Traditional experimental techniques like NMR[35,36] or scattering[37-39] capable of monitoring the conformational changes of HMWSM that are isolated and embedded in a lipophilic medium dispersed in water are usually not well suited for this purpose. Since the hydrophobicity of HMWSM drives their partitioning from the water phase into lipophilic aggregates such as micelles, vesicles, or lamellae, the local concentration of the

HMWSM in these lipophilic aggregates is orders of magnitude larger than their overall concentration in the continuous water phase. This significant increase in the local concentration of the HMWSM results from the fact that the volume generated by the lipophilic aggregates is orders of magnitude smaller than that of the continuous phase. For instance, since the volume of a methyl and methylene group equal 49 and 28, $Å^3$,[40] respectively, and knowing that the aggregation number (N_{agg}) and CMC of SDS equal 71 and 8 mM,[41] respectively, the dodecyl tails of SDS in 1 L of a 50 mM SDS solution would only generate 9 mL of hydrophobic environment resulting in a 1000/9 = 111-fold increase in the concentration of a HMWSM in the lipophilic aggregates. Consequently, ensuring that isolated HMWSM are probed in lipophilic aggregates requires working at relatively low mg/L concentrations of HMWSM resulting in a low signal from the HMWSM that must be separated from that of the lipophilic medium present in large excess. Such experimental conditions are challenging for most techniques and require that the signal of the HMWSP be amplified, typically through isotope labeling for NMR[42,43] or scattering[44,45] studies. Unfortunately, the prohibitive costs associated with isotope labeling and long acquisition times on these instruments are often a considerable barrier to such studies.

However, recent reports suggest that the conformation of macromolecules, that have been labeled with the fluorescent dye pyrene, can be characterized by determining the average rate constant ($\langle k \rangle$) for pyrene excimer formation (PEF) between the pyrenyl labels covalently attached onto the macromolecule.[46-52] As shown in Equation 3.1, $\langle k \rangle$ is equal to the product of the bimolecular rate constant (k_{diff}) for diffusive encounters between the pyrenyl labels and the local concentration ($[Py]_{loc}$) of the pyrenyl labels inside the macromolecular volume. k_{diff} represents all the dynamic aspects affecting PEF such as solvent viscosity or the internal dynamics of the macromolecule, and since $[Py]_{loc}$ is directly related to the local density of the macromolecule, $\langle k \rangle$ can be used to probe macromolecular conformations.[46]

$$\langle k \rangle = k_{diff} \times [Py]_{loc} \quad (3.1)$$

The recently uncovered ability of PEF to probe macromolecular conformations[46] was applied earlier to study in *N*,*N*-dimethylformamide (DMF) and dimethyl sulfoxide (DMSO) the conformation of a series of five 0-generation polyamidoamine dendrimers (PyCX-PAMAM-G0 with $X = 4$, 6, 8, 10, and 12) that had been end-labeled with 1-pyrene-butyric, -hexanoic, -octanoic, -decanoic, and -dodecanoic acid, respectively.[50-52] The chemical structure of these pyrene-labeled dendrimers is shown in Figure 3.1.

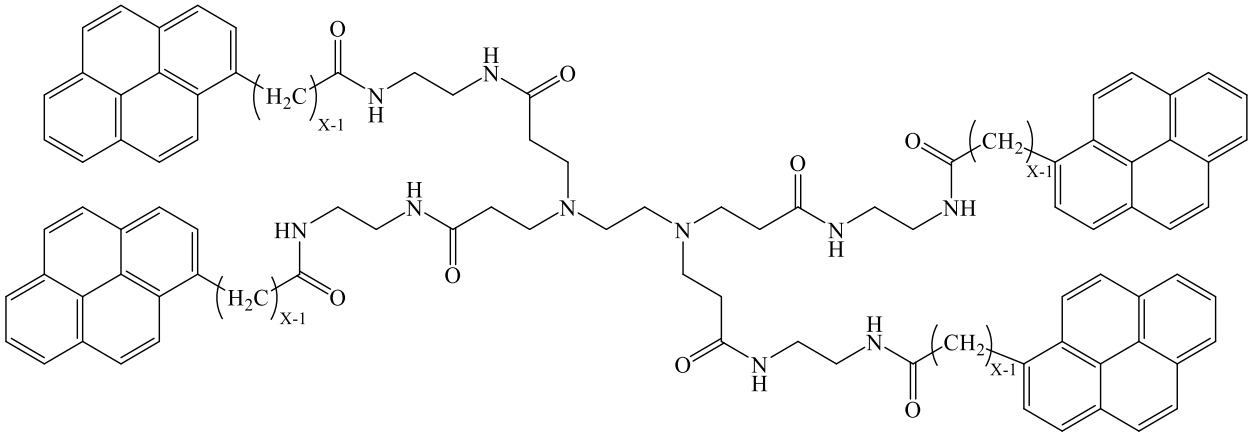


Figure 3.1. Chemical structure of the PyCX-PAMAM-G0 dendrimers with $X = 4$, 6, 8, 10, and 12.

Since the dye pyrene is hardly soluble in water (solubility in water equals 0.7 mM)[53] and PAMAM-G0 is insoluble in apolar organic solvents, the PyCX-PAMAM-G0 samples are examples of HMWSM. Furthermore, hydrophobically modified PAMAM dendrimers are being investigated as potential DDV, in part due to the reduction in their cytotoxicity upon reacting their terminal amines with hydrophobes.[10,12] Earlier studies have established that $[Py]_{loc}$ in Equation 3.1 could be estimated for pyrene end-labeled dendrimers like the PyCX-PAMAM-

G0 samples by assuming that the conformation of their internal segments was governed by Gaussian statistics.[50,51] These studies showed that for two types of pyrene end-labeled dendrimers in DMF and DMSO, $<k>$ increased linearly with increasing $[Py]_{loc}$.[46-48,50-52] Interestingly this well-established relationship was found to break down for the PyCX-PAMAM-G0 samples with a long decanoyl ($X = 10$) or dodecanoyl ($X = 12$) linker between the pyrenyl end-groups and the PAMAM dendrimer as they interacted with spherical surfactant micelles in water.[52] These two samples exhibited a conformational inversion resulting from strong hydrophobic interactions between their longer alkyl linker and the hydrophobic interior of the surfactant micelles that brought the pyrenyl labels closer to each other and with their end pointing outward toward the micellar interface with water instead of inward toward the micellar core. A schematic representation of these expected conformations for PyCX-PAMAM-G0 dendrimers in SDS micelles is given in Figures 3.2A and B. Earlier studies have used molecular pyrene to probe the interactions between PAMAM dendrimers and SDS or DTAB surfactants, but interpretation of the fluorescence data is complicated by the fact that the pyrene probe and the dendrimers might not always reside in a same microdomain.[54-56] In contrast, the covalent attachment of the pyrene probe to the PAMAM dendrimers in the PyCX-PAMAM-G0 samples greatly facilitates the interpretation of the fluorescence results since the pyrene probe reports directly on the properties of the PyCX-PAMAM-G0 dendrimer. The conformational inversion identified in this earlier study[52] represented an illustration of how PEF could be applied to characterize the conformation of a HMWSM encapsuled in a surfactant micelle.

The fact that surfactant aggregates exhibit a wide variety of shapes, sizes, and microenvironments induced by the simple adjustment of the surfactant composition in the micellar assembly suggests that the surfactant composition of micellar aggregates might have an important effect on the conformation of HMWSM. For instance, mixtures of DTAB with an excess of SDS have been found by pyrene excimer formation to form large micellar

aggregates[57] that adopt a triaxial ellipsoidal shape in aqueous solution as determined by small angle neutron scattering (SANS).[58]

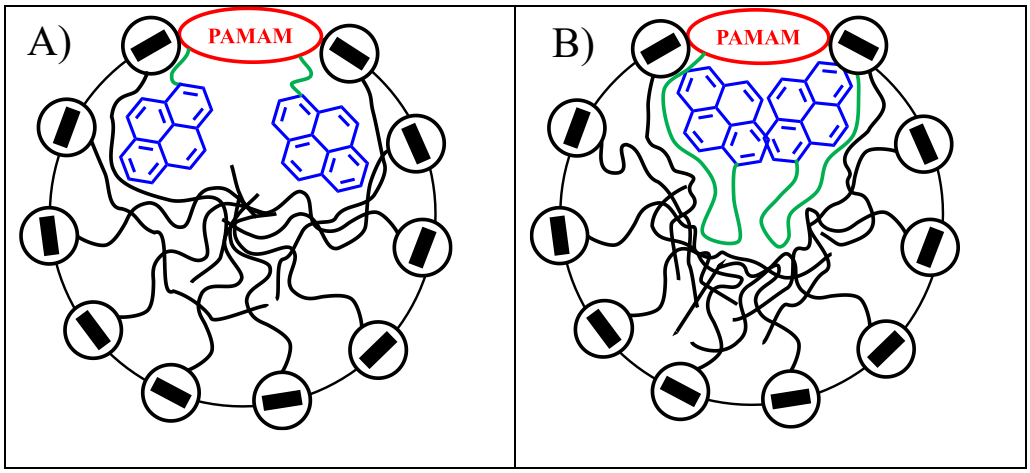


Figure 3.2. Schematic representation of the conformation of the PyCX-PAMAM-G0 samples in SDS micelles A) with $X = 4$, 6, and 8 and B) with $X = 10$ and 12. The sulfate headgroups of SDS are spread apart resulting in a small packing parameter[59] and a higher surface curvature.

As the molar fraction (f_{DTAB}) of DTAB in the surfactant mixture increased from 0.15 to 0.20 and 0.25, the main axis of the ellipsoids was reported to increase from 3.3 to 4.3 and 6.1 nm, respectively. These extended structures are a consequence of the reduction in electrostatic repulsion between the sulfate headgroups of the SDS molecules upon addition of DTAB. Compared to the curvature of spherical micelles, regions of the micellar aggregates that are more elongated have a lower surface curvature corresponding to a more balanced composition of the oppositely charged surfactants approaching the equicharge point and resulting in a larger packing parameter.[59] In contrast, the domains capping the elongated sections of the micellar aggregates of SDS and DTAB mixtures exhibit a larger surface curvature and are richer in the surfactant in excess (SDS in this case). The sulfate headgroups present in excess in the more highly curved regions capping the elongated sections of the mixed micelles experience stronger electrostatic repulsion resulting in a smaller packing parameter. Consequently, surfactant

micellar aggregates formed from mixtures of SDS and DTAB offer different microenvironments within a same aggregate, with which HMWSM would interact differently. In the case of the PyCX-PAMAM-G0 dendrimers, the dendrimers with long alkyl linkers connecting the pyrenyl moieties to the PAMAM dendrimers would be expected to undergo a conformational inversion in the capping regions of the elongated micellar aggregates similar to their behavior in SDS micelles. Because the capping regions are SDS-rich, they have a higher surface curvature, and would behave similarly to SDS micelles. In contrast, mixtures of oppositely charged surfactants generate environments, that are much more hydrophobic due to reduced access of water molecules through the tightly held oppositely charged headgroups.[60] In turn, the conformational inversion observed for the PyCX-PAMAM-G0 dendrimers having a longer alkyl linker connecting the pyrenyl moieties to the polar PAMAM core would be disfavored in these more hydrophobic micellar environments. Thus, the partitioning of the PyCX-PAMAM-G0 dendrimers in the different regions of the micellar aggregates should result in a range of conformations that could be probed through the PEF-methodology.[46-52] To assess whether this was indeed the case, PEF was applied to characterize the conformation of the PyCX-PAMAM-G0 dendrimers with X = 4, 6, 8, 10, and 12 in aqueous solutions of mixtures of SDS and DTAB for molar fractions (f_{DTAB}) of DTAB in the surfactant mixtures ranging from 0 to 0.3.

3.3 EXPERIMENTAL

Materials: The synthesis and characterization by ^{1}H NMR and mass spectrometry of the PyCX-PAMAM-G0 samples with X = 4, 6, 8, 10, and 12 has been reported in earlier publications.[50-52] SDS and DTAB were purchased from Aldrich and used as received. Doubly distilled deionized water from Millipore Milli-RO 10 Plus and Milli-Q UF Plus (Bedford, MA) was used to prepare all aqueous solutions.

PyCX-PAMAM-G0 sample preparation: Since the PyCX-PAMAM-G0 samples had been found earlier to generate negligible levels of pyrene aggregation inside DTAB micelles,[52] all PyCX-PAMAM-G0 aqueous solutions with 50 mM SDS/DTAB mixtures were prepared according to the following method. DTAB powder was added to a 20 mL vial and its mass was recorded. A 1 mM PyCX-PAMAM-G0 stock solution in DMSO was preheated to 60 ºC and approximately 12 mL of this solution was transferred into the vial. About 1 mL of chloroform was then added to the vial and the solid mixture was allowed to completely dissolve. The solution was then dried under constant air flow and a layer of white paste formed on the inner surface of the vial. The vial was then kept in a vacuum oven at room temperature overnight. This process had been found to ensure the removal of the chloroform.[52] The sample was then redissolved in 2 – 5 mL of MilliQ water first to ensure that the concentration of DTAB was above its CMC (15 mM), DTAB micelles would form, and the PAMAM dendrimers were isolated in the DTAB micelles, where the pyrenyl labels would be properly solvated. The required amount of SDS in dry powder form was then added to the solution to achieve the desired f_{DTAB} value for a given SDS:DTAB mixture. MilliQ water (5 – 8 mL) was further added to adjust the total surfactant concentration to 50 mM.

UV-Vis absorption measurements: The absorption spectra of the PyCX-PAMAM-G0 aqueous solutions with 50 mM SDS:DTAB surfactant mixtures were acquired with a Cary 100 UV-Visible spectrophotometer using a 5.0 cm pathlength quartz cuvette. The longer pathlength compared to the standard 1 cm absorption cell enabled the accurate measurement of the absorbance for a 0.6×10^{-6} M PyCX-PAMAM-G0 concentration with a reasonable signal-to-noise ratio.

Steady-state fluorescence: The fluorescence spectra were acquired with a HORIBA QM-400 spectrofluorometer equipped with a xenon arc-lamp as the excitation source and using a 1 nm-wide excitation and emission slit width. The solutions were excited at 344 nm and the

fluorescence of the PyCX-PAMAM-G0 solutions were monitored from 350 to 650 nm. The steady-state fluorescence (SSF) spectra were analyzed to obtain the fluorescence intensity of the pyrene monomer (I_M) and excimer (I_E) by integrating the fluorescence spectrum of the pyrene monomer from 376 to 382 nm and of the pyrene excimer from 500 to 530 nm, respectively. Dividing I_E by I_M yielded the I_E/I_M(SSF) ratio, which was taken as a measure of the PEF efficiency for a given PyCX-PAMAM-G0 solution.

Time-resolved fluorescence: The fluorescence decays of the pyrene monomer and excimer for the PyCX-PAMAM-G0 aqueous solutions were acquired according to the time-correlated single photon counting method with a FluoroHub time-resolved fluorometer from HORIBA equipped with a 336 nm DeltaDiode laser. The pyrene monomer and excimer fluorescence decays had both 20,000 counts at their decay maximum and were acquired at 379 and 510 nm over 1,024 channels with a time-per-channel of 0.44 and 0.87 ns and a 370 and 495 nm cut off filter, respectively. The cut off filters were used to prevent stray light from reaching the photomultiplier tube detector. The instrument response function (IRF) was obtained with a triangular aluminium monolith with the emission wavelength set at the same 336 nm wavelength as for the excitation.

Global model free analysis of the monomer and excimer fluorescence decays: Earlier studies have identified the existence of three pyrene species contributing to the fluorescence of pyrene-labeled macromolecules (PyLM) when probed according to the model free analysis (MFA).[61] The first species represents those pyrenyl labels (Py_{diff}*) forming excimer by diffusive encounters. The second species describes the pyrenyl labels (Py_{free}*) that are not attached to the macromolecule and emit as if they were free in solution with their lifetime (τ_M). Typically, the two pyrene species *E0** and *D** represent those pyrenyl labels that are involved in well and poorly stacked pyrene dimers leading to excimer fluorescence. *E0** and *D** are formed either by diffusive encounters from the species Py_{diff}* or by direct excitation of a pyrene aggregate

(Py_{agg}*). The pyrene species *E0** and *D** involved in well and poorly stacked pyrene dimers emit with their shorter and longer lifetimes τ_{E0} and τ_D, respectively. The global MFA of the pyrene monomer and excimer fluorescence decays yields the molar fractions f_{diff}, f_{free}, f_{E0}, and f_D of the pyrene species Py_{diff}*, Py_{free}*, *E*0*, and *D**, respectively, with f_{agg} being equal to the sum $f_{E0} + f_D$ representing the aggregated pyrenes (Py_{agg}*).

The MFA takes advantage of the fact that any fluorescence decay can be fitted with a sum of exponentials. Consequently, the fluorescence decays of the pyrene monomer are fitted with the sum of exponentials shown in Equation S3.1 in Supporting Information (SI), where the front part of Equation S3.1 describes PEF by diffusive encounters whereas the last exponential with the lifetime τ_M in the equation represents the species Py_{free}*. Equation S3.1 can then be used to derive Equation S3.2 using the kinetics expected for PEF. The pre-exponential factors (a_i) and decay times (τ_i) obtained from the MFA of the fluorescence decays in the front part of Equation S3.1 were used to calculate the average lifetime $<\tau>$ with Equation 3.2. $<\tau>$ could then be used to determine $<k>$ according to Equation 3.2.

$$< k >= \frac{\sum_{i=1}^{n} a_i}{\sum_{i=1}^{n} a_i \tau_i} - \frac{1}{\tau_M} = \frac{1}{< \tau >} - \frac{1}{\tau_M} \tag{3.2}$$

The parameters retrieved from the MFA could be combined into Equation 3.3 to yield the I_E/I_M(MFA) ratio.

$$I_E / I_M (MFA) = \frac{(f_{diffE0}\tau_{E0} + f_{diffD}\tau_D) < k >< \tau > + f_{E0}\tau_{E0} + f_D\tau_D}{(f_{diffE0} + f_{diffD}) < \tau > + f_{free}\tau_M} \tag{3.3}$$

The global MFA of the pyrene monomer and excimer fluorescence decays involved

convoluting the IRF with Equation S3.1 and S3.2 and comparing both convolution products with the experimental decays after optimization of the MFA parameters according to the Marquardt-Levenberg algorithm.[62] A fit was deemed satisfactory if the global χ^2 was smaller than 1.3 and the residuals and autocorrelation of the residuals were randomly distributed around zero.

Local concentration of pyrenyl labels for a PyCX-PAMAM-G0 sample: During a PEF experiment, one pyrenyl label of a PyCX-PAMAM-G0 sample is excited and the n_{Py} = 3 remaining pyrenyl labels are in the ground-state. Within the macromolecular volume (V_{den}) defined by the dendrimer, the local concentration ($[Py]_{loc}$) experienced by the excited pyrenyl label simply equals n_{Py}/V_{den}. A measure of V_{den} is obtained by taking the cube of the average distance (L_{Py}) separating every two ends of the dendrimer given in Equation 3.4. L_{Py} has been derived mathematically for low generation PAMAM dendrimers earlier by assuming that the internal segments of the PAMAM dendrimers obey Gaussian statistics.[49]

$$L_{Py}^2(N) = \left(2a + \frac{\left[2 - 2^{N+2} + (N+1)\times 2^{N+3}\right]b + 2^{N+1}c + 2^{N+1} - 1}{2^{N+2} - 1} \right) \times l^2 \qquad (3.4)$$

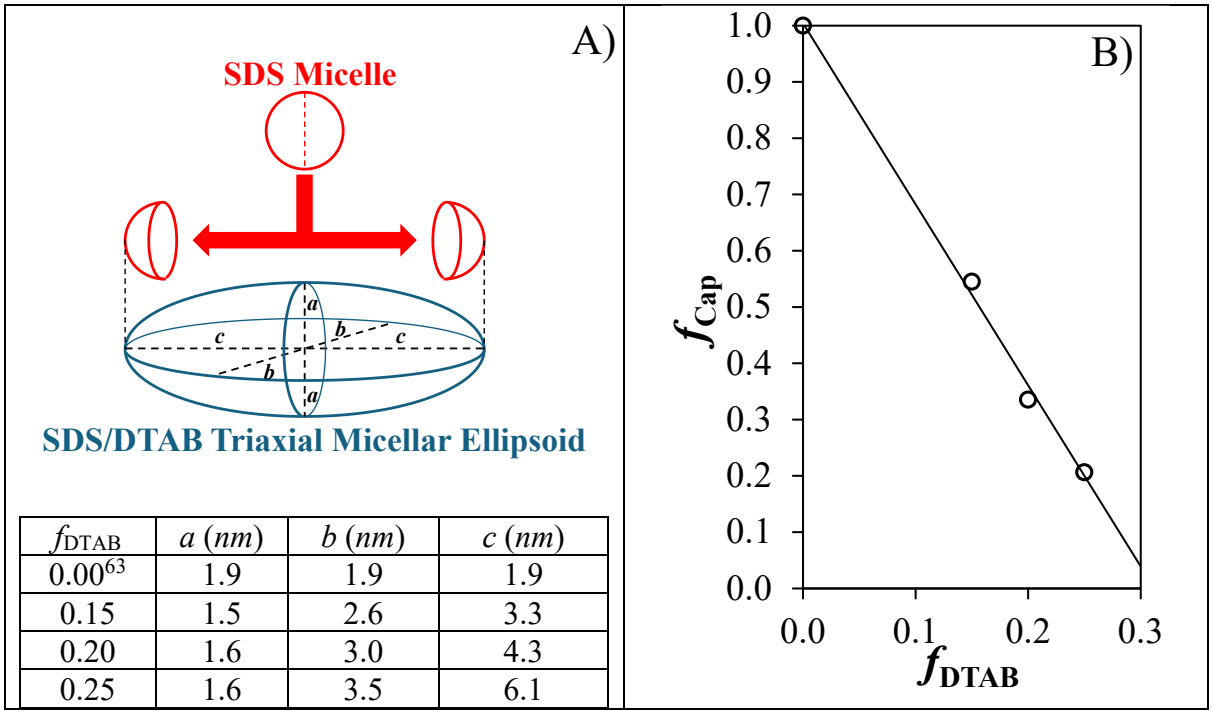
The parameters used in Equation 3.4 are the generation number (N) equal to 0 for the PyCX-PAMAM-G0 samples, the number of carbon atoms (a) in the linker connecting the pyrene moiety to the PAMAM dendrimer equal to X (= 4, 6, 8, 10, and 12), the number of non-hydrogen atoms (b = 7) in the aminoethyl propionamide building block of the PAMAM dendrimer, and the number of non-hydrogen atoms (c = 4) in the ethylene diamine core of the dendrimer.[50]

Calculation of the theoretical average rate constant (<k>th) for PEF in the SDS:DTAB mixed micelles: SANS experiments have established that SDS:DTAB micelles can be viewed as

triaxial ellipsoids as shown in Figure 3.3.[58] Consequently, these ellipsoidal mixed micelles have an elongated section of lower surface curvature and higher packing parameter composed of a mixture of SDS and DTAB. The capping ends of the ellipsoids with a much higher surface curvature are mainly composed of the surfactant in excess, SDS in these experiments. As a first approximation, the capping sections of the ellipsoids were represented by two hemispheres, whose combined volume equaled that of an SDS micelle. The volume fraction (f_{Cap} = $V_{micelle}/V_{ellipsoid}$) of the two capping sections of the ellipsoids was calculated based on the parameters listed in Figure 3.3A[58] and plotted as a function of f_{DTAB} in Figure 3.3B. The assumption that the capping ends of the ellipsoids have a volume equal to that of SDS micelles was made by noting that the equivalent radius (R) for the ellipsoid cross-section πab assumed to be a circle (= πR^2) equals 2.0 (±0.2) nm for the data listed in Figure 3.3A, which is close to the radius of 1.9 calculated for a spherical SDS micelle.[63] As f_{DTAB} increased, the contribution of the capping section to the ellipsoid volume decreased linearly as shown in Figure 3.3B.

The linear relationship obtained in Figure 3.3B provided an easy means to calculate the theoretical average rate constant $\langle k \rangle^{th}$ for PEF weighted by the volume contributions of the capping hemispheres (f_{Cap}) and the reminder of the ellipsoid referred to as the Core ($f_{Core} = 1 - f_{Cap}$) as described in Equation 3.5. In Equation 3.5, $\langle k \rangle^{Cap}$ and $\langle k \rangle^{Core}$ are the average rate constants for PEF in the two capping hemispheres of the ellipsoids taken as the experimental $\langle k \rangle$ found for pure SDS micelles and the core of the ellipsoids after excluding the capping ends, respectively.

$$\langle k \rangle^{th} = f_{cap} \times \langle k \rangle^{Cap} + (1 - f_{cap}) \times \langle k \rangle^{Core} \quad (3.5)$$



f_{DTAB}	*a* (*nm*)	*b* (*nm*)	*c* (*nm*)
0.00[63]	1.9	1.9	1.9
0.15	1.5	2.6	3.3
0.20	1.6	3.0	4.3
0.25	1.6	3.5	6.1

Figure 3.3. A) Schematic representation with values of the *a*, *b*, and *c* semi-axes for the triaxial SDS:DTAB micellar ellipsoid whose capping ends have a surfactant composition expected to approach those of an SDS micelle and B) plot of f_{cap} as a function of f_{DTAB}.

3.4 RESULTS

The PyCX-PAMAM-G0 samples, where the four amino terminals of the PAMAM-G0 dendrimer were labeled with a hydrophobic 1-pyrenealkanoyl derivative, were highly hydrophobic and could not dissolve in water despite the presence of their water-soluble PAMAM-G0 core. Adding either 50 mM SDS or DTAB, a surfactant concentration that is above their respective critical micelle concentration (CMC) of 8[64,41] and 15[64] mM, resulted in the formation of surfactant micelles, whose hydrophobic interior helped solubilise the pyrenyl labels of the PyCX-PAMAM-G0 samples, while keeping the PAMAM-G0 core at the micellar interface with water.[52] While pure SDS or DTAB micelles are typically spherical with a large micellar surface curvature due to their small packing parameter, mixing anionic SDS and cationic DTAB results in smaller effective cross-section for their headgroups by replacing the

electrostatic repulsion between same-charge headgroups by attraction between oppositely charged headgroups, which increases the packing parameter and reduces the surface curvature of the micellar aggregates. Consequently, SDS:DTAB surfactant mixtures provide a means for probing how the composition of a micellar aggregate affects the conformation of the PyCX-PAMAM-G0 dendrimers. In these experiments, the concentration of the PyCX-PAMAM-G0 samples was kept below 0.6 μM corresponding to mass concentrations of the dendrimers lower than 1.25 mg/L and the total surfactant concentration in the SDS:DTAB mixtures was kept at 50 mM. Under these conditions, the probability of finding two dendrimers in a same surfactant micelle was negligible, ensuring that the fluorescence signal reported on single dendrimers embedded in surfactant micelles. The conformation of the PyCX-PAMAM-G0 samples was characterized by PEF as f_{DTAB} was increased from 0.0 to 0.3. No mixture with $f_{DTAB} > 0.3$ was considered since the surfactant solutions turned turbid for $f_{DTAB} = 0.32$[57] indicating the formation of larger structures such as vesicles at higher DTAB contents.

Interactions between the PyCX-PAMAM-G0 samples and the micellar aggregates enabled the solubilization of their hydrophobic pyrenyl moieties as illustrated in the absorption spectra acquired with a 5 cm absorption cell shown in Figure 3.4A for a 50 mM solution of 75:25 SDS:DTAB mixture. The absorption bands between 300 and 350 nm are sharp reflecting the successful solubilization of the pyrenyl groups in the SDS:DTAB micellar aggregates. Excitation of the aqueous PyCX-PAMAM-G0 solutions at 344 nm yielded the fluorescence spectra shown in Figure 3.4B after being normalized to unity at 379 nm corresponding to the 0-0 transition of pyrene. The fluorescence spectra exhibited the expected spectral features of pyrene, with sharp emission bands between 370 and 410 nm corresponding to the pyrene monomer and the pyrene excimer emitting a broad structureless emission centered at around 480 nm.

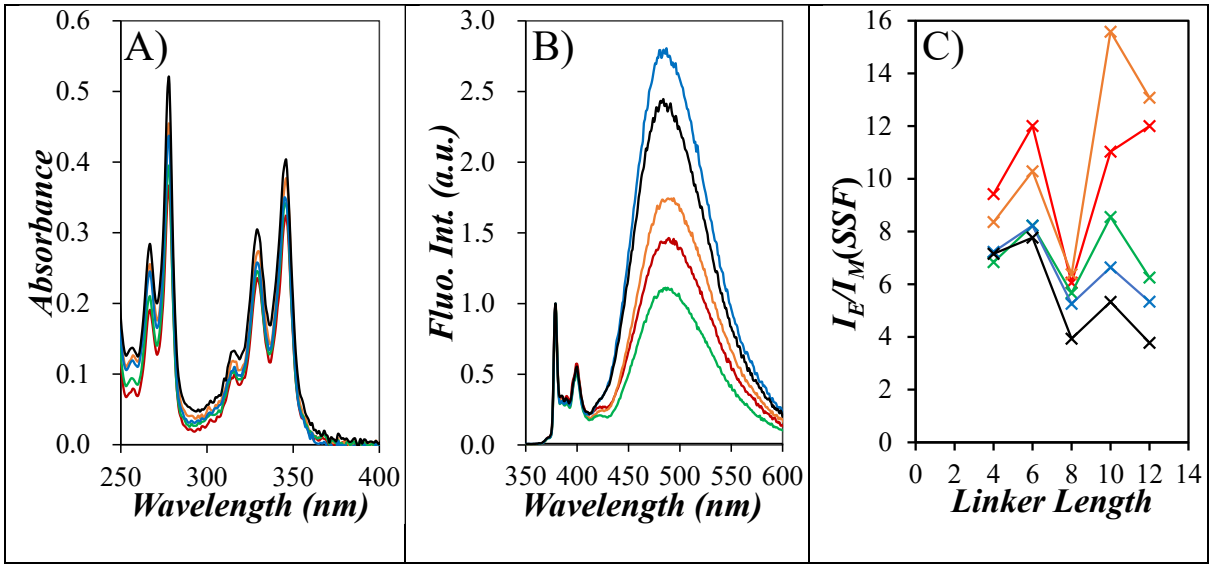


Figure 3.4. (A) Absorption and (B) fluorescence spectra for the PyCX-PAMAM-G0 samples with *X* equal to (red) 4, (orange) 6, (green) 8, (blue) 10, and (black) 12 in a 50 mM aqueous solution of the 75:25 SDS:DTAB mixture and C) plot of I_E/I_M(SSF) as a function of linker length (*X*) in a 50 mM aqueous solution of the (red) 100:0, (orange) 90:10, (green) 80:20, (blue) 75:25, and (black) 70:30 SDS:DTAB mixtures.

The ratio of the fluorescence intensity of the excimer (I_E) over that of the monomer (I_M) taken from the steady-state fluorescence (SSF) spectra yielded the I_E/I_M(SSF) ratio, which represented the efficiency of a pyrene-labeled macromolecule (PyLM) at forming an excimer. The I_E/I_M(SSF) ratio for a same series of PyCX-PAMAM-G0 samples was plotted as a function of the linker length in Figure 3.4C for each SDS:DTAB mixture investigated in this study. No clear behavior could be identified out of the trends shown in Figure 3.4C. This outcome was expected however, since the I_E/I_M(SSF) ratio is known to be very sensitive to minute quantities of unattached pyrene derivative,[65,66] with a content of unattached pyrenyl labels that varies from sample to sample. Elimination of the fluorescence signal emitted by the unattached pyrene derivatives can be achieved from the analysis of the fluorescence decays since unattached pyrene derivatives emit with the long lifetime (τ_M) of the pyrene monomer that can be easily separated from the much shorter-lived pyrenyl species attached onto the dendrimers that form

excimer on a faster time scale.[47-52]

To this end, the fluorescence decays of the pyrene monomer and excimer of the PyCX-PAMAM-G0 samples were acquired and a representative pair of pyrene monomer and excimer fluorescence decays are presented in Figures 3.5A and B, respectively. The fluorescence decay of the pyrene monomer in Figure 3.5A showed a bimodal behavior, with a short component describing excimer formation through diffusive encounters between pyrenyl labels (Py_{diff}*) and a much longer-lived component representing the contribution from unattached free pyrenyl labels (Py_{diff}*). The excimer fluorescence decay shows a risetime characteristic of PEF by diffusive encounters between two pyrenyl labels (Py_{diff}*) followed by a longer-lived component due to the excimer emission with the two characteristic lifetimes τ_{E0} and τ_D of the pyrenyl species *E*0* and *D**, respectively. The monomer and excimer fluorescence decays were fitted globally according to the model free analysis (MFA).[61] The fits were excellent as illustrated in Figures 3.5A and B, yielding residuals and autocorrelation of the residuals that were randomly distributed around zero and resulting in χ^2 that were lower than 1.3. The pre-exponential factors, decay times, molar fractions of the different pyrenyl species, and the lifetime τ_{E0} and τ_D of the two excimers were retrieved, and they are provided in Tables S3.1-S3.8 in the Supporting Information (SI). The parameters retrieved from the MFA of the fluorescence decays were combined into Equation 3.3 to yield I_E/I_M(MFA), which was plotted as a function of I_E/I_M(SSF) in Figure 3.5C. All the data points clustered around the diagonal indicating that the I_E/I_M(MFA) ratios calculated with the MFA parameters provided a good representation of the I_E/I_M(SSF) ratios. The correspondence between the I_E/I_M(SSF) and I_E/I_M(MFA) ratios observed in Figure 3.5C is a hallmark of PEF, which has been observed for a wide variety of PyLM in different solvents.[67] Its observation in Figure 3.4C implies that the parameters retrieved from the MFA of the fluorescence decays to calculate I_E/I_M(MFA) describe the fluorescence properties of the PyLM under study accurately. The MFA parameters were

used to calculate the I_E/I_M(MFA,f_{free}=0) ratio, where the contribution from the pyrenyl derivatives not attached to the dendrimer was eliminated, the average rate constant (<k>) for PEF by diffusive encounters between pyrenyl labels, and the molar fractions f_{diff} and f_{agg} (= 1 – f_{diff}) of the pyrene species that formed excimer by diffusive encounters or direct excitation of a pyrene dimer, respectively.

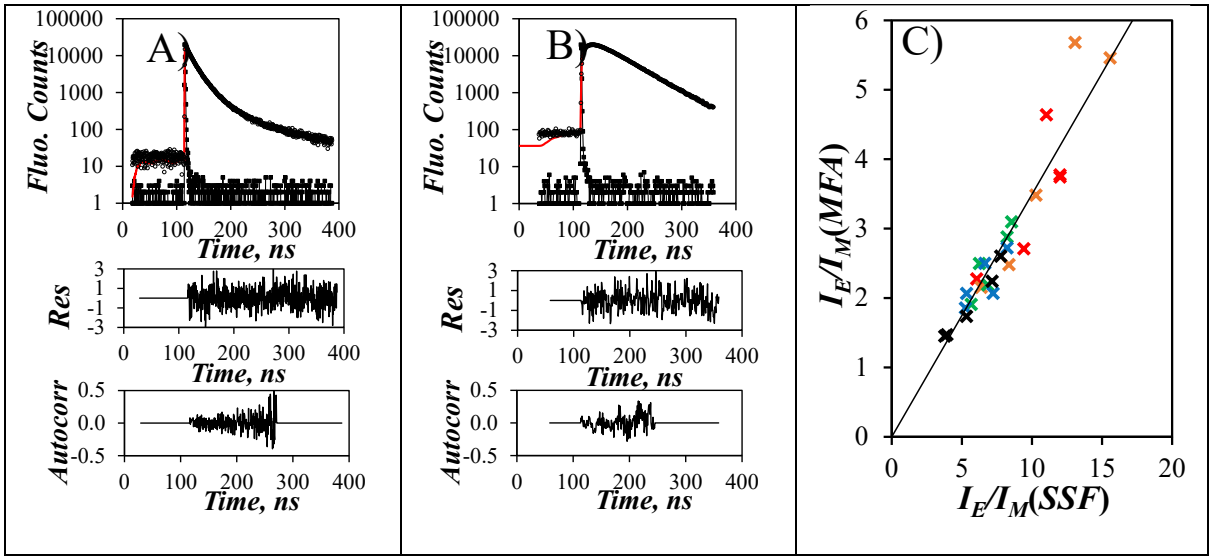


Figure 3.5. Fluorescence decays of A) the pyrene monomer (λ_{em} = 379 nm) and B) the pyrene excimer (λ_{em} = 510 nm) of the PyC6-PAMAM-G0 sample in the 50 mM 75:25 SDS:DTAB solution. λ_{ex} = 340 nm, χ^2 = 1.03. C) Plot of I_E/I_M(MFA) as a function of I_E/I_M(SSF) for the PyCX-PAMAM-G0 samples in a 50 mM aqueous solution of the (red) 100:0, (orange) 90:10, (green) 80:20, (blue) 75:25, and (black) 70:30 SDS:DTAB mixtures.

One clear advantage of using I_E/I_M(MFA) in Figure 3.5C is that by accounting for those pyrenyl species (Py_{free}*) that do not form excimer, there contributions can be eliminated by simply setting f_{free} equal to zero in Equation 3.3 to yield the I_E/I_M(MFA,f_{free}=0) ratio. Using the MFA parameters obtained in an earlier publication for the PyCX-PAMAM-G0 species in two organic solvents, namely DMF and DMSO, [49,52] I_E/I_M(MFA,f_{free}=0) was plotted as a function of linker length in Figure 3.6A.

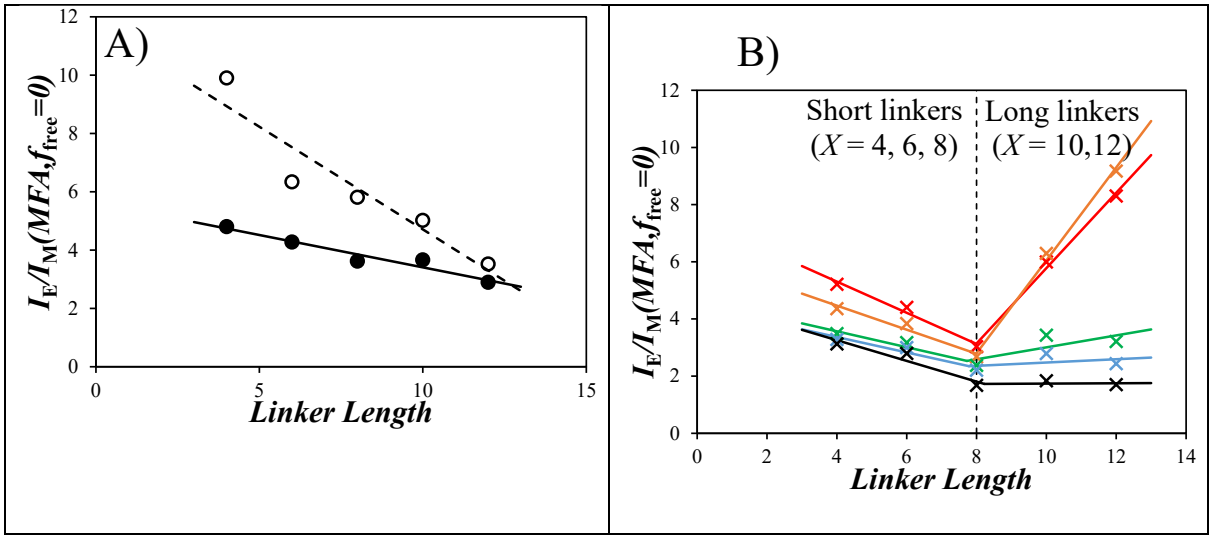


Figure 3.6. Plots of I_E/I_M(MFA,f_{free}=0) as a function of linker length for the PyCX-PAMAM-G0 samples in A) (O) DMF and (●) DMSO and B) in a 50 mM aqueous solution of the (red) 100:0, (orange) 90:10, (green) 80:20, (blue) 75:25, and (black) 70:30 SDS:DTAB mixtures.

The trends obtained for the PyCX-PAMAM-G0 samples in DMF and DMSO indicate that I_E/I_M(MFA,f_{free}=0) decreases continuously with increasing linker length. This behavior is expected since a longer linker connecting the four pyrene groups to the PAMAM-G0 core decreases $[Py]_{loc}$ resulting in fewer pyrene-pyrene encounters and a lower I_E/I_M(MFA,f_{free}=0) ratio. I_E/I_M(MFA,f_{free}=0) is also significantly larger in DMF with a lower solvent viscosity of 0.79 mPa·s at 25 °C than in DMSO with a higher solvent viscosity of 1.99 mPa·s at 25 °C.[68] Since PEF is a diffusion-controlled process, the rate constant for diffusive encounters between pyrenyl labels is inversely proportional to solvent viscosity and it is thus reasonable that I_E/I_M(MFA,f_{free}=0), which reflects the PEF efficiency, be lower in more viscous DMSO than in more fluid DMF. The clear trend shown in Figure 3.6A would have been impossible to identify from the I_E/I_M(SSF) ratios in DMF and DMSO shown in Figure 3.4C, that include the contribution of the Py_{free}* species, as was illustrated in earlier publications.[49,51]

I_E/I_M(MFA,f_{free}=0) was calculated for the PyCX-PAMAM-G0 samples in the surfactant mixtures and it was plotted as a function of the length of the alkanoyl linker in Figure 3.6B.

Compared to the zig-zag pattern observed for I_E/I_M(SSF) in Figure 3.4C, much clearer trends are obtained in Figure 3.6B. As for all PyCX-PAMAM-G0 samples in DMF and DMSO, the PyCX-PAMAM-G0 samples with X = 4, 6, and 8 yielded an I_E/I_M(MFA,f_{free}=0) ratio that decreased with increasing linker length reflecting the decrease in $[Py]_{loc}$. But the I_E/I_M(MFA,f_{free}=0) ratio for the PyCX-PAMAM-G0 samples with X equal to 10 and 12 showed a higher-than-expected I_E/I_M(MFA,f_{free}=0) ratio for all surfactant mixtures. This V-shaped pattern in Figure 3.6B, which was reported for the first time in pure SDS and DTAB micelles in an earlier publication,[52] was attributed to a conformational inversion experienced by the PyCX-PAMAM-G0 samples with the longer alkanoyl linkers induced by strong hydrophobic interactions between the micellar core and the linkers (compare Figures 3.2A and B). These interactions led to the pyrenyl labels being brought closer to each other with the pyrene ends pointing toward the micellar interface with water instead of toward the micellar core.

Interestingly, the magnitude of the conformational inversion identified in Figure 3.6B appeared to decrease as more DTAB was added to the SDS solution. Since the addition of DTAB is expected to reduce the electrostatic repulsion between the negatively charged SDS headgroups, the catanionic surfactant aggregates are expected to be larger than the pure surfactant micelles, as reported in the literature,[57,58] and to exhibit a lower surface curvature resulting from an increase in the packing parameter. Consequently, the plots shown in Figure 3.6B suggest that the PEF efficiency described by the I_E/I_M(MFA,f_{free}=0) ratio responds to the geometry of the micellar aggregates for the PyCX-PAMAM-G0 samples with X = 10 and 12, with the larger mixed surfactant aggregates yielding a less pronounced conformational inversion for these dendrimer samples.

While the Py_{free}* species is known to significantly affect the I_E/I_M(SSF) ratio for pyrene-labeled dendrimers, this ratio can also be affected by the presence of aggregated pyrenyl labels (Py_{agg}*) described by their molar fraction (f_{agg}) determined from the global MFA of the

fluorescence decays. After eliminating the contribution from the Py_{free}* species, the molar fractions f_{diff} and f_{agg} (= 1 – f_{diff}) for the species Py_{diff}* and Py_{agg}* forming excimer by diffusive encounters between pyrenyl labels or direct excitation of a pyrene aggregate, respectively, were calculated and plotted as a function of linker length in Figure 3.7A. Except for the PyCX-PAMAM-G0 samples with X = 10 and 12 in the 100:0 and 90:10 SDS:DTAB mixtures, all other f_{agg} values were lower than 0.15 indicating that PEF occurred predominantly through diffusive encounters between the pyrenyl labels. The larger f_{agg} values obtained for PyCX-PAMAM-G0 samples with the longer linkers in the 100:0 and 90:10 SDS:DTAB mixtures reflect the higher $[Py]_{loc}$ experienced by these dendrimer samples induced through conformational inversion of their pyrenyl end groups. For SDS:DTAB mixtures with $f_{DTAB} \geq$ 0.20, all f_{agg} values are lower than 0.15 indicating that PEF occurs mostly through diffusive encounters between pyrenyl moieties. The larger micellar aggregates obtained for the higher f_{DTAB} values ($f_{DTAB} \geq 0.20$)[57,58] provide enlarged hydrophobic domains that better solubilized the pyrenyl labels of the PyCX-PAMAM-G0 samples with X = 10 and 12. Yet, the trends obtained with I_E/I_M(MFA,f_{free}=0) in Figure 3.6B still show a break for the PyCX-PAMAM-G0 samples in the surfactant mixtures with $f_{DTAB} \geq 0.20$, although the break is less pronounced than for the samples studied for $f_{DTAB} \leq 0.10$.

Whereas the I_E/I_M(SSF) ratio is affected by the pyrenyl species Py_{free}* and Py_{agg}*, $\langle k \rangle$, which describes PEF through diffusive encounters between pyrenyl labels, has been shown to truly reflect $[Py]_{loc}$,[46-52] and thus report on the conformation of the dendrimer samples. $\langle k \rangle$ was calculated according to Equation 3.2 and it was plotted in Figure 3.7B as a function of $[Py]_{loc}$ determined with Equation 3.4 for the PyCX-PAMAM-G0 dendrimers.

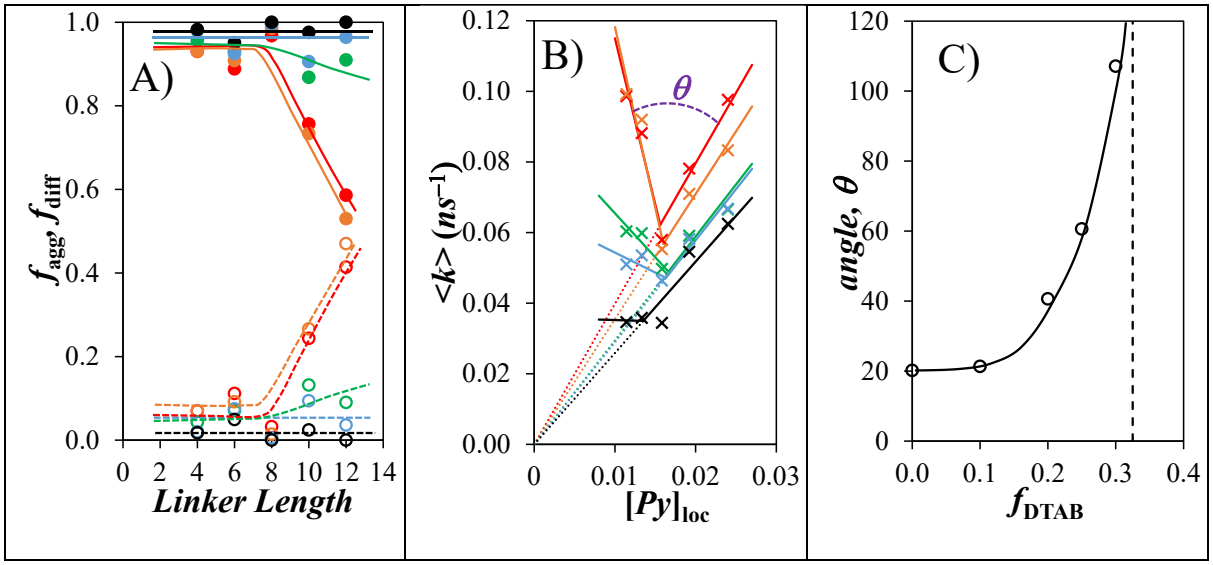


Figure 3.7. Plots of A) (solid) f_{diff} and (hollow) f_{agg} and B) <*k*> for the PyCX-PAMAM-G0 samples in a 50 mM aqueous solution of the (red) 100:0, (orange) 90:10, (green) 80:20, (blue) 75:25, and (black) 70:30 SDS:DTAB mixtures. C) Plot of the angle θ as a function of the composition of the catanionic surfactant mixture. The vertical dashed line in Figure 3.7C indicates the solubility limit of the SDS:DTAB mixture found to equal $f_{DTAB} = 0.32$.

Since $[Py]_{loc}$ was calculated by assuming that the internal segments of the PyCX-PAMAM-G0 samples obey Gaussian statistics,[49] the straight line passing through the origin when <*k*> was plotted as a function of $[Py]_{loc}$ for the PyCX-PAMAM-G0 samples with $X = 4$, 6, and 8 supports the validity of this assumption in all SDS:DTAB mixtures considered in this study. The linear <*k*>-*vs.*-$[Py]_{loc}$ relationship passing through the origin is a general trend that is expected to hold for any pyrene-labeled dendrimers dissolved in an organic solvent as has been reported in numerous publications.[52-52] The deviation of <*k*> from this linear relationship for the PyCX-PAMAM-G0 samples with $X = 10$ and 12 confirms the conclusion reached with the I_E/I_M(MFA,f_{free}=0) plots shown in Figure 3.6B, that $[Py]_{loc}$ is higher than expected for these samples due to the conformational inversion experienced by the pyrenyl end groups (see Figure 3.2B).[52] Interestingly, the magnitude of the deviation from the linear <*k*>-*vs.*-$[Py]_{loc}$ trends for the dendrimer samples with the longer linkers appear to decrease with increasing f_{DTAB}. This

point was confirmed by plotting the angle (θ) between the lines obtained for the PyCX-PAMAM-G0 samples with X = 4, 6, and 8 on the one hand, and X = 8, 10, and 12 on the other hand, as a function of f_{DTAB} in Figure 3.7C. θ was found to increase sharply from 21 to 107 ^{o} with increasing f_{DTAB}, with a θ value of 180 ^{o} representing a perfect alignment of the data points. Consequently, all the data presented so far confirmed that for all the SDS:DTAB mixtures considered, the PyCX-PAMAM-G0 samples with X = 10 and 12 behaved differently from the samples with X = 4, 6, and 8. The following discussion aims to rationalize how the conformation of the PyCX-PAMAM-G0 samples is affected by f_{DTAB} for mixed surfactant micelles.

3.5 DISCUSSION

The main effect of mixing two oppositely charged surfactants like SDS and DTAB is to increase significantly the size (N_{agg}) of the resulting surfactant aggregates.[57,58] In the process, the spherical micelles obtained from pure SDS or DTAB surfactants transform into much larger surfactant aggregates such as cylinders, ellipsoids, disks, vesicles, or bilayers.[64] The formation of these different supramolecular entities is simply a consequence of the increase in the packing parameter of the surfactants[59] resulting from the decrease in the effective cross-section of their headgroups due to the cancellation of electrostatic repulsion between same-charge headgroups when oppositely charged surfactants are present. The increase in the packing parameter results in a decrease of the surface curvature of the surfactant aggregates for SDS and DTAB mixtures leading to an increase in N_{agg}[57] and the formation of much larger objects.[58] To ensure that the surfactant headgroups are separated by the fully extended length (l) of the alkyl tails, one dimension of these objects remains set at 2×l as was observed for the SDS:DTAB triaxial ellipsoids, where the semi-axis a = 1.6 nm[58] in Figure 3.3A corresponds to an SDS or DTAB surfactant with a fully stretched dodecyl tail including the sulfate head group.[70] This condition

restricts the type of objects that can be generated by mixtures of oppositely charged surfactants where the increase in N_{agg} is accompanied by a large increase in the lateral size of the surfactant assembly in one (length for cylinders or prolates) or two (diameter for oblates, vesicles, or bilayers) dimensions. Considering these effects, one question worth asking is whether the large increase in the lateral dimensions of the self-assemblies resulting from mixtures of oppositely charged surfactants could affect the conformation of the PyCX-PAMAM-G0 dendrimers. Indeed, since the size of the PyCX-PAMAM-G0 samples depends on the length of the alkanoyl linker connecting the pyrene moiety to the PAMAM-G0 dendrimer,[49] an increase in the lateral dimension(s) of the surfactant aggregates could provide more room to accommodate the PyCX-PAMAM-G0 samples with a longer linker, which could affect their conformation.

However, it is unlikely that changes in the geometrical size of the surfactant aggregates might affect the dendrimer conformation because the PyCX-PAMAM-G0 samples are very small to start with. The end-to-end distance (L_{Py}), calculated with Equation 3.4 by assuming that the internal segments of the dendrimers obey Gaussian statistics,[49] equals 1.20, 1.30, 1.38, 1.46, and 1.54 nm for the PyCX-PAMAM-G0 samples with $X = 4$, 6, 8, 10, and 12, respectively, which is smaller than the diameter of the pure surfactant micelles. Indeed, pure SDS or DTAB micelles with a respective N_{agg} value of 71[41] or 51[69] have a spherical hydrophobic interior that is 3.6 or 3.2 nm in diameter based on the published volume of a methyl (CH_3, 49 Å^3) or a methylene (CH_2, 28 Å^3) group.[40] We note that the larger radius for a spherical SDS micelles reported in Figure 3.3A (1.9 nm) includes the sulfate groups in the volume calculation assumed to be spheres of radius 2.4 Å.[70] Assuming Gaussian statistics, the radial distribution function of the PyCX-PAMAM-G0 dendrimers is presented in Figure 3.8A and it also suggests that the probability of finding the two ends of the PAMAM dendrimers at distances greater than 3.0 nm is negligible. Consequently, all dendrimers should have sufficient room to fit inside the pure SDS or DTAB surfactant micelles. Furthermore, the shortest distance separating two

headgroups across the shortest symmetry axis of the ellipsoidal surfactant aggregate would equal $2\times a$ = 3.2 nm according to the data listed in Figure 3.3A for the SDS:DTAB mixed micelles, which is larger than the dimension of the PyCX-PAMAM-G0 dendrimers. Consequently, the increase in size observed from micelles made of pure surfactants and mixtures of oppositely charged surfactants should not affect the conformation of the dendrimers based on a geometric argument alone.

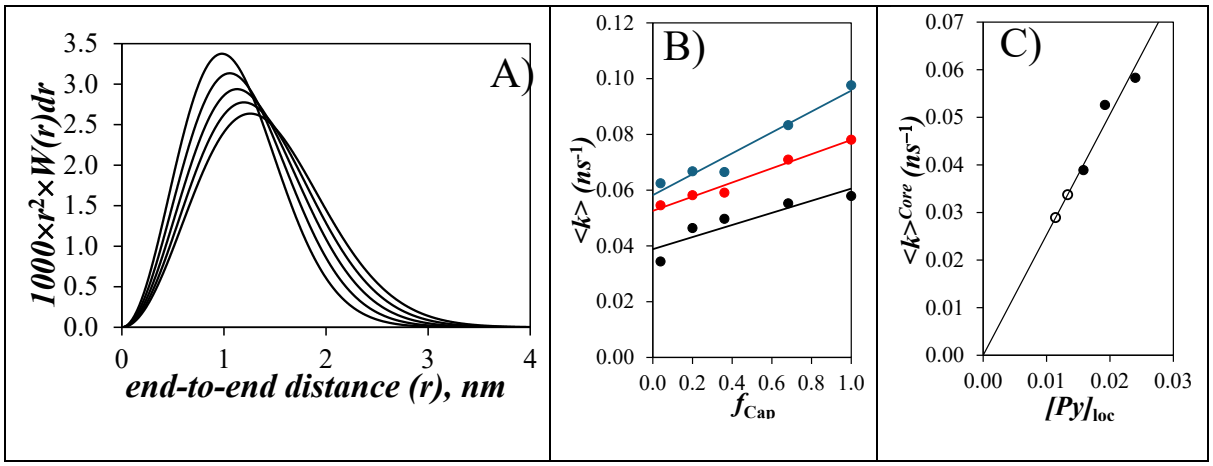


Figure 3.8. A) Radial distribution function ($r^2\times W(r)$) for the end-to-end distance of the PyCX-PAMAM-G0 samples. From left to right: X = 4, 6, 8, 10, and 12. B) Plot of $\langle k\rangle$ as a function of the volume fraction (f_{Cap}) of the capping hemispheres in the triaxial ellipsoids for the PyCX-PAMAM-G0 samples with X = (blue) 4, (red) 6, and (black) 8. C) $\langle k\rangle$ values extrapolated to f_{Cap} = 0 in Figure 3.8B ($\langle k\rangle^{Core}$) plotted as a function of $[Py]_{loc}$ for (●) the PyCX-PAMAM-G0 samples with X = 4, 6, and 8 and (○) predicted $\langle k\rangle^{Core}$ values for the PyCX-PAMAM-G0 samples with X = 10 and 12.

A likelier explanation for the reduction in the conformational inversion observed for the PyCX-PAMAM-G0 samples with X = 10 and 12 is the partitioning of these samples between the capping hemispheres and the ellipsoidal core of the mixed micelles. As shown in Figure 3.3A, the capping ends experience the largest curvature similar to that of a spherical micelle

made of a single surfactant. The capping ends approach the dimension of two hemispheres and are mostly composed of the surfactant in excess, SDS in the present study, which is subject to strong electrostatic repulsion. This region of the ellipsoids, whose composition is similar to that of pure SDS micelles, yields the conformational inversion that was reported for the PyC10- and PyC12-PAMAM-G0 samples in SDS micelles. A more balanced mixture of the oppositely charged surfactants is found in the central section of the ellipsoids where the reduction in electrostatic repulsion between their headgroups yields a more elongated configuration with a lower surface curvature. The tighter packing of the oppositely charged surfactant headgroups in the ellipsoid core results in a more hydrophobic environment,[60] which reduces the drive of the longer alkyl linkers to interact with the alkyl tails of the surfactant, that would otherwise lead to the conformational inversion of the PyCX-PAMAM-G0 samples with the decanoyl and dodecanoyl linkers.[52]

To substantiate this proposal, a theoretical expression for $\langle k \rangle^{th}$ was derived with Equation 3.5, which assumes that the experimental $\langle k \rangle$ value is the volume-weighted average of the $\langle k \rangle$ values obtained in the capping hemispheres ($\langle k \rangle^{Cap}$) and the core ($\langle k \rangle^{Core}$) of the triaxial ellipsoids. While $\langle k \rangle^{Cap}$ can be assumed to take the experimental $\langle k \rangle$ values obtained for the SDS micelles, $\langle k \rangle^{Core}$ needed to be determined. To this end, the experimental $\langle k \rangle$ values obtained for the PyCX-PAMAM-G0 samples with $X = 4$, 6, and 8 were plotted as a function of the volume fraction (f_{Cap}) of the two capping hemispheres in Figure 3.8B, taken as the ratio of their combined volume, assumed to equal that of an SDS micelle, divided by the volume of the triaxial ellipsoid. The $\langle k \rangle$-*vs.*-f_{Cap} plots could be approximated as straight lines in Figure 3.8B whose Y-intercept represented the $\langle k \rangle^{Core}$ value for the PyCX-PAMAM-G0 samples in infinitely long SDS:DTAB mixed micelles with no contribution from the capping regions. Plotting $\langle k \rangle^{Core}$ as a function of $[Py]_{loc}$ in Figure 3.8C yielded another straight line, which was used as a calibration curve to predict the $\langle k \rangle^{Core}$ value for the PyCX-PAMAM-G0 dendrimers

with X = 10 and 12.

The $\langle k \rangle^{th}$ values were determined by applying Equation 3.5 and using the experimental $\langle k \rangle$ values for the PyCX-PAMAM-G0 samples in SDS micelles for $\langle k \rangle^{Cap}$ and the $\langle k \rangle^{Core}$ values in Figure 3.8C. The $\langle k \rangle^{th}$ values were plotted as a function of $[Py]_{loc}$ in Figure 3.9 along with the experimental $\langle k \rangle$ values for comparison. The trends obtained with the $\langle k \rangle^{th}$-*vs*.-$[Py]_{loc}$ matched the general behavior obtained with the experimental $\langle k \rangle$ values. The checkmark pattern was clearly visible in the $\langle k \rangle$-*vs*.-$[Py]_{loc}$ plots for f_{DTAB} = 0.10 in Figure 3.9A, but the checkmark pattern became progressively less pronounced with increasing f_{DTAB}, becoming hardly noticeable for f_{DTAB} = 0.30 in Figure 3.9D.

The qualitative agreement between the $\langle k \rangle^{th}$ and $\langle k \rangle$ trends obtained in Figure 3.9 suggests that the main consequence of working with large catanionic micelles is that they generate an environment that is more hydrophobic than that of the spherical micelles formed with pure surfactants. In turn, the more hydrophobic environment affects the conformation of HMWSM like the PyCX-PAMAM-G0 dendrimers with a decanoyl or dodecanoyl linker. Electrostatic repulsion between the same charge headgroups of surfactants constituting pure SDS or pure DTAB micelles leads to a hydrophobicity gradient from the more polar micellar interface with water to the more hydrophobic micellar interior. This hydrophobic gradient induces the longer decanoyl and dodecanoyl linkers of the PyCX-PAMAM-G0 samples to interact with the interior of the SDS micelles resulting in the conformational inversion (see Figure 3.2B).[52] In contrast, strong electrostatic attraction between the oppositely charged headgroups of SDS and DTAB in catanionic micelles prepared with a mixture of both surfactants results in a more hydrophobic interface with water for the mixed micelles.[60]

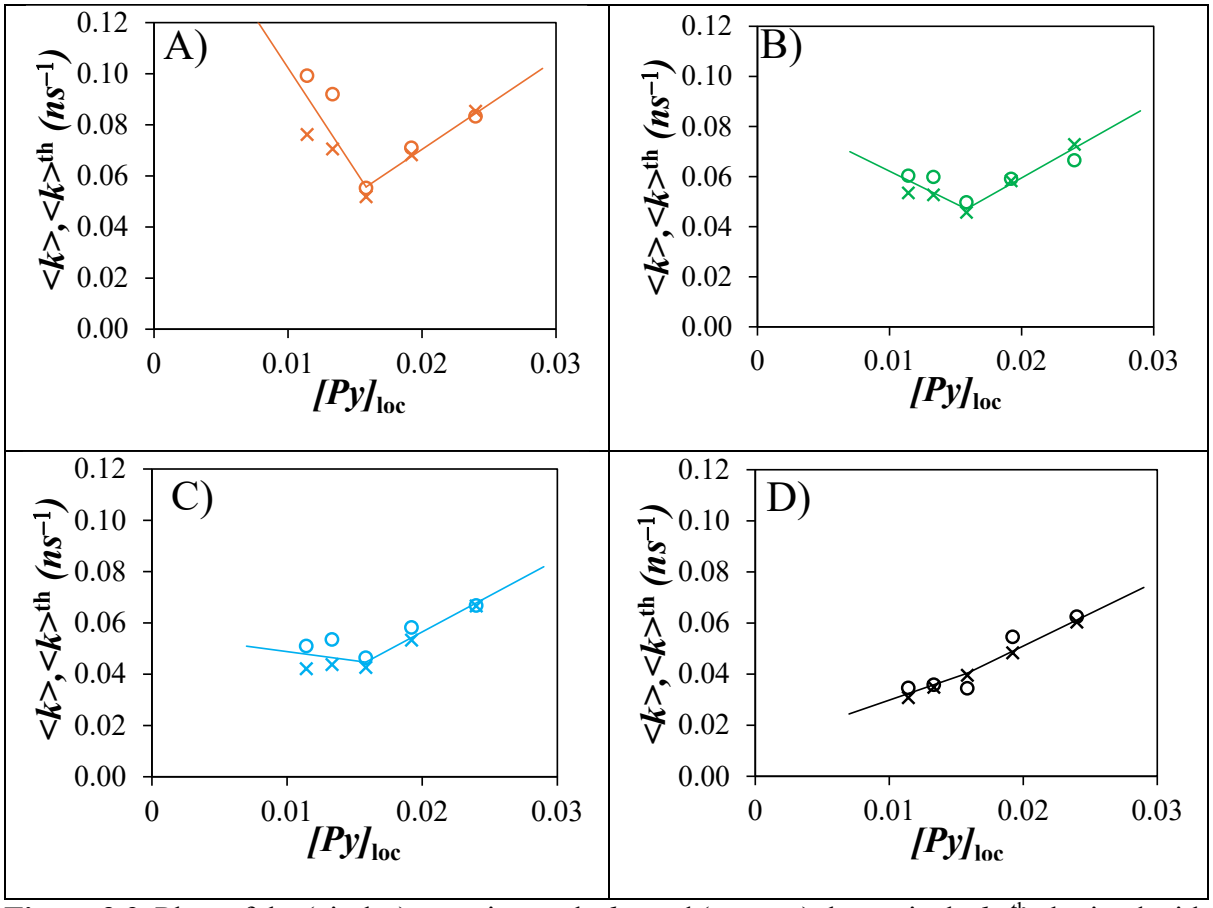


Figure 3.9. Plots of the (circles) experimental <*k*> and (crosses) theoretical <*k*>th obtained with the PyCX-PAMAM-G0 samples as a function of $[Py]_{loc}$ for f_{DTAB} equal to A) 0.10, B) 0.20, C) 0.25, and D) 0.30.

Consequently, the PyCX-PAMAM-G0 samples with X = 10 and 12 are less likely to experience a hydrophobicity gradient in catanionic micelles, which leads to a less pronounced conformational inversion as illustrated in Figures 3.7B and 3.9D. A schematic representation of the conformation of the PyCX-PAMAM-G0 associated with their location in the mixed micelles is shown in Figure 3.10.

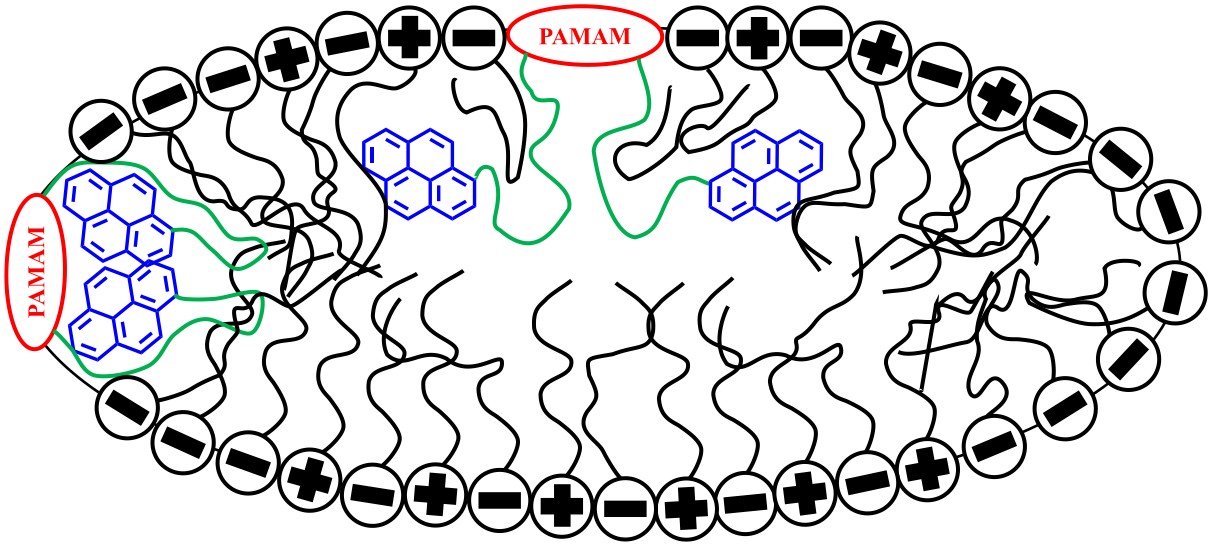


Figure 3.10. Schematic representation of the DSD:DTAB mixed micelles hosting a PyCX-PAMAM-G0 dendrimer with an inverted conformation in the capping hemisphere and with a regular conformation in the core section of the ellipsoidal micellar aggregates.

3.6 CONCLUSION

PEF was applied to probe how the composition of micelles made of oppositely charged surfactants affects the conformation of PyCX-PAMAM-G0 dendrimers as they interacted with the micelles. With increasing f_{DTAB}, the magnitude of the conformational inversion identified earlier for the PyCX-PAMAM-G0 dendrimers with the longer decanoyl and dodecanoyl linkers in SDS micelles[52] was diminished. This effect was attributed to the formation of more hydrophobic ellipsoidal domains made by the oppositely charged surfactants SDS and DTAB that generated tight ion pairs hindering the access of water molecules to the interface of the mixed micelles with water. In turn, the more hydrophobic core region of the ellipsoids reduced the drive of the longer decanoyl and dodecanoyl linkers to interact with the interior of the mixed surfactant aggregates resulting in a diminished conformational inversion. The complex behavior found for the $<k>$-*vs*.-$[Py]_{loc}$ trends in Figure 3.7B was found to be a consequence of the partitioning of the PyCX-PAMAM-G0 samples in the highly curved more polar capping

hemispheres composed mostly of SDS surfactants and the more hydrophobic central portion of the mixed micelles. As f_{DTAB} increased and the micellar aggregates increased in length, the contribution of the capping hemispherical ends of the ellipsoidal micelles decreased, which reduced the molar fraction of PyCX-PAMAM-G0 dendrimers with a longer decanoyl or dodecanoyl linker undergoing conformational inversion.

In summary, PEF was used in this study to identify the underlying physical phenomena controlling the conformation of the PyCX-PAMAM-G0 dendrimers as they interacted with mixed SDS:DTAB micellar aggregates whose DTAB content was increased from 0 to 30 mol%. Such a detailed description of the behavior of these HMWSM would be much more challenging to extract from more traditional NMR or scattering experiments.

Chapter 4: Two Distinct Regions in Surfactant Aggregates Identified with Pyrene-Labeled PAMAM Dendrimers

4.1 OVERVIEW

The conformational sensitivity of pyrene labeled generation-0 polyamidoamine (PyCX-PAMAM-G0) dendrimers to the hydrophobicity gradient (HG) of its surrounding was exploited to probe the interior of non-spherical surfactant aggregates (NSSA) resulting from the addition of NaCl to aqueous solutions of sodium dodecyl sulfate (SDS) spherical micelles. By characterizing the dendrimer conformation quantitatively using pyrene excimer formation (PEF), we identified two distinct regions in the NSSA, namely a polar edge region with a high HG and highly curved surface, which always consists of a constant number of charged SDS molecules, and a more hydrophobic middle region generated by the rest of the surfactants that are partially neutralized by Na^+ ions, exhibiting low HG and small surface curvature.

4.2 INTRODUCTION

Decades of studies on surfactant aggregates have led to a solid general understanding of their properties in water.[1,2] Their interior is constituted of the hydrophobic alkyl tails of the surfactant molecules, whose headgroups point outwards into the aqueous solution. They can adopt spherical, ellipsoidal, cylindrical, or lamellar geometries,[3-12] which are controlled by their critical packing parameter.[13] Yet, a more detailed understanding of their heterogeneous chemical composition at the molecular level is lagging due to their highly dynamic nature. Contrary to macromolecules, which can be covalently labeled at specific positions, the labeling of surfactant aggregates with molecular probes results in their continuous drift toward the region of the aggregate that best matches the properties of the probes, thus preventing a clear assignment of the different regions of the surfactant aggregates being probed. The pyrene-labeled generation-0 PAMAM dendrimers (PyCX-PAMAM-G0) recently introduced as fluorescent molecular probes reporting on the hydrophobicity gradient (HG) found in surfactant aggregates seem to circumvent this problem.[14,15] They sit at the surface of surfactant aggregates and probe their entire interior, thus reporting on the whole aggregates. The PyCX-PAMAM-G0 dendrimers are used herein to identify two distinct regions in the non-spherical surfactant aggregates (NSSA) generated by the addition of NaCl to aqueous solutions of sodium dodecyl sulfate (SDS), namely the polar charged edge region and the hydrophobic middle region. The identification of these two regions leads to a simple mechanism for the formation of NSSA.

The chemical composition of the PyCX-PAMAM-G0 dendrimers, whose structure is shown in Figure 4.1, endows them with the distinctive ability to sense the HG inside surfactant micelles.[14,15] Since pyrene is insoluble in water (solubility = 0.7 μM in water),[16] a PAMAM-G0 dendrimer decorated with four 1-pyrenealkanoyl groups is insoluble in water despite its water-soluble PAMAM core. However, the dendrimers can be incorporated inside surfactant

micelles where the polar PAMAM core, being unable to interact with the hydrophobic interior of the micelles, sits at the micellar interface with water[17-19] and the pyrenyl moieties locate themselves at the interface between the outer palisade and the hydrophobic core of surfactant micelles.[20-24] The shorter butanoyl (*X*=4), hexanoyl (*X*=6), and octanoyl (*X*=8) linkers connecting the pyrene moieties to the PAMAM core have been found to not interact with the hydrophobic interior of surfactant micelles and non-spherical surfactant aggregates (NSSA) in contrast to the longer decanoyl (*X*=10) and dodecanoyl (*X*=12) linkers.[14,15] The interactions between the longer decanoyl and dodecanoyl linkers and the micellar interior lead the dendrimers with longer linkers to undergo a conformational inversion that brings the pyrenyl labels closer to each other resulting in an increase in the local pyrene concentration ($[Py]_{loc}$) as shown in the top moiety of Figure 4.1B. Because the average rate constant ($\langle k \rangle$) of pyrene excimer formation (PEF) between an excited and a ground-state pyrenyl label covalently attached onto a macromolecule is directly proportional to $[Py]_{loc}$,[25] the conformational inversion of the PyC10- and PyC12-PAMAM-G0 dendrimers was identified experimentally from a significant increase in $\langle k \rangle$ for pure sodium dodecyl sulfate (SDS) or pure dodecyltrimethylammonium bromide (DTAB) micelles[14] and catanionic mixtures of the two.[15] This conformational inversion is a consequence of the HG generated between the polar micellar interface with water, where the PAMAM-G0 dendrimer resides, and the hydrophobic core of the micelles, that the longer linkers interact with. This conformational inversion represents an interesting new experimental tool that is being applied for probing the interior of surfactant aggregates at the molecular level.[14,15]

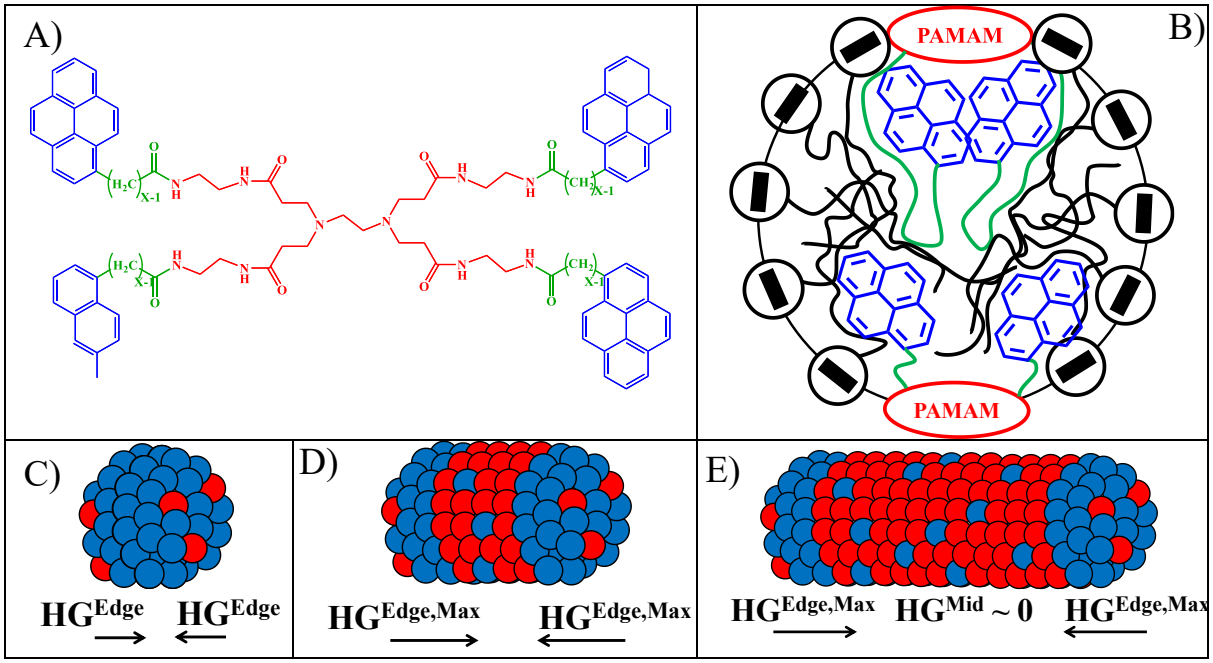


Figure 4.1. A) Chemical structure of the PyCX-PAMAM-G0 dendrimers with $X = 4$, 6, 8, 10, and 12 and B) illustration of a PyCX-PAMAM-G0 sample in an SDS micelle (top; $X = 10$, 12) undergoing and (bottom; $X = 4$, 6, 8) not undergoing a conformational inversion. Depiction of the spatial arrangement of the (blue) charged and (red) partially neutralized SDS molecules in the (C) SDS micelles, (D) elongated NSSA, and (E) extended rod-like NSSA.

SDS is probably the most studied surfactant[26-28] and its aggregates in water have been the focus of intense study. The attention paid to SDS micelles stems not only from its widespread use in numerous applications[26-28] but also from the expectation that the physical phenomena identified for the behavior of SDS micelles are likely to also apply to other surfactant systems. In aqueous solution, SDS forms small spherical micelles but in the presence of NaCl or dodecyltrimethylammonium bromide (DTAB), the small micelles morph into much larger non-spherical surfactant aggregates (NSSA) such as cylinders, ellipsoids, or lamellae.[3-12] The formation of NSSA is rationalized with the critical packing parameter (*cpp*),[13] which equals $v/(a \times l)$, where v is the volume of the alkyl tail of the surfactant, a is the cross-section of the surfactant headgroup at the micellar interface with water, and l is the length of the surfactant

tail. While *v* and *l* for a given ionic surfactant can be viewed as constant, *a* can be modified by adjusting the electrostatic force generated by the surfactant headgroup. In water, the negatively charged SDS headgroups generate strong electrostatic repulsion resulting in a large *a*, a small *cpp*, a high surface curvature at the micellar surface, and small spherical SDS micelles with an aggregation number of about 70.[5,7,8] Adding NaCl or DTAB decreases electrostatic repulsion between the surfactant headgroups which experience a smaller *a* resulting in a larger *cpp*, a lower curvature at the micellar surface, resulting in larger surfactant aggregates that are no longer spherical.[4-13] The departure from a sphere for the larger NSSA is caused by the requirement that at least one dimension of the NSSA remain constant and equal to about 2×*l* to ensure that the surfactant tails are in contact across the diameter of a cylinder or the thickness of a membrane bilayer in a lamella. The constraint that the surfactant aggregates be non-spherical with a region of low surface curvature also imposes that the NSSA edges be covered by surfactant structures with a much larger surface curvature to prevent exposure to water of the hydrophobic surfactant tails found at the edges. This condition can only be met if the surfactants at the edges of the NSSA have a small *cpp*, which can only be achieved if *a* is large or the surfactant headgroups are charged and strongly repel each other. This logical conclusion thus dictates that NSSA have a hydrophobic middle region constituted of surfactants with partially neutralized headgroups that are densely packed and highly polar edge regions constituted of surfactants that are not neutralized and enable electrostatic stabilization of the NSSA. Upon adding NaCl or DTAB, the NSSA become larger since the addition of either or both NaCl or DTAB reduces the number of fully charged SDS molecules remaining in the solution to form the edge region and ensure stabilization of the NSSA. The difference in polarity between the charged edges and the hydrophobic middle region of NSSA must induce an HG oriented along the largest dimension of the NSSA (the main axis of a cylinder or prolate or the lateral axes of lamellae or oblates) starting from the surface of the polar and negatively

charged edges and pointing toward the middle region of the NSSA. These concepts are illustrated in Figures 4.1C-E for the formation of cylindrical NSSA. Furthermore, the edges must be much more mobile than the middle region of the NSSA, since the edges are mainly constituted of charged SDS molecules similarly to SDS micelles with an interior that is much more mobile than that of the NSSA.[7,8] Due to their enhanced mobility and their HG, NSSA edges could provide an entry point for amphiphilic molecules in water that could then diffuse to different regions of the NSSA. Based on these considerations, the edges of NSSA represent important features that should warrant their characterization. Yet even their existence is never discussed in scientific literature.[29,31]

The absence of information about the charged edge region of NSSA inducing an HG is likely a consequence of the highly dynamic nature of the surfactants forming micelles and NSSA.[32-34] The fleeting nature of these self-assemblies makes it fiendishly challenging to probe a specific region of an NSSA whose constituting surfactants are in constant flux. For instance, fluorescent molecular probes used to target the interior of SDS micelles and NSSA locate themselves in the region of the NSSA that best matches their solubility, reporting on that specific region whose location in the NSSA is usually undefined.[35-37] Since the recently introduced PyCX-PAMAM-G0 dendrimers appear to distribute themselves randomly throughout NSSA, they represent an appealing macromolecular probe capable of sensing the HG generated at the NSSA edges.[14,15]

The change in the conformational inversion of the PyCX-PAMAM-G0 dendrimers with X = 10 and 12 was followed by monitoring their $\langle k \rangle$ value as they interacted with NSSA generated by 50 mM SDS with an NaCl concentration increasing from 0 to 620 mM. The significant rise and fall of $\langle k \rangle$ observed exclusively for the PyC10- and PyC12-PAMAM-G0 dendrimers with increasing NaCl concentration represents a clear illustration of changes in the balance between the large and small HG generated at the polar edges and in the hydrophobic

middle region of the NSSA, respectively. Contrary to earlier studies[38-40] aiming to probe surfactant-dendrimer interactions with molecular pyrene, which would sometime target only one of the two components instead of their complex, the covalent attachment of pyrene to the PAMAM-G0 dendrimers ensures that the fluorescence signal precisely reflects the behavior of the dendrimers.

4.3 RESULTS

The synthesis and chemical characterization of the PyCX-PAMAM-G0 samples were described in earlier publications.[14Error! Bookmark not defined.,41] The preparation of the PyCX-PAMAM-G0 solutions with a constant ~1 mg/L or 0.6 μM concentration in a 50 mM SDS aqueous solution with NaCl concentration ranging between 0 and 620 mM is described as Supporting Information. The extremely low PyCX-PAMAM-G0 concentration is necessary to enable the solubilization of the dendrimers and to ensure that the probability of incorporating two or more dendrimers per NSSA was negligible despite the ~100-fold concentration increase experienced by the dendrimers as they occupy the apolar domains generated by the 50 mM SDS aqueous solution. The fluorescence spectra of the PyCX-PAMAM-G0 solutions were acquired and they show the expected spectral features of a pyrene-labeled macromolecule, with the pyrene monomer exhibiting sharp fluorescence bands between 370 and 410 nm and the excimer emitting a broad structureless fluorescence centered around 480 nm. These features were clearly observed in Figures 4.2A and B presenting the normalized fluorescence spectra of the PyC12-PAMAM-G0 dendrimers in 50 mM SDS acquired at different NaCl concentrations. The fluorescence spectra normalized at 379 nm corresponding to the 0-0 transition of pyrene showed an increase in excimer formation for PyC12-PAMAM-G0 in Figure 4.2A when the NaCl concentration was increased from 0 to 200 mM followed by a decrease in excimer formation in Figure 4.2B when the NaCl concentration was increased further from 200 to 620

mM. These effects were summarized in Figure 4.2C where the fluorescence intensity ratio (I_E/I_M) of the excimer to the monomer was plotted as a function of NaCl concentration for all the PyCX-PAMAM-G0 dendrimers.

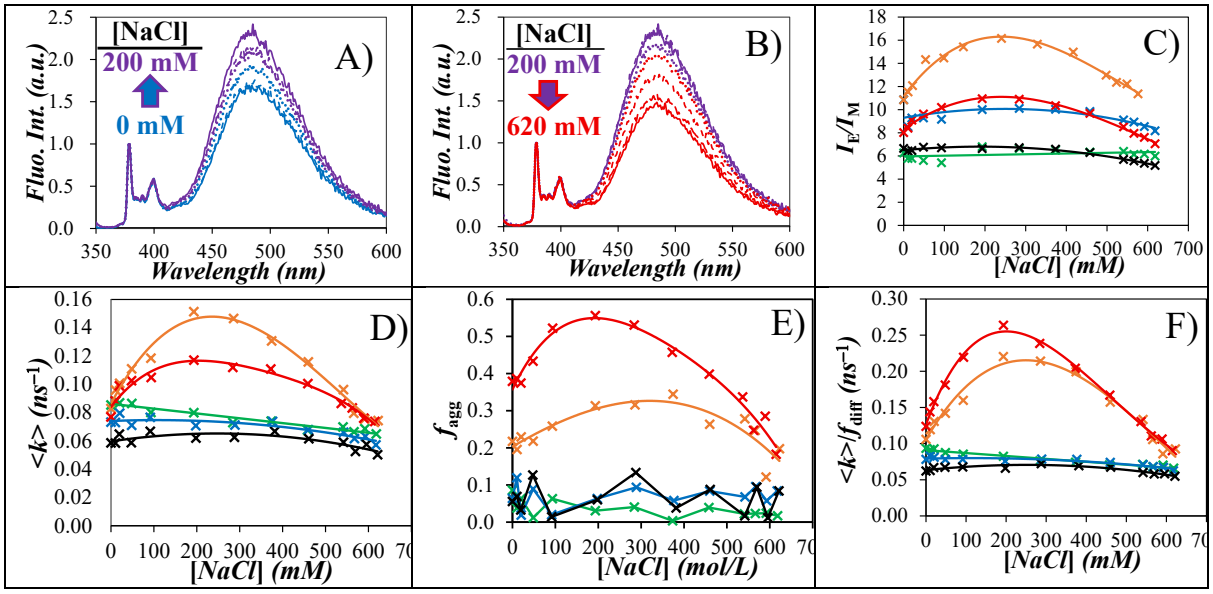


Figure 4.2. Fluorescence spectra normalized at the 0-0 transition of pyrene for A) PyC12-PAMAM-G0 for [NaCl] increasing from (bottom) 0 to (top) 200 mM, B) PyC12-PAMAM-G0 for [NaCl] increasing from (top) 200 to (bottom) 620 mM, and plots of C) I_E/I_M, D) $\langle k \rangle$, E) f_{agg}, and F) $\langle k \rangle/f_{diff}$ as a function of [NaCl] for (green) PyC4-, (blue) PyC6-, (black) PyC8-, (orange) PyC10-, and (red) PyC12-PAMAM-G0. [SDS] = 50 mM, [Py] = 2.4 μM, λ_{ex} = 344 nm.

Like the average rate constant $\langle k \rangle$, the I_E/I_M ratio should also be proportional to the local pyrene concentration ($[Py]_{loc}$) generated by the pyrenyl labels within the macromolecular volume of the PyCX-PAMAM-G0 dendrimers.[42] Based on their chemical structure (see Figure 4.1), PyC10-PAMAM-G0 should yield the second lowest $[Py]_{loc}$ and thus the second lowest I_E/I_M ratio. Instead, its I_E/I_M ratio takes the second highest value. Such discrepancies in the magnitude of the I_E/I_M ratios are common for pyrene-labeled macromolecules due to the

presence of residual unattached pyrene derivative, as has been discussed numerous times.[14,15,41] As such, the I_E/I_M ratios cannot be directly compared from one sample to another, but their trend generated from a single sample is informative as the residual amount of unattached pyrene derivative remains constant and I_E/I_M reflects how $[Py]_{loc}$ varies as a function of NaCl concentration for a given PyCX-PAMAM-G0 samples.

In this respect, the I_E/I_M ratio showed little variation over the 0 – 620 mM NaCl concentration range for the PyCX-PAMAM-G0 samples with $X = 4$, 6, and 8 indicating little change in $[Py]_{loc}$. This is expected since these dendrimers do not undergo a conformational inversion in surfactant micelles and are therefore not sensitive to a change in HG. In contrast, the I_E/I_M-*vs.*-[NaCl] profiles showed significant changes for the PyCX-PAMAM-G0 samples with $X = 10$ and 12. Since a change in $[Py]_{loc}$ for the PyC10- and PyC12-PAMAM-G0 samples reflects a change in the HG experienced by the dendrimers, these trends indicate that the NSSA formed by SDS generate an HG that increases from a NaCl concentration of 0 to 200 mM before decreasing from 200 to 620 mM. For a more quantitative analysis, the global model free analysis (MFA) of the fluorescence decays acquired with the PyCX-PAMAM-G0 samples was conducted next.

Global MFA of the fluorescence decays of the pyrene monomer and excimer yielded the average rate constant ($\langle k \rangle$) for PEF and the molar fractions f_{diff} and f_{agg} (= $1 - f_{diff}$) of pyrenyl labels forming excimer by diffusive encounters between two pyrenes and direct excitation of a pyrene aggregate, respectively.[14,15,25,41] f_{agg} was negligible at all NaCl concentrations in Figure 4.2E for the PyCX-PAMAM-G0 samples with $X = 4$, 6, and 8 and $\langle k \rangle$ showed little variation for these samples in Figure 4.2D mimicking their I_E/I_M trends in Figure 4.2C. In contrast, both $\langle k \rangle$ and f_{agg} for the PyC10- and PyC12-PAMAM-G0 samples in Figures 4.2D and E passed through a maximum mirroring the trends shown for the I_E/I_M ratios in Figure 4.2C. The increase in $\langle k \rangle$ reflects an increase in $[Py]_{loc}$ resulting in an increase in f_{agg} for the PyCX-PAMAM-G0

samples with a decanoyl and dodecanoyl linker. Since the increase in f_{agg} reduced the number of pyrenyl labels available for PEF and thus $[Py]_{loc}$ and $<k>$, $<k>$ was scaled up by using the $[<k>/f_{diff}]^{exp}$ ratio to account for the changes in f_{agg}, as has been done earlier for a series of six pyrene end-labeled dendrimers with a *bis*-hydroxymethyl propionic acid backbone.[43,44] The $[<k>/f_{diff}]^{exp}$ ratio was plotted in Figure 4.2F against the NaCl concentration, where it provided a more quantitative and consistent depiction of the I_E/I_M trends shown in Figure 4.2C, with the PyC4-, PyC6, and PyC8-PAMAM-G0 samples taking low $[<k>/f_{diff}]^{exp}$ ratios, that varied little with NaCl concentration, while the PyC10- and PyC12-PAMAM-G0 samples showed a significant maximum centered at about 200 mM NaCl. The $[<k>/f_{diff}]^{exp}$-*vs.*-[NaCl] trends in Figure 4.2F are now discussed with respect to the volume fraction (f_{Mid}) of the middle hydrophobic region of the NSSA.

4.4 DISCUSSION

The schematic representation of NSSA in Figures 4.1D and E suggests that they are constituted of two distinct regions. One region has a high surface curvature and represents the polar edges of the NSSA made of surfactants whose headgroups are charged. The other region has a low surface curvature and represents the hydrophobic middle region constituted of surfactants whose headgroups are partially charged after neutralization with a Na^+ cation. If a classic cylindrical geometry is assumed for the NSSA as suggested in Figures 4.1D and E and suggested in some experimental studies,[4,7] an important parameter describing the composition of NSSA would be the volume fractions f_{Mid} and f_{Edge} (= 1 – f_{Mid}) representing the hydrophobic middle and the polar edge regions, respectively. Assuming that the two hemispherical edges in Figures 4.1D and E are well represented by a spherical SDS micelle as done in an earlier study,[15] a simple expression of f_{Mid} and f_{Edge} would be given by Equation 4.1, where N_{agg}([NaCl]) represents the aggregation number of an NSSA at a given NaCl concentration. N_{agg}([NaCl] = 0

M) in Equation 4.1 is for a spherical SDS micelle formed in the absence of NaCl.

$$f_{Mid} = 1 - f_{Edge} = 1 - \frac{N_{agg}([NaCl] = 0\,M)}{N_{agg}([NaCl])} \tag{4.1}$$

To calculate the volume fractions f_{Mid} and f_{Edge} in Equation 4.1, the N_{agg}([NaCl]) values of NSSA for SDS aqueous solutions with NaCl reported in the literature[4,8] were plotted as a function of NaCl concentration in Figure 4.3A and fitted with the empirical Equation 4.2.

$$N_{agg}([NaCl]) = (46.761\times[NaCl]^4 - 25.803\times[NaCl]^3 + 2.051\times[NaCl]^2 + 0.4369\times[NaCl] + 0.979)\times (146.17\times[NaCl] + 74.643) \tag{4.2}$$

The N_{agg}([NaCl]) values calculated with Equation 4.2 were used to determine f_{Mid} with Equation 4.1, and the $[<k>/f_{diff}]^{exp}$ ratios in Figure 4.2F were plotted as a function of f_{Mid} in Figure 4.3B. Within experimental error, $[<k>/f_{diff}]^{exp}$ in Figure 4.3B varied little with f_{Mid} for the PyCX-PAMAM-G0 samples having a shorter linker reflecting the constancy of $[Py]_{loc}$ for these constructs as reported earlier.[14,15] Most strikingly, the $[<k>/f_{diff}]^{exp}$ values for both PyC10- and PyC12-PAMAM-G0 samples now clustered around two straight lines. $[<k>/f_{diff}]^{exp}$ first increased linearly with increasing f_{Mid} up to a f_{Mid}^{Max} value of about 0.3 corresponding to the maximum $[<k>/f_{diff}]^{exp}$ value at about 200 mM NaCl concentration, before decreasing linearly with increasing f_{Mid} for $f_{Mid} > f_{Mid}^{Max}$. The increase in $[<k>/f_{diff}]^{exp}$ at low NaCl concentration with increasing f_{Mid} reflects an increase in $[Py]_{loc}$ which is attributed to a more pronounced conformational inversion. Such high degree of inversion can only be induced by the high HG found in the edge region of the NSSA referred to as HG^{Edge}, which is defined by the charged

surfactant headgroups at one end of the edge region and the boundary with the hydrophobic middle region of the NSSA at the other end. Therefore, this increment in $[<k>/f_{diff}]^{exp}$ further suggests that the buildup of HG^{Edge} continues with increasing micelle size and f_{Mid} until $f_{Mid} = f_{Mid}^{Max}$, where HG^{Edge} reaches its maximum value ($HG^{Edge,Max}$) and remains constant for NaCl concentrations greater than 200 mM (see Figures 4.1D and E). Since HG^{Edge} induces the conformational inversion observed for the PyC10- and PyC12-PAMAM-G0 dendrimers, it is associated with the $[<k>/f_{diff}]^{Edge}$ ratio, that increases from $[<k>/f_{diff}]^{SDS}$ for pure SDS micelles without NaCl to a maximum value of $[<k>/f_{diff}]^{Edge,Max}$ at f_{Mid}^{Max}, and remains constant for $f_{Mid} > f_{Mid}^{Max}$.

On the other hand, the HG in the hydrophobic middle section of the NSSA constituted by the neutralized SDS molecules, denoted as HG^{Mid}, approaches 0 and is associated with a $[<k>/f_{diff}]^{Mid}$ ratio taking a small value. As the middle region of the NSSA grows with increasing NaCl concentration, the probability of finding the PyC10- and PyC12-PAMAM-G0 samples in the hydrophobic middle region (shown in red in Figures 4.1D and E) increases. Since the two dendrimers with a longer linker have a lower $[<k>/f_{diff}]^{Mid}$ ratio compared to the $[<k>/f_{diff}]^{Edge,Max}$ ratio at the capping edges of the NSSA (shown in blue in Figures 4.1C-E), the overall experimental $[<k>/f_{diff}]^{exp}$ ratio decreases in Figure 4.3B due to the partitioning of the dendrimers between the two regions. The linear $[<k>/f_{diff}]^{exp}$-*vs*-f_{Mid} trends for the PyC10- and PyC12-PAMAM-G0 dendrimers shown in Figure 4.3B were well described by Equation 4.3, which reflects the partitioning of the dendrimers between the edge and middle regions of the NSSA described by their $[<k>/f_{diff}]^{Edge}$ and $[<k>/f_{diff}]^{Mid}$ values, respectively. In Equation 4.3, $[<k>/f_{diff}]^{Mid}$ is constant and its value is given in Table 4.1 whereas $[<k>/f_{diff}]^{Edge}$ is a function of f_{Mid}, that takes the expression given in Table 4.2 which depends on the ratios $[<k>/f_{diff}]^{Edge,Max}$ and $[<k>/f_{diff}]^{SDS}$ and the fraction f_{Mid}^{Max}, which were defined earlier.

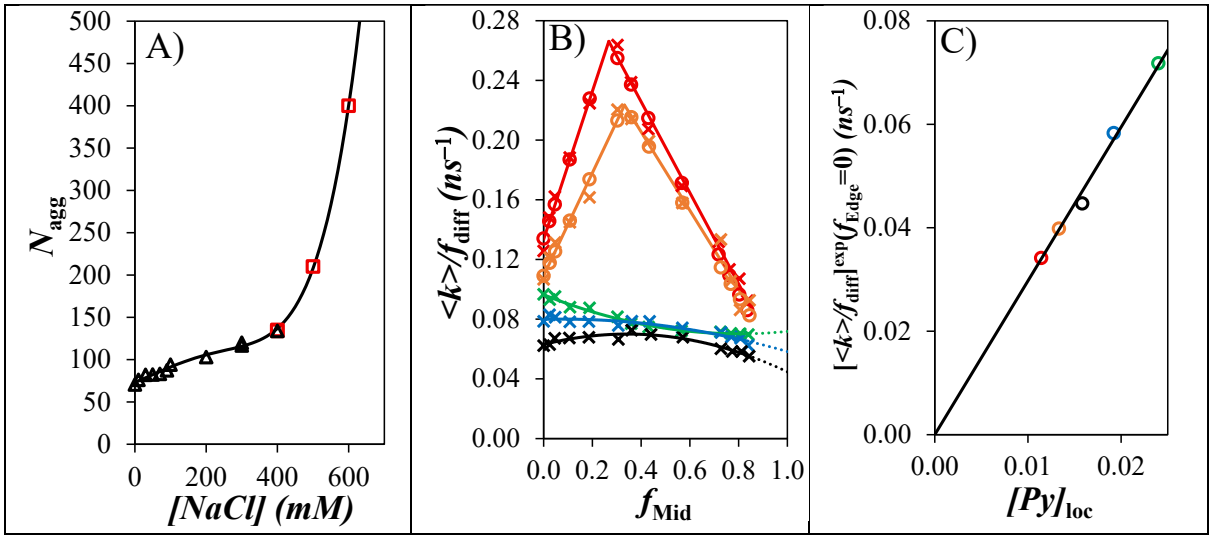


Figure 4.3. A) Plot of A) N_{agg} as a function of [NaCl] for N_{agg} values obtained from references (black triangles) #8 and (red squares) #4, B) (crosses) $[<k>/f_{diff}]^{exp}$ and (hollow circles) $[<k>/f_{diff}]^{th}$ as a function of f_{Mid}, C) $[<k>/f_{diff}]^{exp}(f_{Mid}=1)$ as a function of $[Py]_{loc}$. Colors for the $[<k>/f_{diff}]^{exp}$ and $[<k>/f_{diff}]^{th}$ symbols: (green) PyC4-PAMAM-G0, (blue) PyC6-PAMAM-G0, (black) PyC8-PAMAM-G0, (orange) PyC10-PAMAM-G0, and (red) PyC12-PAMAM-G0. [SDS] = 50 mM, [Py] = 2.4 μM.

$$[<k>/f_{diff}]^{th} = [<k>/f_{diff}]^{Edge} + ([<k>/f_{diff}]^{Mid} - [<k>/f_{diff}]^{Edge}) \times f_{Mid} \quad (4.3)$$

The $[<k>/f_{diff}]^{Mid}$ ratio representing the PyCX-PAMAM-G0 samples located in the hydrophobic middle region of the NSSA that would not undergo a conformational inversion was obtained by extrapolating the $[<k>/f_{diff}]^{exp}$-*vs.*-f_{Mid} trends for the PyCX-PAMAM-G0 samples with X = 4, 6, and 8 in Figure 4.3B to f_{Mid} = 1 representing a hypothetical infinitely long cylinder to yield their $[<k>/f_{diff}]^{exp}(f_{Mid} = 1)$ value. The $[<k>/f_{diff}]^{exp}(f_{Mid} = 1)$ values of the PyCX-PAMAM-G0 dendrimers with X = 4, 6, and 8 were plotted as a function of $[Py]_{loc}$ in Figure 4.3C, where $[Py]_{loc}$ is the local pyrene concentration of the dendrimer, which was calculated earlier by assuming that their internal segments obey Gaussian statistics.[41] The $[<k>/f_{diff}]^{exp}(f_{Mid} = 1)$ ratios of the PyCX-PAMAM-G0 samples with the shorter linkers aligned

around a straight line passing through the origin as expected, which could be further used as a calibration curve to estimate the $[<k>/f_{diff}]^{exp}(f_{Mid} = 1)$ ratios taken as the $[<k>/f_{diff}]^{Mid}$ ratio of the PyC10- and PyC12-PAMAM-G0 samples, whose values have been reported in Table 4.1. The constant $[<k>/f_{diff}]^{Edge,Max}$ ratio obtained at NaCl concentrations higher than ~200 mM, was determined by entering f_{Mid}^{Max} at the intercept of the two straight lines in Figure 4.3B into Equation 4.3 and equating $[<k>/f_{diff}]^{th}$ to $[<k>/f_{diff}]^{exp}$. The $[<k>/f_{diff}]^{Edge,Max}$ ratios retrieved for the PyC10- and PyC12-PAMAM-G0 samples are listed in Table 4.1 along with their f_{Edge}^{Max} and $[<k>/f_{diff}]^{SDS}$ values. $[<k>/f_{diff}]^{Edge,Max}$ is close to 10-times larger than $[<k>/f_{diff}]^{Mid}$ reflecting the much higher $HG^{Edge,Max}$ and degree of conformational inversion experienced by the dendrimers with the longer decanoyl and dodecanoyl linkers in the polar edge region of the NSSA compared to the apolar middle region, where $HG^{Mid} \sim 0$. For NaCl concentrations lower than 200 mM where $0 \leq f_{Mid} \leq f_{Mid}^{Max}$, the decrease in $[<k>/f_{diff}]^{exp}$ with increasing f_{Mid}, due to the partitioning of the dendrimers between the edges with a large $[<k>/f_{diff}]^{Edge}$ and the middle region with a small $[<k>/f_{diff}]^{Mid}$, is offset by the small f_{Mid} values and the large increase experienced by $[<k>/f_{diff}]^{Edge}$ from $[<k>/f_{diff}]^{SDS}$ to $[<k>/f_{diff}]^{Edge,Max}$. The outcome is the linear increase in $[<k>/f_{diff}]^{exp}$ with increasing f_{Mid} observed in Figure 4.3B for the dendrimers with the longer linkers. Using the $[<k>/f_{diff}]^{Mid}$, $[<k>/f_{diff}]^{Edge,Max}$, and $[<k>/f_{diff}]^{SDS}$ ratios and f_{Mid}^{Max} listed in Table 4.1, the theoretical $[<k>/f_{diff}]^{th}$ ratio could be calculated with Equation 4.3 using the expression of $[<k>/f_{diff}]^{Edge}$ in Table 4.2. The excellent agreement found between the $[<k>/f_{diff}]^{th}$ and $[<k>/f_{diff}]^{exp}$ ratios in Figure 4.3B validates the parametrization of the experimental data assuming the existence of two distinct regions in NSSA, namely the edge and middle regions.

Table 4.1. $[<k>/f_{diff}]^{Mid}$, $[<k>/f_{diff}]^{Edge,Max}$, and $[<k>/f_{diff}]^{SDS}$ ratios and f_{Mid}^{Max} determined experimentally and used in Equation 4.3 to predict the theoretical $[<k>/f_{diff}]^{th}$ ratio.

	$[<k>/f_{diff}]^{Mid}$	$[<k>/f_{diff}]^{Edge,Max}$	$[<k>/f_{diff}]^{SDS}$	f_{Mid}^{Max}
PyC10-PAMAM-G0	0.040	0.314	0.109	0.332
PyC12-PAMAM-G0	0.034	0.351	0.134	0.267

Table 4.2. Mathematical expression of $[< k > / f_{diff}]^{Edge}$ in Equation 4.3

$0< f_{Mid} < f_{Mid}^{Max}$	$f_{Mid}^{Max} < f_{Mid} <1$
$\frac{[< k > / f_{diff}]^{Edge,Max}(1- f_{Mid}^{Max}) f_{Mid} +[< k > / f_{diff}]^{SDS}(f_{Mid}^{Max} - f_{Mid})}{f_{Mid}^{Max}(1- f_{Mid})}$	$[< k > / f_{diff}]^{Edge,Max}$

Besides providing a rationale for the change in the $[<k>/f_{diff}]^{exp}$ ratio for the PyC10- and PyC12-PAMAM-G0 samples by invoking their partitioning between the polar and curved capping edge region and the hydrophobic and less curved middle region of the NSSA, the strikingly linear $[<k>/f_{diff}]^{exp}$-*vs.*-f_{Mid} trends in Figure 4.3B illustrate the importance of the volume fraction f_{Mid}, and consequently f_{Edge} (= 1 – f_{Mid}). Interestingly, Equation 4.1 implies that f_{Edge} is not only the volume fraction of the capping edges in the NSSA, but it also represents the molar fraction of charged SDS molecules in an NSSA. The corollary to this revised definition of f_{Edge} is that the number of charged SDS molecules in an NSSA at any NaCl concentration remains constant and equal to the number of charged SDS molecules in an SDS micelle without NaCl given by N_{agg}([NaCl]=0 M) in Equation 4.2. This surprisingly simple insight provides a means for checking the feasibility of possible mechanisms for the formation of NSSA. For instance, one could consider that the partially neutralized SDS molecules being more hydrophobic than their non-neutralized counterparts would self-assemble first and more rapidly into large hydrophobic cylindrical or disk-like surfactant aggregates, leaving the remaining charged SDS molecules to form SDS micelles more slowly due to electrostatic

repulsion between the charged SDS molecules. The large hydrophobic surfactant aggregates would have open edges exposing the hydrophobic dodecyl tails of the surfactants to water. Over time, diffusive encounters between the hydrophobic surfactant aggregates of neutralized SDS molecules and charged SDS micelles would lead to the formation of NSSA which would have a same number of charged SDS molecules localized at their edges (see Figure 4.4).

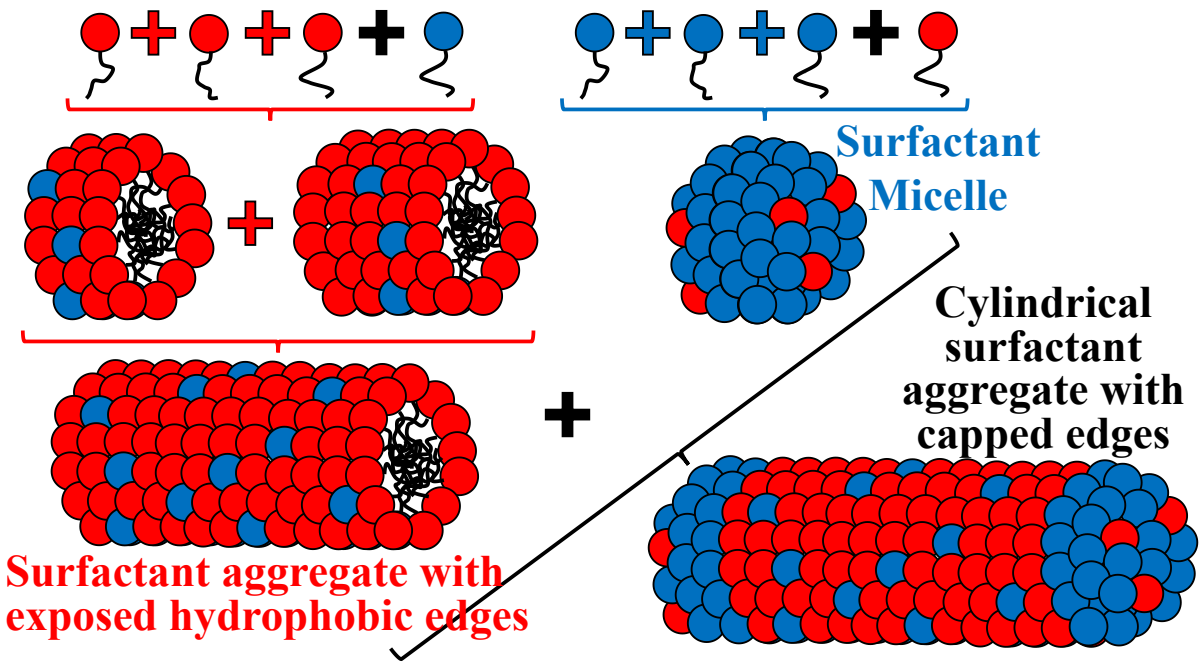


Figure 4.4. Possible mechanism for the formation of cylindrical NSSA from the encounter between a (blue) SDS micelle and a (red) hydrophobic surfactant aggregate with exposed hydrophobic edges.

Furthermore, increasing the NaCl concentration would increase the number of neutralized SDS molecules, whose hydrophobicity would lead to their association into larger aggregates, and reduce the number of charged SDS molecules resulting in fewer SDS micelles. Since fewer SDS micelles would form, the hydrophobic surfactant aggregates made of neutralized SDS molecules would grow larger until they would eventually encounter one of the few remaining SDS micelles, leading to the formation of larger NSSA at higher NaCl

concentration. In the proposed mechanism illustrated in Figure 4.4, the charged edges of the NSSA ensure their electrostatic stabilization.

4.5 CONCLUSION

This study illustrates how PyCX-PAMAM-G0 dendrimers can be employed as fluorescent molecular probes for surfactant assemblies. In particular, the conformational inversion experienced by the PyC10- and PyC12-PAMAM-G0 dendrimers described by the ratio $[\langle k \rangle / f_{diff}]^{exp}$ and the strikingly linear relationships between $[\langle k \rangle / f_{diff}]^{exp}$ and f_{Mid} uncovered in Figure 4.3B demonstrated the existence of two distinct regions in NSSA among which the dendrimers partition themselves randomly. Perhaps more importantly, the direct dependency of $[\langle k \rangle / f_{diff}]^{exp}$ on f_{Mid} led to the conclusion that a constant number of charged SDS molecules forms the edge region of the NSSA and that the remaining SDS molecules that are partially neutralized occupy the middle region of the NSSA. This representation of the NSSA was illustrated in Figures 4.1C-E providing the basis for the mechanism presented in Figure 4.4 to describe the formation of NSSA. The simplicity of this mechanism and its wide applicability for understanding the formation of NSSA provides a unifying principle to rationalize the numerous experimental observations reported in the scientific literature about NSSA.

Chapter 5: Effect of Salt Concentration on Catanionic Surfactant Aggregates Probed by Pyrene Excimer Formation (PEF) with Pyrene End-Labeled Polyamidoamine (PAMAM) Dendrimers

5.1 OVERVIEW

The effect of NaCl concentration on the size of non-spherical surfactant aggregates (NSSA) consisting of an 80:20 sodium dodecyl sulfate (SDS):dodecyltrimethylammonium bromide (DTAB) mixture in aqueous solution was studied at a total surfactant concentration of 50 mM. This was accomplished by following the conformation of five pyrene end-labeled generation 0 polyamidoamine (PAMAM-G0) dendrimers as they interacted with the SDS:DTAB NSSA at NaCl concentrations of 10, 20, 50, and 100 mM. The dendrimers referred to as the PyCX-PAMAM-G0 samples were labeled with 4 identical pyrenyl moieties connected to the PAMAM-G0 core with either (X=4) butyroyl, (X=6) hexanoyl, (X=8) octanoyl, (X=10) decanoyl, or (X=12) dodecanoyl linker. The model free analysis (MFA) was applied to their fluorescence decays to obtain the ratio $[\langle k \rangle / f_{diff}]^{exp}$ as a measure of the local concentration ($[Py]_{loc}$), which was used to describe the conformation of the dendrimers as they interacted with the NSSA. For all NaCl concentrations, the PyC4-, PyC6-, and PyC8-PAMAM-G0 dendrimers yielded a $[\langle k \rangle / f_{diff}]^{exp}$ ratio that decreased with increasing linker length as expected if the internal segments connecting the pyrenyl groups obeyed Gaussian statistics. The $[\langle k \rangle / f_{diff}]^{exp}$ ratios of PyC10- and PyC12-PAMAM-G0 were larger than that of PyC8-PAMAM-G0, indicating that the former dendrimers underwent a conformational inversion upon interacting with the NSSA. The magnitude of the conformational inversion was found to decrease with increasing NaCl concentration. This behavior was in-keeping with the PyC10- and PyC12-PAMAM-G0 dendrimers partitioning between the polar edges and the hydrophobic middle region of the NSSA. This was further confirmed by proposing a theoretical framework that could handle all the $[\langle k \rangle / f_{diff}]^{exp}$ ratios obtained to date which further supported the existence of two regions in the NSSA and the partitioning of the dendrimers among those two regions. Such structural insight into NSSA should prove valuable to develop a better fundamental understanding of their behavior.

5.2 INTRODUCTION

Micelles are self-assembled nanoscale objects formed by surfactants. They have garnered significant attention due to their usage in a wide variety of applications such as in paints, household detergents, personal care products, cosmetics, and pharmaceuticals.[1 - 5] This sustained industrial interest has been accompanied by the development of a fundamental understanding of their basic properties.[6,7] One particularly fascinating feature of surfactant aggregates is their ability to self-assemble into spheres, ellipsoids, cylinders, micelles, or lamellae, where the final shape of the self-assembled surfactant aggregate is defined by the critical packing parameter (*cpp*) of the surfactant.[8] The *cpp* equals the ratio $v/(a \times l)$, where v is the volume of the surfactant alkyl tail, a is the cross-section of the surfactant headgroup, and l is the effective alkyl tail length. The *cpp* of a wedge-shaped surfactant with a big headgroup (large a) and a short tail (small l and v) is small, usually less than 1/3, and the surfactant forms spherical micelles. In contrast, the *cpp* of a cylindrical surfactant with a small headgroup (small a) and a long alkyl tail (large l and v) has a large *cpp* close to unity and the surfactant forms lamellae. Since the volume and length of the alkyl tail of a given surfactant are fixed, any phenomenon affecting the size of an ionic surfactant headgroup and thus a will affect its *cpp*. Adding salt or an oppositely charged surfactant to an aqueous solution of a surfactant reduces the effective size of its headgroup, which is being neutralized, and increases its *cpp* resulting in the formation of non-spherical surfactant aggregates (NSSA).[9-17]

While the relationship between *cpp* and the shape of the NSSA is well understood, much less appreciated are its implications on the structures closing the edges of the NSSA. For if the addition of a salt or an oppositely charged surfactant increases the *cpp* of the surfactant of interest and leads to the formation of a cylinder or a lamella, it leaves their edges constituted of the surfactant hydrophobic alkyl tails exposed to water. To prevent this, the edges of the NSSA must be capped by a structure having a much higher surface curvature and composed of

surfactants with a much smaller *cpp* and thus a larger headgroup cross section. This simple constraint has several implications. First, it imposes that the edges of the NSSA be constituted of charged surfactants, since they have a larger *a*, as illustrated in Figures 5.1A and B for a cylindrical and disk-like NSSA, respectively. Second, the difference in hydrophobicity between the charged edges and the hydrophobic middle region of the NSSA must induce a hydrophobicity gradient (HG) in the edge region of the NSSA as was found for NSSA generated from SDS and DTAB mixtures.[18] Not only do the NSSA edges exhibit an HG, but they should also be more dynamic than the hydrophobic middle region, where the neutralized surfactants are packed more closely to each other and which is known to have a higher microviscosity than the interior of pure surfactant micelles. Consequently, the edge region of NSSA have some very interesting properties, which have been overlooked by the scientific community, who has focused instead on the sole characterization of the hydrophobic middle region.

The main challenge to study specific regions of NSSA resides in their highly dynamic nature. Contrary to a macromolecule, which can be labeled at specific structural units located at well-defined positions in a macromolecule, the equivalent structural units in a NSSA are the surfactants, which are constantly moving independently of each other within the NSSA without the constraint of being linked to each other as in a macromolecule. Furthermore, molecular probes that are introduced to NSSA tend to diffuse toward a location within the NSSA, where the probe has some affinity, but which is difficult to identify experimentally.[19-21] In this context, the recently introduced pyrene end-labeled generation-0 polyamidoamine (PyCX-PAMAM-G0 with $X = 4$, 6, 8, 10, and 12) dendrimers,[22-25] whose chemical structure is shown in Figure 5.1C, represent an appealing new fluorescent probe to probe the NSSA interior.[18,22] Due to its four hydrophobic 1-pyrenealkanoyl pendants, the PyCX-PAMAM-G0 dendrimers are insoluble in water but can be incorporated in a surfactant aqueous solution through interactions with NSSA. Because of its polarity, the PAMAM-G0 core cannot enter the hydrophobic interior of a NSSA

and sits at its surface.[26-28] The pyrenyl moieties are known to reside at the interface between the palisade and the interior of surfactant micelles.[29-33] The shorter alkanoyl linkers with X = 4, 6, and 8 have been found not to interact with the hydrophobic interior of NSSA but the longer linkers with X = 10 and 12 resulted in strong interactions with the NSSA interior.[18-23] By pulling on the pyrenyl labels and bringing them together, these interactions led to an increase in the local pyrene concentration ($[Py]_{loc}$) inside the NSSA, which could be probed by fitting the fluorescence decays of the pyrene monomer and excimer according to the model free analysis (MFA) to obtain the experimental ratio $[<k>/f_{diff}]^{exp}$, which is directly proportional to $[Py]_{loc}$.[23] These experiments use pyrene excimer formation (PEF) between an excited and a ground-state pyrene moiety covalently attached onto a PAMAM-G0 dendrimer to determine the average rate constant ($<k>$) of PEF and the molar fraction (f_{diff}) of pyrenyl labels undergoing diffusive PEF. The early experiments were conducted with aqueous solutions of sodium dodecyl sulfate (SDS) to which NaCl[23] or dodecyltrimethylammonium bromide (DTAB)[18] were added to neutralize the SDS headgroups and generate large NSSA.

Due to its dependency on $[Py]_{loc}$, the ratio $[<k>/f_{diff}]^{exp}$ responds to the hydrophobicity gradient (HG) generated between the polar surface of the dendrimer, where the PAMAM-G0 core resides, and the hydrophobic interior of the NSSA, that the longer decanoyl and dodecanoyl linkers interact with.[18-23] Because the NSSA generate a hydrophobic region toward the center of the NSSA where the surfactants with a neutralized headgroups are shown in red in Figures 5.1A and B, the NSSA can be divided into a polar edge and hydrophobic middle regions between which the PyC10- and PyC12-PAMAM-G0 samples partition themselves and adopt different conformations as illustrated in Figure 5.1D. In the hydrophobic middle region, the HG is weak and the $[<k>/f_{diff}]$ ratio takes a small and constant value equal to $[<k>/f_{diff}]^{Mid}$. In the edge region, a strong HG is generated between the polar surface and the interface between the edge and the middle region and $[<k>/f_{diff}]^{exp}$ takes a large value equal to

$[\langle k\rangle/f_{diff}]^{Edge}$. $[\langle k\rangle/f_{diff}]^{Edge}$ increases from $[\langle k\rangle/f_{diff}]^{SDS}$ obtained for pure SDS micelles to $[\langle k\rangle/f_{diff}]^{Edge,Max}$ obtained when the hydrophobic middle region is large enough to generate an HG that no longer changes with an increase in the size of the middle region. Because the HG responds directly to the size of the hydrophobic middle region of an NSSA, $[\langle k\rangle/f_{diff}]^{exp}$ was found to be directly related to the molar fractions f_{Mid} and f_{Edge} (= 1 – f_{Mid} = $N_{agg}(SDS)/N_{agg}(NSSA)$) in Chapter 4 representing the volume fractions of the middle and edge regions of the NSSA, respectively. By definition, f_{Edge} is also the molar fraction of charged surfactant in an NSSA taken as the ratio of the aggregation number ($N_{agg}(SDS)$) of pure SDS micelles divided by the aggregation number of the NSSA ($N_{agg}(NSSA)$). The definition of f_{Edge} is particularly well suited for the cylindrical representation of a NSSA in Figure 5.1A, where merging the two hemispherical caps would yield a pure SDS micelle.

Taken separately, the $[\langle k\rangle/f_{diff}]^{exp}$ trends obtained for aqueous solutions of SDS as a function of either NaCl concentration or the molar fraction of DTAB in the solution are well described by the parameters $[\langle k\rangle/f_{diff}]^{Mid}$, $[\langle k\rangle/f_{diff}]^{Edge}$, $[\langle k\rangle/f_{diff}]^{Edge,Max}$, $[\langle k\rangle/f_{diff}]^{SDS}$, and f_{Edge}. Unfortunately, the $[\langle k\rangle/f_{diff}]^{exp}$ trends obtained from the fluorescence of pyrene in aqueous solutions of SDS interacting with either NaCl or DTAB cannot be directly compared since cationic-aromatic interactions are absent when NaCl interacts with SDS but take place between the trimethylammonium headgroups of DTAB and the pyrene moieties,[34-37] when DTAB interacts with SDS. In turn, these cationic-aromatic interactions affect the dependency of $[Py]_{loc}$, and thus $[\langle k\rangle/f_{diff}]^{exp}$ which is directly proportional to $[Py]_{loc}$, on the HG when the size of NSSA is modified by adding DTAB to an SDS aqueous solution but not when adding NaCl.

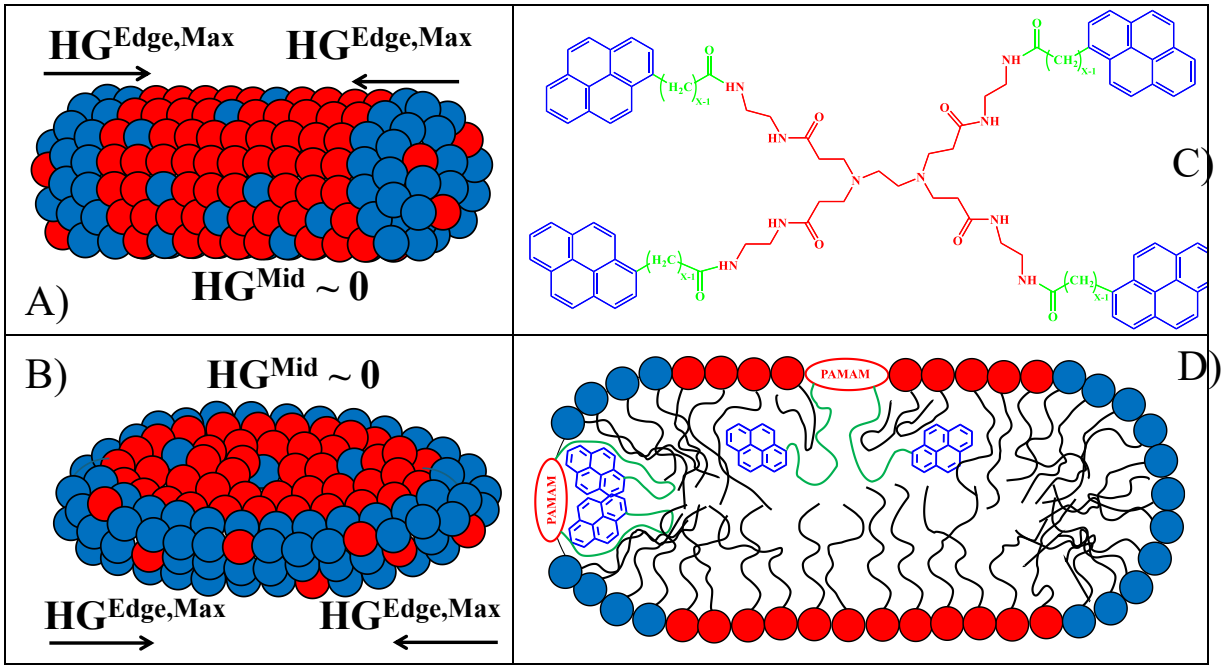


Figure 5.1. Illustration of A) a cylinder and B) a disk constituted of (red) surfactants with a large *cpp* and whose headgroups are partially neutralized and of (blue) surfactants with a small *cpp* and whose headgroups are charged. C) Chemical structure of the PyCX-PAMAM-G0 dendrimers with $X = 4$, 6, 8, 10, and 12. (red) PAMAM core, (green) alkanoyl linker, and (blue) pyrenyl labels. D) Expected conformation of the PyC10- and PyC12-PAMAM-G0 dendrimers in the (left) polar edge and (middle-top) hydrophobic middle regions of the NSSA.

The present study addresses this discrepancy between the experiments carried out with either NaCl or DTAB by conducting a new series of experiments with an 80:20 SDS:DTAB surfactant mixture as a function of NaCl concentration in order to bridge both effects. N_{agg}(NSSA) was measured for the NSSA with the MFA[38] to determine f_{Edge} and the correction factor $[\langle k\rangle/f_{diff}]^{A-C}$ was determined to account for the aromatic-cationic interactions between the pyrenyl moieties of the PyCX-PAMAM-G0 samples and the trimethylammonium headgroups of DTAB. Application of the $[\langle k\rangle/f_{diff}]^{A-C}$ correction factor to all the $[\langle k\rangle/f_{diff}]^{exp}$ ratios obtained to date yielded master straight lines for the PyC10- and PyC12-PAMAM-G0 dendrimers around which all the $[\langle k\rangle/f_{diff}]^{exp}$ ratios clustered thereby demonstrating the

generality of the methodology applied. The fact that no less than 16 $[<k>/f_{diff}]^{exp}$ ratios clustered together when plotted as a function of f_{Edge} confirms the importance of this parameter, which imposes that the number of charged SDS molecules in NSSA remains constant and equal to that found in a pure SDS micelle (~ 70).[11,12,39] As was already highlighted in a previous publication[23] and Chapter 4, this result leads to the conclusion that pure SDS micelles are involved in the formation of these NSSA probably through diffusive collisions with pre-formed aggregates of neutralized surfactants forming the hydrophobic middle region.

5.3 EXPERIMENTAL

Materials: Pyrene (98%), tetrahydrofuran (THF, ≥99.0%, distilled in glass, Honeywell Riedel-de Haën), sodium chloride (99%), SDS (>99%), and DTAB (≥98%) were purchased from Aldrich and used as received. The synthesis and characterization by ^{1}H NMR and mass spectrometry of the PyCX-PAMAM-G0 samples with X = 4, 6, 8, 10, and 12 has been reported in earlier publications.[22,24] Doubly distilled deionized water from Millipore Milli-RO 10 Plus and Milli-Q UF Plus (Bedford, MA) was used to prepare all aqueous solutions.

PyCX-PAMAM-G0 sample preparation: Since the PyCX-PAMAM-G0 dendrimers had been found earlier to generate negligible level of pyrene aggregation inside DTAB micelles,[22] all PyCX-PAMAM-G0 aqueous solutions were prepared by adding 10 μL of a concentrated solution of PyCX-PAMAM-G0 dendrimers in DMSO to a 20 mL vial with the desired amount of DTAB powder. The mixture was resuspended in 5 mL of chloroform and sonicated for 5 minutes. Then, the chloroform and DMSO were evaporated under a constant air flow and the DTAB/PyCX-PAMAM-G0 mixture was further dried at room temperature in a vacuum oven overnight. The mixture was redissolved in water to which the desired amount of SDS powder was added to generate a surfactant solution with 40 mM SDS and 10 mM DTAB. The required volume of a 1 M NaCl solution was then added to 10 mL of the dendrimers solutions in an

80:20 SDS:DTAB mixture to obtain NaCl concentrations of 10, 20, 50, and 100 mM. The PyCX-PAMAM-G0 concentration in the 50 mM surfactant aqueous solutions varied between 0.1 and 0.6 μM.

Preparation of 50 mM surfactant solution with NaCl and 0.45 μM pyrene: All aqueous solutions with molecular pyrene were prepared by using a 0.1 mM pyrene stock solution in THF. For the N_{agg} measurements, a small volume (100 μL) of the pyrene stock solution in THF was transferred to a 6 mL vial and dried under constant air flow. The desired amount of a 50 mM surfactant solution with a given NaCl concentration was transferred to the 6 mL vial with pyrene to generate five solutions containing 50 mM surfactant, the selected NaCl concentration, and a pyrene concentration ranging from 0.05 to 0.35 mM. This mixture was sonicated for 5 minutes and kept in a shaker at 50 °C for 12 hours. The absorption spectrum and pyrene monomer and excimer fluorescence decays of these five solutions were acquired. For each set of experiments conducted with a given NaCl concentration, one solution was further diluted to a pyrene concentration of 0.45 μM by adding the same 50 mM surfactant solution with NaCl but without pyrene. This dilute 0.45 μM pyrene solution, whose concentration is below the solubility limit of 0.7 μM for pyrene in water,[40] was used to determine the lifetime of the pyrene monomer isolated in the NSSA obtained at the selected NaCl concentration.

For the CMC determination of the 80:20 SDS:DTAB mixtures, fluorescence experiments were conducted with a low 0.45 μM pyrene concentration, that would be below the 0.7 μM saturation limit of pyrene in water, which was prepared by placing 60 mg of the 0.1 mM pyrene stock solution in THF, drying it under a constant air flow, and adding 120 g of MilliQ water. The suspension was then placed in a shaker at 50 °C for 12 hours to ensure complete dissolution of pyrene in water without surfactant. When dissolution was accomplished, the aqueous solution of pyrene was then split into four 30 mL solutions, to which the desired amount of a 1 M NaCl solution was added to obtain an NaCl concentration of 10, 20, 50, and 100 mM. These

solutions were then mixed with a 50 mM surfactant aqueous solution prepared with the same 0.45 μM pyrene concentration and NaCl concentration to obtain solutions with a same 0.45 μM pyrene concentration and NaCl concentration and a range of surfactant concentrations varying from 10 μM to 5 mM. The fluorescence spectra of these solutions were then acquired and analyzed to determine their fluorescence intensity ratios I_E/I_M and I_1/I_3, whose definitions are provided in the section *Steady-state fluorescence,* and which were plotted as a function of surfactant concentration for CMC determination.

Dynamic light scattering (DLS) measurements: All DLS measurements on aqueous solutions of an 80:20 SDS:DTAB mixtures with salt concentrations of 0, 10, 20, 50, and 100 mM were conducted with a Zetasizer NS90 instrument from Malvern Analytics using a 1.0 cm pathlength quartz cuvette. The autocorrelation function of the scattering signal was acquired 3 times for each sample and the average size distribution was determined from which the number average hydrodynamic diameter (D_h) was calculated.

UV-Vis absorption measurements: The absorption spectra of molecular pyrene and the PyCX-PAMAM-G0 dendrimers in aqueous solutions of 40 mM SDS and 10 mM DTAB mixtures were acquired with a Cary 100 UV-Visible spectrophotometer using either a 1.0 cm or a 5.0 cm pathlength quartz cuvette. The UV cell with a 5.0 cm pathlength ensured that solutions with a low pyrene concentration resulting in an absorbance of 0.1 or less with the 1.0 cm pathlength cuvette would yield absorption spectra with a reasonable signal-to-noise ratio.

Steady-state fluorescence: A HORIBA QM-400 spectrofluorometer equipped with a xenon arc-lamp was used to acquire the fluorescence spectra with a 1 nm width for all the slits in the excitation and emission monochromators. The more concentrated (0.5 mM ~ 5 mM) surfactant solutions were excited at 279 nm to minimize the scattering from the solution, and the diluted ones (10 μM – 0.5 mM) were excited at 336 nm to maximize fluorescence signal. The fluorescence spectra were acquired from 350 to 530 nm or 350 to 650 nm for the excitation at

279 nm and 336 nm, respectively. Analysis of the steady-state fluorescence (SSF) spectra yielded the fluorescence intensity ratio I_E/I_M(SSF) obtained from the fluorescence intensity of the pyrene monomer (I_M) and excimer (I_E) calculated by integrating the fluorescence spectrum from 376 to 382 nm and from 495 to 520 nm, respectively. The I_E/I_M(SSF) ratio is a measure of the PEF efficiency. The maximum intensity value of the first (I_1) peak divided by that of the third (I_3) peak in the fluorescence spectrum of the pyrene monomer yielded the I_1/I_3 ratio, which responds to the polarity of the environment where molecular pyrene resides.[41,42]

Time-resolved fluorescence: The pyrene monomer and excimer fluorescence decays obtained for pyrene in aqueous solutions of an 80:20 SDS:DTAB mixture with a 50 mM total surfactant concentration were acquired according to the time-correlated single photon counting method with a FluoroHub time-resolved fluorometer from HORIBA fitted with a 336 nm DeltaDiode laser. All fluorescence decays were acquired over 1,024 channels with a time-per-channel of 0.87 ns and 20,000 counts at their decay maximum using an emission wavelength of 379 and 510 nm and a 370 and 495 nm cut off filter for the pyrene monomer and excimer, respectively. The cut off filters reduced the amount of stray light reaching the photomultiplier tube detector. The instrument response function (IRF) was obtained by collecting the scattering photons generated by irradiating a triangular aluminum monolith and setting the emission wavelength at the same 336 nm wavelength of the excitation source. The fluorescence decays of solutions with the higher pyrene concentrations used for N_{agg} determination were acquired with the front-face geometry while solutions with a pyrene concentration of 2.5 μM or lower were acquired with the standard right-angle geometry.[43]

Global model free analysis of the monomer and excimer fluorescence decays: The monomer and excimer fluorescence decays of molecular pyrene and the pyrenyl labels of the PyCX-PAMAM-G0 samples were fitted globally according to the model free analysis (MFA) with Equations S5.1 and S5.2, respectively, which are given in the Supporting Information (SI).[44]

Equation S5.1 for the fluorescence decays of the pyrene monomer is a sum of exponentials, where the longest decay time is fixed in the analysis to equal the lifetime (τ_M) of the pyrene monomer. The pre-exponential factor of this exponential is related to the molar fraction (f_{Mfree}) of pyrenyl moieties (Py_{free}*) that do not form excimer and emit as if they were free in solution. The sum of the other exponentials in Equation S5.1 represents those excited pyrenes (Py_{diff}*) forming excimer by diffusive encounters, whose molar fraction (f_{Mdiff}) is determined from the sum of the corresponding pre-exponential factors. The species Py_{diff}* can also be detected in the excimer fluorescence decays fitted with Equation S5.2, which yields the molar fraction f_{Ediff}. Finally, direct excitation of pre-aggregated pyrene moieties with molar fractions f_{EE0} and f_{ED} results in the instantaneous formation of a pyrene excimer $E0$* or D*, where the pyrene moieties are well or poorly stacked resulting in a short (τ_{E0}) or long (τ_D) lifetime, respectively. The indices M and E for the molar fractions indicate that a given pyrene species is detected in the monomer and excimer fluorescence decay, respectively. Combining the molar fractions f_{Mdiff}, f_{Mfree}, f_{Ediff}, f_{EE0}, and f_{ED} yields the molar fractions f_{diff}, f_{free}, f_{E0}, and f_D of the pyrenyl species Py_{diff}*, Py_{free}*, $E0$*, and D*, respectively. All decay times (τ_i) and pre-exponential factors (a_i) used in Equation S5.1, and the molar fractions and lifetimes retrieved from the global MFA of the pyrene monomer and excimer fluorescence decays have been listed in Tables S5.1-S5.2 in SI. They were obtained by comparing the experimental fluorescence decays with the convolution of the IRF and Equation S5.1 and S5.2 and optimization of the parameters according to the Marquardt-Levenberg algorithm.[45] The fits were deemed satisfactory if the global χ^2 was smaller than 1.3 and the residuals and autocorrelation of the residuals were randomly distributed around zero.

Determination of N_{agg} for NSSA with the MFA parameters: The monomer and excimer fluorescence decays of molecular pyrene dissolved in aqueous solutions of an 80:20 SDS:DTAB mixture with a 50 mM total surfactant concentration were acquired and fitted

according to the MFA to retrieve f_{Mfree}. Since the distribution of pyrene molecules in NSSA follows a Poisson distribution, the molar fraction (f_{Mfree}) of the species Py_{free}* represents the Poisson probability equal to $exp(-<n>)$ of finding a micelle with one excited pyrene and no ground-state pyrene resulting in the equality shown in Equation 5.1. With $<n>$ known, it was plotted as a function of the pyrene concentration ([*Py*]) in the solution. The slope of the resulting $<n>$-*vs*.-[*Py*] straight line yielded N_{agg}. This methodology based on the MFA to determine N_{agg} for surfactant micelles has been described in greater details in an earlier publication.[38]

$$< n >= -Ln(f_{Mfree}) = N_{agg} \times \frac{[Py]}{[SDS]+[DTAB]-CMC} \tag{5.1}$$

Calculation of the absolute I_E/I_M(*MFA*) *ratio for the PyCX-PAMAM-G0 samples in NSSA*: The global MFA of the fluorescence decays yielded the pre-exponential factors (a_i) and decay times (τ_i) used in the front part of Equation S5.1. They were combined in Equation 5.2 to calculate the average lifetime $<\tau>$ and in turn, the average rate constant $<k>$ for PEF with Equation 5.3.[44]

$$< \tau >= \frac{\sum_{i=1}^{n} a_i \tau_i}{\sum_{i=1}^{n} a_i} \tag{5.2}$$

$$< k >= \frac{1}{< \tau >} - \frac{1}{\tau_M} \tag{5.3}$$

The parameters retrieved from the MFA could be combined into Equation 5.4 to yield the I_E/I_M(MFA) ratio.[44]

$$I_E / I_M(MFA) = \frac{(f_{diffE0}\tau_{E0} + f_{diffD}\tau_D) < k >< \tau > + f_{E0}\tau_{E0} + f_D\tau_D}{(f_{diffE0} + f_{diffD}) < \tau > + f_{free}\tau_M} \tag{5.4}$$

Local concentration of pyrenyl labels for a PyCX-PAMAM-G0 sample: The local concentration ($[Py]_{loc}$) of ground-state pyrenyl labels inside a PyCX-PAMAM-G0 dendrimer is given by Equation 5.5, where n_{Py} (= 3) is the number of ground-state pyrenyl labels in the PyCX-PAMAM-G0 samples, where one of the pyrenyl labels is excited to form an excimer, L_{Py} is the square root of the average squared end-to-end distance of the dendrimer ends, and A is a geometric factor that would equal $\pi/6$ if the dendrimer volume were a sphere.[46] In practice, A is a constant and $[Py]_{loc}$ and $(n_{Py}/L_{Py})^3$ are used interchangeably.

$$[Py]_{loc} = \frac{n_{Py}}{A \times (L_{Py})^3} \tag{5.5}$$

An expression of L_{Py} was derived earlier for low generation ($N \leq 4$) PAMAM dendrimers by assuming that the internal segments of the PAMAM dendrimers obeyed Gaussian statistics and its expression is given in Equation 5.6. In Equation 5.6, the parameters a, b, and c are the number of carbon atoms in the linker connecting the pyrene moiety to the PAMAM dendrimer, which equals X (= 4, 6, 8, 10, and 12), the number of non-hydrogen atoms in the aminoethyl propionamide building block of the PAMAM dendrimer, which equals 7, and the number of non-hydrogen atoms in the ethylene diamine core of the dendrimer, which equals 4, respectively.[24]

$$L_{Py}^2(N) = \left(2a + \frac{\left[2 - 2^{N+2} + (N+1) \times 2^{N+3} \right] b + 2^{N+1} c + 2^{N+1} - 1}{2^{N+2} - 1} \right) \times l^2 \tag{5.6}$$

Spatial partitioning theory: Since the experimentally determined ratio $[\langle k \rangle / f_{diff}]^{exp}$ for a

pyrene-labeled macromolecule (PyLM) is directly proportional to $[Py]_{loc}$,[47,48] which reflects the PyLM conformation, $[<k>/f_{diff}]^{exp}$ was employed to monitor the conformation of the PyCX-PAMAM-G0 dendrimers with the longer decanoyl and dodecanoyl linkers as they interacted with the NSSA.[18-23] In the case of NSSA prepared without DTAB by addition of NaCl[23] to an SDS solution, $[<k>/f_{diff}]^{exp}$ reflected the partitioning of the dendrimers between the edge region and the middle region of the NSSA shown in Figures 5.1A and B for cylindrical and a disk-like NSSA, respectively. In the edge region, the dendrimers experience a strong HG, which leads to a conformational inversion (see Figure 5.1D) and results in a large $[<k>/f_{diff}]^{Edge}$ value, that increases with the build up of the hydrophobic middle region from $[<k>/f_{diff}]^{SDS}$ for pure SDS micelles to $[<k>/f_{diff}]^{Edge,Max}$ when the middle region reaches a critical volume beyond which the HG in the edges no longer changes. In the hydrophobic region, the dendrimers with the longer linkers adopt their natural conformation (see Figure 5.1D) and their internal segments obey Gaussian statistics resulting in a low $[<k>/f_{diff}]^{Mid}$ ratio. By partitioning between the edge and middle regions of the NSSA, the dendrimers with the longer linkers experience an $[<k>/f_{diff}]^{exp}$, that can be represented mathematically by $[<k>/f_{diff}]^{th}$ as the average of $[<k>/f_{diff}]^{Edge}$ and $[<k>/f_{diff}]^{Mid}$ weighed by the volume fractions f_{Edge} and f_{Mid} (= 1 – f_{Edge}) of the edge and middle regions, respectively. Assuming that the two hemispherical edges of a cylindrical NSSA amount to a pure SDS micelle in water as was done in two earlier studies,[23,24] f_{Edge} is given by Equation 5.7, where N_{agg}(SDS) and N_{agg}(NSSA) are the aggregation number of a pure SDS micelle in water and the NSSA under study, respectively.

$$f_{Edge} = \frac{N_{agg}(SDS)}{N_{agg}(NSSA)} \tag{5.7}$$

While an excellent match was found between $[<k>/f_{diff}]^{exp}$ and $[<k>/f_{diff}]^{th}$ for NSSA

generated by adding NaCl to an SDS aqueous solution, NSSA produced from mixtures of SDS and DTAB induced aromatic-cationic interactions between the pyrene moieties and the trimethylammonium headgroups of DTAB,[34-37] which need to be accounted for. These aromatic-cationic interactions diminish the conformational inversion experienced by the dendrimers with longer linkers located in the edge region[18,22] and decrease the $[<k>/f_{diff}]^{Edge}$ value by an amount $[<k>/f_{diff}]^{A\text{-}C}$ weighed by the molar fraction (f_{DTAB}) of DTAB in the surfactant mixture used to prepare the NSSA. These considerations led to Equation 5.8 used to calculate $[<k>/f_{diff}]^{th}$, which accounts for the partitioning of the dendrimers with a longer linker between the edge and middle region of the NSSA and the reduction of $[<k>/f_{diff}]^{Edge}$ by the presence of DTAB in the NSSA. In the case of the three dendrimers PyC4-, PyC6-, and PyC8-PAMAM-G0, which do not undergo a conformational inversion, the expression for $[<k>/f_{diff}]^{th}$ also holds with $[<k>/f_{diff}]^{Edge}$ being equal to $[<k>/f_{diff}]^{SDS}$.

$$[<k>/f_{diff}]^{th} = f_{Edge}\times([<k>/f_{diff}]^{Edge} - f_{DTAB}\times[<k>/f_{diff}]^{A\text{-}C}) + (1 - f_{Edge})\times[<k>/f_{diff}]^{Mid} \quad (5.8)$$

The values of $[<k>/f_{diff}]^{Edge}$ and $[<k>/f_{diff}]^{Mid}$ were determined in an earlier publication[23] using the mathematical expression of $[<k>/f_{diff}]^{Edge}$ in Table 5.1 for the PyC10- and PyC12-PAMAM-G0 dendrimers and the specific values of the parameters $[<k>/f_{diff}]^{Edge,Max}$, $[<k>/f_{diff}]^{Mid}$, $[<k>/f_{diff}]^{SDS}$, and f_{Mid}^{Max} given in Table 5.2. To determine $[<k>/f_{diff}]^{A\text{-}C}$, $[<k>/f_{diff}]^{th}$ was set to equal $[<k>/f_{diff}]^{Mid}$ for an f_{DTAB} value of 0.32 corresponding to the solubility limit of mixtures of SDS and DTAB, beyond which very large NSSA were obtained for which the edges could be neglected. Solving for $[<k>/f_{diff}]^{A\text{-}C}$ yielded Equation 5.9, from which $[<k>/f_{diff}]^{A\text{-}C}$ values of 0.856 ns^{-1} and 0.991 ns^{-1} were retrieved for PyC10- and PyC12-PAMAM-G0, respectively, by using the parameters listed in Table 5.2. $[<k>/f_{diff}]^{Edge,Max}$ was used in lieu of $[<k>/f_{diff}]^{Edge}$ in Equation 5.9 because the very large NSSA obtained for $f_{DTAB} = 0.32$ are passed

the maximum value taken by $[<k>/f_{diff}]^{exp}$ at $f_{Edge} = f_{Edge}^{Max}$.

$$[<k>/f_{diff}]^{A-C} = \frac{[<k>/f_{diff}]^{Edge,Max} - [<k>/f_{diff}]^{Mid}}{f_{DTAB}} \quad (5.9)$$

Table 5.1. Mathematical expression of $[<k>/f_{diff}]^{Edge}$ used in Equation 5.8 for the PyC10- and PyC12-PAMAM-G0 dendrimers

$0 < f_{Edge} < f_{Edge}^{Max}$	$f_{Edge}^{Max} < f_{Edge} < 1$
$[<k>/f_{diff}]^{Edge,Max}$	$\frac{[<k>/f_{diff}]^{Edge,Max} f_{Edge}^{Max}(1-f_{Edge}) + [<k>/f_{diff}]^{SDS}(f_{Edge} - f_{Edge}^{Max})}{(1-f_{Edge}^{Max}) f_{Edge}}$

Table 5.2. $[<k>/f_{diff}]^{Mid}$, $[<k>/f_{diff}]^{Edge,Max}$, and $[<k>/f_{diff}]^{SDS}$ ratios and f_{Mid}^{Max} determined in earlier publication along with $[<k>/f_{diff}]^{A-C}$ calculated with Equation 5.9.

	$[<k>/f_{diff}]^{Mid}$ (ns^{-1})	$[<k>/f_{diff}]^{Edge,Max}$ (ns^{-1})	$[<k>/f_{diff}]^{SDS}$ (ns^{-1})	$[<k>/f_{diff}]^{A-C}$ (ns^{-1})	f_{Edge}^{Max}
PyC4-PAMAM-G0	0.056	_	0.097	0	_
PyC6-PAMAM-G0	0.052	_	0.079	0	_
PyC8-PAMAM-G0	0.035	_	0.062	0	_
PyC10-PAMAM-G0	0.032	0.314	0.109	0.856	0.668
PyC12-PAMAM-G0	0.027	0.351	0.134	0.991	0.733

5.4 RESULTS AND DISCUSSION

Characterization of the Critical Micelle Concentration (CMC)

The fluorescence spectra of the solutions with a low and constant 0.45 μM pyrene concentration, a fixed NaCl concentration, and varying surfactant concentrations were acquired, and they are shown in Figures 5.2A-C for the 100 mM NaCl concentration. Hardly any excimer emission

was observed in the fluorescence spectra acquired at surfactant concentrations below 0.1 mM in Figure 5.2A indicating that pyrene is well dissolved in the aqueous solution at the low pyrene concentration of 0.45 μM. Furthermore, the I_1/I_3 ratio is large and equals 1.91 (±0.03) typical of pyrene dissolved in water.[42]

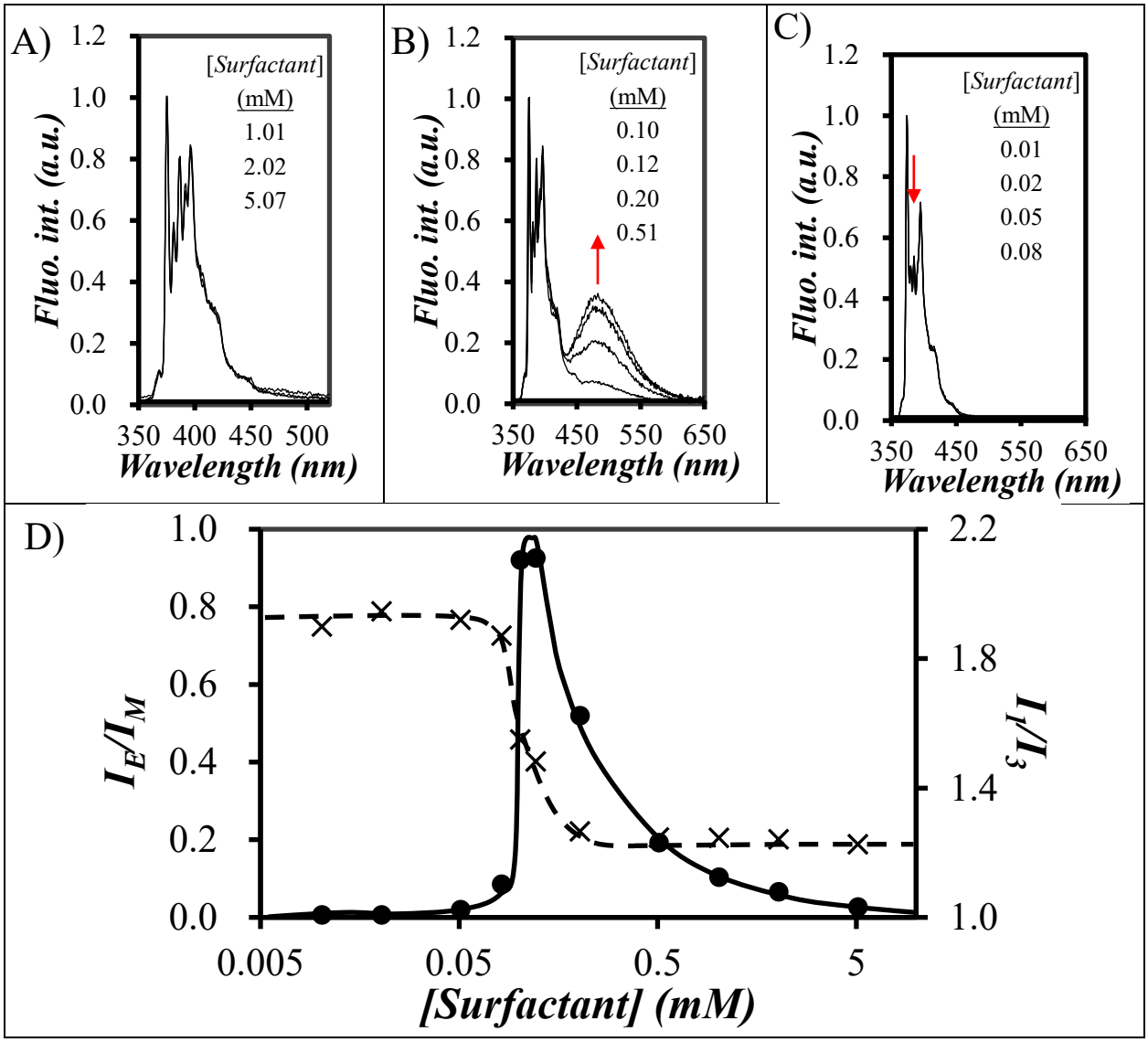


Figure 5.2. Fluorescence spectra of 0.45 μM pyrene and 100 mM NaCl in surfactant solution with total surfactant concentration ranging A) from 5.07 to 1.01 mM, B) from 0.51 to 0.10 mM, and C) from 0.08 to 0.01 mM. D) I_E/I_M(SSF) and I_1/I_3 retrieved from the fluorescence spectra plotted against total surfactant concentration.

Excimer formation was observed in Figure 5.2B for surfactant concentrations between 0.1 and 0.5 mM reflecting the formation of NSSA, which concentrated the pyrene molecules resulting in pyrene excimer formation. In the same range of surfactant concentrations, the I_1/I_3 ratio showed some significant variations indicating that the local environment of pyrene was changing from polar water to the more hydrophobic microdomains generated by the NSSA. For surfactant concentrations larger than 0.5 mM, hardly any excimer emission was observed in the fluorescence spectra in Figure 5.2C and the I_1/I_3 ratio remained constant and equal to 1.24 (±0.01) indicative that the environment probed by pyrene was more hydrophobic than water and must have been that of the NSSA interior.

A more quantitative analysis of the fluorescence spectra was obtained by plotting the I_E/I_M and I_1/I_3 ratios as a function of surfactant concentration in Figure 5.2D for an NaCl concentration of 100 mM. As described with the fluorescence spectra in Figures 5.2A – C, the I_1/I_3 ratio remained constant and equal to 1.91 (±0.03) up to an SDS concentration of 0.08 mM indicating that pyrene was in water, decreased down to a value of 1.24 (±0.01) as the surfactant concentration increased from 0.08 to 0.20 mM reflecting the progressive incorporation of pyrene into the NSSA, before remaining constant and equal to 1.24 (±0.01) for surfactant concentration larger than 0.20 mM confirming the incorporation of pyrene into the NSSA interior. The trend obtained with the I_E/I_M(SSF) ratio agrees with the trend obtained with the I_1/I_3 ratio. I_E/I_M is small for surfactant concentrations below 0.08 mM indicating that the low pyrene concentration prevents excimer formation in water, passes through a maximum for surfactant concentrations between 0.10 and 0.12 mM reflecting the formation of NSSA, where pyrene is concentrated and forms excimer, and decreases rapidly to zero as the surfactant concentration increases past 0.12 mM and the pyrene molecules distribute themselves among different NSSA. Based on the plot in Figure 5.2D, the CMC of the 80:20 SDS:DTAB mixture

with 100 mM NaCl would equal 0.11 (±0.01) mM. The CMC of the 80:20 SDS:DTAB surfactant mixture in water was found to equal 0.20 mM. The CMC of the 80:20 SDS:DTAB mixture at the low NaCl concentrations of 10, 20, and 50 mM were obtained in the same manner and found to remain constant and equal to 0.13 (±0.03) mM.

Determination of the Aggregation Number (N_{agg}) of NSSA

The pyrene monomer and excimer fluorescence decays of the 50 mM surfactant solutions with a fixed NaCl concentration and a pyrene concentration ranging from 0.05 to 0.35 mM were acquired and globally fitted according to the MFA. An example of the pyrene monomer and excimer fluorescence decay fits with the MFA are shown in Figure 5.3A and B, respectively.

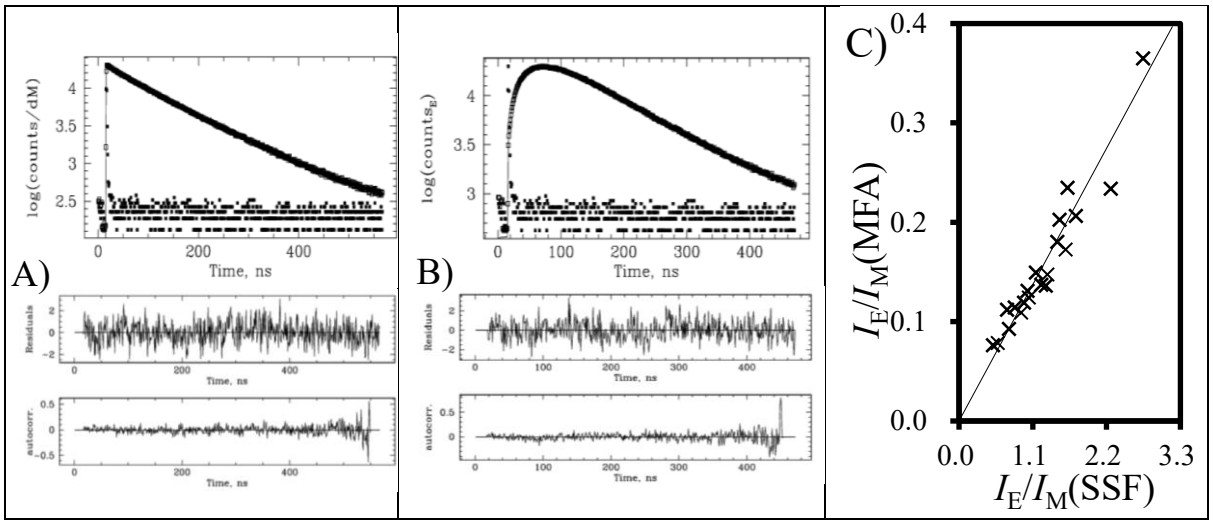


Figure 5.3. A) Monomer and B) excimer fluorescence decay of 0.15 mM molecular pyrene in mixed micelle solution with 100 mM NaCl. C) Plot of I_E/I_M(MFA) from Equation 5.4 as a function of I_E/I_M(SSF) for all the pyrene solutions with 40 mM SDS and 10 mM DTAB and 0, 10, 20, 50, and 100 mM NaCl.

Figures 5.3A and B show the residuals and autocorrelation of the residuals randomly distributed around zero reflecting the good quality of the fit. The parameters retrieved from the

MFA of the fluorescence decays were combined in Equation 5.4 to calculate the I_E/I_M(MFA) ratio, which was compared in Figure 5.3C to the I_E/I_M(SSF) ratio obtained from the analysis of the fluorescence spectra. The data points clustered around the diagonal indicating that the MFA parameters provided a good description of the photophysical processes leading to PEF in the solution and could thus be trusted.

The most important parameter for N_{agg} determination is the molar fraction (f_{Mfree}) of pyrene detected in the pyrene monomer fluorescence decays that are isolated in NSSA and cannot form excimer, since f_{Mfree} yields the average number (<*n*>) of pyrenes per micelle according to Equation 5.1.[38] <*n*> was plotted as a function of pyrene concentration in Figure 5.4A and straight lines passing through the origin were obtained, whose slope yielded N_{agg} according to Equation 5.1. The N_{agg} values obtained for 50 mM surfactant solutions of an 80:20 SDS:DTAB mixture with different salt concentrations were listed in Table 5.1 along with the NSSA concentration given by the inverse of the slope of the straight lines in Figure 5.4A.

Table 5.1. Mixed micelle concentration and their aggregation number at different NaCl concentrations.

[NaCl]	[Micelle] (mM)	N_{agg}	D_h *(nm)*
0	/	210[14]	3.9 (±0.1)
10	0.184 (±0.002)	228 (±3)	4.1 (±0.1)
20	0.164 (±0.004)	255 (±6)	5.0 (±0.1)
50	0.138 (±0.004)	305 (±4)	7.1 (±0.6)
100	0.106 (±0.005)	396 (±4)	14.4 (±0.3)

The N_{agg} values of the 80:20 SDS:DTAB mixtures plotted as a function of NaCl concentration were compared to the N_{agg} values obtained for NSSA made of pure SDS in Figure 5.4B.[23] The 80:20 SDS:DTAB mixtures yielded NSSA, that were much larger than those obtained with pure SDS and whose size increased much more quickly with NaCl concentration

compared to the NSSA prepared from pure SDS.

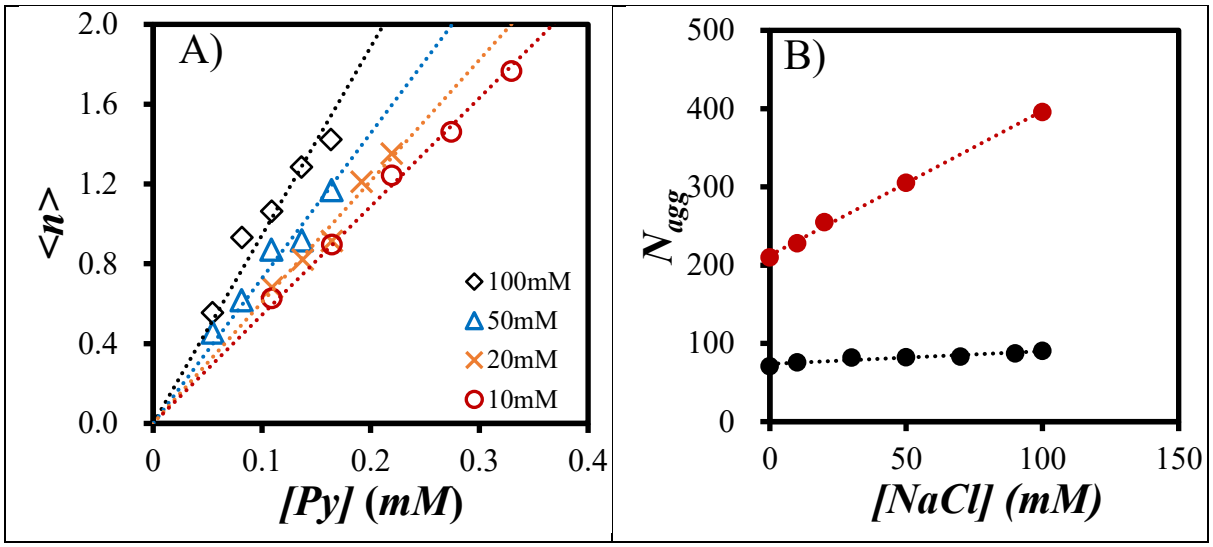


Figure 5.4. Plots of A) <*n*> as a function of pyrene concentration for various NaCl concentrations and B) N_{agg} as a function of NaCl concentration for NSSA made of (red circles) an 80:20 SDS:DTAB mixture and (black disks) pure SDS.[38]

Hydrodynamic diameter (D_h) of Mixed Micelles

The number-average hydrodynamic diameter (D_h) of the NSSA at different NaCl concentrations was measured by DLS with solutions having a 40 mM SDS and 10 mM DTAB concentration. For each NaCl concentration, the autocorrelation function of the light scattering intensity was measured 3 times, and the averaged histogram by number of their hydrodynamic diameter (D_h) is shown in Figure 5.5A. With increasing NaCl concentration, the histograms shift to higher D_h in Figure 5.5A reflecting an increase in the size of the mixed micelles. This observation agrees with the increase in N_{agg} with increasing NaCl concentration found from the fluorescence measurements. The D_h values retrieved for the 80:20 SDS:DTAB mixtures are listed in Table 5.1 for the NaCl concentrations studied. D_h was then plotted as a function of N_{agg} in Figure 5.5B. D_h was found to increase with increasing N_{agg} confirming the increasing

size of the NSSA with increasing NaCl concentration established by fluorescence in Figure 5.4B.

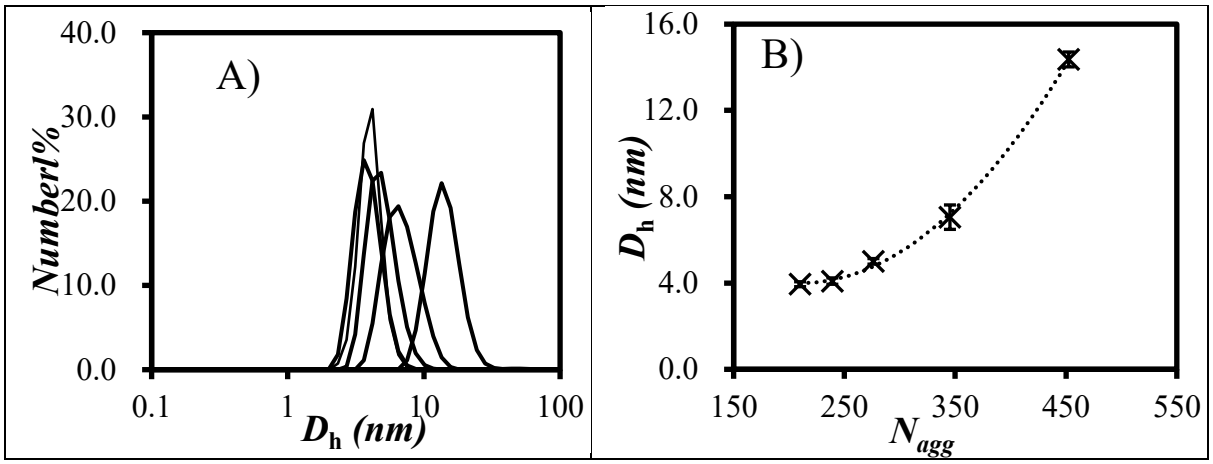


Figure 5.5. Plots of A) the number fraction of the NSSA as a function of the hydrodynamic diameter; Traces from left to right for solutions with 10, 20, 50, and 100 NaCl respectively and B) hydrodynamic diameter of NSSA as a function of N_{agg}.

Dendrimer conformation in NSSA as a function of NaCl concentration

The aqueous solutions of the PyCX-PAMAM-G0 dendrimers with 40 mM SDS and 10 mM DTAB and an NaCl concentration equal to 0, 10, 20, 50, and 100 mM were first characterized by UV-Vis absorption to assess qualitatively the solvation of the pyrenyl labels from the sharpness of the absorption bands (see Figures S5.8 in SI) and steady-state fluorescence to ensure that the solutions exhibited the expected spectral features of a pyrene-labeled macromolecule (see Figures S5.9). The solutions are now characterized by time-resolved fluorescence to probe the conformation of the dendrimers in the NSSA. Global MFA of the pyrene monomer and excimer fluorescence decays yielded the average rate constant ($<k>$) for PEF and the molar fraction (f_{diff}) of pyrenyl labels forming excimer by diffusive encounters. Dividing $<k>$ by f_{diff} resulted in the $[<k>/f_{diff}]^{exp}$ ratio, which is proportional to $[Py]_{loc}$ and thus

reflects the conformation of the dendrimers.[23,47,48] The $[<k>/f_{diff}]^{exp}$ ratios and the molar fraction ($f_{agg} = 1 - f_{diff}$) of aggregated pyrenyl labels were plotted as a function of NaCl concentration in Figures 5.6A and B, respectively.

The $[<k>/f_{diff}]^{exp}$ ratios of the PyCX-PAMAM-G0 samples with a short linker showed a slight decrease with increasing NaCl concentration and their value decreased with increasing linker length as expected since a longer linker results in a lower $[Py]_{loc}$ and $[<k>/f_{diff}]^{exp}$ ratios. This behavior suggests that the internal segments of the dendrimers with a short linker obey Gaussian statistics as already found in other surfactant systems.[22,23] The $[<k>/f_{diff}]^{exp}$ ratios of the dendrimers with a longer decanoyl and dodecanoyl linker departed from this trend since their values was always larger than that of the PyC8-PAMAM-G0 dendrimer indicating that their internal segments did not obey Gaussian statistics and that they underwent a conformational inversion. However, the $[<k>/f_{diff}]^{exp}$ ratios of the PyC10- and PyC12-PAMAM-G0 dendrimers drifted from a high value similar to that of the PyC4-PAMAM-G0 dendrimer at low NaCl concentration to a value close to that of the PyC8-PAMAM-G0 dendrimer at high NaCl concentration. This behavior indicated that the magnitude of the conformational inversion experienced by the PyC10- and PyC12-PAMAM-G0 dendrimers decreased with increasing concentration as would be expected if a larger fraction of the dendrimers would partition in the hydrophobic middle region of the NSSA. The f_{agg} values shown in Figure 5.6B indicate that the variations in the $[<k>/f_{diff}]^{exp}$ ratios cannot be attributed to changes in the aggregation level of the pyrenyl labels since f_{agg} remains very small at all NaCl concentrations in Figure 5.6B.

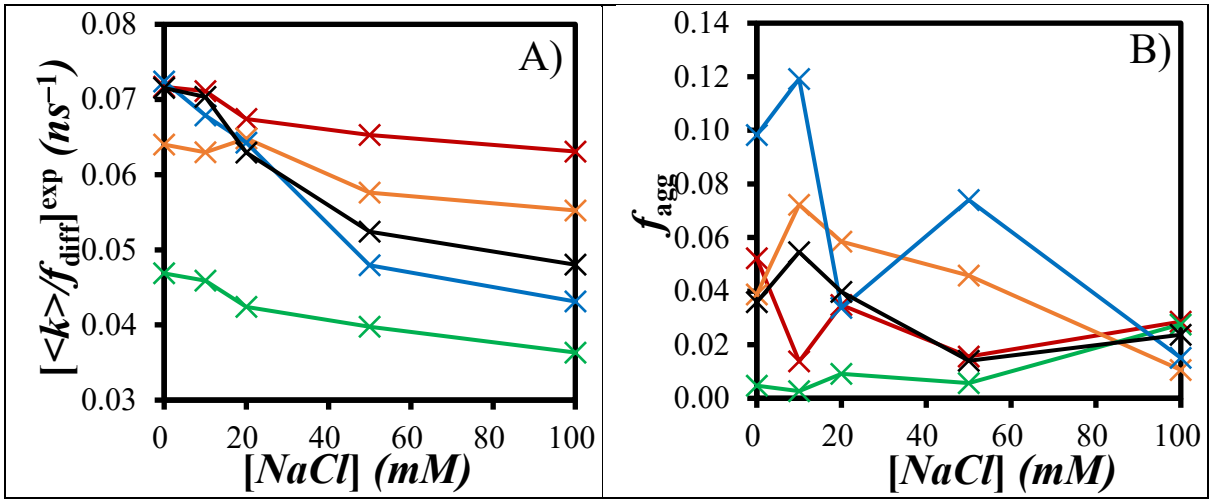


Figure 5.6. Plots of A) the $[\langle k\rangle/f_{diff}]^{exp}$ ratio and B) f_{agg} as a function of NaCl concentration for the PyCX-PAMAM-G0 samples in aqueous solutions of 40 mM SDS and 10 mM DTAB. The red, orange, green, blue, and black crosses are for the PyC4-, PyC6-, PyC8-, PyC10-, and PyC12-PAMAM-G0 samples, respectively.

To assess the merit of the phenomenological description of the NSSA as being constituted of the edge and middle regions among which the PyCX-PAMAM-G0 samples distribute themselves as illustrated in Figure 5.1D, the $[\langle k\rangle/f_{diff}]^{exp}$ values presented in Figure 5.6A were compared to their corresponding theoretical $[\langle k\rangle/f_{diff}]^{th}$ values calculated with Equation 5.8. Equation 5.8 accounts for the reduction in $[\langle k\rangle/f_{diff}]^{exp}$ resulting from aromatic-cationic interactions between the pyrene moieties of the dendrimers and the DTAB trimethylammonium headgroups.[34-37] The trends obtained by plotting the experimental and theoretical $[\langle k\rangle/f_{diff}]$ ratios for the solutions with NaCl are presented in Figure 5.7, where the experiments conducted without NaCl were omitted since they have already been published.[22] The good agreement obtained between the $[\langle k\rangle/f_{diff}]^{th}$ and $[\langle k\rangle/f_{diff}]^{exp}$ values presented in Figure 5.7 for NaCl concentrations equal to 10, 20, 50, and 100 mM supports the notion that the NSSA are made of two regions among which the dendrimers partition themselves randomly. It also validates the use of Equation 5.8 to represent the $[\langle k\rangle/f_{diff}]^{exp}$ ratio obtained for the PyCX-PAMAM-G0

dendrimers interacting with the NSSA obtained in aqueous solutions of the catanionic 80:20 SDS:DTAB mixture at different NaCl concentrations.

The Spatial Partitioning Theory (SPT)

At this stage of the study, the spatial partitioning theory (SPT) invoking the existence of an edge and a middle region in NSSA has been shown to hold for PyCX-PAMAM-G0 dendrimers in pure SDS micelles with NaCl,[23] as well as in mixed micelles with (in this study) or without NaCl,[18] provided that the cationic–aromatic interactions between the trimethylammonium headgroups of DTAB and pyrene were taken into account.[34-37] In all three studies described in Chapters 3, 4, and 5, the SPT is based on the common assumption that the enlarged NSSA hosting PAMAM dendrimers consist of two regions, namely an edge region with charged surfactant headgroups resulting in a more curved surface and a high hydrophobicity gradient (HG), and a middle region with neutralized surfactant headgroups resulting in a relatively less curved surface and a low HG. The edge bears the same number (N_{agg}(SDS)) of SDS molecules found in a pure SDS micelle in water. The number of surfactant molecules constituting the middle region of the NSSA is thus equal to N_{agg}(NSSA) – N_{agg}(SDS).

Based on this model, the change in NSSA size, whether induced by the addition of NaCl, DTAB, or both, is attributed to the expansion of the middle region. In other words, starting from a pure SDS micelle in water, any increase in N_{agg} requires the incorporation of surfactant molecules into the middle region. The model also attributes changes in $[\langle k \rangle / f_{diff}]^{exp}$ to the spatial partitioning of the PyCX-PAMAM-G0 dendrimers in the two regions defined by the NSSA.

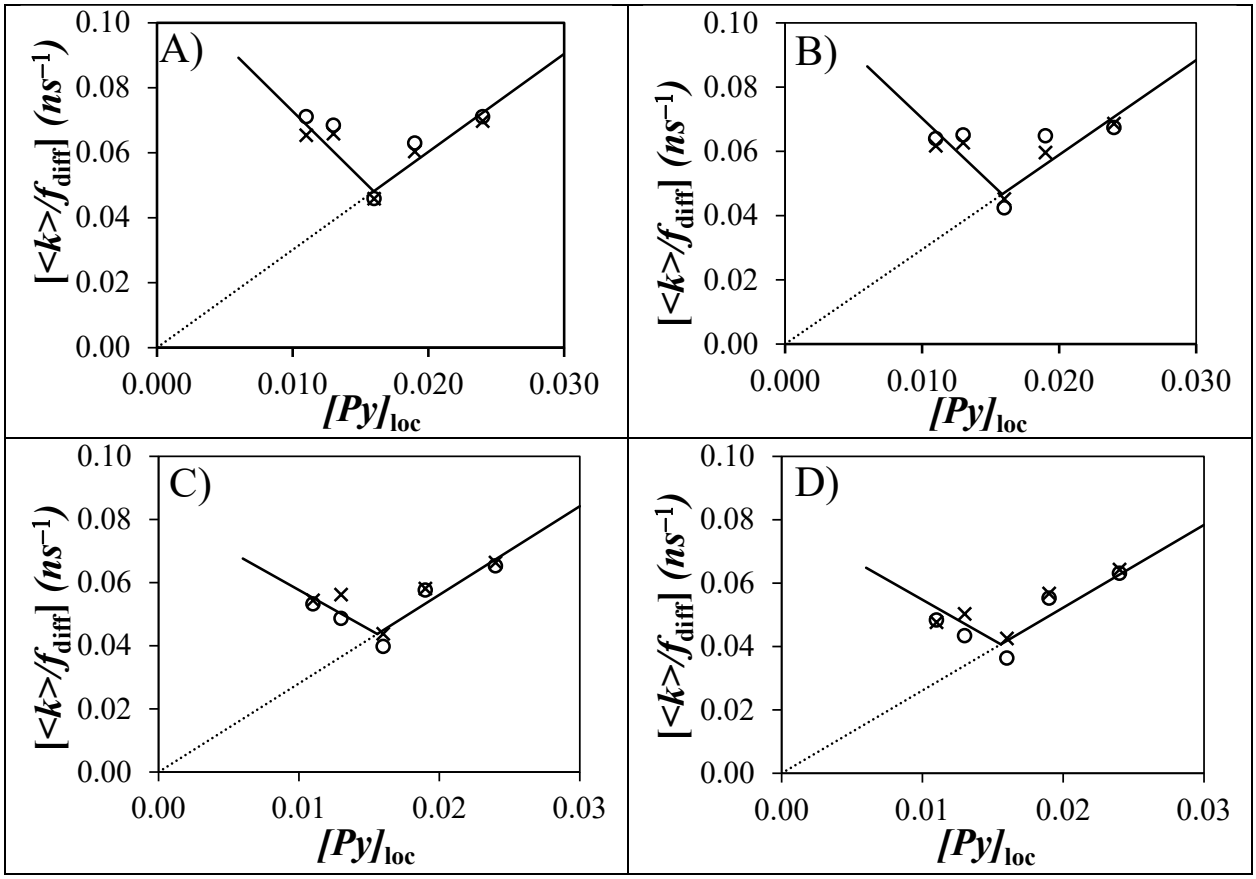


Figure 5.7. Comparison of (crosses) $[<k>/f_{diff}]^{th}$ calculated from Equation 5.8 and (circles) $[<k>/f_{diff}]^{exp}$ obtained from the global MFA of the fluorescence decays plotted as a function of $[Py]_{loc}$ for NaCl concentrations equal to A)10, B) 20, C) 50, and D) 100 mM.

Because the same assumption underlies the $[<k>/f_{diff}]^{exp}$ results obtained in all three studies, the $[<k>/f_{diff}]^{exp}$ ratios should conform to Equation 5.8. Equation 5.8 accounts for the partitioning of the dendrimers between the two regions of the NSSA and the reduction in $[<k>/f_{diff}]^{exp}$ by the product $f_{Edge}\times f_{DTAB}\times[<k>/f_{diff}]^{A\text{-}C}$, where f_{Edge} is the volume fraction of the NSSA occupied by the edges defined in Equation 5.7, f_{DTAB} is the molar fraction of DTAB molecules in the surfactant mixture, and $[<k>/f_{diff}]^{A\text{-}C}$ is the $[<k>/f_{diff}]$ ratio representing the interactions between pyrene and the DTAB headgroups. To this end, the trends obtained with the experimental and theoretical quantities $[<k>/f_{diff}] + f_{Edge}\times f_{DTAB}\times[<k>/f_{diff}]^{A\text{-}C}$ for the PyC10-

and PyC12-PAMAM-G0 samples and the experimental and theoretical [$<k>/f_{diff}$] ratios for the PyC4-, PyC6-, and PyC8-PAMAM-G0 samples were compared in Figure 5.8 for the results obtained in the three studies. All experimental data clustered around the theoretical lines expected for the $[<k>/f_{diff}]^{exp}$ ratios of the dendrimers obtained under different conditions. The general agreement found between experimental and theoretical trends in Figure 5.8 supports the model proposed for the compartmentalization of the NSSA into two regions and the partitioning of the dendrimers among these two regions.

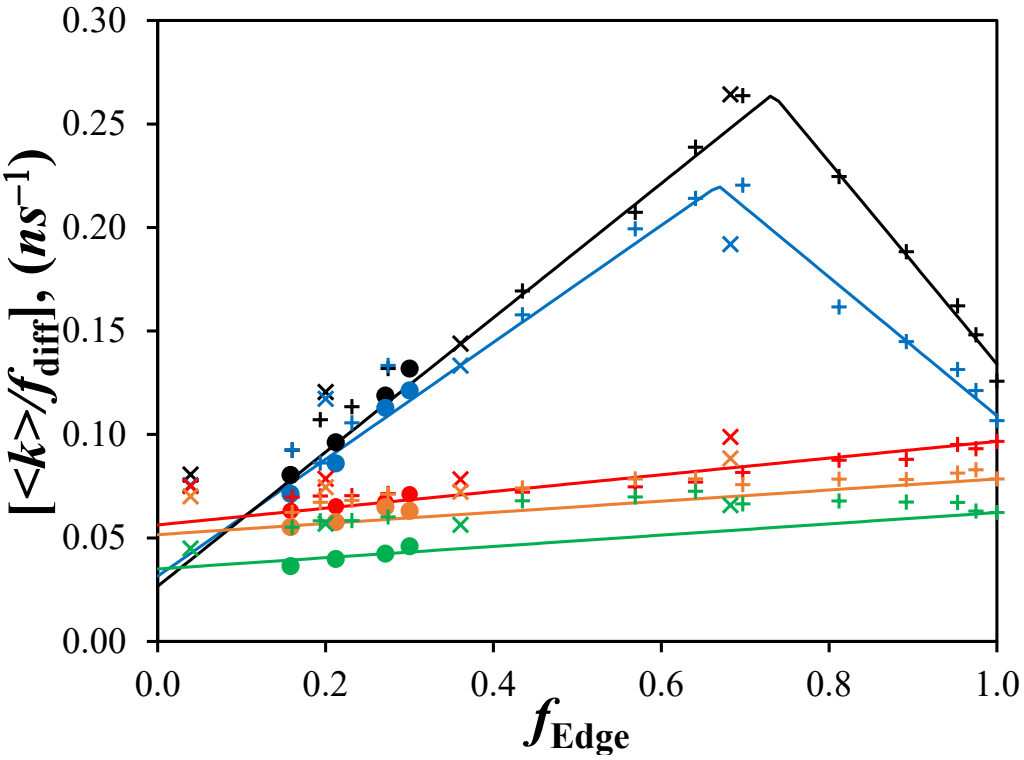


Figure 5.8. Plot of $[<k>/f_{diff}]^{exp}$ for the (red) PyC4-, (orange) PyC6-, and (green) PyC8-PAMAM-G0 samples and $[<k>/f_{diff}]^{exp}+f_{\underline{Edge}}\times f_{DTAB}\times[<k>/f_{diff}]^{A\text{-}C}$ for the (blue) PyC10- and (black) PyC12-PAMAM-G0 samples. (+) data obtained for SDS with NaCl, (×) data obtained for SDS:DTAB mixtures without salt, (●) data obtained for an 80:20 SDS:DTAB mixture with NaCl (this study), and (solid lines) trendlines generated by $[<k>/f_{diff}]^{th}$ calculated with Equation 5.8.

5.5 CONCLUSION

The conformational inversion experienced by the PyCX-PAMAM-G0 samples with longer linkers was employed to confirm the existence of two distinct regions inside the NSSA. Following a first study, where NSSA were produced by adding NaCl to a 50 mM SDS solution,[23] and a second study, where NSSA were prepared from a series of catanionic SDS and DTAB mixtures,[18] the present study considered the formation of NSSA by adding salt to a solution of a surfactant mixture with a fixed 80:20 SDS:DTAB molar ratio. As salt was added to the 80:20 SDS:DTAB mixture, N_{agg}(NSSA) increased from 210 to 396 (±4) when the NaCl concentration increased from 0 to 100 mM. The $[<k>/f_{diff}]^{exp}$ ratio of the PyC10- and PyC12-PAMAM-G0 samples continuously decreased in Figure 5.6A as the NaCl concentration increased from 0 to 100 mM. Accounting for the aromatic-cationic interactions between the pyrene moieties and the DTAB trimethylammonium headgroups with the $[<k>/f_{diff}]^{A\text{-}C}$ ratio, which reduced the $[<k>/f_{diff}]^{Edge}$ ratio experienced by the dendrimers in the edge region, resulted in an excellent match between the experimental $[<k>/f_{diff}]^{exp}$ and the $[<k>/f_{diff}]^{th}$ ratios in Figure 5.7. Since the derivation of $[<k>/f_{diff}]^{th}$ in Equation 5.8 involved the partitioning of the PyC10- and PyC12-PAMAM-G0 dendrimers between the polar edges and the hydrophobic middle region of the NSSA, the good agreement between $[<k>/f_{diff}]^{exp}$ and $[<k>/f_{diff}]^{th}$ in Figure 5.7 further validates the notion that NSSA are composed of two regions, as had been proposed in the two earlier studies.[18,23] This was further supported by noting that all the $[<k>/f_{diff}]^{exp}$ ratios obtained for the PyCX-PAMAM-G0 samples in this and two earlier studies dealing with various NSSA clustered around master lines in Figure 5.8. The fact that all $[<k>/f_{diff}]^{exp}$ ratios obeyed a same function of f_{Edge} given by Equation 5.8 confirmed the generality of the partitioning model proposed in Figure 5.1D for the dendrimers and supports the mechanism proposed earlier to predict the formation of NSSA.[23] The simplicity and far-reaching

implications of the spatial partitioning theory about the composition of NSSA will provide a useful rational for the formation and behavior of NSSA.

Chapter 6: Concluding Remarks and Future Work

6.1 THESIS CONCLUSION

This thesis presented a systematic investigation into the conformational behavior of generation-0 polyamidoamine dendrimers end-labeled with 1-pyrenealkanoyl groups (PyCX-PAMAM-G0) as they interacted with various surfactant aggregates. By applying the highly sensitive technique of pyrene excimer formation (PEF) and leveraging the global model-free analysis (MFA) of fluorescence decays, these dendrimers were employed both as subjects of conformational studies as they interacted with surfactant aggregates and as molecular probes to reveal some under-examined features of surfactant assemblies.

In Chapter 2, the conformation of the dendrimers was characterized in polar organic solvents and micellar environments. It was found that the internal segments of the dendrimers with short alkanoyl linkers obeyed Gaussian statistics in all systems, while those with longer linkers exhibited a conformational inversion when embedded in surfactant micelles made of sodium dodecyl sulfate (SDS) or dodecyltrimethylammonium bromide (DTAB). This effect was attributed to strong hydrophobic interactions between the long alkanoyl linkers of the dendrimers and the micellar core. These findings not only demonstrated an interesting experimental means for characterizing the conformation of hydrophobically modified, water-soluble macromolecules (HMWSM) like the PyCX-PAMAM-G0 dendrimers but also raised the possibility of using a similar approach to study the behavior of biological macromolecules such as amphipathic peptides interacting with biological membranes.

The third chapter extended this investigation to mixed micelles composed of oppositely charged surfactants (SDS and DTAB), revealing that increasing DTAB content reduced the extent of conformational inversion for the PyC10- and PyC12-PAMAM-G0 dendrimers. This behavior was linked to a change in the hydrophobicity gradient (HG) experienced by the dendrimers as the shape of the surfactant aggregates evolved from a sphere for pure SDS micelles to elongated ellipsoids for the SDS/DTAB mixtures with distinct polar and

hydrophobic regions and led to the establishment of the spatial partitioning theory (SPT). The SPT was validated for the mixed micelles from the agreement found between the theoretical and experimental average rate constant (<*k*>) for PEF obtained for the dendrimers embedded in the surfactant aggregates. The confirmation in Chapter 3 that the dendrimers partitioned themselves between the two distinct regions constituting the mixed micelles led to the proposal that the PyCX-PAMAM-G0 dendrimers could be employed for probing the interior of other surfactant aggregates. This proposal was investigated in the following chapters.

In Chapters 4 and 5, the PyCX-PAMAM-G0 dendrimers were used as molecular probes to probe the edges of non-spherical surfactant aggregates (NSSA) formed by adding salt (NaCl) or DTAB and NaCl into SDS aqueous solutions. These experiments confirmed the existence of two distinct microdomains within the NSSA: a polar edge region with a curved surface and a high HG composed of a fixed number of charged SDS molecules, and a hydrophobic middle region with a flatter surface and a low HG composed of partially neutralized surfactants. The excellent agreement between the experimental and predicted [$<k>/f_{diff}$] ratios and the linear relationships between the [$<k>/f_{diff}$] ratios and f_{Mid} demonstrated that the dendrimers with longer linkers partitioned themselves between both regions in the NSSA resulting in the observed conformational inversion patterns. This conclusion further demonstrated the universality of the SPT in all NSSA that were studied in this thesis and led to a possible mechanism for the formation of NSSA presenting these two regions.

In summary, the results of this thesis offer a new framework for understanding the interactions between dendrimers and surfactant aggregates and provide compelling evidence for a general two-region model for NSSA. The ability of pyrene-labeled dendrimers to probe local environments with molecular-level precision demonstrates their potential as versatile tools in soft matter and colloid science. This work lays a solid foundation for future studies aimed at unraveling the internal characteristics of assemblies made of complex biological or

synthetic amphiphilic molecules as well as the conformation and behavior of hydrophobically modified macromolecules encapsulated in surfactant aggregates.

6.2 FUTURE WORK

By demonstrating the applicability of PEF to the characterization of the internal composition of NSSA and the conformation of embedded HMWSM, this thesis opens the gate for several appealing studies. For NSSA related research, similar studies could be conducted using a positively charged surfactant like DTAB as the reference surfactant instead of SDS in this thesis to further generalize the SPT. Based on the current understanding about NSSA and their mechanism of formation, an edge region composed of about 50 DTAB molecules, which is the N_{agg} of DTAB micelles formed in pure water, would be expected for NSSA formed by aqueous solutions of DTAB to which salt or an oppositely charged surfactant like SDS would be added. Such result, if observed, would provide strong evidence that the mechanism of NSSA formation is general and applies to all NSSA formed through partial neutralization of a reference surfactant with salt or oppositely charged surfactants. These experiments could be extended to other surfactants such as gemini surfactants with two charged headgroups or non-ionic surfactants to check if the two-region behavior can be reproduced with these different surfactants. Furthermore, the effect of other parameters such as the solution temperature, pH, or the tail length of the oppositely charged surfactant could help improve the understanding of all types of NSSA. The effect that such parameters have on aqueous surfactant solutions would provide valuable information for research and development in the many fields where surfactants are involved. For instance, most personal care products and detergents now contain SDS and multiple types of non-ionic surfactants, and the use of hot water (in bath, dishwashers…) is very common. Many foods and cosmetics with emulsifiers are stored at lower temperature, with the generalized use of pH modifiers such as citric acid. Moreover, lipid

bilayers would also be worth studying as examples of NSSA without edges to investigate how the PyCX-PAMAM-G0 dendrimers interact with these bilayer structures at the molecular level. The dual region feature found with the NSSA might also exist in smaller bilayer structures such as in the vesicles formed during endocytosis and those used in pharmaceutical applications such as for drug delivery vehicles.

On the other hand, information about the conformation of other HMWSM as they interact with surfactant aggregates could be determined by labeling a WSM with pyrene derivatives and applying the methodology described in this thesis. Examples of other dendritic molecules could involve dendrimers with a bis-hydroxymethylpropionic acid (HMPA) or a polyethyleneimine backbone, which are commercially available. The HMPA dendrimers are of interest since they are neutral and do not get charged with changes in pH contrary to the PyCX-PAMAM-G0 dendrimers. Other studies could also involve PAMAM-G1 dendrimers with eight amine terminals, which could be modified with twice more 1-pyrenealkanoyl groups. How these dendritic macromolecules would interact with different types of surfactant aggregates would provide some generality to the trends obtained so far with the PyCX-PAMAM-G0 dendrimers.

Overall, the characterization of the conformation of pyrene-labeled dendrimers in restricted domains, and the subsequent use of this information to elucidate the chemical composition of these domains, represents a valuable research direction with applicability to many fields.

Letters of Copyright Permission

ACS Publications
Most Trusted. Most Cited. Most Read.

Probing Macromolecular Conformation in Restricted Geometry by PEF: Application to Hydrophobically Modified PAMAM Dendrimers Isolated Inside Surfactant Micelles

Author: Donghan Liu, Sanjay Patel, Yuting Xie, et al
Publication: The Journal of Physical Chemistry B
Publisher: American Chemical Society
Date: Jan 1, 2025

Copyright © 2025, American Chemical Society

Quick Price Estimate

This service provides permission for reuse only. If you do not have a copy of the portion you are using, you may copy and paste the content and reuse according to the terms of your agreement. Please be advised that obtaining the content you license is a separate transaction not involving RightsLink.

This type of permission is granted free of charge. Please note the following:

- Permission is granted for your request in both print and electronic formats, and translations.
- If figures and/or tables were requested, they may be adapted or used in part.
- Please print this page for your records and send a copy of it to your publisher/graduate school.
- Appropriate credit for the requested material should be given as follows: "Reprinted (adapted) with permission from {COMPLETE REFERENCE CITATION}. Copyright {YEAR} American Chemical Society." Insert appropriate information in place of the capitalized words.
- One-time permission is granted only for the use specified in your RightsLink request. No additional uses are granted (such as derivative works or other editions). For any additional uses, please submit a new request for each such use.

If credit is given to another source for the material you requested from RightsLink, permission must be obtained from that source.

Please note, this service provides permission for re-use only. You must have a valid license to access the content you wish to re-use.

ACS Publications
Most Trusted. Most Cited. Most Read.

Conformation of Pyrene End-Labeled Polyamidoamine Dendrimers in Catanionic Surfactant Micelles Probed by Pyrene Excimer Formation

Author: Donghan Liu, Sanjay Patel, Jean Duhamel
Publication: Langmuir
Publisher: American Chemical Society
Date: Jul 1, 2025

Copyright © 2025, American Chemical Society

Quick Price Estimate

This service provides permission for reuse only. If you do not have a copy of the portion you are using, you may copy and paste the content and reuse according to the terms of your agreement. Please be advised that obtaining the content you license is a separate transaction not involving RightsLink.

This type of permission is granted free of charge. Please note the following:

- Permission is granted for your request in both print and electronic formats, and translations.
- If figures and/or tables were requested, they may be adapted or used in part.
- Please print this page for your records and send a copy of it to your publisher/graduate school.
- Appropriate credit for the requested material should be given as follows: "Reprinted (adapted) with permission from {COMPLETE REFERENCE CITATION}. Copyright {YEAR} American Chemical Society." Insert appropriate information in place of the capitalized words.
- One-time permission is granted only for the use specified in your RightsLink request. No additional uses are granted (such as derivative works or other editions). For any additional uses, please submit a new request for each such use.

If credit is given to another source for the material you requested from RightsLink, permission must be obtained from that source.

Please note, this service provides permission for re-use only. You must have a valid license to access the content you wish to re-use.

References

Chapter 1

1. Tomalia, D. A.; Baker, H.; Dewald, J.; Hall, M.; Kallos, G.; Martin, S.; Roeck, J.; Ryder, J.; Smith, P. A New Class of Polymers: Starbust-Dendritic Macromolecules. *Polym. J.* **1985**, *17*, 117-132.
2. Alamos-Musre, S.; Beltrán-Chacana, D.; Moyano, J.; Márquez-Miranda, V.; Duarte, Y.; Miranda-Rojas, S.; Olguín, Y.; Fuentes, J. A.; González-Nilo, D.; Otero, M. C. From Structure to Function: The Promise of PAMAM Dendrimers in Biomedical Applications. *Pharmaceutics* **2025**, *17*, 927.
3. Patle, R. Y.; Meshram, J. S. The Advanced Synthetic Modifications and Applications of Multifunctional PAMAM Dendritic Composites. *React. Chem. Eng.* **2022**, *7*, 9–40.
4. Maity, T.; Gosika, M.; Pascal, T. A.; Maiti, P. K. Molecular Insights into the Physics of Poly(Amidoamine)-Dendrimer-Based Supercapacitors. arXiv October 22, 2022.
5. Abedi-Gaballu, F.; Dehghan, G.; Ghaffari, M.; Yekta, R.; Abbaspour-Ravasjani, S.; Baradaran, B.; Ezzati Nazhad Dolatabadi, J.; Hamblin, M. R. PAMAM Dendrimers as Efficient Drug and Gene Delivery Nanosystems for Cancer Therapy. *Appl. Mat. Today* **2018**, *12*, 177–190.
6. Kolhatkar, R. B.; Kitchens, K. M.; Swaan, P. W.; Ghandehari, H. Surface Acetylation of Polyamidoamine (PAMAM) Dendrimers Decreases Cytotoxicity While Maintaining Membrane Permeability. *Bioconjugate Chem.* **2007**, *18*, 2054–2060.
7. Luu, N. H.; Ly, H. Q.; Nguyen, C. V.; Dinh, L. T.; Nguyen, T. N.; Phan, C. M.; Nguyen, M. L.; Vu, H. H.; Luu, C. H.; Hoang Thi, T. T. Cholesterol-Conjugated PAMAM Dendrimers: Enhancing Stability, Drug Delivery Efficiency, and In Vitro Anticancer Performance. *J. Polym. Sci.* **2024**, *63*, 541–553

8. Ayatollahi, S.; Hashemi, M.; Kazemi Oskuee, R.; Salmasi, Z.; Mokhtarzadeh, A.; Alibolandi, M.; Abnous, K.; Ramezani, M. Synthesis of Efficient Gene Delivery Systems by Grafting Pegylated Alkylcarboxylate Chains to PAMAM Dendrimers: Evaluation of Transfection Efficiency and Cytotoxicity in Cancerous and Mesenchymal Stem Cells. *J. Biomater. Appl*. **2015**, *30*, 632–648.

9. Kumar, A.; Nutan, B.; Jewrajka, S. K. Stability and Acidic pH-Mediated Leakage of Guest Molecules from Self-Assembly of Poly(Amidoamine)-Graft-Alkyl Copolymers. *Polymer* **2019**, *183*, 121894.

10. Yang, D.; Gao, S.; Fang, Y.; Lin, X.; Jin, X.; Wang, X.; Ke, L.; Shi, K. The π–π Stacking-Guided Supramolecular Self-Assembly of Nanomedicine for Effective Delivery of Antineoplastic Therapies. *Nanomed.* **2018**, *13*, 3159–3177.

11. Pishavar, E.; Attaranzadeh, A.; Alibolandi, M.; Ramezani, M.; Hashemi, M. Modified PAMAM Vehicles for Effective TRAIL Gene Delivery to Colon Adenocarcinoma: In Vitro and in Vivo Evaluation. *Artif. Cells Nanomed. Biotechnol.* **2018**, *46* (sup3), 503–513.

12. Yiyun, C.; Na, M.; Tongwen, X.; Rongqiang, F.; Xueyuan, W.; Xiaomin, W.; Longping, W. Transdermal Delivery of Nonsteroidal Anti-Inflammatory Drugs Mediated by Polyamidoamine (PAMAM) Dendrimers. *J. Pharm. Sci.* **2007**, *96*, 595–602.

13. Barraza, L. F.; Jiménez, V. A.; Alderete, J. B. Methotrexate Complexation with Native and PEGylated PAMAM-G4: Effect of the PEGylation Degree on the Drug Loading Capacity and Release Kinetics. *Macromol. Chem. Phys.* **2016**, *217*, 605–613.

14. Parimi, S.; Barnes, T. J.; Callen, D. F.; Prestidge, C. A. Mechanistic Insight into Cell Growth, Internalization, and Cytotoxicity of PAMAM Dendrimers. *Biomacromolecules* **2010**, *11*, 382–389.

15. Fox, L. J.; Richardson, R. M.; Briscoe, W. H. PAMAM Dendrimer - Cell Membrane Interactions. *Adv. Colloid Interface Sci.* **2018**, *257*, 1–18.

16. He, X.; Lin, M.; Lu, T.; Qu, Z.; Xu, F. Molecular Analysis of Interactions between a PAMAM Dendrimer–Paclitaxel Conjugate and a Biomembrane. *Phys. Chem. Chem. Phys*. **2015**, *17*, 29507–29517.

17. Myers, D. *Surfactant Science and Technology*; John Wiley & Sons, 2020, pp. 3-8.

18. Israelachvili, J. N. *Intermolecular and Surface Forces*; Academic Press, 2011, pp. 535-577.

19. Almgren, M.; Swarup, S. Size of Sodium Dodecyl Sulfate Micelles in the Presence of Additives. 2. Aromatic and Saturated Hydrocarbons. *J. Phys. Chem.* **1982**, *86*, 4212-4216.

20. Duplâtre, G.; Ferreira Marques, M. F.; Da Graça Miguel, M. Size of Sodium Dodecyl Sulfate Micelles in Aqueous Solutions as Studied by Positron Annihilation Lifetime Spectroscopy. *J. Phys. Chem.* **1996**, *100*, 16608–16612.

21. Almgren, M.; Gimel, J. C.; Wang, K.; Karlsson, G.; Edwards, K.; Brown, W.; Mortensen, K. SDS Micelles at High Ionic Strength. A Light Scattering, Neutron Scattering, Fluorescence Quenching, and CryoTEM Investigation. *J. Colloid Interface Sci.* **1998**, *202*, 222–231.

22. Liu, X.; Chen, X.; Wang, J.; Chen, G.; Zhang, H. Hydrogen-Bonded Polymers with Bent-Shaped Side Chains and Poly(4-Vinylpridine) Backbone: Phase Behavior and Thin Film Morphologies. *Macromolecules* **2014**, *47*, 3917–3925.

23. Hura, G. L.; Budworth, H.; Dyer, K. N.; Rambo, R. P.; Hammel, M.; McMurray, C. T.; Tainer, J. A. Comprehensive Macromolecular Conformations Mapped by Quantitative SAXS Analyses. *Nat. Methods* **2013**, *10*, 453–454.

24. Singh, P. S. Chapter 6 - Small-Angle Scattering Techniques (SAXS/SANS). In Membrane Characterization; Hilal, N., Ismail, A. F., Matsuura, T., Oatley-Radcliffe, D., Eds.; Elsevier, 2017; pp 95–111.

25. Podzimek, S. The Use of GPC Coupled with a Multiangle Laser Light Scattering Photometer for the Characterization of Polymers. On the Determination of Molecular Weight, Size and Branching. *J. Appl. Polym. Sci.* **1994**, *54*, 91–103.

26. Bergström, M.; Pedersen, J. S. Formation of Tablet-Shaped and Ribbonlike Micelles in Mixtures of an Anionic and a Cationic Surfactant. *Langmuir* **1999**, *15*, 2250–2253.

27. Hammouda, B. SANS from Polymers—Review of the Recent Literature. *Polym. Rev.* **2010**, *50*, 14–39.

28. Wang, X.; Guerrand, L.; Wu, B.; Li, X.; Boldon, L.; Chen, W.-R.; Liu, L. Characterizations of Polyamidoamine Dendrimers with Scattering Techniques. *Polymers* **2012**, *4*, 600–616.

29. Krueger, S.; Perez-Salas, U. A.; Gregurick, S. K.; Kuzmanovic, D. Small Angle Neutron Scattering from Proteins, Nucleic Acids, and Viruses. In *Neutron Scattering in Biology*; Springer: Berlin, 2006; pp 161–185.

30. Cadogan, S. P.; Hahn, C. J.; Rausch, M. H.; Fröba, A. P. Study on the Applicability of Dynamic Light Scattering (DLS) to Microemulsions Including Supercritical Carbon Dioxide-Swollen Micelles. *J. Colloid Interface Sci.* **2017**, *499*, 202–208.0020

31. Stetefeld, J.; McKenna, S. A.; Patel, T. R. Dynamic Light Scattering: A Practical Guide and Applications in Biomedical Sciences. *Biophys. Rev.* **2016**, *8*, 409–427.

32. Weiss, J. N. Dynamic Light Scattering (DLS) Spectroscopy. In *Dynamic Light Scattering Spectroscopy of the Human Eye*; Springer: Cham, **2022**; pp 13–17.

33. Tuukkanen, A. T.; Spilotros, A.; Svergun, D. I. Progress in Small-Angle Scattering from Biological Solutions at High-Brilliance Synchrotron. *IUCrJ* **2017**, *4*, 518–528.

34. Skou, S.; Gillilan, R. E.; Ando, N. Synchrotron-Based Small-Angle X-Ray Scattering of Proteins in Solution. *Nat. Protoc.* **2014**, *9*, 1727-1739.

35. Dyer, K. N.; Hammel, M.; Rambo, R. P.; Tsutakawa, S. E.; Rodic, I.; Classen, S.; Tainer, J. A.; Hura, G. L. High-Throughput SAXS for the Characterization of Biomolecules in

Solution: A Practical Approach. In *Structural Genomics: General Applications*; Chen, Y. W., Ed.; Humana Press: Totowa, NJ, 2014; pp 250.

36. Hugel, T.; Seitz, M. The Study of Molecular Interactions by AFM Force Spectroscopy. *Macromol. Rapid Commun.* **2001**, *22*, 989–1016.
37. Lostao, A.; Lim, K.; Pallarés, M. C.; Ptak, A.; Marcuello, C. Recent Advances in Sensing the Inter-Biomolecular Interactions at the Nanoscale – A Comprehensive Review of AFM-Based Force Spectroscopy. *Int. J. Biol. Macromol.* **2023**, *238*, 124089.
38. Suga, M.; Asahina, S.; Sakuda, Y.; Kazumori, H.; Nishiyama, H.; Nokuo, T.; Alfredsson, V.; Kjellman, T.; Stevens, S. M.; Cho, H. S.; Cho, M.; Han, L.; Che, S.; Anderson, M. W.; Schüth, F.; Deng, H.; Yaghi, O. M.; Liu, Z.; Jeong, H. Y.; Stein, A.; Sakamoto, K.; Ryoo, R.; Terasaki, O. Recent Progress in Scanning Electron Microscopy for the Characterization of Fine Structural Details of Nanomaterials. *Prog. Solid State Chem.* **2014**, *42*, 1–21.
39. Datye, A.; DeLaRiva, A. Scanning Electron Microscopy (SEM). In *Springer Handbook of Advanced Catalyst Characterization*; Wachs, I. E., Bañares, M. A., Eds.; Springer International Publishing: Cham, 2023; pp 359–380.
40. Braidy, N.; Béchu, A.; de Souza Terra, J. C.; Patience, G. S. Experimental Methods in Chemical Engineering: Transmission Electron Microscopy—TEM. *Can. J. Chem. Eng.* **2020**, *98*, 628–641.
41. Franken, L. E.; Grünewald, K.; Boekema, E. J.; Stuart, M. C. A. A Technical Introduction to Transmission Electron Microscopy for Soft-Matter: Imaging, Possibilities, Choices, and Technical Developments. *Small* **2020**, *16*, 1906198.
42. Sun, W. Principles of Atomic Force Microscopy. In Cai, J. (Ed.) *Atomic Force Microscopy in Molecular and Cell Biology*; Springer: Singapore, 2018; pp 1–28.

43. Akhtar, K.; Khan, S. A.; Khan, S. B.; Asiri, A. M. Scanning Electron Microscopy: Principle and Applications in Nanomaterials Characterization. In Sharma, S. (Ed.) *Handbook of Materials Characterization*; Springer: Cham, 2018; pp 113–145.

44. Tang, C. Y.; Yang, Z. Chapter 8 – Transmission Electron Microscopy (TEM). In *Membrane Characterization*; Hilal, N., Ismail, A. F., Matsuura, T., Oatley-Radcliffe, D., Eds.; Elsevier, 2017; pp 145–159.

45. Khullar, P.; Singh, V.; Mahal, A.; Kaur, H.; Singh, V.; Banipal, T. S.; Kaur, G.; Bakshi, M. S. Tuning the Shape and Size of Gold Nanoparticles with Triblock Polymer Micelle Structure Transitions and Environments. *J. Phys. Chem. C* **2011**, *115*, 10442–10454.

46. Drummy, L. F.; Yang, J.; Martin, D. C. Low-Voltage Electron Microscopy of Polymer and Organic Molecular Thin Films. *Ultramicroscopy* **2004**, *99*, 247–256.

47. King, M. V. Dimensional Changes in Cells and Tissues during Specimen Preparation for the Electron Microscope. *Cell Biophys.* **1991**, *18*, 31–55.

48. Talmon, Y. Staining and Drying-Induced Artifacts in Electron Microscopy of Surfactant Dispersions. *J. Colloid Interface Sci.* **1983**, *93*, 366–382.

49. Yatcilla, M. T.; Herrington, K. L.; Brasher, L. L.; Kaler, E. W.; Chiruvolu, S.; Zasadzinski, J. A. Phase Behavior of Aqueous Mixtures of Cetyltrimethylammonium Bromide (CTAB) and Sodium Octyl Sulfate (SOS). *J. Phys. Chem.* **1996**, *100*, 5874–5879.

50. Mal, A.; Bag, S.; Ghosh, S.; Moulik, S. P. Physicochemistry of CTAB-SDS Interacted Catanionic Micelle-Vesicle Forming System: An Extended Exploration. *Colloids Surf. A Physicochem. Eng. Asp.* **2018**, *553*, 633–644.

51. Saghi, Z.; Midgley, P. A. Electron Tomography in the (S)TEM: From Nanoscale Morphological Analysis to 3D Atomic Imaging. *Annu. Rev. Mater. Res.* **2012**, *42*, 59–79.

52. Bohdanecký, M. A Semiempirical Formulation of the Effect of Random Branching on Intrinsic Viscosity. *Macromolecules* **1977**, *10*, 971–975.

53. Aerts, J. Prediction of Intrinsic Viscosities of Dendritic, Hyperbranched and Branched Polymers. *Comput. Theor. Polym. Sci.* **1998**, *8*, 49–54.

54. Carriere, C. J.; Bagley, E. B. Calculation of the Persistence Length of Solubilized Starches from Intrinsic Viscosity Measurements. *J. Rheol.* **1999**, *43*, 753–763.

55. Raja, A.; Wilfert, P. K.; Picken, S. J. Charge Mediated Changes to the Intrinsic Viscosity of Biopolymer Systems. *Polymers* **2024**, *16*, 2894.

56. Yekta, A.; Duhamel, J.; Brochard, P.; Adiwidjaja, H.; Winnik, M. A. A Fluorescent Probe Study of Micelle-like Cluster Formation in Aqueous Solutions of Hydrophobically Modified Poly(Ethylene Oxide). *Macromolecules* **1993**, *26*, 1829–1836.

57. Siu, H.; Duhamel, J. Associations between a Pyrene-Labeled Hydrophobically Modified Alkali Swellable Emulsion Copolymer and Sodium Dodecyl Sulfate Probed by Fluorescence, Surface Tension, and Viscometry. *Macromolecules* **2006**, *39*, 1144–1155.

58. Chen, S.; Siu, H.; Duhamel, J. Interactions between Hydrophobically Modified Alkali-Swellable Emulsion Polymers and Sodium Dodecyl Sulfate Probed by Fluorescence and Rheology. *J. Phys. Chem. B* **2014**, *118*, 351–361.

59. Galan, A.; Lulic, K.; Wang, J.; Wicher, B.; Huc, I.; Duhamel, J.; Maurizot, V. Coaxial Assembly of Helical Aromatic Foldamers by Metal Coordination. *Chem. Commun.* **2023**, *59*, 5253–5256.

60. Rodger, A. Circular Dichroism Spectroscopy of Biomacromolecules. In *Encyclopedia of Biophysics*; Springer, Berlin, Heidelberg, 2018; pp 1–3.

61. Lee, M. S.; Cao, B. Nuclear Magnetic Resonance Chemical Shift: Comparison of Estimated Secondary Structures in Peptides by Nuclear Magnetic Resonance and Circular Dichroism. *Protein Eng.* **1996**, *9*, 15–25.

62. Krois, D.; Lehner, H. Peptide-Mediated Conformational Changes in Bilipeptides: Evidence for the Occurrence of Stretched Species. *J. Chem. Soc., Perkin Trans. 2* **1990**, 1745–1755.

63. Lindon, J. C.; Ferrige, A. G. Digitisation and Data Processing in Fourier Transform NMR. *Prog. Nucl. Magn. Reson. Spectrosc.* **1980**, *14*, 52–57.

64. Karslake, C.; Piotto, M. E.; Pak, Y. K.; Weiner, H.; Gorenstein, D. G. 2D NMR and Structural Model for a Mitochondrial Signal Peptide Bound to a Micelle. *Biochemistry* **1990**, *29*, 9872–9878.

65. Zhang, F.; Adnani, N.; Vazquez-Rivera, E.; Braun, D. R.; Tonelli, M.; Andes, D. R.; Bugni, T. S. Application of 3D NMR for Structure Determination of Peptide Natural Products. *J. Org. Chem.* **2015**, *80*, 8713–8719.

66. Böhm, G.; Muhr, R.; Jaenicke, R. Quantitative Analysis of Protein Far UV Circular Dichroism Spectra by Neural Networks. *Protein Eng.* **1992**, *5*, 191–195.

67. Rodger, A. Far UV Protein Circular Dichroism. In *Encyclopedia of Biophysics*; Springer, Berlin, Heidelberg, 2018; pp 1–6.

68. Kelly, S. M.; Price, N. C. The Use of Circular Dichroism in the Investigation of Protein Structure and Function. *Curr. Protein Pept. Sci.* **2000**, *1*, 349–384.

69. Liu, Z.; Shi, X.; Shu, W.; Qi, S.; Wang, X.; He, X. The Effect of Hydration and Dehydration on the Conformation, Assembling Behavior and Photoluminescence of PBLG. *Soft Matter* **2022**, *18*, 4396–4401.

70. Greenfield, N. J. Using Circular Dichroism Spectra to Estimate Protein Secondary Structure. *Nat. Protoc.* **2006**, *1*, 2876–2890.

71. Kelly, S. M.; Jess, T. J.; Price, N. C. How to Study Proteins by Circular Dichroism. *Biochim. Biophys. Acta - Proteins Proteomics* **2005**, *1751*, 119–139.

72. Miles, A. J.; Wallace, B. A. Circular Dichroism Spectroscopy of Membrane Proteins. *Chem. Soc. Rev.* **2016**, *45*, 4859–4872.

73. Stryer, L.; Haugland, R. Energy Transfer: A Spectroscopic Ruler. *Proc. Natl. Acad. Sci. U.S.A.* **1967**, *2*, 719–726.

74. Jares-Erijman, E. A.; Jovin, T. M. FRET Imaging. *Nat. Biotechnol.* **2003**, *21*, 1387–1395.

75. Zimmer, K. J. L.; Johnson, R. E.; Little, H.; Duhamel, J.; Manderville, R. A. Harnessing a Fluorescent Nucleobase Surrogate for Supramolecular FRET-Aptamer Detection and Target-Site Mapping. *ACS Sens.* **2025**, *10*, 1822–1832.

76. Cuniberti, C.; Perico, A. Intramolecular Excimers and Microbrownian Motion of Flexible Polymer Molecules in Solution. *Eur. Polym. J.* **1977**, *13*, 369–374.

77. Winnik, M. A.; Redpath, T.; Richards, D. H. The Dynamics of End-to-End Cyclization in Polystyrene Probed by Pyrene Excimer Formation. *Macromolecules* **1980**, *13*, 328–335.

78. Winnik, M.A. End-to-End Cyclization of Polymer Chains. *Acc. Chem. Res.* **1985**, *18*, 73–79.

79. Duhamel, J. Global Analysis of Fluorescence Decays to Probe the Internal Dynamics of Fluorescently Labeled Macromolecules. *Langmuir* **2014**, *30*, 2307–2324.

80. Little, H.; Patel, S.; Duhamel, J. Probing the Inner Local Density of Complex Macromolecules by Pyrene Excimer Formation. *Phys. Chem. Chem. Phys.* **2023**, *25*, 26515-26525.

81. Behera, G. B.; Mishra, B. K.; Behera, P. K.; Panda, M. Fluorescent Probes for Structural and Distance Effect Studies in Micelles, Reversed Micelles and Microemulsions. *Adv. Colloid Interface Sci.* **1999**, *82*, 1–42.

82. Danino, D.; Talmon, Y.; Zana, R. Alkanediyl-α,ω-Bis(Dimethylalkylammonium Bromide) Surfactants (Dimeric Surfactants). 5. Aggregation and Microstructure in Aqueous Solutions. *Langmuir* **1995**, *11*, 1448–1456.

83. Herrington, K. L.; Kaler, E. W.; Miller, D. D.; Zasadzinski, J. A.; Chiruvolu, S. Phase Behavior of Aqueous Mixtures of Dodecyltrimethylammonium Bromide (DTAB) and Sodium Dodecyl Sulfate (SDS). *J. Phys. Chem.* **1993**, *97*, 13792–13802.

84. Wattebled, L.; Laschewsky, A.; Moussa, A.; Habib-Jiwan, J.-L. Aggregation Numbers of Cationic Oligomeric Surfactants: A Time-Resolved Fluorescence Quenching Study. *Langmuir* **2006**, *22*, 2551–2557.

85. Kalyanasundaram, K.; Thomas, J. K. Environmental Effects on Vibronic Band Intensities in Pyrene Monomer Fluorescence and their Application in Studies of Micellar Systems. *J. Am. Chem. Soc.* **1977**, *44*, 2039–2044.

86. Dong, D. C.; Winnik, M. A. The Py Scale of Solvent Polarities. Solvent Effects on the Vibronic Fine Structure of Pyrene Fluorescence and Empirical Correlations with ET and Y Values. *Photochem. Photobiol.* **1982**, *35*, 17–21.

87. Kim, D.; Amos, R. C.; Gauthier, M.; Duhamel, J. Assemblies of Hydrophobically Modified Starch Nanoparticles Probed by Surface Tension and Pyrene Fluorescence. *ACS Symp. Ser.-Mol. Assembl.: Charact. Appl.* **2020**, *Chapter 5*, 61–75.

88. Liu, D.; Duhamel, J.; Gauthier, M. Synthesis and Characterization of Furan-Based Non-Ionic Surfactants (Fbnios). *Langmuir* **2023**, *39*, 8974–8983.

89. Tachiya, M. Application of a Generating Function to Reaction Kinetics in Micelles. Kinetics of Quenching of Luminescent Probes in Micelles. *Chem. Phys. Lett.* **1975**, *33*, 289–292.

90. Turro, N. J.; Yekta, A. Luminescent Probes for Detergent Solutions. A Simple Procedure for Determination of Mean Aggregation Number of Micelles. *J. Am. Chem. Soc.* **1978**, *100*, 5951–5952.

91. Birks, J. B.; Dyson, D. J.; Munro, I. H. 'Excimer' Fluorescence II. Lifetime Studies of Pyrene Solutions. *Proc. R. Soc. Lond. A Math. Phys. Sci.* **1963**, *275*, 575–588.

92. Siu, H.; Duhamel, J. Comparison of the Association Level of a Hydrophobically Modified Associative Polymer Obtained from an Analysis Based on Two Different Models. *J. Phys. Chem. B* **2005**, *109*, 1770–1780.

93. Patel, S.; McNelles, S. A.; Adronov, A.; Duhamel, J. Intramacromolecular Conformational Changes in Low Generation PAMAM Dendrimers Probed by Pyrene Excimer Formation. *J. Phys. Chem. B* **2023**, *127*, 8040–8048.

94. Patel, S.; Duhamel, J. Macromolecular Conformation of Low-Generation PAMAM Dendrimers Probed by Pyrene Excimer Formation. *Macromolecules* **2023**, *56*, 4012–4021.

95. Ba-Salem, A. O.; Duhamel, J. Determination of the Aggregation Number of Pyrene-Labeled Gemini Surfactant Micelles by Pyrene Fluorescence Quenching Measurements. *Langmuir* **2021**, *37*, 6069–6079.

96. Siu, H.; Duhamel, J. Comparison of the Association Level of a Pyrene-Labeled Associative Polymer Obtained from an Analysis Based on Two Different Models. *J. Phys. Chem. B* **2005**, *109*, 1770–1780.

97. Duhamel, J. New Insights in the Study of Pyrene Excimer Fluorescence to Characterize Macromolecules and Their Supramolecular Assemblies in Solution. *Langmuir* **2012**, *28*, 6527–6538.

98. Costa, T.; de Meilo, J. S. S.; Castro. C. S.; Gago, S.; Pillinger, M.; Goncalves, I. S. Picosecond Dynamics of Dimer Formation in a Pyrene-Labeled Polymer. *J. Phys. Chem. B* **2010**, *114*, 12439–12447.

99. Fowler, M. A.; Duhamel, J.; Bahun, G. J.; Adronov, A.; Zaragoza-Galán, G.; Rivera, E. Studying Pyrene-Labeled Macromolecules with the Model Free Analysis. *J. Phys. Chem. B* **2012**, *116*, 14689–14699.

100. Liu, D.; Patel, S.; Xie, Y.; Zhang, H.; Duhamel, J. Probing Macromolecular Conformation in Restricted Geometry by PEF: Application to Hydrophobically Modified PAMAM Dendrimers Isolated Inside Surfactant Micelles. *J. Phys. Chem. B* **2025**, *129*, 1144–1153.

101. Cao, X.; Casier, R.; Little, H.; Duhamel, J. Characterization of the Distribution of Pyrene Molecules in Confined Geometries with the Model Free Analysis and its Applications. *J. Phys. Chem. B* **2017**, *121*, 11325–11332.

102. Shah, S. S.; Khan, A. M. Determination of Critical Micelle Concentration (CMC) of Sodium Dodecyl Sulfate (SDS) and the Effect of Low Concentration of Pyrene on Its CMC Using ORIGIN Software. *JCSP* **2011**, *30*, 186.

103. Shah, S. S.; Jamroz, N. U.; Sharif, Q. M. Micellization Parameters and Electrostatic Interactions in Micellar Solution of Sodium Dodecyl Sulfate (SDS) at Different Temperatures. *Colloids Surf. A: Physicochem. Eng. Asp.* **2001**, *178*, 199–206.

104. Elarbi, F. M.; Ettarhouni, Z. O.; Abdussalam-Mohammed, W.; Mezoughi, A. B. Study on the Effects of Biologically Active Amino Acids on the Micellization of Anionic Surfactant Sodium Dodecyl Sulfate (SDS) at Different Temperatures. *Chemistry* **2022**, *4*, 146–155.

105. Cid, A.; Mejuto, J. C.; Orellana, P. G.; López-Fernández, O.; Rial-Otero, R.; Simal-Gandara, J. Effects of Ascorbic Acid on the Microstructure and Properties of SDS Micellar Aggregates for Potential Food Applications. *Food Res. Int.* **2013**, *50*, 143–148.

106. Seebunrueng, K.; Santaladchaiyakit, Y.; Srijaranai, S. Study on the Effect of Chain-Length Compatibility of Mixed Anionic–Cationic Surfactants on the Cloud-Point Extraction of Selected Organophosphorus Pesticides. *Anal. Bioanal. Chem.* **2012**, *404*, 1539–1548.

107. Duplâtre, G.; Ferreira Marques, M. F.; da Graça Miguel, M. Size of Sodium Dodecyl Sulfate Micelles in Aqueous Solutions as Studied by Positron Annihilation Lifetime Spectroscopy. *J. Phys. Chem.* **1996**, *100*, 16608–16612.

108. Us'yarov, O. G. Small-Angle X-Ray Scattering in Sodium Dodecyl Sulfate Solutions and Micelle Clustering. *Colloid J.* **2016**, *78*, 698–704.

109. Sammalkorpi, M.; Karttunen, M.; Haataja, M. Ionic Surfactant Aggregates in Saline Solutions: Sodium Dodecyl Sulfate (SDS) in the Presence of Excess Sodium Chloride (NaCl) or Calcium Chloride (CaCl2). *J. Phys. Chem. B* **2009**, *113*, 5863–5870.

110. Ikeda, S.; Hayashi, S.; Imae, T. Rodlike Micelles of Sodium Dodecyl Sulfate in Concentrated Sodium Halide Solutions. *J. Phys. Chem.* **1981**, *85*, 106–112.

111. Lianos, P.; Zana, R. Use of Pyrene Excimer Formation to Study the Effect of Sodium Chloride on the Structure of Sodium Dodecyl Sulfate Micelles. *J. Phys. Chem.* **1980**, *84*, 3339–3341.

112. Ranganathan, R.; Tran, L.; Bales, B. L. Surfactant- and Salt-Induced Growth of Normal Sodium Alkyl Sulfate Micelles Well above Their Critical Micelle Concentrations. *J. Phys. Chem. B* **2000**, *104*, 2260–2264.

113. Bergström, M.; Pedersen, J. S. Formation of Tablet-Shaped and Ribbonlike Micelles in Mixtures of an Anionic and a Cationic Surfactant. *Langmuir* **1999**, *15*, 2250–2253.

114. Kamenka, N.; Chorro, M.; Talmon, Y.; Zana, R. Study of Mixed Aggregates in Aqueous Solutions of Sodium Dodecyl Sulfate and Dodecyltrimethylammonium Bromide. *Colloids Surf.* **1992**, *67*, 213–222.

115. Bergström, M.; Pedersen, J. S. A Small Angle Neutron Scattering (SANS) Study of Tablet-Shaped and Ribbonlike Micelles Formed from Mixtures of an Anionic and a Cationic Surfactant. *J. Phys. Chem. B* **1999**, *103*, 8502–8513.

116. Liu, D.; Patel, S.; Duhamel, J. Conformation of Pyrene End-Labeled Polyamidoamine Dendrimers in Catanionic Surfactant Micelles Probed by Pyrene Excimer Formation. *Langmuir* **2025**, *41*, 20986–20998.

Chapter 2

1. Casier, R.; Duhamel, J. The Effect of Glycine on the Local Conformation and Internal Backbone Dynamics of Polypeptides. *Macromolecules* **2021**, *54*, 8904–8912.
2. Casier, R.; Duhamel, J. Blob-Based Approach to Estimate the Folding Time of Proteins Supported by Pyrene Excimer Fluorescence Experiments. *Macromolecules* **2020**, *53*, 9823–9835.
3. Casier, R.; Duhamel, J. Appraisal of Blob-Based Approaches in the Prediction of Protein Folding Times. *J. Phys. Chem. B* **2023**, *127*, 8852-8859.
4. Morse, D.C. Viscoelasticity of Concentrated Isotropic Solutions of Semiflexible Polymers. 1. Model and Stress Tensor. *Macromolecules* **1998**, *31*, 7030–7043.
5. Morse, D.C. Viscoelasticity of Concentrated Isotropic Solutions of Semiflexible Polymers. 2. Linear Response. *Macromolecules* **1998**, *31*, 7044–7067.
6. Tassieri, M. Dynamics of Semiflexible Polymer Solutions in the Tightly Entangled Concentration Regime. *Macromolecules* **2017**, *50*, 5611–5618.
7. Smilgies, D.-M.; Folta-Stogniew, E. Molecular Weight-Gyration Radius Relation of Globular Proteins: A Comparison of Light Scattering, Small-Angle X-Ray Scattering, and Structure-Based Data. *J. Appl. Cryst.* **2015**, *48*, 1604-1606.
8. Hopkins, J. B.; Thorne, R. E. Quantifying Radiation Damage in Biomolecular Small-Angle X-Ray Scattering. *J. Appl. Cryst.* **2016**, *49*, 880-890.
9. Wang, X.; Guerrand, L.; Wu, B.; Li, X.; Bolden, L.; Chen, W.-R.; Liu, L. Characterization of Polyamidoamine Dendrimers with Scattering Techniques. *Polymers* **2012**, *4*, 600-616.
10. Yoo, H.-S.; Hirao, A. Precise Synthesis of Dendrimer-Like Star-Branched Polymers, a New Class of Well-Defined Hyperbranched Polymers. in Complex Macromolecular Architectures. Eds. Hadjichristidis, N.; Hirao, A.; Tezuka, Y.; Du Prez, P. Wiley (Asia), 2011, pp 133-168.

11. Garcia de la Torre, J.; Hernandez Cifre, J. G. Hydrodynamic Properties of Biomacromolecules and Macromolecular Complexes: Concepts and Methods. A Tutorial Mini-Review. *J. Mol. Biol.* **2020**, *432*, 2930-2948.
12. Di Carluccio, C.; Concetta Forgione, M.; Martini, S.; Berti, F.; Molinaro, A.; Marchetti, R.; Silipo, A. Investigation of Protein-Ligand Complexes by Ligand-Based NMR Methods. *Carbohydr. Res.* **2021**, *503*, 108313.
13. Lameiras, P.; Nuzillard, J.-M. Tailoring the Nuclear Overhauser Effect for the Study of Small and Medium-Sized Molecules by Solvent Viscosity Manipulations. *Prog. Nucl. Magn. Reson. Spectrosc.* **2021**, *123*, 1-50.
14. Little, H.; Patel, S.; Duhamel, J. Probing the Inner Local Density of Complex Macromolecules by Pyrene Excimer Formation. *Phys. Chem. Chem. Phys.* **2023**, *25*, 26515-26525.
15. Patel, S.; Duhamel, J. Advantages of Pyrene Excimer Formation (PEF) over Fluorescence Resonance Energy Transfer (FRET) for Probing the Conformation of Macromolecules in Solution. *Macromolecules* **2024***, 57*, 8421-8431.
16. Little, H.; Thoma, J.; Yeung, R.; D'Sa, A.; Duhamel, J. Persistence Length and Encounter Frequency Determination from Fluorescence Studies of Pyrene-Labeled Poly(oligo(ethylene glycol) methyl ether methacrylate)s. *Macromolecules* **2023**, *56*, 3562-3573.
17. Thoma, J.; Little, H.; Duhamel, J.; Zhang, L.; Leung, T. Persistence Length of PEGMA Bottle Brushes Determined by Pyrene Excimer Fluorescence. *Polymers* **2023**, *15*, 3958.
18. Lulic, K.; Muller, G.; Gutierrez, R.; Little, H.; Duhamel, J. Flexibility of Poly(alkyl methacrylate)s Characterized by their Persistence Length Determined Through Pyrene Excimer Formation. *Polymers* **2024**, *16*, 2126.

19. Thoma, J. L.; Duhamel, J. Characterization of the Local Volume Probed by the Side Chain Ends of Poly(oligo(ethylene glycol) 1-Pyrenemethyl ether methacrylate) Bottle Brushes in Solution Using Pyrene Excimer Fluorescence. *Macromolecules* **2021**, *54*, 9341-9350.
20. Patel, S.; Duhamel, J. Macromolecular Conformation of Low Generation PAMAM Dendrimers Probed by Pyrene Excimer Formation. *Macromolecules* **2023**, *56*, 4012-4021.
21. Patel, S.; McNelles, S.; Adronov, A.; Duhamel, J. Intra-Macromolecular Conformational Changes in Low Generation PAMAM Dendrimers Probed by Pyrene Excimer Formation. *J. Phys. Chem. B* **2023**, *127*, 8040-8048.
22. Fox, L. J.; Slastanova, A.; Taylor, N.; Wlodek, M.; Bikondoa, O.; Richardson, R. M.; Briscoe, W. H. Interactions between PAMAM Dendrimers and DOPC Lipid Multilayers: Membrane Thinning and Structural Disorder. *Biochim. Biophys. Acta-Gen. Subj.* **2021**, *1865*, 129542.
23. Zhang, K.; Wang, Y.; Yu, A.; Zhang, Y.; Tang, H.; Zhu, X. X. Cholic Acid-Modified Dendritic Multimolecular Micelles and Enhancement of Anticancer Drug Therapeutic Effect. *Bioconjugate Chem.* **2010**, *21*, 1596-1601.
24. Zhao, Y.; Zeng, Q.; Wu, F.; Li, J.; Pan, Z.; Shen, P.; Yang, L.; Xu, T.; Cai, L.; Guo, L. Novel Naproxen-Peptide-Conjugated Amphiphilic Dendrimer Self-Assembly Micelles for Targeting Drug Delivery to Osteosarcoma Cells. *RSC Adv.* **2016**, *6*, 60327-60335.
25. Matai, I.; Gopinath, P. Hydrophobic Myristic Acid Modified PAMAM Dendrimers Augment the Delivery of Tamoxifen to Breast Cancer Cells. *RSC Adv.* **2016**, *6*, 24808-24819.
26. Denora, N.; Laquintana, V.; Lopalco, A.; Lacobazzi, R. M.; Lopedota, A.; Cutrignelli, A.; Lacobellis, G.; Annese, C.; Cascione, M.; Leporatti, S., et al. *In Vitro* Targeting and Imaging the Translocator Protein TSPO 18-kDa through G(4)-PAMAM-FITC Labeled Dendrimer. *J. Control. Release* **2013**, *172*, 1111-1125.

27. Carloni, R.; Ottaviani, M. F.; Ficker, M.; Christensen J. B. Interactions of Functionalized PAMAM Dendrimers with Model Cell Membranes Studied via Spin-Labelling Technique. *J. Phys. Chem. B* **2022**, *126*, 9686-9694.

28. He, X.; Lin, M.; Lu, T.; Qu, Z.; Xu, F. Molecular Analysis of Interactions between a PAMAM Dendrimer-Paclitaxel Conjugate and a Biomembrane. *Phys. Chem. Chem. Phys.* **2015**, *17*, 29507-29517.

29. Siriwardena, T. N.; Stach, M.; He, R.; Gan, B.-H.; Javor, S.; Heitz, M.; Ma, L.; Cai, X.; Chen, P.; Wei, D., et al. Lipidated Peptide Dendrimers Killing Multidrug-Resistant Bacteria. *J. Am. Chem. Soc.* **2018**, *140*, 423-432.

30. Pearson, R. M.; Patra, N.; Hsu, H.-J.; Uddin, S.; Kral, P.; Hong, S. Positively Charged Dendron Micelles Display Negligible Cellular Interactions. *ACS Macro Lett.* **2013**, *2*, 77-81.

31. Zhou, L.; Li, J.; Yu, B.; Zhang, J.; Hu, H.; Cong. H.; Shen, Y. The Drug Loading Behavior of PAMAM Dendrimer: Insights from Experimental and Simulation Study. *Sci. China Technol. Sci.* **2023**, *66*, 1129-1140.

32. Jafari, M.; Mehrnejad, F.; Talandashti, R.; Doustdar, F.; Vakili, M. R.; Lavasanifar, A. Effect of the Lipid Composition and Cholesterol on the Membrane Selectivity of Low Generation PAMAM Dendrimers: A Molecular Dynamics Simulation Study. *Appl. Surf. Sci.* **2021**, *540*, 148274.

33. Kelly, C. V.; Leroueil, P. R.; Orr, B. G.; Banaszak Holl, M. M.; Andricioaei, I. Poly(amidoamine) Dendrimers on Lipid Bilayers II: Effects of Bilayer Phase and Dendrimer Termination. *J. Phys. Chem. B* **2008**, *112*, 9346-9353.

34. Bales, B. L.; Almgren, M. Fluorescence Quenching of Pyrene by Copper (II) in Sodium Dodecyl Sulfate Micelles. Effect of Micelle Size as Controlled by Surfactant Concentration. *J. Phys. Chem.* **1995**, *99*, 15153-15162.

35. Yan, H.; Cui, P.; Liu, C.-B.; Yuan, S.-L. Molecular Dynamics Simulations of Pyrene Solubilized in a Sodium Dodecyl Sulfate Micelle. *Langmuir* **2012**, *28*, 4931-4938.

36. Yang, X.; Lu, G.; She, B.; Liang, X.; Yin, R.; Guo, C.; Yi, X.; Dang, X. Cosolubilization of 4,4'-Dibromodiphenyl Ether, Naphthalene, and Pyrene Mixtures in Various Surfactant Micelles. *Chem. Eng. J.* **2015**, *260*, 74-82.

37. Lebedeva, N.; Ranganathan, R.; Bales, B. L. Location of Spectroscopic Probes in Self-Aggregating Assemblies. II. The Location of Pyrene and Other Probes in Sodium Dodecyl Sulfate Micelles. *J. Phys. Chem. B* **2007**, *111*, 5781-5793.

38. Liang, X.; Marchi, M.; Guo, C.; Dang, Z.; Abel, S. Atomistic Simulation of Solubilization of Polycylic Aromatic Hydrocarbons in a Sodium Dodecyl Sulfate Micelle. *Langmuir* **2016**, *32*, 3645-3654.

39. Torres-Luna, C.; Fan, X.; Domszy, R.; Hu, N.; Wang, N. S.; Yang, A. Hydrogel-Based Ocular Drug Delivery Systems for Hydrophobic Drugs. *Eur. J. Pharm. Sci.* **2020**, *154*, 105503.

40. Maji, I.; Mahajan, S.; Sriram, A.; Medtiya, P.; Vasave, R.; Khatri, D. K.; Kumar, R.; Singh, S. B.; Madan, J.; Singh, P. K. Solid Self-Emuslifying Drug Delivery System: Superior Mode for Oral Delivery of Hydrophobic Cargos. *J. Control. Release* **2021**, *337*, 646-660.

41. Xu, L.; Wang, X.; Liu, Y. ; Yang, G.; Falconer, R. J.; Zhao, C.-X. Lipid Nanoparticles for Drug Delivery. *Adv. NanoBiomed. Res.* **2022**, *2*, 2100109.

42. Press, W.H.; Flanery, B.P.; Tenkolsky, S.A.; Vetterling, W.T. *Numerical Recipes in Fortran: The Art of Scientific Computing*; Cambridge University Press: New York, NY, USA, 1992; pp. 523−528.

43. Siu, H.; Duhamel, J. Comparison of the Association Level of a Hydrophobically Modified Associative Polymer Obtained from an Analysis Based on Two Different Models. *J. Phys. Chem. B* **2005**, *109*, 1770-1780.

44. Duhamel, J. New Insights in the Study of Pyrene Excimer Fluorescence to Characterize Macromolecules and their Supramolecular Assemblies in Solution. *Langmuir* **2012**, *28*, 6527-6538.

45. Costa, T.; Seixas de Melo, J.; Burrows, H. D. Fluorescence Behavior of a Pyrene End-Capped Poly(ethylene oxide) in Organic Solvents and in Dioxane – Water Mixtures. *J. Phys. Chem. B* **2009**, *113*, 618-626.

46. Winnik, F. M. Photophysics of Preassociated Pyrenes in Aqueous Polymer Solutions and in Other Organized Media. *Chem. Rev.* **1993**, *93*, 587-614.

47. Fowler, M.; Hisko, V.; Henderson, J.; Casier, R.; Li, L.; Thoma, J.; Duhamel, J. DiPyMe in SDS Micelles – Artefacts and their Implications on Micellar Properties. *Langmuir* **2015**, *31*, 11971-11981.

48. Shah, S. K.; Chatterjee, S. K.; Bhattarai, A. The Effect of Methanol on the Micellar Properties of Dodecyltrimethylammonium Bromide (DTAB) in Aqueous Medium at Different Temperatures. *J. Surface Deterg.* **2016**, *19*, 201-207.

49. Kim, D.; Amos, R. C.; Gauthier, M.; Duhamel, J. Assemblies of Hydrophobically Modified Starch Nanoparticles Probed by Surface Tension and Pyrene Fluorescence. *ACS Symposium Series-Molecular Assemblies: Characterization and Applications.* Ed. Nagarajan, R. 2020, Chapter 5, pp 61-75.

50. Pisarcik, M.; Devinsky, F.; Pupak, M. Determination of Micelle Aggregation Numbers of Alkyltrimethylammonium Bromide and Sodium Dodecyl Sulfate Surfactants Using Time-Resolved Fluorescence Quenching. *Open Chem.* **2015**, *13*, 922-931.

51. Yip, J.; Duhamel, J.; Bahun, G.; Adronov, A. A Study of the Branch Ends of a Series of Pyrene-Labeled Dendrimers Based on Pyrene Excimer Formation. *J. Phys. Chem. B* **2010**, *114*, 10254-10265.

52. Chen, S.; Duhamel, J.; Bahun, G.; Adronov, A. Effect of Fluorescent Impurities in the Study of Pyrene-Labeled Macromolecules by Fluorescence. *J. Phys. Chem. B* **2011**, *115*, 9921-9929.

53. Farhangi, S.; Casier, R.; Li, L.; Thoma, J.; Duhamel, J. Characterization of the Long Range Internal Dynamics of Pyrene-Labeled Macromolecules by Pyrene Excimer Fluorescence. *Macromolecules* **2016**, *49*, 9597-9604.

54. Fowler, M. A.; Duhamel, J.; Bahun, G. J.; Adronov, A.; Zaragoza-Galán, G.; Rivera, E. Studying Pyrene-Labeled Macromolecules with the Model Free Analysis. *J. Phys. Chem. B* **2012**, *116*, 14689-14699.

55. Kalyanasundaram, K.; Thomas, J. K. Environmental Effects on Vibronic Band Intensities in Pyrene Monomer Fluorescence and their Application in Studies of Micellar Systems. *J. Am. Chem. Soc.* **1977**, *99*, 2039-2044.

56. Dong, D. C.; Winnik, M. A. The Py Scale of Solvent Polarities. Solvent Effects on the Virbonic Fine Structure of Pyrene Fluorescence and Empirical Correlations with *E*T and *Y* Values. *Photochem. Photobiol.* **1982**, *35*, 17-21.

57. Dong, D. C.; Winnik, M. A. The Py Scale of Solvent Polarities. *Can. J. Chem.***1984**, *62*, 2560-2565.

58. Farhangi, S.; Duhamel, J. A Pyrenyl Derivative with a Four Atom-Linker that Can Probe the Local Polarity of Pyrene-Labeled Macromolecules. *J. Phys. Chem. B* **2016**, *120*, 834-842.

59. Ba Salem, A.; Duhamel, J. Synthesis and Characterization of a Pyrene-Labeled Gemini Surfactant Sensitive to the Polarity of its Environment. *Langmuir* **2021**, *37*, 13824-13837.

60. McNelles, S.; Thoma, J.; Adronov, A.; Duhamel, J. Quantitative Characterization of the Molecular Dimensions of Flexible Dendritic Macromolecules by Pyrene Excimer Fluorescence. *Macromolecules* **2018**, *51*, 1586-1590.

61. Thoma, J.; McNelles, S. A.; Adronov, A.; Duhamel, J. Direct Measure of the Local Concentration of Pyrenyl Groups in Pyrene-Labeled Dendrons Derived from the Rate of Fluorescence Collisional Quenching. *Polymers* **2020**, *12*, 2919.

62. Rumble, J.R. Viscosity of Liquids. In *CRC Handbook of Chemistry and Physics*, 101st ed.; (Electronic ed.); CRC Press: Boca Raton, FL, USA; Taylor & Francis: Abingdon, UK, 1978; pp. 239–242.

63. Lakowicz, J. R. Principles of Fluorescence Spectroscopy, 3rd Ed. Springer: Singapore, 2006, p 278.

64. Almgren, M.; Swarup, S. Size of Sodium Dodecyl Sulfate Micelles in the Presence of Additives: 2. Aromatic and Saturated Hydrocarbons. *J. Phys. Chem.* **1982**, *86*, 4212-4216.

65. Wasylishen, R. E.; Kwak, J. C. T.; Gao, Z.; Verpoorte, E.; Macdonald, J. B.; Dickson, R. M. NMR Studies of Hydrocarbons Solubilized in Aqueous Micellar Solutions. *Can. J. Chem.* **1991**, *69*, 822-833.

66. Malliaris, A.; Le Moigne, J.; Sturm, J.; Zana, R. Temperature Dependence of the Micelle Aggregation Number and Rate of Intramicellar Excimer Formation in Aqueous Surfactant Solutions. *J. Phys. Chem.***1985**, *89*, 2709-2713.

67. Almgren, M.; Bedhage, B.; Mukhtar, E. Fluorescence Study of the Weak Interaction Between Pyrene and Quaternary Ammonium Groups. *J. Photochem. Photobiol. A* **1991**, *59*, 323-334.

68. Xing, H.; Yan, P.; Xiao, J.-X. Unusual Location of the Pyrene Probe Solubilized in Micellar Solutions of Tetraalkylammonium Perfluorooctanoates. *Soft Matter* **2013**, *9*, 1164-1171.

69. Berkeley Kauffman, W.; Fuselier, T.; He, J.; Wimley, W. C. Mechanism Matters: A Taxonomy of Cell Penetrating Peptides. *Trends Biochem. Sci.* **2015**, *40*, 749-764.

70. Jauset, T.; Beaulieu, M.-E. Bioactive Cell Penetrating Peptides and Proteins in Cancer: A Bright Future Ahead. *Curr. Opin. Pharmacol.* **2019**, *47*, 133-140.
71. Ruseska, I.; Zimmer, A. Internalization Mechanisms of Cell-Penetrating Peptides. *Belstein J. Nanotechnol.* **2020**, *11*, 101-123.
72. Zorko, M.; Jones, S.; Langel, U. Cell-Penetrating Peptides in Protein Mimicry and Cancer Therapeutics. *Adv. Drug Deliv. Rev.* **2022**, *180*, 114044.

Chapter 3

1. Assiri, A. A.; Glover, K.; Mishra, D.; Waite, D.; Vora, L. K.; Thakur, R. R. S. Block Copolymer Micelles as Ocular Drug Delivery Systems. *Drug Discov. Today.* **2024,** *29*, 1-21.
2. Beach, M. A.; Nayanathara, U.; Gao, Y.; Zhang, C.; Xiong, Y.; Wang, Y.; Suh, G. K. Polymeric Nanoparticles for Drug Delivery. *Chem. Rev.* **2024**, *124*, 5505-5616.
3. Sinsinbar, G.; Bindra, A. K.; Liu, S.; Chia, T. W.; Eng, E. C. Y.; Loo, S. Y.; Lam, J. H.; Schultheis, K.; Nallani, M. Amphiphilic Block Copolymer Nanostructures as a Tunable Delivery Platform: Perspective and Framework for the Future Drug Product Development. *Biomacromolecules* **2024**, *25*, 541-563.
4. Stevens, C. A.; Kaur, K.; Klok, H.-A. Self-Assembly of Protein-Polymer Conjugates for Drug Delivery. *Adv. Drug Deliv. Rev.* **2021**, *174*, 447-460.
5. Hwang, D.; Ramsey, J. D.; Kabanov, A. V. Polymeric Micelles for the Delivery of Poorly Soluble Drugs: from Nanoformulation to Clinical Approval. *Adv. Drug Deliv. Rev.* **2020**, *156*, 80-118.
6. Yousefi, M.; Narmani, A.; Jafari, S. M. Dendrimers as Efficient Nanocarriers for the Protection and Delivery of Bioactive Phytochemicals. *Adv. Colloid Interface Sci.* **2020**, *278*, 102125.
7. Bordat, A.; Boissenot, T.; Nicolas, J.; Tsapis, N. Thermoresponsive Polymer Nanocarriers for Biomedical Applications. *Adv. Drug Deliv. Rev.* **2019**, *138*, 167-192.
8. Cabral, H.; Miyata, K.; Osada, K.; Kataoka, K. Block Copolymer Micelles in Nanomedicine Applications. *Chem. Rev.* **2018**, *118*, 6844-6892.
9. Gao, C.; Bhattarai, P.; Chen, M.; Zhang, N.; Hameed, S.; Yue, X.; Dai, Z. Amphiphilic Drug Conjugates as Nanomedicines for Combined Cancer Therapy. *Bioconjugate Chem.* **2018**, *29*, 3967-3981.

10. Carloni, R.; Ottaviani, M. F.; Ficker, M.; Christensen, J. B. Interactions of Functionalized PAMAM Dendrimers with Model Cell Membranes Studied via Spin-Labeling Technique. *J. Phys. Chem. B* **2022**, *126*, 9686-9694.
11. Siriwardena, T. N.; Stach, M.; He, R.; Gan, B.-H.; Javor, S.; Heitz, M.; Ma, L.; Cai, X.; Chen, P.; Wei, D., et al. Lipidated Peptide Dendrimers Killing Multidrug-Resistant Bacteria. *J. Am. Chem. Soc.* **2018**, *140*, 423-432.
12. Matai, I.; Gopinath, P. Hydrophobic Myristic Acid Modified PAMAM Dendrimers Augment the Delivery of Tamoxifen to Breast Cancer Cells. *RSC Adv.* **2016**, *6*, 24808-24819.
13. Zhao, Y.; Zheng, Q.; Wu, F.; Li, J.; Pan, Z.; Shen, P.; Yang, L.; Xu, T.; Cai, L.; Guo, L. Novel Naproxen-Peptide-Conjugated Amphiphilic Dendrimer Self-Assembly Micelles for Targeting Drug Delivery to Osteosarcoma Cells. *RSC Adv.* **2016**, *6*, 60327.
14. Zhou, L.; Li, J.; Yu, B.; Zhang, J.; Hu, H.; Cong. H.; Shen, Y. The Drug Loading Behavior of PAMAM Dendrimer: Insights from Experimental and Simulation Study. *Sci. China Technol. Sci.* **2023**, *66*, 1129-1140.
15. Jafari, M.; Mehrnejad, F.; Talandashti, R.; Doustdar, F.; Vakili, M. R.; Lavasanifar, A. Effect of the Lipid Composition and Cholesterol on the Membrane Selectivity of Low Generation PAMAM Dendrimers: A Molecular Dynamics Simulation Study. *Appl. Surf. Sci.* **2021**, *540*, 148274.
16. Fox, L. J.; Slastanova, A.; Taylor, N.; Wlodek, M.; Bikondoa, O.; Richardson, R. M.; Briscoe, W. H. Interactions between PAMAM Dendrimers and DOPC Lipid Multilayers: Membrane Thinning and Structural Disorder. *Biochim. Biophys. Acta-Gen. Subj.* **2021**, *1865*, 129542.

17. He, X. C.; Lin, M.; Lu, T. J.; Qu, Z. G.; Xu, F. Molecular Analysis of Interactions between a PAMAM Dendrimer-Paclitaxel Conjugate and a Biomembrane. *Phys. Chem. Chem. Phys.* **2015**, *17*, 29507.
18. Kelly, C. V.; Leroueil, P. R.; Orr, B. G.; Banaszak Holl, M. M.; Andricioaei, I. Poly(amidoamine) Dendrimers on Lipid Bilayers II: Effects of Bilayer Phase and Dendrimer Termination. *J. Phys. Chem. B* **2008**, *112*, 9346-9353.
19. Poellmann, M. J.; Javius-Jones, K.; Hopkins, C.; Lee, J. W.; Hong, S. Dendritic-Linear Copolymer and Dendron Lipid Nanoparticles for Drug and Gene Delivery. *Bioconjugate Chem.* **2022**, *33*, 2008-2017.
20. Mekuria, S. L.; Ouyang, Z.; Song, C.; Rodrigues, J.; Shen, M.; Shi, X. Dendrimer-Based Nanogels for Cancer Nanomedicine Applications. *Bioconjugate Chem.* **2022**, *33*, 87-96.
21. Baghbanbashi, M.; Kakkar, A. Polymerosomes: Soft Nanoparticles from Miktoarm Stars for Applications in Drug Delivery. *Pharmaceutics* **2022**, *19*, 1687-1703.
22. Pooresmaeil, M.; Javanbakht, S.; Namazi, H.; Shaabani, A. Application or Function of Citric Acid in Drug Delivery Platforms. *Med. Res. Rev.* **2022**, *42*, 800-849.
23. Kavand, A.; Anton, N.; Vandamme, T.; Serra, C. A.; Chan-Seng, D. Synthesis and Functionalization of Hyperbranched Polymers for Targeted Drug Delivery. *J. Control. Release* **2020**, *321*, 285-311.
24. Alsehli, M.; Gauthier, M. Dendritic Polymer Micelles for Drug Delivery. *In Bioinspired Materials Science and Engineering, First Ed.* Eds Yang, G.; Xiao, L.; Lamboni, L. Wiley & Sons, 2018 pp 311-336.
25. Cheng, W.; Wu, D.; Liu, Y. Michael Addition Polymerization of Trifunctional Amine and Acrylic Monomer: A Versatile Platform for Development of Biomaterials. *Biomacromolecules* **2016**, *17*, 3115-3126.

26. Mohammadifar, E.; Kharat, A. N.; Adeli, M. Polyamindoamine and Polyglycerol; their Linear, Dendritic, and Linear-Dendritic Architectures as Anticancer Drug Delivery Systems. *J. Mater. Chem. B* **2015**, *3*, 3896-3921.

27. Verduzco, R.; Li, X.; Pesek, S. L.; Stein, G. E. Structure, Function, Self-Assembly, and Applications of Bottlebrush Copolymers. *Chem. Soc. Rev.* **2015**, *44*, 2405-2420.

28. Müllner, M. Molecular Polymer Bottlebrushes in Nanomedicine: Therapeutic and Diagnostic Applications. *Chem. Commun.* **2022**, *58*, 5683-5716.

29. Zhang, Z.; Li, Z.; Shi, Y.; Chen, Y. Molecular Bottlebrushes as Emerging Nanocarriers: Material Design and Biomedical Applications. *Langmuir* **2024**, *40*, 7286-7299.

30. Daneshmand, S.; Golmohammadzadeh, S.; Jaafari, M. R.; Movaffagh, J.; Rezaee, M.; Sahebkar, A.; Malaekeh-Nikouei, B. Encapsulation Challenges, the Substantial Issue in Solid Lipid Nanoparticles Characterization. *J. Cell. Biochem.* **2018**, *119*, 4251-4264.

31. Chountoulesi, M.; Naziris, N.; Pippa, N.; Demetzos, C. The Significance of Drug-to-Lipid Ratio to the Development of Optimized Liposomal Formulation. *J. Liposome Res.* **2018**, *28*, 249-258.

32. Marques, S. S.; Segundo, M. A. Nanometrics Goes beyond Size: Assessment of Nanoparticle Concentration and Encapsulation Efficiency in Nanocarriers. *TrAC, Trends Anal. Chem.* **2024**, *174*, 117762.

33. Deprey, K.; Becker, L.; Kritzer, J.; Plückthun, A. Trapped! A Critical Evaluation of Methods for Measuring Total Cellular Uptake versus Cytosolic Localization. *Bioconjugate Chem.* **2019**, *30*, 1006-1027.

34. Abourehab, M. A. S.; Ansari, M. J.; Singh, A.; Hassan, A.; Abdelgawad, M. A.; Shrivastav, P.; Abualsoud, B. M.; Amaral, L. S.; Pramanik, S. Cubosomes as an Emerging Platform for Drug Delivery: A Review of the State of the Art. *J. Mat. Chem. B* **2022**, *10*, 2781-2819.

35. Di Carluccio, C.; Forgione, M. C.; Martini, S.; Berti, F.; Molinaro, A.; Marchetti, R.; Silipo, A. Investigation of Protein-Ligand Complexes by Ligand-Base NMR Methods. *Carbohydr. Res.* **2021**, *503*, 108313.

36 Lameiras, P.; Nuzillard, J.-M. Tailoring the Nuclear Overhauser Effect for the Study of Small and Medium-Sized Molecules by Solvent Viscosity Manipulations. *Prog. Nucl. Magn. Reson. Spectrosc.* **2021**, *123*, 1-50.

37. Grigoras, A.-G. Investigation of Cellulose-Based Materials Applied in Life Science Using Laser Light Scattering Methods. *Polymers* **2024**, *16*, 1170.

38. Smilgies, D.-M.; Folta-Stogniew, E. Molecular Weight-Gyration Radius Relation of Globular Proteins: A Comparison of Light Scattering, Small Angle X-Ray Scattering, and Structure-Based Data. *J. Appl. Crystallogr.* **2015**, *48*, 1604-1606.

39. Wang, X.; Guerrand, L.; Wu, B.; Li, X.; Boldon, L.; Chen, W.-R.; Liu, L. Characterizations of Polyamidoamine Dendrimers with Scattering Techniques. *Polymers* **2012**, *4*, 600-616.

40. Almgren, M.; Swarup, S. Size of Sodium Dodecyl Sulfate Micelles in the Presence of Additives. 2. Aromatic and Saturated Hydrocarbons. *J. Phys. Chem.* **1982**, *86*, 4212-4216.

41. Fowler, M.; Hisko, V.; Henderson, J.; Casier, R.; Li, L.; Thoma, J. L.; Duhamel, J. DiPyMe in SDS Micelles: Artifacts and their Implications in the Interpretation of Micellar Properties. *Langmuir* **2015**, *31*, 11971-11981.

42. Ding, Y.; Fujimoto, L. M.; Yao, Y.; Plano, G. V.; Marassi, F. M. Influence of the Lipid Membrane Environment on Structure and Activity of the Outer Membrane Protein Ail from *Yersinia Pestis*. *Biochim. Biophys. Acta* **2015**, *1848*, 712-720.

43. Ahlawat, S.; Mote, K. R.; Lakomek, N.-A.; Agarwal, V. Solid-State NMR: Methods for Biological Solids. *Chem. Rev.* **2022**, *122*, 9643-9737.

44. Breyton, C.; Gabel, F.; Lethier, M.; Flayhan, A.; Durand, G.; Jault J.-M.; Juillan-Binard, C.; Imbert, L.; Moulin, M.; Ravaud, S.; Hartlein, M.; Ebel, C. Small Angle Neutron Scattering for the Study of Solubilized Membrane Proteins. *Eur. Phys. J. E.* **2013**, *36*, 71.
45. Krueger, S. Small-Angle Neutron Scattering Contrast Variation Studies of Biological Complexes: Challenges and Triumphs. *Curr. Opin. Struct. Biol.* **2022**, *74*, 102375.
46. Little, H.; Patel, S.; Duhamel, J. Probing the Inner Local Density of Complex Macromolecules by Pyrene Excimer Formation. *Phys. Chem. Chem. Phys.* **2023**, *25*, 26515-26525.
47. McNelles, S.; Thoma, J.; Adronov, A.; Duhamel, J. Quantitative Characterization of the Molecular Dimensions of Flexible Dendritic Macromolecules by Pyrene Excimer Fluorescence. *Macromolecules* **2018**, *51*, 1586-1590.
48. Thoma, J.; McNelles, S. A.; Adronov, A.; Duhamel, J. Direct Measure of the Local Concentration of Pyrenyl Groups in Pyrene-Labeled Dendrons Derived from the Rate of Fluorescence Collisional Quenching. *Polymers* **2020**, *12*, 2919.
49. Thoma, J. L.; Duhamel, J. Characterization of the Local Volume Probed by the Side Chain Ends of Poly(oligo(ethylene glycol) 1-Pyrenemethyl ether methacrylate) Bottle Brushes in Solution Using Pyrene Excimer Fluorescence. *Macromolecules* **2021**, *54*, 9341-9350.
50. Patel, S.; Duhamel, J. Macromolecular Conformation of Low Generation PAMAM Dendrimers Probed by Pyrene Excimer Formation. *Macromolecules* **2023**, *56*, 4012-4021.
51. Patel, S.; McNelles, S.; Adronov, A.; Duhamel, J. Intra-Macromolecular Conformational Changes in Low Generation PAMAM Dendrimers Probed by Pyrene Excimer Formation. *J. Phys. Chem. B* **2023**, *127*, 8040-8048.
52. Liu, D.; Patel, S.; Xie, Y.; Zhang, H.; Duhamel, J. Probing Macromolecular Conformation in Restricted Geometry by PEF: Application to Hydrophobically Modified PAMAM Dendrimers Isolated Inside Surfactant Micelles. *J. Phys. Chem. B* **2025**, *129*, 1144-1153.

53. Kim, D.; Amos, R. C.; Gauthier, M.; Duhamel, J. Assemblies of Hydrophobically Modified Starch Nanoparticles Probed by Surface Tension and Pyrene Fluorescence. *ACS Symposium Series-Molecular Assemblies: Characterization and Applications.* Ed. Nagarajan, R. 2020, Chapter 5, pp 61-75.

54. Caminati, G.; Turro, N. J.; Tomalia, D. A. Photophysical Investigation of Starburst Dendrimers and their Interactions with Anionic and Cationic Surfactants. *J. Am. Chem. Soc.* **1990**, *112*, 8515.

55. Esumi, K.; Kuwabara, K.; Chiba, T.; Kobayashi, F.; Mizutani, H.; Torigoe, K. *Colloids Surf. A: Physicochem. Eng. Asp.* **2002**, *197*, 141-146.

56. Bakshi, M. S.; Kaura, A. Fluorescence Studies of Interactions of Ionic Surfactants with Poly(amidoamine) Dendrimers. *J. Colloid Interface Sci.* **2005**, *284*, 680-686.

57. Herrington, K. L.; Kaler, E. W.; Miller, D. D.; Zasadzinski, J. A.; Chiruvolu, S. Phase Behavior of Aqueous Mixtures of Dodecytrimethylammonium Bromide (DTAB) and Sodium Dodecyl Sulfate (SDS). *J. Phys. Chem.* **1993**, *97*, 13792-13802.

58. Bergström M.; Pedersen J. S. Formation of Tablet-Shaped and Ribbonlike Micelles in Mixtures of an Anionic and a Cationic Surfactant. *Langmuir* **1999**, 15, 2250–2253.

59. Israelachvili, J. N.; Mitchell, D. J.; Ninham, B. W. Theory of Self-Assembly of Hydrocarbon Amphiphiles into Micelles and Bilayers. *J. Chem. Soc., Faraday Trans. 2* **1976**, *72*, 1525-1568.

60. Ba Salem, A.; Gong, R.; Duhamel, J. Characterization of the Interactions between Unassociated Cationic Pyrene-Labeled Gemini Surfactant and Anionic Sodium Dodecyl Sulfate. *Langmuir* **2022**, *38*, 7484-7495.

61. Duhamel, J. New Insights in the Study of Pyrene Excimer Fluorescence to Characterize Macromolecules and their Supramolecular Assemblies in Solution. *Langmuir* **2012**, *28*, 6527-6538.

62. Press, W.H.; Flanery, B.P.; Tenkolsky, S.A.; Vetterling, W.T. *Numerical Recipes in Fortran: The Art of Scientific Computing*; Cambridge University Press: New York, NY, USA, 1992; pp. 523−528.

63. Volume of an SDS micelle calculated by assuming a spherical shape with N_{agg} = 71, and the respective volume of a methylene, methyl and sulfate groups equals V_{CH2} = 28 Å^3,[40] V_{CH3} = 49 Å^3,[40] and V_{SO4} = 58 Å^3, where the sulfate ion in aqueous solution is a sphere of radius equal to 2.4 Å.[70]

64. Tadros, T. *Encyclopedia of Colloid and Interface Science;* Springer, Berlin, Heidelberg, 2013, pp 107, 563.

65. Yip, J.; Duhamel, J.; Bahun, G.; Adronov, A. A Study of the Branch Ends of a Series of Pyrene-Labeled Dendrimers Based on Pyrene Excimer Formation. *J. Phys. Chem. B* **2010**, *114*, 10254-10265.

66. Effect of Fluorescent Impurities in the Study of Pyrene-Labeled Macromolecules by Fluorescence. Chen, S.; Duhamel, J.; Bahun, G.; Adronov, A. *J. Phys. Chem. B* **2011**, *115*, 9921-9929.

67. Fowler, M. A.; Duhamel, J.; Bahun, G. J.; Adronov, A.; Zaragoza-Galán, G.; Rivera, E. Studying Pyrene-Labeled Macromolecules with the Model Free Analysis. *J. Phys. Chem. B* **2012**, *116*, 14689-14699.

68. Rumble, J. R. Viscosity of Liquids. In *CRC Handbook of Chemistry and Physics*, 101st ed.; (Electronic ed.). CRC Press: Taylor & Francis. 1978; p 239-242.

69. Pisárčik, M.; Devínsky, F.; Pupák, M. Determination of Micelle Aggregation Numbers of AlkylTrimethylammonium Bromide and Sodium Dodecyl Sulfate Surfactants Using Time-Resolved Fluorescence Quenching. *Open Chem.* **2015**, *13*, 922-931.

70. Marcus, Y. Ionic Radii in Aqueous Solutions. *Chem. Rev.* **1988**, *88*, 1475-1498.

Chapter 4

1. Meyer, D. Surfactant Science and Technology, 4th Ed. Wiley, Hoboken, NJ, 2020.
2. Kronberg, B.; Holmberg, K.; Lindman, B. Surface Chemistry of Surfactants and Polymers. Wiley, Chichester, WS, 2014.
3. Turro, N. J.; Yekta, A. Luminescent Probes for Detergent Solutions. A Simple Procedure for Determination of the Mean Aggregation Number of Micelles. *J. Am. Chem. Soc.* **1978**, *100*, 5951-5952.
4. Lianos, P.; Zana, R. Use of Pyrene Excimer Formation to Study the Effect of NaCl on the Structure of Sodium Dodecyl Sulfate Micelles. *J. Phys. Chem.* **1980**, *84*, 3339-3341.
5. Cabane, B.; Duplessix, R.; Zemb, T. High Resolution Neutron Scattering on Ionic Surfactant Micelles: SDS in Water. *J. Phys.* **1985**, *46*, 2161-2178.
6. Bergström, M.; Pedersen, J. S. Structure of Pure SDS and DTAB Micelles Determined by Small-Angle Neutron Scattering (SANS). *Phys. Chem. Chem. Phys.* **1999**, *1*, 4437-4446.
7. Ranganathan, R.; Peric, M.; Medina, R.; Garcia, U.; Bales, B. L.; Almgren, M. Size, Hydration, and Shape of SDS/Heptane Micelles Investigated by Time-Resolved Fluorescence Quenching and Electron Spin Resonance. *Langmuir* **2001**, *17*, 6765-6770.
8. Fowler, M.; Hisko, V.; Henderson, J.; Casier, R.; Li, L.; Thoma, J.; Duhamel, J. DiPyMe in SDS Micelles – Artefacts and their Implications on Micellar Properties. *Langmuir* **2015**, *31*, 11971-11981.
9. Herrington, K. L.; Kaler, E. W.; Miller, D. D.; Zasadzinski, J. A.; Chiruvolu, S. Phase Behavior of Aqueous Mixtures of Dodecyltrimethylammonium Bromide (DTAB) and Sodium Dodecyl Sulfate (SDS). *J. Phys. Chem.* **1993**, *97*, 13792-13802.
10. Bergström, M.; Pedersen, J. S. A Small Angle Neutron Scattering (SANS) Study of Tablet-Shaped and Ribbonlike Micelles Formed from Mixtures of an Anionic and a Cationic Surfactant. *J. Phys. Chem. B* **1999**, *103*, 8502-8513.

11. Prévost, S.; Gradzielski, M. SANS Investigation of the Microstructures in Catanionic Mixtures of SDS/DTAC and the Effect of Various Salts. *J. Colloid Interface Sci.* **2009**, *337*, 472-484.
12. Krauss, I. R.; Imperatore, R.; De Santis, A.; Luchini, A.; Paduano, L.; D'Errico, G. Structure and Dynamics of Cetyltrimethylammonium Chloride-Sodium Dodecyl Sulfate (CTAC-SDS) Catanionic Vesicles: High-Value Nano-Vehicles from Low-Cost Surfactants. *J. Colloid Interface Sci.* **2017**, *501*, 112-122.
13. Israelachvili, J. N.; Mitchell, D. J.; Ninham, B. W. Theory of Self-Assembly of Hydrocarbon Amphiphiles into Micelles and Bilayers. *J. Chem. Soc., Faraday Trans. 2* **1976**, *72*, 1525-1568.
14. Liu, D.; Patel, J.; Xie, Y.; Zhang, H.; Duhamel, J. Probing Macromolecular Conformations in Restricted Geometries: Application to Hydrophobically Modified PAMAM Dendrimers Isolated in Surfactant Micelles. *J. Phys. Chem. B* **2025**, *129*, 1144-1153.
15. Liu, D.; Patel, J.; Duhamel, J. Conformation of Pyrene End-Labeled Polyamidoamine Dendrimers in Catanionic Surfactant Micelles Probed by Pyrene Excimer Formation. *Langmuir* **2025**, *41*, 20986-20998.
16. Kim, D.; Amos, R. C.; Gauthier, M.; Duhamel, J. Assemblies of Hydrophobically Modified Starch Nanoparticles Probed by Surface Tension and Pyrene Fluorescence. *ACS Symposium Series-Molecular Assemblies: Characterization and Applications.* Ed. Nagarajan, R. 2020, Chapter 5, pp 61-75.
17. Carloni, R.; Ottaviani, M. F.; Ficker, M.; Christensen J. B. Interactions of Functionalized PAMAM Dendrimers with Model Cell Membranes Studied via Spin-Labelling Technique. *J. Phys. Chem. B* **2022**, *126*, 9686-9694.
18. Jafari, M.; Mehrnejad, F.; Talandashti, R.; Doustdar, F.; Vakili, M. R.; Lavasanifar, A. Effect of the Lipid Composition and Cholesterol on the Membrane Selectivity of Low

Generation PAMAM Dendrimers: A Molecular Dynamics Simulation Study. *Appl. Surf. Sci.* **2021**, *540*, 148274.

19. Kelly, C. V.; Leroueil, P. R.; Orr, B. G.; Banaszak Holl, M. M.; Andricioaei, I. Poly(amidoamine) Dendrimers on Lipid Bilayers II: Effects of Bilayer Phase and Dendrimer Termination. *J. Phys. Chem. B* **2008**, *112*, 9346-9353.
20. Bales, B. L.; Almgren, M. Fluorescence Quenching of Pyrene by Copper (II) in Sodium Dodecyl Sulfate Micelles. Effect of Micelle Size as Controlled by Surfactant Concentration. *J. Phys. Chem.* **1995**, *99*, 15153-15162.
21. Yan, H.; Cui, P.; Liu, C.-B.; Yuan, S.-L. Molecular Dynamics Simulations of Pyrene Solubilized in a Sodium Dodecyl Sulfate Micelle. *Langmuir* **2012**, *28*, 4931-4938.
22. Yang, X.; Lu, G.; She, B.; Liang, X.; Yin, R.; Guo, C.; Yi, X.; Dang, X. Cosolubilization of 4,4'-Dibromodiphenyl Ether, Naphthalene, and Pyrene Mixtures in Various Surfactant Micelles. *Chem. Eng. J.* **2015**, *260*, 74-82.
23. Lebedeva, N.; Ranganathan, R.; Bales, B. L. Location of Spectroscopic Probes in Self-Aggregating Assemblies. II. The Location of Pyrene and Other Probes in Sodium Dodecyl Sulfate Micelles. *J. Phys. Chem. B* **2007**, *111*, 5781-5793.
24. Liang, X.; Marchi, M.; Guo, C.; Dang, Z.; Abel, S. Atomistic Simulation of Solubilization of Polycylic Aromatic Hydrocarbons in a Sodium Dodecyl Sulfate Micelle. *Langmuir* **2016**, *32*, 3645-3654.
25. Little, H.; Patel, S.; Duhamel, J. Probing the Inner Local Density of Complex Macromolecules by Pyrene Excimer Formation. *Phys. Chem. Chem. Phys.* **2023**, *25*, 26515-26525.
26. Correira, E. L.; Brown, N.; Ervin, A.; Papavassiliou, D. V.; Razavi, S. Contamination in Sodium Dodecyl Sulfate Solutions: Insight from the Measurements of Surface Tension and Surface Rheology. *Langmuir* **2022**, *38*, 7179-7189.

27. Salomon, G.; Giordano-Labadie, F. Surfactant Irritations and Allergies. *Eur. J. Dermatol.* **2022**, *32*, 677-681.
28. Otzen, D. E.; Pedersen, J. N.; Rasmussen, H. O.; Pedersen, J. S. How Do Surfactants Unfold and Refold Proteins? *Adv. Colloid Interface Sci.* **2022**, *308*, 102754.
29. Ghosh, S.; Ray, A.; Pramanik, N. Self-Assembly of Surfactants: An Overview on General Aspects of Amphiphiles. *Biophys. Chem.* **2020**, *265*, 106429.
30. Waghule, T.; Saha, R. N.; Alexander, A.; Singhvi, G. Tailoring the Multifunctional Properties of Phospholipids for Simple to Complex Self-Assemblies. *J. Control. Release* **2022**, *349*, 460-474.
31. Dufourc, E. J. Bicelles and Nanodiscs for Biophysical Chemistry. *Biochim. Biophys. Acta-Biomembr.* **2021**, *1863*, 183478.
32. Rharbi, Y.; Winnik, M. A. Solute Exchange Between Surfactant Micelles by Micelle Fragmentation and Fusion. *Adv. Colloid Interface Sci.* **2001**, *89-90*, 25-46.
33. Sammalkorpi, M.; Karttunen, M.; Haataja, M. Micelle Fission through Surface Instability and Formation of Interdigitating Stalk. *J. Am. Chem. Soc.* **2008**, *130*, 17977-17980.
34. Kahana, A.; Lancet, D.; Palmai, Z. Micellar Composition Affects Lipid Accretion Kinetics in Molecular Dynamics Simulations: Support for Lipid Network Reproduction. *Life*, **2022**, *12*, 955
35. Winnik, F. M.; Regismond, S. T. A. Fluorescence Methods in the Study of the Interactions of Surfactants with Polymers. *Colloid Surf. A: Physicochem. Eng. Asp.* **1996**, *118*, 1-39.
36. Mabrouk, M. M.; Hamed, N. A.; Mansour, F. R. Spectroscopic Methods for Determination of Critical Micelle Concentrations of Surfactants; a Comprehensive Review. *Appl. Spec. Rev.* **2023**, *58*, 206-234.
37. Roy, T.; Padhi, S. A Meticulous Focus on the Determination of Critical Micelle Concentration Employing Fluorescence Spectroscopy. *J. Fluoresc.* **2025**, *in press*.

38. Caminati, G.; Turro, N. J.; Tomalia, D. A. Photophysical Investigation of Starburst Dendrimers and their Interactions with Anionic and Cationic Surfactants. *J. Am. Chem. Soc.* **1990**, *112*, 8515.

39. Esumi, K.; Kuwabara, K.; Chiba, T.; Kobayashi, F.; Mizutani, H.; Torigoe, K. *Colloids Surf. A: Physicochem. Eng. Asp.* **2002**, *197*, 141-146.

40. Bakshi, M. S.; Kaura, A. Fluorescence Studies of Interactions of Ionic Surfactants with Poly(amidoamine) Dendrimers. *J. Colloid Interface Sci.* **2005**, *284*, 680-686.

41. Patel, S.; Duhamel, J. Macromolecular Conformation of Low Generation PAMAM Dendrimers Probed by Pyrene Excimer Formation. *Macromolecules* **2023**, *56*, 4012-4021.

42. Cuniberti, C.; Perico, A. Intramolecular Excimer Formation in Polymers. *Eur. Polym. J.* **1980**, *16*, 887-893.

43. McNelles, S.; Thoma, J.; Adronov, A.; Duhamel, J. Quantitative Characterization of the Molecular Dimensions of Flexible Dendritic Macromolecules by Pyrene Excimer Fluorescence. *Macromolecules* **2018**, *51*, 1586-1590.

44. Thoma, J.; McNelles, S. A.; Adronov, A.; Duhamel, J. Direct Measure of the Local Concentration of Pyrenyl Groups in Pyrene-Labeled Dendrons Derived from the Rate of Fluorescence Collisional Quenching. *Polymers* **2020**, *12*, 2919.

Chapter 5

1. Cho, H.; Lai, T.C.; Tomoda, K. *et al.* Polymeric Micelles for Multi-Drug Delivery in Cancer. *AAPS PharmSciTech.* **2015**, *16*, 10–20.
2. Malaiya, A.; Jain, D.; Yadav, A, K. Nanoparticles and pancreas cancer. *Nano Drug Delivery Strategies for the Treatment of Cancers*; Yadav, A. K.; Gupta, U.; Sharma, R., Eds.; Academic Print Elsevier, 2021, pp145–164.
3. Salomon, G.; Giordano-Labadie, F. Surfactant Irritations and Allergies. *Eur. J. Dermatol.* **2022**, *32*, 677-681.
4. Myers, D. Surfactant Science and Technology 4th Ed. Wiley, **2020**.
5. Aisha; Batool, I.; Iftekhar, S.; Babar Taj, M.; Correia Carabiniero, S. A.; Ahmad, F.; Khan, M. I.; Shanable, A.; Alshater, H. Wetting the Surface: A Deep Dive into Chemistry and Applications of Surfactants. *Clean. Chem. Eng.* **2025**, *11*, 100197.
6. Ghosh, S.; Ray, A.; Pramanik, N. Self-Assembly of Surfactants: An Overview on General Aspects of Amphiphiles. *Biophys. Chem.* **2020**, *265*, 106429.
7. Sorrenti, A.; Illa, O.; Ortuno, R. M. Amphiphiles in Aqueous Solution: Well Beyond a Soap Bubble. *Chem. Soc. Rev.* **2013**, *42*, 8200-8219.
8. Israelachvili, J. N.; Mitchell, D. J.; Ninham, B. W. Theory of Self-Assembly of Hydrocarbon Amphiphiles into Micelles and Bilayers. *J. Chem. Soc., Faraday Trans. 2* **1976**, *72*, 1525-1568.
9. Lianos, P.; Zana, R. Use of Pyrene Excimer Formation to Study the Effect of NaCl on the Structure of Sodium Dodecyl Sulfate Micelles. *J. Phys. Chem.* **1980**, *84*, 3339-3341.
10. Bergström, M.; Pedersen, J. S. Structure of Pure SDS and DTAB Micelles in Brine Determined by Small-Angle Neutron Scattering (SANS). *Phys. Chem. Chem. Phys.* **1999**, *1*, 4437-4446.

11. Ranganathan, R.; Peric, M.; Medina, R.; Garcia, U.; Bales, B. L.; Almgren, M. Size, Hydration, and Shape of SDS/Heptane Micelles Investigated by Time-Resolved Fluorescence Quenching and Electron Spin Resonance. *Langmuir* **2001**, *17*, 6765-6770.
12. Fowler, M.; Hisko, V.; Henderson, J.; Casier, R.; Li, L.; Thoma, J.; Duhamel, J. DiPyMe in SDS Micelles – Artefacts and their Implications on Micellar Properties. *Langmuir* **2015**, *31*, 11971-11981.
13. Kaler, E. W.; Murthy, A. K.; Rodriguez, B. E.; Zasadzinski, J. A. N. *Science* **1989**, *245*, 1371-1374.
14. Herrington, K. L.; Kaler, E. W.; Miller, D. D.; Zasadzinski, J. A.; Chiruvolu, S. Phase Behavior of Aqueous Mixtures of Dodecyltrimethylammonium Bromide (DTAB) and Sodium Dodecyl Sulfate (SDS). *J. Phys. Chem.* **1993**, *97*, 13792-13802.
15. Bergström, M.; Pedersen, J. S. A Small Angle Neutron Scattering (SANS) Study of Tablet-Shaped and Ribbonlike Micelles Formed from Mixtures of an Anionic and a Cationic Surfactant. *J. Phys. Chem. B* **1999**, *103*, 8502-8513.
16. Prévost, S.; Gradzielski, M. SANS Investigation of the Microstructures in Catanionic Mixtures of SDS/DTAC and the Effect of Various Salts. *J. Colloid Interface Sci.* **2009**, *337*, 472-484.
17. Krauss, I. R.; Imperatore, R.; De Santis, A.; Luchini, A.; Paduano, L.; D'Errico, G. Structure and Dynamics of Cetyltrimethylammonium Chloride-Sodium Dodecyl Sulfate (CTAC-SDS) Catanionic Vesicles: High-Value Nano-Vehicles from Low-Cost Surfactants. *J. Colloid Interface Sci.* **2017**, *501*, 112-122.
18. Liu, D.; Patel, J.; Duhamel, J. Conformation of Pyrene End-Labeled Polyamidoamine Dendrimers in Catanionic Surfactant Micelles Probed by Pyrene Excimer Formation. *Langmuir* **2025**, *41*, 20986-20998.

19. Winnik, F. M.; Regismond, S. T. A. Fluorescence Methods in the Study of the Interactions of Surfactants with Polymers. *Colloid Surf. A: Physicochem. Eng. Asp.* **1996**, *118*, 1-39.

20. Mabrouk, M. M.; Hamed, N. A.; Mansour, F. R. Spectroscopic Methods for Determination of Critical Micelle Concentrations of Surfactants; a Comprehensive Review. *Appl. Spec. Rev.* **2023**, *58*, 206-234.

21. Roy, T.; Padhi, S. A Meticulous Focus on the Determination of Critical Micelle Concentration Employing Fluorescence Spectroscopy. *J. Fluoresc.* **2025**, *in press*.

22. Liu, D.; Patel, S.; Duhamel, J. Conformation of Pyrene End-Labeled Polyamidoamine Dendrimers in Catanionic Surfactant Micelles Probed by Pyrene Excimer Formation. *Langmuir* **2025**, *41*, 20986–20998.

23. Liu, D.; Patel, S.; Duhamel, J. Two Distinct Regions in Surfactant Aggregates Identified with Pyrene-Labeled Dendrimers. *Submitted* **2025**.

24. Patel, S.; Duhamel, J. Macromolecular Conformation of Low Generation PAMAM Dendrimers Probed by Pyrene Excimer Formation. *Macromolecules* **2023**, *56*, 4012-4021.

25. Patel, S.; McNelles, S.; Adronov, A.; Duhamel, J. Intra-Macromolecular Conformational Changes in Low Generation PAMAM Dendrimers Probed by Pyrene Excimer Formation. *J. Phys. Chem. B* **2023**, *127*, 8040-8048.

26. Carloni, R.; Ottaviani, M. F.; Ficker, M.; Christensen J. B. Interactions of Functionalized PAMAM Dendrimers with Model Cell Membranes Studied via Spin-Labelling Technique. *J. Phys. Chem. B* **2022**, *126*, 9686-9694.

27. Jafari, M.; Mehrnejad, F.; Talandashti, R.; Doustdar, F.; Vakili, M. R.; Lavasanifar, A. Effect of the Lipid Composition and Cholesterol on the Membrane Selectivity of Low Generation PAMAM Dendrimers: A Molecular Dynamics Simulation Study. *Appl. Surf. Sci.* **2021**, *540*, 148274.

28. Kelly, C. V.; Leroueil, P. R.; Orr, B. G.; Banaszak Holl, M. M.; Andricioaei, I. Poly(amidoamine) Dendrimers on Lipid Bilayers II: Effects of Bilayer Phase and Dendrimer Termination. *J. Phys. Chem. B* **2008**, *112*, 9346-9353.
29. Bales, B. L.; Almgren, M. Fluorescence Quenching of Pyrene by Copper (II) in Sodium Dodecyl Sulfate Micelles. Effect of Micelle Size as Controlled by Surfactant Concentration. *J. Phys. Chem.* **1995**, *99*, 15153-15162.
30. Yan, H.; Cui, P.; Liu, C.; Yuan, S. Molecular Dynamics Simulations of Pyrene Solubilized in a Sodium Dodecyl Sulfate Micelle. *Langmuir* **2012**, *28*, 4931-4938.
31. Yang, X.; Lu, G.; She, B.; Liang, X.; Yin, R.; Guo, C.; Yi, X.; Dang, X. Cosolubilization of 4,4'-Dibromodiphenyl Ether, Naphthalene, and Pyrene Mixtures in Various Surfactant Micelles. *Chem. Eng. J.* **2015**, *260*, 74-82.
32. Lebedeva, N.; Ranganathan, R.; Bales, B. L. Location of Spectroscopic Probes in Self-Aggregating Assemblies. II. The Location of Pyrene and Other Probes in Sodium Dodecyl Sulfate Micelles. *J. Phys. Chem. B* **2007**, *111*, 5781-5793.
33. Liang, X.; Marchi, M.; Guo, C.; Dang, Z.; Abel, S. Atomistic Simulation of Solubilization of Polycylic Aromatic Hydrocarbons in a Sodium Dodecyl Sulfate Micelle. *Langmuir* **2016**, *32*, 3645-3654.
34. Wasylishen, R. E.; Kwak, J. C. T.; Gao, Z.; Verpoorte, E.; Macdonald, J. B.; Dickson, R. M. NMR Studies of Hydrocarbons Solubilized in Aqueous Micellar Solutions. *Can. J. Chem.* **1991**, *69*, 822-833.
35. Malliaris, A.; Le Moigne, J.; Sturm, J.; Zana, R. Temperature Dependence of the Micelle Aggregation Number and Rate of Intramicellar Excimer Formation in Aqueous Surfactant Solutions. *J. Phys. Chem.***1985**, *89*, 2709-2713.

36. Almgren, M.; Bedhage, B.; Mukhtar, E. Fluorescence Study of the Weak Interaction Between Pyrene and Quaternary Ammonium Groups. *J. Photochem. Photobiol. A* **1991**, *59*, 323-334.
37. Xing, H.; Yan, P.; Xiao, J.-X. Unusual Location of the Pyrene Probe Solubilized in Micellar Solutions of Tetraalkylammonium Perfluorooctanoates. *Soft Matter* **2013**, *9*, 1164-1171.
38. Cao, X.; Casier, R.; Little, H.; Duhamel, J.Characterization of the Distribution of Pyrene Molecules in Confined Geometries with the Model Free Analysis and its Applications. *J. Phys. Chem. B* **2017**, *121*, 11325-11332.
39. Cabane, B.; Duplessix, R.; Zemb, T. High Resolution Neutron Scattering on Ionic Surfactant Micelles: SDS in Water. *J. Phys.* **1985**, *46*, 2161-2178.
40. Kim, D.; Amos, R. C.; Gauthier, M.; Duhamel, J. Assemblies of Hydrophobically Modified Starch Nanoparticles Probed by Surface Tension and Pyrene Fluorescence. *ACS Symposium Series-Molecular Assemblies: Characterization and Applications.* Ed. Nagarajan, R. 2020, Chapter 5, pp 61-75.
41. Kalyanasundaram, K.; Thomas, J. K. Environmental Effects on Vibronic Band Intensities in Pyrene Monomer Fluorescence and their Application in Studies of Micellar Systems. *J. Am. Chem. Soc.* **1977**, *99*, 2039−2044.
42. Dong, D. C.; Winnik, M. A. The Py Scale of Solvent Polarities. *Photochem. Photobiol.* **1982**, *35*, 17−21.
43. Lakowicz, J. R. Principles of Fluorescence, 3rd Ed. Springer, NY, 2006, pp 284-287.
44. Duhamel, J. New Insights in the Study of Pyrene Excimer Fluorescence to Characterize Macromolecules and their Supramolecular Assemblies in Solution. *Langmuir* **2012**, *28*, 6527-6538.

45. Press, W.H.; Flanery, B.P.; Tenkolsky, S.A.; Vetterling, W.T. *Numerical Receipes in Fortran: The Art of Scientific Computing*; Cambridge University Press: New York, NY, USA, 1992; pp 523−528.
46. Little, H.; Patel, S.; Duhamel, J. Probing the Inner Local Density of Complex Macromolecules by Pyrene Excimer Formation. *Phys. Chem. Chem. Phys.* **2023**, *25*, 26515-26525.
47. McNelles, S.; Thoma, J.; Adronov, A.; Duhamel, J. Quantitative Characterization of the Molecular Dimensions of Flexible Dendritic Macromolecules by Pyrene Excimer Fluorescence. *Macromolecules* **2018**, *51*, 1586-1590.
48. Thoma, J.; McNelles, S. A.; Adronov, A.; Duhamel, J. Direct Measure of the Local Concentration of Pyrenyl Groups in Pyrene-Labeled Dendrons Derived from the Rate of Fluorescence Collisional Quenching. *Polymers* **2020**, *12*, 2919.

S2 References

1. Kim, D.; Amos, R. C.; Gauthier, M.; Duhamel, J. Assemblies of Hydrophobically Modified Starch Nanoparticles Probed by Surface Tension and Pyrene Fluorescence. *ACS Symposium Series-Molecular Assemblies: Characterization and Applications. Ed. Nagarajan, R.* 2020, Chapter 5, pp 61-75.
2. Winnik, F. M. Photophysics of Preassociated Pyrenes in Aqueous Polymer Solutions and in Other Organized Media. *Chem. Rev.* **1993**, 93, 587-614.
3. Zhang, M.; Duhamel, J.; van Duin, M.; Meessen, P. Characterization of the Distribution of Maleic Anhydride Grafted onto Ethylene-Propylene Copolymers. *Macromolecules* **2004**, 37, 1877-1890.
4. Press, W. H.; Flannery, B. P.; Teukolsky, S. A.; Vetterling, W. T. Numerical Recipes. *The Art of Scientific Computing (Fortran Version);* Cambridge University Press: Cambridge, 1992, p 82.

S3 References

1. Press, W. H.; Flannery, B. P.; Teukolsky, S. A.; Vetterling, W. T. Numerical Recipes. *The Art of Scientific Computing (Fortran Version)*; Cambridge University Press: Cambridge 1992, p 82,.

S4 References

1. Patel, S.; Duhamel, J. Macromolecular Conformation of Low Generation PAMAM Dendrimers Probed by Pyrene Excimer Formation. *Macromolecules* **2023**, 56, 4012-4021.
2. Patel, S.; McNelles, S.; Adronov, A.; Duhamel, J. Intra-Macromolecular Conformational Changes in Low Generation PAMAM Dendrimers Probed by Pyrene Excimer Formation. *J. Phys. Chem. B,* **2023**, 127, 8040-8048.

3. Liu, D.; Patel, S.; Xie, Y.; Zhang, H.; Duhamel, J. Probing Macromolecular Conformation in Restricted Geometry by PEF: Application to Hydrophobically Modified PAMAM Dendrimers Isolated Inside Surfactant Micelles. *J. Phys. Chem. B,* **2025**, *129*, 1144–1153.
4. Duhamel, J. New Insights in the Study of Pyrene Excimer Fluorescence to Characterize Macromolecules and their Supramolecular Assemblies in Solution. *Langmuir* **2012**, 28, 6527-6538.
5. Press, W. H.; Flannery, B. P.; Teukolsky, S. A.; Vetterling, W. T. Numerical Recipes. *The Art of Scientific Computing (Fortran Version);* Cambridge University Press: Cambridge, 1992, p 82.

S5 References

1. Press, W. H.; Flannery, B. P.; Teukolsky, S. A.; Vetterling, W. T. Numerical Recipes. *The Art of Scientific Computing (Fortran Version);* Cambridge University Press: Cambridge, 1992, p 82.

Appendix: Supporting Information (SI)

Appendix A: S2-SI for Chapter 2

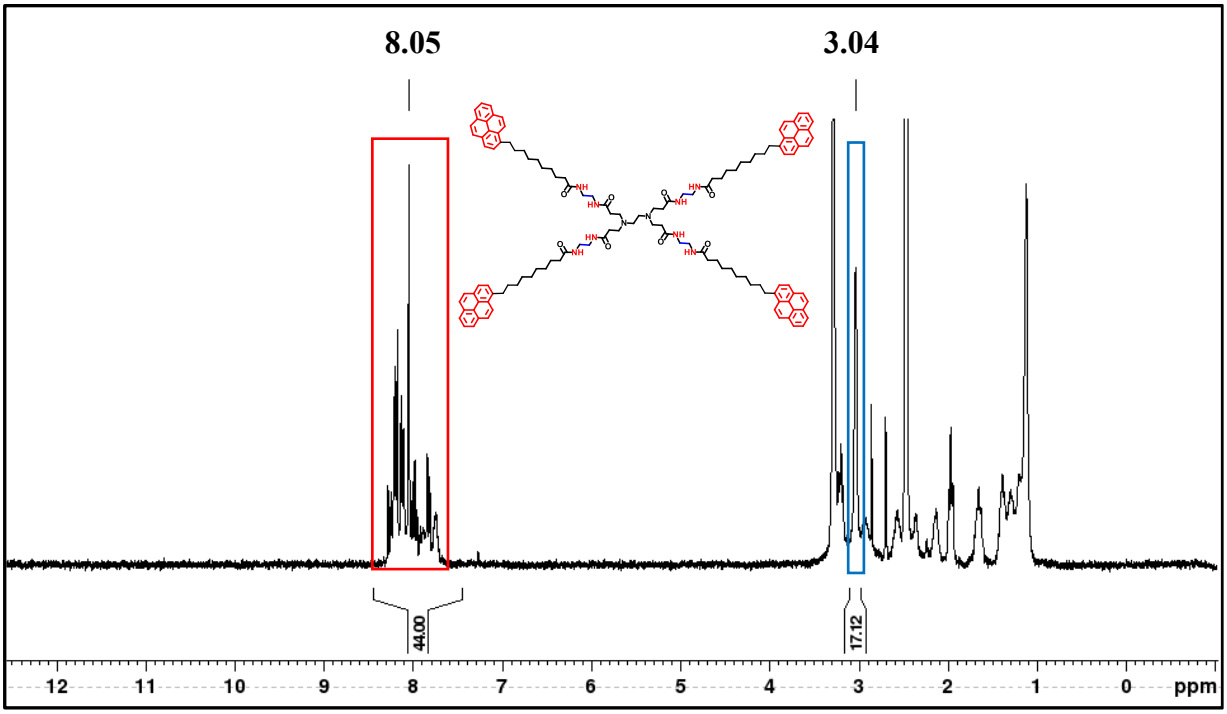


Figure S2.1. ^{1}H NMR spectrum of PAMAM-G0 labeled with 1-pyrenedecanoic acid (PyC10-PAMAM-G0) in d_6-DMSO. Peaks in the red block represent the pyrene and amide bond hydrogens. Peaks in the blue block represent the hydrogens of the four ethylenediamine groups in the side chains.

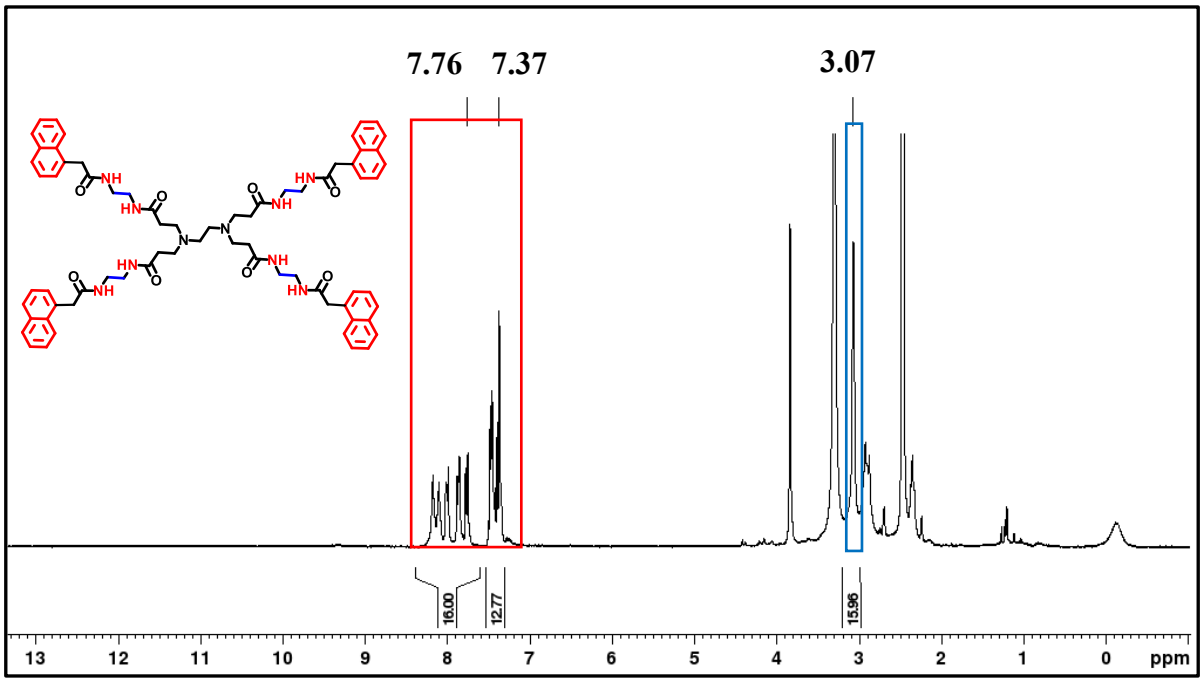


Figure S2.2. ^{1}H NMR spectrum of PAMAM-G0 labeled with 1-naphthaleneacetic acid (NpC2-PAMAM-G0) in d_6-DMSO. Peaks in the red block represent the naphthalene and amide bond hydrogens. Peaks in the blue block represent the hydrogens of the ethylenediamine groups in the side chains.

B] Mass spectra of the PyCX-PAMAM-G0 and NpC2-PAMAM-G0 dendrimers generated by Matrix assisted laser desorption/ionization – time of flight mass spectroscopy (MALDI-ToF MS)

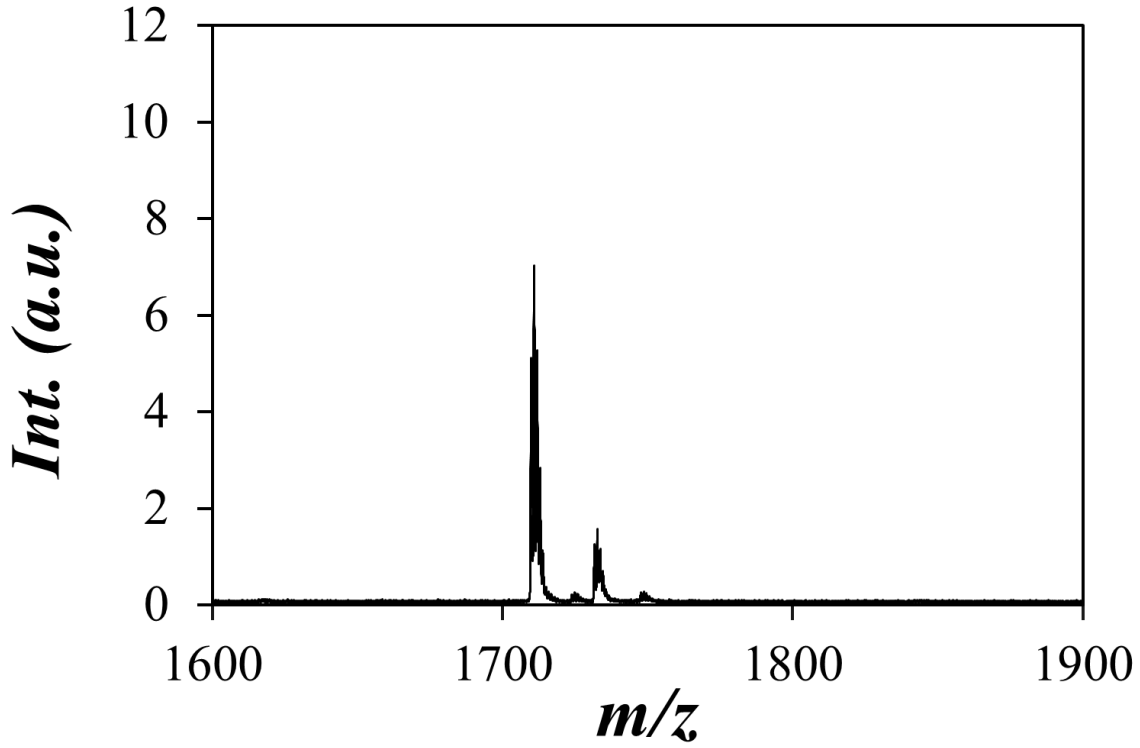


Figure S2.3. Mass spectrum of PAMAM-G0 labeled with 1-pyrenehexanoic acid. The major m/z peaks observed at 1709.8 g/mol and 1731.6 g/mol represent the charged dendrimer (expected molar mass = 1710.2 g/mol) and a charged complex between the dendrimer and a sodium ion (expected molar mass = 1733.2 g/mol), respectively.

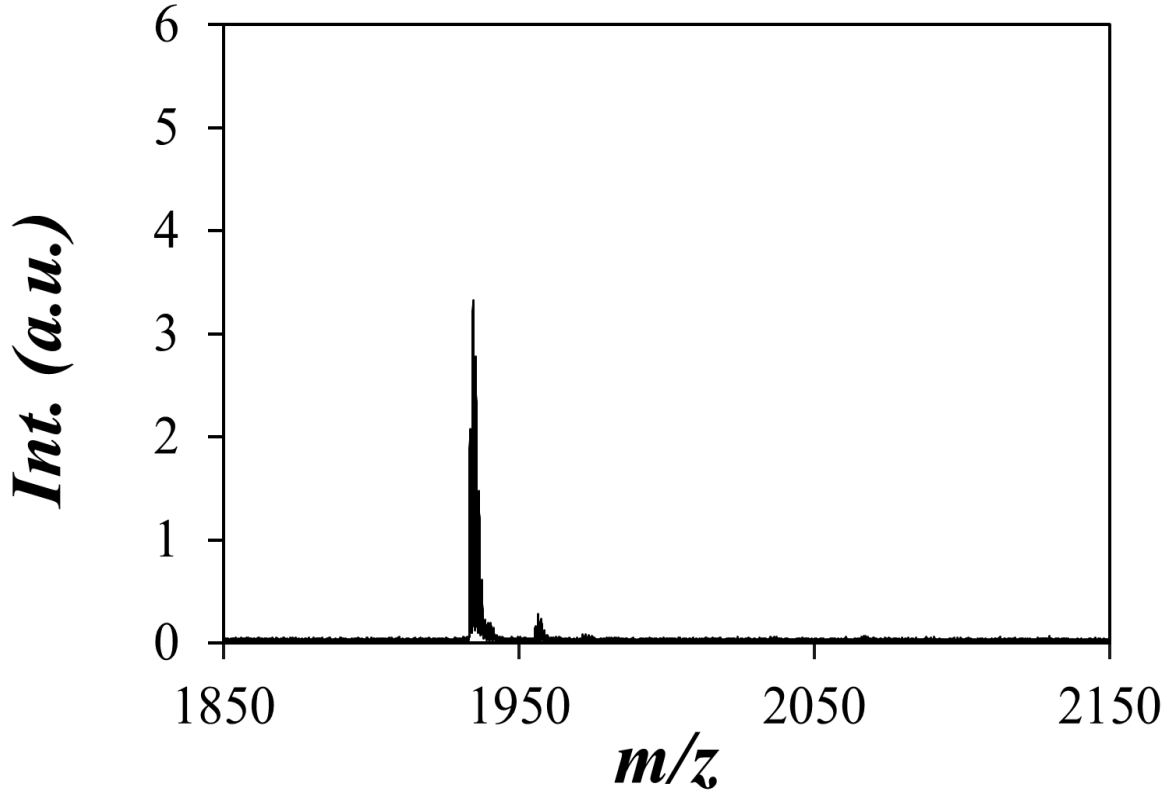


Figure S2.4. Mass spectrum of PAMAM-G0 labeled with 1-pyrenedecanoic acid. The major m/z peaks observed at 1933.5 g/mol and 1955.6 g/mol represent the charged dendrimer (expected molar mass = 1934.6 g/mol) and a charged complex between the dendrimer and a sodium ion (expected molar mass = 1957.6 g/mol), respectively.

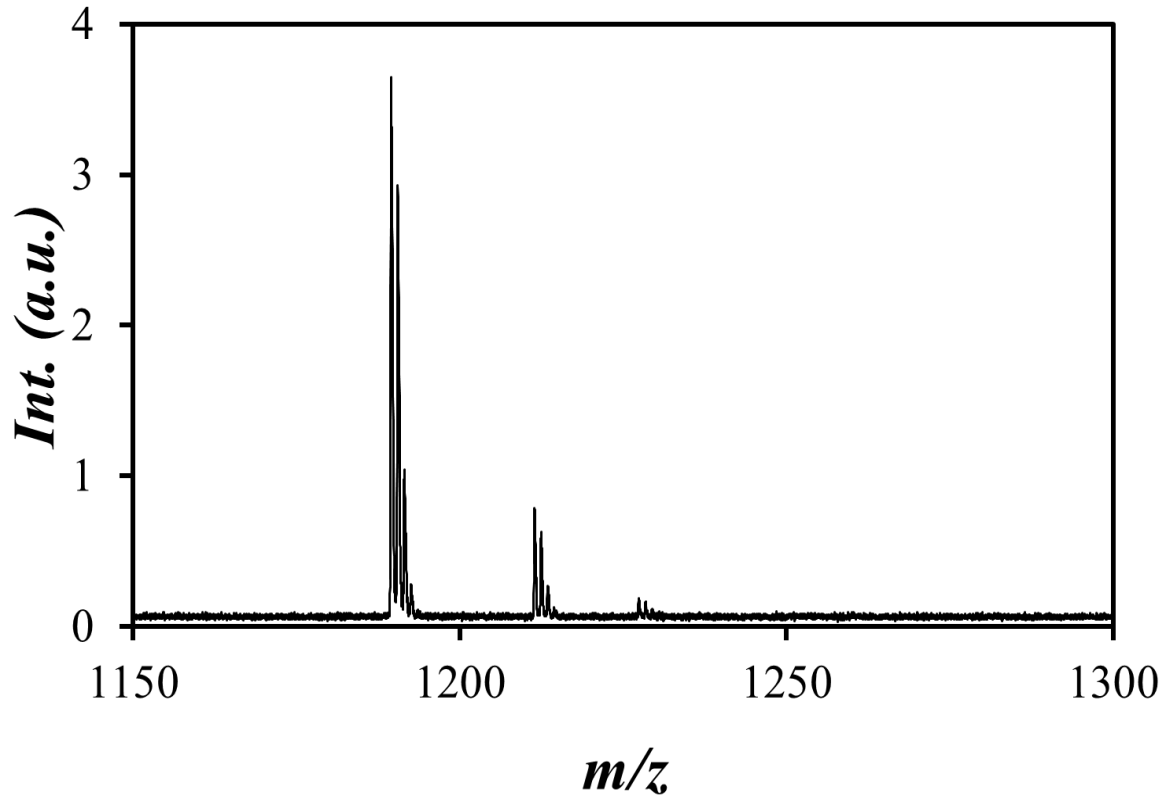


Figure S2.5. Mass spectrum of PAMAM-G0 labeled with 1-naphthaleneacetic acid. The major m/z peaks observed at 1189.5 g/mol and 1211.4 g/mol represent the charged dendrimer (expected molar mass = 1189.5 g/mol) and a charged complex between the dendrimer and a sodium ion (expected molar mass = 1212.5 g/mol), respectively.

C] Sample preparation

In this study, extreme attention was paid to the establishment of experimental conditions that would minimize aggregation of the pyrenyl labels in the PyCX-PAMAM-G0 samples associated with the surfactant micelles. This was a challenging task as pyrene, with a solubility of 0.7 μM in water,[48] is very hydrophobic, which complicates the solubilization of the PyCX-PAMAM-G0 samples in the surfactant micelles in water. Several methods were implemented to dissolve the PyCX-PAMAM-G0 samples in the 50 mM surfactant aqueous solutions and two of these methods are described hereafter.

DMSO Method: According to the DMSO Method, 10 mL of a 50 mM aqueous surfactant solution was prepared along with a 1 mM PyCX-PAMAM-G0 stock solution in DMSO. The PyCX-PAMAM-G0 stock solution in DMSO was preheated to 65 ºC to ensure the full dissolution of the dendrimers and a small volume, between 5 and 15 μL depending on the desired final concentration of PyCX-PAMAM-G0 sample in the 50 mM surfactant aqueous solution, was added directly into the surfactant solution yielding a 0.5-to-1.5 μM PyCX-PAMAM-G0 aqueous solution with 50 mM surfactant.

Hybrid Method: In the Hybrid Method, the desired amount of SDS or DTAB was added into an empty round bottom flask and its mass was recorded. The flask was sealed with a rubber septum. A small volume (5-15 μL) of preheated 1 mM PyCX-PAMAM-G0 stock solution in DMSO was transferred into the sealed flask. About 10 mL of chloroform was then added to the flask and the mixture was sonicated. The suspension was then dried under constant air flow resulting in a film containing the PyCX-PAMAM-G0 samples and the surfactant. This process was sufficient to remove the chloroform for the SDS mixtures but not for the DTAB mixtures. For DTAB, the mixtures were left in a vacuum oven overnight to ensure that the chloroform had been removed. The resulting film of surfactant and PyCX-PAMAM-G0 sample was then

redissolved in 10 mL of MilliQ™ water.

D] Assessment of the solubility of the PyCX-PAMAM-G0 samples in 50 mM surfactant aqueous solutions based on the analysis of pyrene excimer fluorescence decays and UV-Vis absorption spectra

The spectral features considered for good solvation of the pyrenyl labels involved the observation of sharp absorption bands in the absorption spectra and a well-defined rise time in the pyrene excimer fluorescence decay. Many experimental conditions used to prepare aqueous solutions of the PyCX-PAMAM-G0 samples with 50 mM surfactant were found to lead to excessive aggregation of the pyrenyl labels in the PyCX-PAMAM-G0 samples, which prevented the characterization of the photophysical properties of these samples.

An example of the absorption spectrum for PyC8-PAMAM-G0 obtained by the DMSO Method is shown as the red trace in Figure S2.6. The absence of the sharp absorption bands around 340 nm in the absorption spectrum reflects aggregation of the pyrenyl labels. However, since a flat baseline was obtained, it suggested that the resulting aggregates involved few PyC8-PAMAM-G0 dendrimers. In contrast, the PyC8-PAMAM-G0 aqueous solution with 50 mM DTAB prepared according to the Hybrid Method yielded the absorption spectrum shown as a black trace in Figure S2.6. This absorption spectrum shows the sharp bands expected for the pyrenyl labels with a peak-to-valley ratio (P_A) of 2.5.

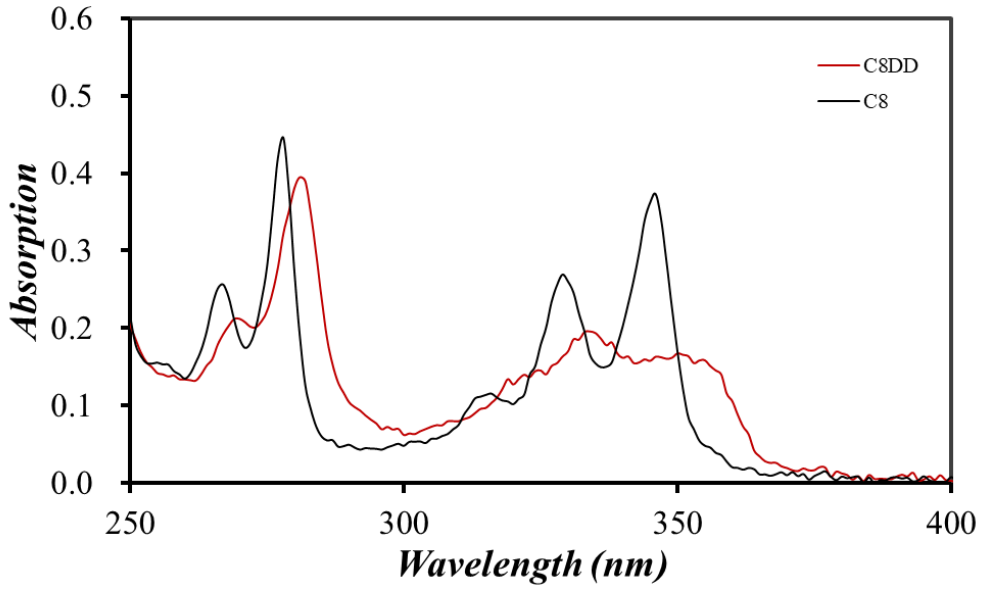


Figure S2.6. Absorption spectra acquired for the PC8-PAMAM-G0 aqueous solution with 50 mM DTAB prepared according to (red trace) the DMSO Method and (black trace) the Hybrid Method. All absorption spectra were acquired with a 5 cm-pathlength UV cell.

Although PA ratios larger than 3.0 would be expected to ensure absence of aggregation,[2] the pyrene excimer fluorescence decay shown in Figure S2.7 exhibited a clear rise time indicating low pyrene aggregation. Global MFA of the pyrene monomer and excimer fluorescence decays yielded an fagg value of 0.03 confirming the absence of pyrene aggregation in this PyC8- PAMAM-G0 solution. Consequently, the Hybrid Method was applied to prepare all aqueous solutions of the PyCX-PAMAM-G0 dendrimers with 50 mM DTAB, which consistently resulted in minimal aggregation between the pyrenyl labels. While the Hydrid Method yielded PyCX-PAMAM-G0 aqueous solutions with 50 mM DTAB that showed little pyrene aggregation based on the sharp spectral bands observed in the absorption spectra (Figure S2.6) and the global MFA of the fluorescence decays (Figure S2.7), this was not the case of the aqueous S11 solutions of the PyCX-PAMAM-G0 samples prepared with 50 mM SDS, which showed poorly resolved rise times in the pyrene excimer fluorescence decays (decay not shown).

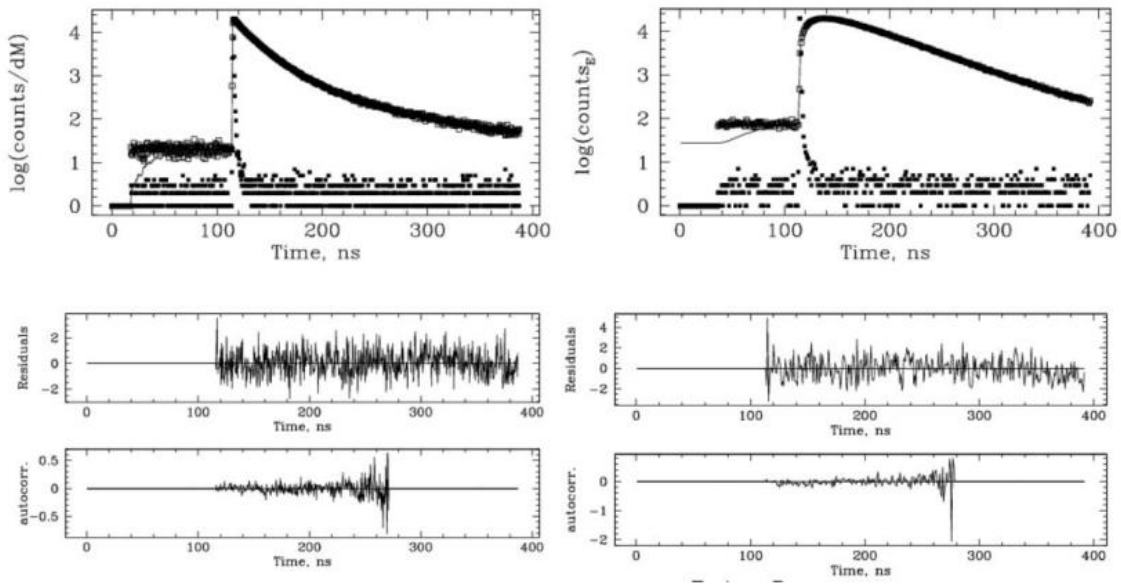


Figure S2.7. Fluorescence decays of the (left) pyrene monomer and (right) pyrene excimer fitted according to the MFA for the PyC8-PAMAM-G0 aqueous solution with 50 mM DTAB. The top panels show the fluorescence decays with the instrument response function and the line of best fit, while the middle and bottom panels show the residuals and the autocorrelation of the residuals, respectively. λ_{ex} = 344 nm and λ_{em} = (left) 378 nm and (right) 510 nm.

For the aqueous solutions with 50 mM SDS, the PyCX-PAMAM-G0 concentration was found to have a strong effect on the level of aggregation of the pyrenyl labels when using the Hybrid Method. An example of the absorption spectra obtained with PyC8-PAMAM-G0 concentrations of 1.0 μmol/L and 0.5 μmol/L resulted in the absorption spectra shown in Figure S2.8. The higher 1.0 μmol/L concentration of PyC8-PAMAM-G0 dendrimers yielded absorption spectra with a slopping baseline indicative of large aggregated species being probably PyC8- S12 PAMAM-G0 aggregates stabilized by the surfactants. Since the sharp bands of solvated pyrenyl labels are also visible around 340 nm, it suggests that some of the PyC8-PAMAM-G0 species were solvated but that a large fraction of the dendrimers remained

aggregated resulting in the slopping baseline due to the scattering of the large aggregates. The fluorescence decays of the pyrene excimer for these solutions showed a less pronounced rise time, and the analysis yielded a relatively large molar fraction (fagg) of aggregated pyrenyl labels equal to 20%.

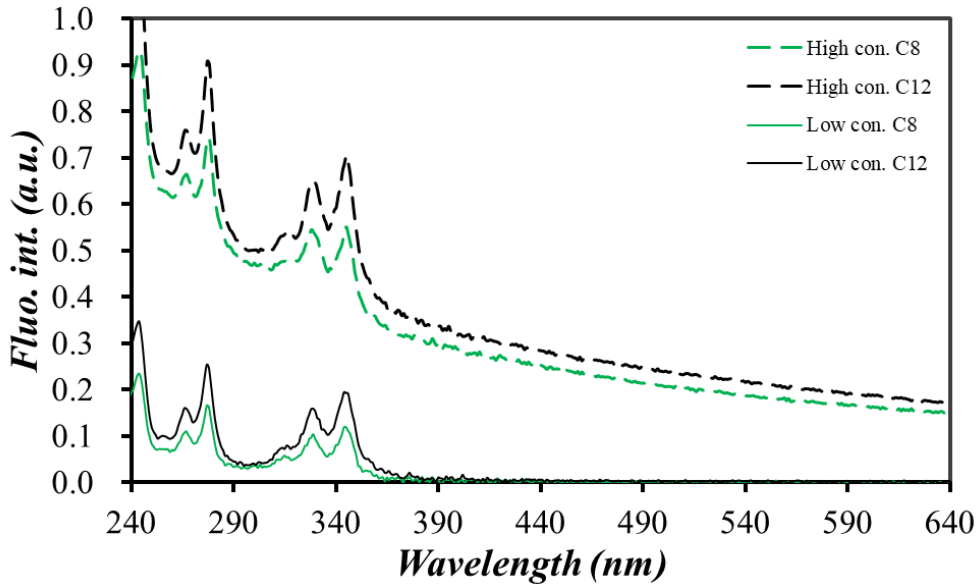


Figure S2.8. Comparison between the aqueous solution of PC8-PAMAM-G0 with dendrimer concentration of (dashed green trace) 1.0 μmol/L and (solid green trace) 0.5 μmol/L, and PyC12-PAMAM-G0 with dendrimer concentration of (dashed black trace) 1.5 μmol/L and (solid black trace) 0.9 μmol/L in 50 mM SDS prepared according to the Hybrid Method. All absorption spectra were acquired with a 5 cm-pathlength UV cell.

Lowering the PyC8-PAMAM-G0 dendrimer concentration from 1.0 to 0.5 μmol/L yielded the absorption spectra shown as solid lines in Figure S2.8 which presented no evidence of S13 scattering, and MFA of the fluorescence decays yielded a reduced fagg of only 8%, which is the same level of aggregation of PyC8-PAMAM-G0 in DMF and DMSO. For PyC12-PAMAM-G0, the same phenomenon was observed from the comparison of the absorption spectra of the 1.5 and 0.9 μmol/L PyC12-PAMAM-G0 in 50 mM SDS solutions presented in

Figure S2.8, with the latter absorption spectrum showing no sloping baseline. The fluorescence decays of the pyrene monomer and excimer for the aqueous solution of PyC8-PAMAM-G0 with 50 mM SDS are shown as representative examples in Figure S2.9. The clear rise time observed in the pyrene excimer fluorescence decay confirmed the quasi-absence of aggregated pyrenyl labels with an fagg value of 0.08. Since application of the Hybrid Method with a low PyCX-PAMAM-G0 concentration yielded absorption spectra with sharp bands around 340 nm characteristic of the pyrenyl labels and the pyrene excimer fluorescence decays showed a well-defined rise time, the Hybrid Method was applied to prepare all the aqueous solutions of PyCX-PAMAM samples with 50 mM SDS using a dendrimer concentration lower than 1 μmol/L.

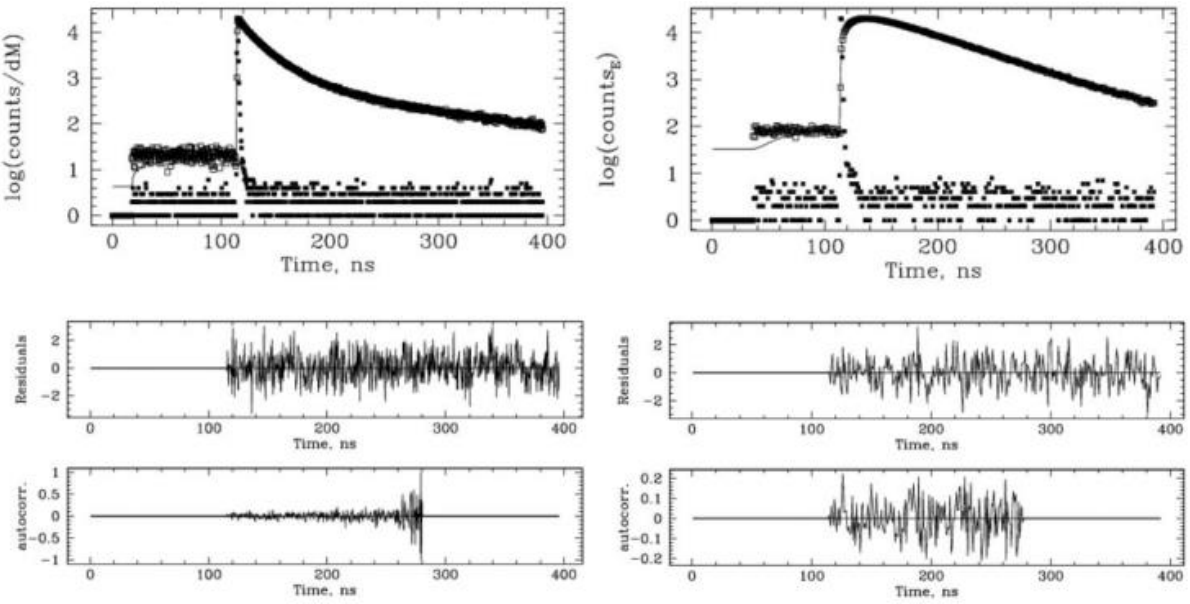


Figure S2.9. Fluorescence decays of the pyrene (left) monomer and (right) excimer for the aqueous solution of PyC8-PAMAM-G0 with 50 mM SDS. The top panels show the fluorescence decays with the instrument response function and the line of best fit, while the middle and bottom panels show the residuals and the autocorrelation of the residuals, respectively. λ_{ex} = 344 nm and λ_{em} = (left) 378 nm and (right) 510 nm.

E] Fluorescence Resonance Energy Transfer (FRET) study of the PyCX-PAMAM-G0 dendrimers

FRET experiments were conducted to assess whether intermolecular excimer formation contributed to the significant increase in observed for the PC10-PAMAM-G0 and PC12-PAMAM-G0 samples in the 50 mM SDS and DTAB solutions. The FRET study conducted for the PyC10-PAMAM-G0 sample in 50 mM SDS solution is described in detail as an example.

In the FRET study, stock solutions of NpC2-PAMAM-G0 and PyC10-PAMAM-G0 in DMSO were prepared separately. An amount of SDS was added into an empty round bottom flask and its mass was recorded. This round bottom flask was then sealed with a rubber septum. The NpC2-PAMAM-G0 stock solution in DMSO was preheated to 65°C and approximately 20 μL of this solution was transferred into the sealed flask. The exact mass of NpC2-PAMAM-G0 stock solution added to the flask was recorded. About 10 mL of chloroform was then added in the flask and the mixture was sonicated. The suspension was then dried under constant air flow before being redissolved in 10 mL of MilliQ™ water. This NpC2-PAMAM-G0 aqueous solution with 50 mM SDS was named the N2-solution. Its fluorescence spectrum was acquired, and it is shown in Figure S2.10. The same treatment was applied to prepare the P10-solution for the PyC10-PAMAM-G0 aqueous solution with 50 mM SDS. Its fluorescence spectrum was acquired and is shown in the same figure. This procedure was repeated once more with a stock solution of the mixture of NpC2-PAMAM-G0 and PyC10-PAMAM-G0 in DMSO prepared with the same dendrimer concentrations as the concentrations used for the fluorescence spectra shown in Figure S2.10. The solution of the mixture in DMSO (20 μL) was placed in a flask that already contained a known mass of SDS and the mass of the NpC2-PAMAM-G0 and PyC10-PAMAM-G0 mixture in DMSO was determined. Chloroform (10 mL) was added. The mixture in chloroform was sonicated before being dried under a constant air flow and the

resulting solid film was dissolved in 10 mL of MilliQ water. This 50 mM SDS aqueous solution with the dendrimer mixture was named Mixture-solution and its spectrum is shown in Figure S2.11.

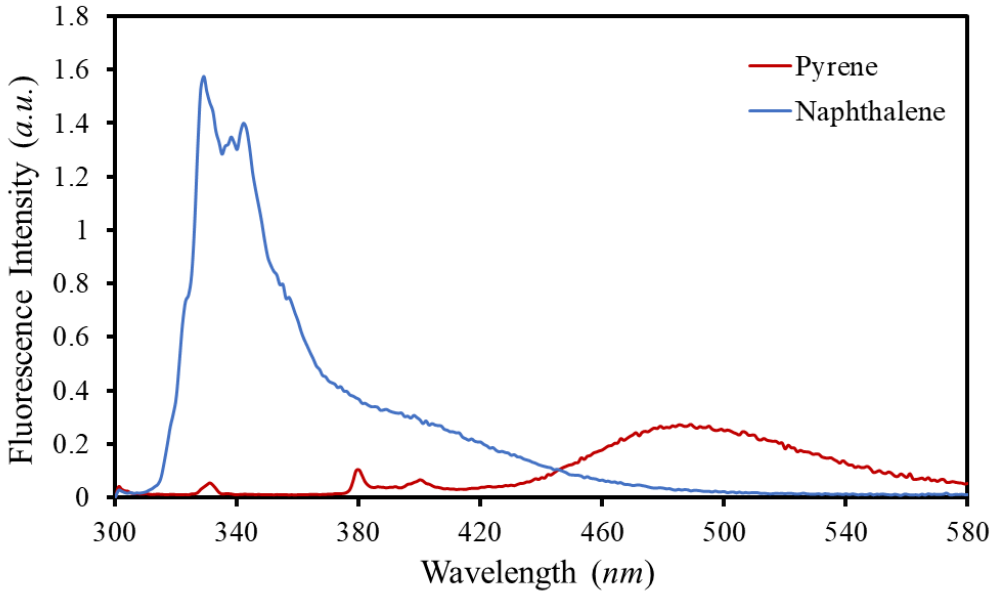


Figure S2.10. Fluorescence spectra of the aqueous solutions of (blue) NpC2-PAMAM-G0 and (red) PyC10-PAMAM-G0 with 50 mM SDS. λ_{ex} = 295 nm.

If FRET were to occur between the excited naphthyl labels of NpC2-PAMAM-G0 and the ground-state pyrenyl labels of the PyC10-PAMAM-G0 samples, the naphthyl emission would be reduced and the pyrenyl emission would be enhanced. Furthermore, since the Förster radius for the naphthalene/pyrene pair equals 3.4 nm,[3] the occurrence of FRET would imply that the NpC2-PAMAM-G0 and PyC10-PAMAM-G0 samples would coexist inside a same micelle. For this reason, the fluorescence spectrum of the Mixture-solution shown in Figure S2.11 was compared to the sum of the fluorescence spectra acquired for the individual 50 mM SDS solutions of NpC2-PAMAM-G0 and PyC10-PAMAM-G0 shown in Figure S2.10.

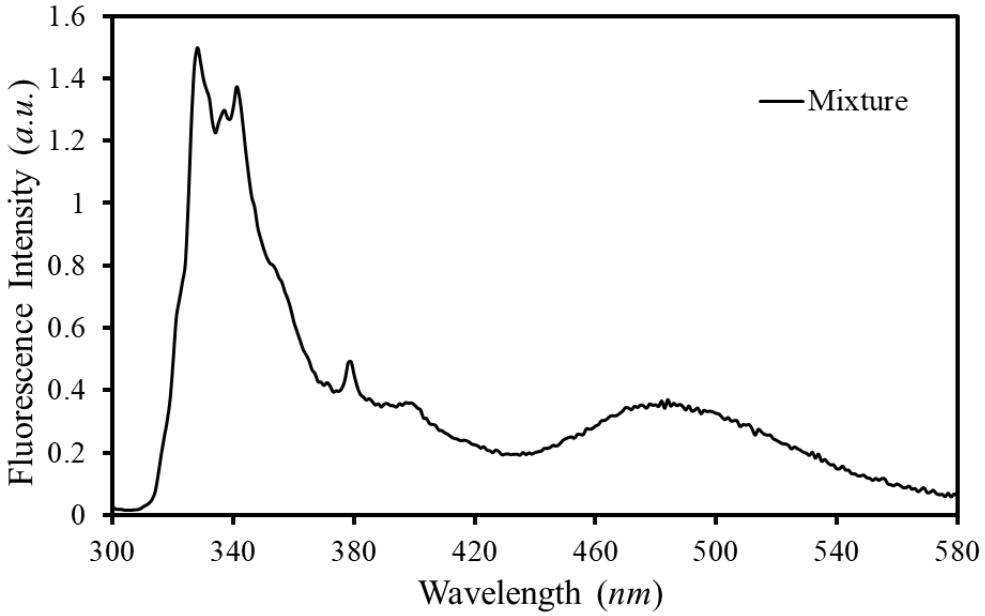


Figure S2.11. Fluorescence spectrum of the aqueous solution of the mixture of NpC2-PAMAM-G0 and PyC10-PAMAM-G0 with 50 mM SDS. λ_{ex} = 295 nm.

To calculate the sum of the two fluorescence spectra in Figure S2.10, their fluorescence intensity was adjusted according to the exact mass of stock solution and water added to each sample so that slight differences in the NpC2-PAMAM-G0 and PyC10-PAMAM-G0 concentrations between the N2, P10, and Mixture-solutions could be accounted for. Meanwhile, both spectra in Figure S2.10 showed the tail end of the scattering peak at 300 nm due to the 295 nm excitation light as well as a small peak at 336 nm due to the Stokes shift of water. Although the peak at 336 nm resulting from the Stokes shift of water could only be seen in the fluorescence spectrum of the P10 solution, it also contributed to the fluorescence spectrum of S18 the N2 solution. To avoid adding these two contributions twice in the sum of the fluorescence spectra of the N2 and P10 solutions, the fluorescence intensity readings with wavelengths between 300 nm and 370 nm were set to zero for the fluorescence spectrum obtained with the P10-solution. The fluorescence intensity of both spectra adjusted for minute

differences in dendrimer concentration were added and the resulting spectrum was plotted in Figure S2.12 as a red dashed line along with the spectrum generated by the 50 mM SDS solution with the mixture of the NpC2-PAMAM-G0 and PyC10-PAMAM-G0 samples plotted as a solid black line for comparison.

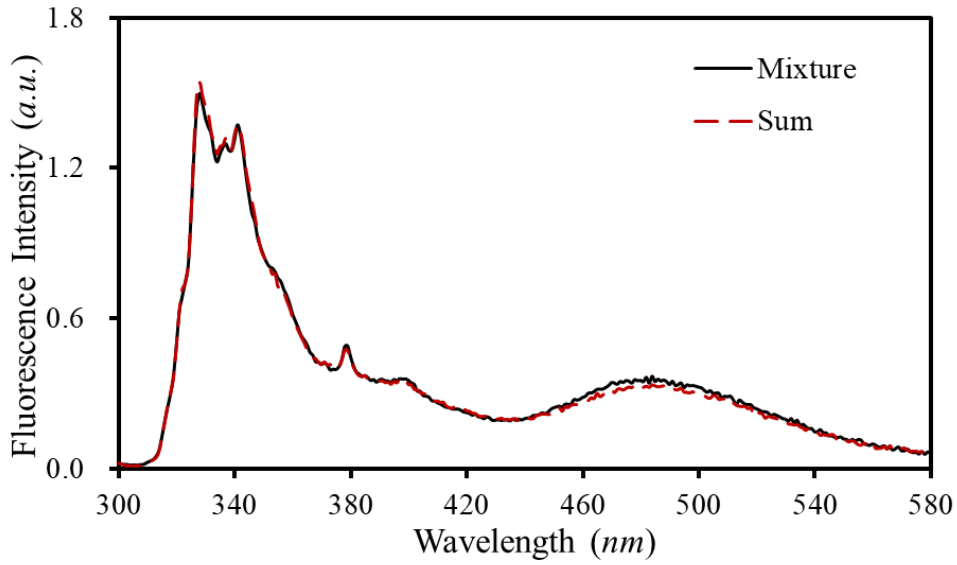


Figure S2.12. Comparison of (red dashed line) the sum of the N2 and P10 fluorescence spectra and (black solid line) the spectrum of the NpC2-PAMAM-G0 and PyC10- PAMAM mixture in 50 mM SDS aqueous solution.

Figure S2.12 indicates that, within experimental error, the spectrum generated by the Mixture-solution overlaps the sum of the fluorescence spectra acquired for the N2 and P10-solutions. This perfect overlap led to the conclusion that FRET could not happen between the NpC2-PAMAM-G0 and PyC10-PAMAM-G0 samples in the 50 mM SDS solution, which demonstrated that the dendrimers existed as isolated molecules in the SDS micelles and that the increase in observed for the PyC10-PAMAM-G0 dendrimer in Figure 1.3C in the main text could not be the result of intermolecular excimer formation inside a same SDS micelle.

The FRET study was then conducted for PyC10-PAMAM-G0 in a 50 mM DTAB aqueous solution and PyC12-PAMAM-G0 in the 50 mM SDS aqueous solution and in the 50 mM DTAB aqueous solution and the comparison of the respective fluorescence spectra is shown in Figures S1.14, S1.15, and S1.16. In each case, a same perfect overlap was found between the fluorescence of the mixture of the NpC2-PAMAM-G0 and PyCX-PAMAM-G0 samples in the 50 mM surfactant aqueous solutions and the fluorescence spectrum obtained by summing the individual fluorescence spectra acquired for the NpC2-PAMAM-G0 and PyCX-PAMAM-G0 samples alone in the 50 mM surfactant aqueous solutions. These results implied that the PyC10- and PyC12-PAMAM-G0 samples were present as isolated macromolecules inside the surfactant micelles and that their increased values could not be the result of intermolecular PEF.

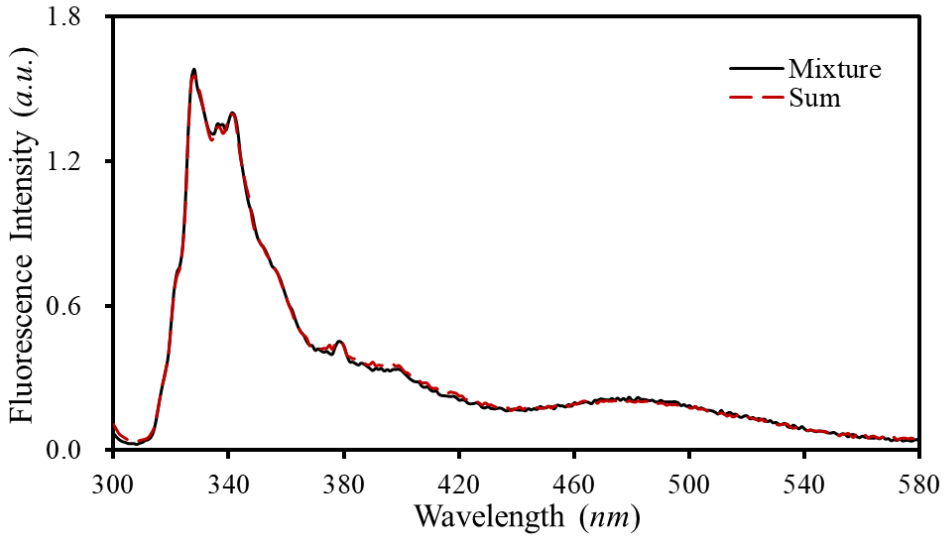


Figure S2.13. Comparison of (dashed red line) the sum of the fluorescence spectra for the NpC2- PAMAM-G0 and PyC12-PAMAM-G0 samples and (black solid line) the fluorescence spectrum of the dendrimer mixture in 50 mM SDS aqueous solution. λ_{ex} = 295 nm.

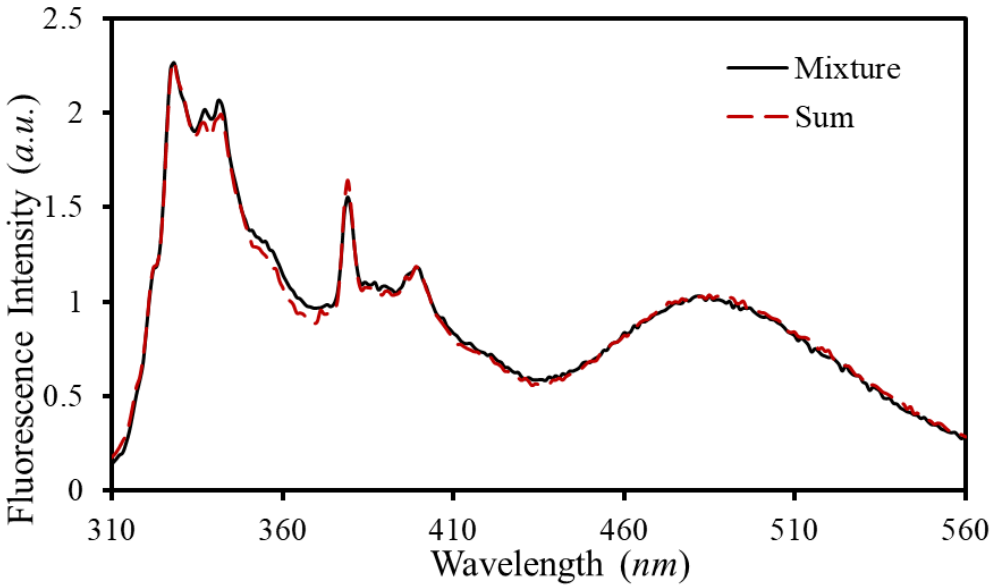


Figure S2.14. Comparison of (dashed red line) the sum of the fluorescence spectra for the NpC2- PAMAM-G0 and PyC10-PAMAM-G0 samples and (black solid line) the fluorescence spectrum of the dendrimer mixture in 50 mM DTAB aqueous solution. λ_{ex} = 295 nm.

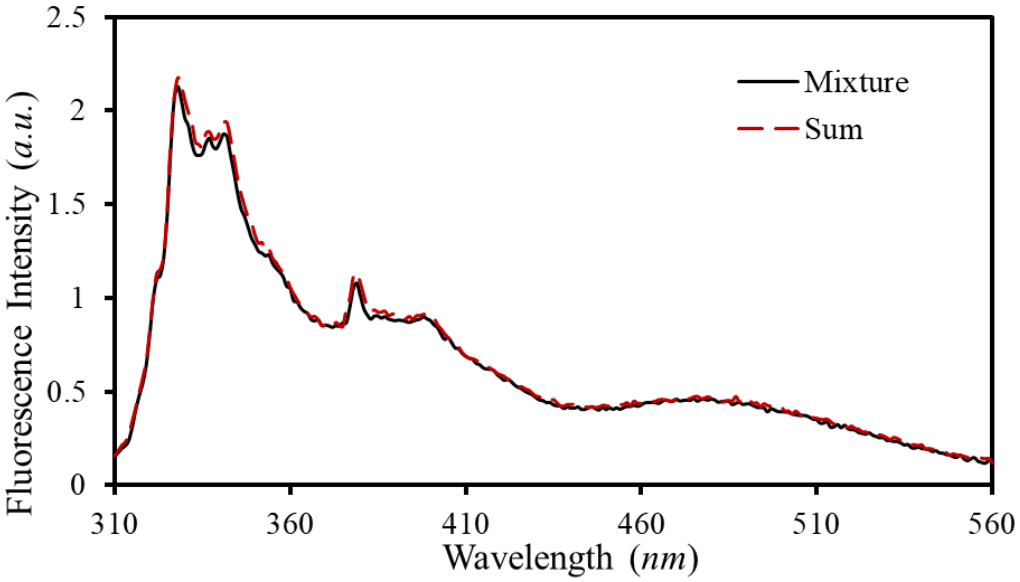


Figure S2.15. Comparison of (dashed red line) the sum of the fluorescence spectra for the NpC2- PAMAM-G0 and PyC12-PAMAM-G0 samples and (black solid line) the fluorescence spectrum of the dendrimer mixture in 50 mM DTAB aqueous solution. λ_{ex} = 295 nm.

E] Global analysis of the monomer and excimer decays of PyCX-PAMAM-G0 using the model free analysis

The fluorescence decays of the pyrene monomer and excimer acquired with the PyCX-PAMAM-G0 samples were fitted globally according to the MFA using Equations S1 and S2, respectively. The parameters in Equations S1 and S2 were optimized according to the Marquardt-Levenberg algorithm.[4] The MFA retrieved the parameters f_{diff} (= $f_{\mathrm{diffE0}} + f_{\mathrm{diffEL}}$), f_{free}, and f_{agg} (= $f_{\mathrm{E0}} + f_{\mathrm{EL}}$), which represent the molar fractions of the pyrene species, which form excimer by diffusion, unreacted pyrene in the solution, and aggregated pyrenes forming excimer by direct excitation.

$$[Py^*]_{(t)} = [Py^*_{diff}]_{(t=0)} \times \sum_{i=1}^{n} a_i \times \exp(-t/\tau_i) + [Py^*_{free}]_{(t=0)} \times \exp(-t/\tau_M) \tag{S2.1}$$

$$[E^*]_{(t)} = -[Py^*_{diff}]_{(t=0)} \times \sum_{i=1}^{n} a_i \frac{\frac{1}{\tau_i} - \frac{1}{\tau_M}}{\frac{1}{\tau_i} - \frac{1}{\tau_{E0}}} \exp(-t/\tau_i) + \left([E0^*]_{(t=0)} + [Py^*_{diff}]_{(t=0)} \times \sum_{i=1}^{n} a_i \frac{\frac{1}{\tau_i} - \frac{1}{\tau_M}}{\frac{1}{\tau_i} - \frac{1}{\tau_{E0}}} \right) \times \exp(-t/\tau_{E0})$$

$$-[Py^*_{diff}]_{(t=0)} \times \sum_{i=1}^{n} a_i \frac{\frac{1}{\tau_i} - \frac{1}{\tau_M}}{\frac{1}{\tau_i} - \frac{1}{\tau_D}} \exp(-t/\tau_i) + \left([D^*]_{(t=0)} + [Py^*_{diff}]_{(t=0)} \times \sum_{i=1}^{n} a_i \frac{\frac{1}{\tau_i} - \frac{1}{\tau_M}}{\frac{1}{\tau_i} - \frac{1}{\tau_D}} \right) \times \exp(-t/\tau_D)$$

$$+ [ES^*]_{(t=0)} \times \exp(-t/\tau_{ES}) \tag{S2.2}$$

F] Parameters obtained from the model free analysis (MFA) of the PyCX-PAMAM-G0 dendrimers

Table S2.1. Parameters retrieved from the MFA of the monomer fluorescence decays of the PyCX-PAMAM-G0 dendrimers in degassed *N,N*-dimethylformamide.

Derivative	a_1	τ_1 **(ns)**	a_2	τ_2 **(ns)**	a_3	τ_3 **(ns)**	f_{Mfree}	τ_M	$\chi 2$
PyC4	0.530	7.470	0.420	12.400	0.000	48.760	0.050	138.000	1.060
PyC6	0.438	6.784	0.541	12.800	0.016	40.888	0.006	132.000	1.201
PyC8	0.610	15.140	0.330	6.570	0.040	39.950	0.020	130.000	1.180
PyC10	0.430	7.986	0.554	14.844	0.012	51.524	0.004	133.000	0.991
PyC12	0.140	4.180	0.740	14.860	0.090	38.550	0.030	130.000	1.050

Table S2.2. Parameters retrieved from the MFA of the excimer fluorescence decays of PyCX-PAMAM-G0 dendrimers in degassed *N,N*-dimethylformamide.

Derivative	f_{diffE0}	f_{EdiffD}	τ_{E0} **(ns)**	τ_D **(ns)**	τ_S **(ns)**	f_{EE0}	f_{ED}	f_{ES}^*	χ^2	f_{agg}
PyC4	0.23	0.42	36.5	51.8	3.5	0.00	0.04	0.31	1.06	**0.040**
PyC6	0.17	0.74	59.5	40.7	-	0.02	0.07	-	1.20	**0.093**
PyC8	0.08	0.82	58.8	46.6	-	0.04	0.05	-	1.18	**0.090**
PyC10	0.19	0.73	56.1	42.3	-	0.01	0.08	-	0.99	**0.087**
PyC12	-	0.93	0	47.0	-	0.00	0.07	-	1.05	**0.070**

Table S2.3. Parameters retrieved from the MFA of the monomer fluorescence decays of PyCX-PAMAM-G0 dendrimers in degassed dimethyl sulfoxide.

Derivative	a_1	τ_1 **(ns)**	a_2	τ_2 **(ns)**	a_3	τ_3 **(ns)**	f_{Mfree}	τ_M	$\chi 2$
PyC4	0.89	5.03	0.07	12.00	0.01	93.81	0.038	173	1.13
PyC6	0.69	5.36	0.27	9.39	0.03	46.27	0.010	161	1.06
PyC8	0.40	4.02	0.55	9.54	0.03	47.74	0.016	161	1.03
PyC10	0.19	4.78	0.74	8.68	0.04	44.84	0.020	161	1.02
PyC12	0.21	4.79	0.67	12.00	0.06	45.81	0.055	161	1.00

Table S2.4. Parameters retrieved from the MFA of the excimer fluorescence decays of PyCX-PAMAM-G0 dendrimers in degassed dimethyl sulfoxide.

Derivative	f_{diff}^{E0}	f_{Ediff}^{D}	τ_{E0} (ns)	τ_D (ns)	τ_S (ns)	f_{EE0}	f_{ED}	f_{ES}^{*}	χ^2	f_{agg}
PyC4	0.30	0.21	52.33	23.54	3.50	0.22	0.00	0.22	1.13	**0.221**
PyC6	0.31	0.66	45.73	50.83	3.50	0.00	0.03	0.00	1.02	**0.028**
PyC8	-	0.97	-	49.99	-	-	0.03	-	1.03	**0.034**
PyC10	0.05	0.88	23.52	50.44	3.50	0.00	0.03	0.04	1.06	**0.027**
PyC12	0.36	0.59	34.65	51.25	-	0.02	0.03	-	1.00	**0.052**

Table S2.5. Parameters retrieved from the MFA of the monomer fluorescence decays of PyCX-PAMAM-G0 dendrimers in 50 mM SDS aqueous solution done in triplicates.

Derivative	a_1	τ_1 (ns)	a_2	τ_2 (ns)	a_3	τ_3 (ns)	f_{Mfree}	τ_M	$\chi 2$
PyC4	0.41	4.83	0.49	10.82	0.03	41.91	0.065	132	1.06
PyC4-2	0.37	4.70	0.54	11.42	0.03	42.39	0.057	132	1.11
PyC4-3	0.26	4.26	0.51	9.51	0.15	19.41	0.077	132	1.11
PyC6	0.24	4.42	0.66	12.40	0.07	30.76	0.036	127	1.19
PyC6-2	0.20	3.14	0.64	10.62	0.15	23.01	0.011	127	1.07
PyC6-3	0.21	4.14	0.71	12.76	0.07	31.45	0.007	127	1.12
PyC8	0.18	3.04	0.55	12.94	0.21	28.42	0.054	127	1.19
PyC8-2	0.20	3.59	0.54	14.01	0.23	29.91	0.034	127	1.10
PyC8-3	0.19	3.48	0.61	14.46	0.17	32.46	0.029	127	1.09
PyC10	0.28	2.98	0.53	11.17	0.15	22.70	0.035	127	0.90
PyC10-2	0.30	2.20	0.53	10.16	0.14	23.65	0.024	127	1.13
PyC10-3	0.28	2.75	0.56	11.71	0.15	24.29	0.011	127	1.08
PyC12	0.28	1.69	0.41	7.74	0.21	20.20	0.103	127	1.14
PyC12-2	0.29	2.09	0.42	8.08	0.21	21.33	0.074	127	1.12
PyC12-3	0.37	2.88	0.49	11.09	0.09	36.71	0.046	127	1.00

Table S2.6. Parameters retrieved from the MFA of the excimer fluorescence decays of PyCX-PAMAM-G0 dendrimers in 50 mM SDS aqueous solution done in triplicates.

Derivative	f_{diffE0}	f_{EdiffD}	τ_{E0} (ns)	τ_D (ns)	τ_S (ns)	f_{EE0}	f_{ED}	f_{ES}	χ^2	f_{agg}	$<f_{agg}>$
PyC4	0.12	0.47	32.9	52.6	3.50	0.00	0.07	0.34	1.06	0.07	
PyC4-2	0.30	0.35	41.8	55.4	3.50	0.00	0.05	0.30	1.10	0.05	**0.05**
PyC4-3	0.10	0.51	30.1	53.4	3.50	0.00	0.02	0.37	1.11	0.02	
PyC6	0.42	0.28	54.6	40.1	3.50	0.08	0.00	0.22	1.19	0.08	
PyC6-2	0.52	0.35	43.6	56.9	3.50	0.02	0.10	0.00	1.07	0.13	**0.10**
PyC6-3	0.65	0.25	50.2	48.2	3.50	0.00	0.10	0.00	1.12	0.10	
PyC8	0.46	0.46	49.9	50.3	3.50	0.00	0.08	0.00	1.19	0.08	
PyC8-2	0.50	0.38	47.3	54.4	3.50	0.01	0.00	0.11	1.10	0.01	**0.03**
PyC8-3	0.55	0.35	50.5	50.6	3.50	0.00	0.01	0.09	1.09	0.01	
PyC10	0.00	0.67	48.2	50.9	3.50	0.09	0.23	0.00	1.07	0.33	
PyC10-2	0.20	0.55	39.0	51.3	3.50	0.00	0.22	0.02	1.13	0.22	**0.24**
PyC10-3	0.04	0.77	43.4	52.7	3.50	0.16	0.02	0.00	1.08	0.18	
PyC12	0.57	0.00	46.4	57.3	3.50	0.17	0.26	0.00	1.14	0.43	
PyC12-2	0.00	0.67	28.0	50.5	3.50	0.46	0.00	0.00	1.12	0.46	**0.40**
PyC12-3	0.04	0.54	48.8	48.5	3.50	0.11	0.20	0.11	1.00	0.31	

Table S2.7. Parameters retrieved from the MFA of the monomer fluorescence decays of the PyCX-PAMAM-G0 dendrimers in 50 mM DTAB solution.

Derivative	a_1	τ_1 (ns)	a_2	τ_2 (ns)	a_3	τ_3 (ns)	f_{Mfree}	τ_M (ns)	$\chi 2$
PyC4	0.39	4.32	0.54	11.3	0.05	65.1	0.019	132	1.14
PyC6	0.23	4.53	0.72	14.4	0.04	40.3	0.003	127	1.08
PyC8	0.172	5.102	0.73	17.7	0.09	47.3	0.009	127	1.08
PyC10	0.16	3.47	0.74	16.4	0.10	35.8	0.003	127	1.08
PyC12	0.28	3.62	0.60	15.5	0.11	41.5	0.015	127	1.22

Table S2.8. Parameters retrieved from the MFA of the excimer fluorescence decays of the PyCX-PAMAM-G0 dendrimers in 50 mM DTAB solution.

Derivative	f_{diffE0}	f_{EdiffD}	τ_{E0} (ns)	τ_D (ns)	τ_S (ns)	f_{EE0}	f_{ED}	f_{ES}	χ^2	f_{agg}
PyC4	0.11	0.49	34.17	48.14	3.50	0.00	0.08	0.32	1.14	**0.08**
PyC6	0.07	0.85	16.02	47.66	3.50	0.00	0.06	0.02	1.08	**0.06**
PyC8	0.61	0.31	47.41	43.94	3.50	0.03	0.00	0.05	1.08	**0.03**
PyC10	0.51	0.39	46.14	50.25	3.50	0.05	0.05	0.00	1.08	**0.10**
PyC12	0.39	0.43	46.49	47.72	3.50	0.00	0.06	0.12	1.22	**0.06**

G] Equations used for the end-to-end distance of the dendrimers

Equation S2.3 was used to calculate the squared average end-to-end distance of the PyCX-PAMAM-G0 dendrimers with *a* (= *X*), *b* (= 7), and *c* (= 4) representing the number of carbon atoms in the linker connecting the pyrene moiety to the PAMAM-G0 dendrimer, the number of non-hydrogen atom in the aminoethyl propionamide building block of the PAMAM dendrimer, and the diaminoethylene core of the dendrimer, respectively.

$$L_{Py}^2(N) = \left(2a + \frac{\left[2 - 2^{N+2} + (N+1) \times 2^{N+3} \right] b + 2^{N+1} c + 2^{N+1} - 1}{2^{N+2} - 1} \right) \times l^2 \qquad \text{(S2.3)}$$

Appendix B: S3-SI for Chapter 3

A] Equations used for the global model free analysis of the monomer and excimer fluorescence decays of the PyCX-PAMAM-G0 samples

The fluorescence decays of the pyrene monomer and excimer acquired with the PyCX-PAMAM-G0 samples were fitted globally according to the MFA using Equations S3.1 and S3.2, respectively. The parameters in Equations S3.1 and S3.2 were optimized according to the Marquardt-Levenberg algorithm.[48] The MFA retrieved the parameters f_{diff} ($= f_{\text{diffE0}} + f_{\text{diffEL}}$), f_{free}, and f_{agg} ($= f_{\text{E0}} + f_{\text{EL}}$), which represent the molar fractions of the pyrene species, which form excimer by diffusion, unreacted pyrenyl derivatives in the solution, and aggregated pyrenes forming excimer by direct excitation.

$$[Py^*]_{(t)} = [Py^*_{diff}]_{(t=0)} \times \sum_{i=1}^{n} a_i \times \exp(-t/\tau_i) + [Py^*_{free}]_{(t=0)} \times \exp(-t/\tau_M) \tag{S3.1}$$

$$[E^*]_{(t)} = -[Py^*_{diff}]_{(t=0)} \times \sum_{i=1}^{n} a_i \frac{\frac{1}{\tau_i} - \frac{1}{\tau_M}}{\frac{1}{\tau_i} - \frac{1}{\tau_{E0}}} \exp(-t/\tau_i) + \left([E0^*]_{(t=0)} + [Py^*_{diff}]_{(t=0)} \times \sum_{i=1}^{n} a_i \frac{\frac{1}{\tau_i} - \frac{1}{\tau_M}}{\frac{1}{\tau_i} - \frac{1}{\tau_{E0}}} \right) \times \exp(-t/\tau_{E0})$$

$$-[Py^*_{diff}]_{(t=0)} \times \sum_{i=1}^{n} a_i \frac{\frac{1}{\tau_i} - \frac{1}{\tau_M}}{\frac{1}{\tau_i} - \frac{1}{\tau_D}} \exp(-t/\tau_i) + \left([D^*]_{(t=0)} + [Py^*_{diff}]_{(t=0)} \times \sum_{i=1}^{n} a_i \frac{\frac{1}{\tau_i} - \frac{1}{\tau_M}}{\frac{1}{\tau_i} - \frac{1}{\tau_D}} \right) \times \exp(-t/\tau_D)$$

$$+[ES^*]_{(t=0)} \times \exp(-t/\tau_{ES}) \tag{S3.2}$$

B] Parameters obtained from the model free analysis (MFA) of the fluorescence decays acquired with the PyCX-PAMAM-G0 samples

Table S3.1. Parameters retrieved from the MFA of the monomer fluorescence decays of the PyCX-PAMAM-G0 dendrimers in 5 mM DTAB and 45 mM SDS aqueous solution.

Derivative	a_1	τ_1 (ns)	a_2	τ_2 (ns)	a_3	τ_3 (ns)	f_{Mfree}	τ_M	$\chi 2$
PyC4	0.25	4.28	0.63	11.41	0.05	38.45	0.059	132	1.07
PyC6	0.30	6.00	0.60	13.66	0.10	27.03	0.010	127	1.24
PyC8	0.20	3.67	0.59	14.88	0.17	33.74	0.029	127	1.06
PyC10	0.31	2.62	0.58	11.09	0.10	27.30	0.012	127	1.16
PyC12	0.42	2.04	0.43	10.00	0.10	36.63	0.043	127	0.99

Table S3.2. Parameters retrieved from the MFA of the excimer fluorescence decays of the PyCX-PAMAM-G0 dendrimers in 5 mM DTAB and 45 mM SDS aqueous solution.

Derivative	f_{diffE0}	f_{EdiffD}	τ_{E0} (ns)	τ_D (ns)	τ_S (ns)	f_{EE0}	f_{ED}	f_{ES}^*	χ^2	f_{agg}
PyC4	0.13	0.51	44.8	49.6	3.5	0.04	0.00	0.32	1.07	**0.05**
PyC6	0.31	0.59	47.0	49.4	3.5	0.01	0.08	0.01	1.24	**0.09**
PyC8	0.49	0.41	47.6	47.6	3.5	0.00	0.01	0.08	1.06	**0.01**
PyC10	0.12	0.62	52.7	47.6	3.5	0.16	0.10	0.00	1.16	**0.27**
PyC12	0.00	0.51	40.8	49.5	3.5	0.24	0.21	0.04	0.99	**0.45**

Table S3.3. Parameters retrieved from the MFA of the monomer fluorescence decays of the PyCX-PAMAM-G0 dendrimers in 10 mM DTAB and 40 mM SDS aqueous solution done in triplicates.

Derivative	a_1	τ_1 (ns)	a_2	τ_2 (ns)	a_3	τ_3 (ns)	f_{Mfree}	τ_M	$\chi 2$
PyC4	0.28	4.90	0.61	14.52	0.05	46.53	0.06	132	1.07
PyC4-2	0.33	5.89	0.56	15.04	0.06	44.15	0.06	132	1.15
PyC4-3	0.15	4.53	0.62	13.57	0.17	29.12	0.06	132	1.04
PyC6	0.22	4.79	0.66	15.01	0.11	33.96	0.01	127	1.12
PyC6-2	0.19	3.46	0.64	13.87	0.16	30.00	0.01	127	1.16
PyC6-3	0.19	4.26	0.65	15.97	0.16	32.63	0.01	127	1.03
PyC8	0.22	3.65	0.49	14.99	0.26	33.24	0.03	127	1.13
PyC8-2	0.21	3.58	0.50	15.73	0.26	35.60	0.03	127	1.13
PyC8-3	0.19	4.60	0.47	16.70	0.30	36.02	0.03	127	1.08
PyC10	0.31	4.32	0.49	15.02	0.19	31.32	0.01	127	1.07
PyC10-2	0.30	3.38	0.50	13.64	0.19	30.07	0.01	127	1.19
PyC10-3	0.25	13.71	0.46	13.71	0.28	28.89	0.01	127	1.13
PyC12	0.34	4.13	0.44	14.39	0.18	35.09	0.03	127	1.03
PyC12-2	0.31	3.14	0.46	11.63	0.21	30.75	0.03	127	1.19
PyC12-3	0.33	4.68	0.43	16.28	0.21	36.69	0.03	127	1.05

Table S3.4. Parameters retrieved from the MFA of the excimer fluorescence decays of the PyCX-PAMAM-G0 dendrimers in 10 mM DTAB and 40 mM SDS aqueous solution done in triplicates.

Derivative	f_{diffE0}	f_{EdiffD}	τ_{E0} (ns)	τ_D (ns)	τ_S (ns)	f_{EE0}	f_{ED}	f_{ES}	χ^2	f_{agg}	$\langle f_{agg} \rangle$
PyC4	0.18	0.44	43.6	52.3	3.50	0.00	0.03	0.35	1.07	0.03	**0.05**
PyC4-2	0.30	0.35	48.9	48.9	3.50	0.02	0.03	0.33	1.15	0.05	
PyC4-3	0.27	0.33	43.5	55.1	3.50	0.00	0.06	0.35	1.04	0.06	
PyC6	0.39	0.52	49.4	49.4	3.50	0.01	0.06	0.02	1.12	0.07	**0.06**
PyC6-2	0.43	0.49	48.9	49.2	3.50	0.00	0.04	0.04	1.16	0.04	
PyC6-3	0.53	0.40	51.8	47.4	3.50	0.00	0.06	0.01	1.03	0.06	
PyC8	0.50	0.41	47.6	47.6	3.50	0.00	0.00	0.09	1.13	0.00	**0.02**
PyC8-2	0.45	0.46	47.0	47.4	3.50	0.00	0.00	0.08	1.13	0.00	
PyC8-3	0.37	0.54	48.5	49.6	3.50	0.00	0.04	0.06	1.08	0.04	
PyC10	0.44	0.43	49.3	48.6	3.50	0.05	0.09	0.00	1.07	0.13	**0.11**
PyC10-2	0.42	0.48	48.0	49.9	3.50	0.05	0.05	0.00	1.19	0.10	
PyC10-3	0.34	0.56	51.2	49.4	3.50	0.01	0.10	0.00	1.13	0.10	
PyC12	0.22	0.65	47.6	48.0	3.50	0.04	0.04	0.05	1.03	0.09	**0.07**
PyC12-2	0.45	0.45	47.8	47.9	3.50	0.01	0.02	0.06	1.19	0.04	
PyC12-3	0.43	0.46	49.7	48.3	3.50	0.00	0.07	0.03	1.05	0.08	

Table S3.5. Parameters retrieved from the MFA of the monomer fluorescence decays of the PyCX-PAMAM-G0 dendrimers in 12.5 mM DTAB and 37.5 mM SDS aqueous solution.

Derivative	a_1	τ_1 (ns)	a_2	τ_2 (ns)	a_3	τ_3 (ns)	f_{Mfree}	τ_M (ns)	$\chi 2$
PyC4	0.28	4.67	0.59	14.04	0.07	45.66	0.06	132	1.03
PyC6	0.19	4.28	0.66	14.67	0.13	32.93	0.01	127	1.03
PyC8	0.22	4.02	0.52	16.55	0.23	36.51	0.03	127	1.05
PyC10	0.32	5.71	0.41	16.09	0.26	29.58	0.01	127	1.19
PyC12	0.30	4.68	0.46	15.82	0.22	36.52	0.02	127	1.04

Table S3.6. Parameters retrieved from the MFA of the excimer fluorescence decays of the PyCX-PAMAM-G0 dendrimers in 12.5 mM DTAB and 37.5 mM SDS aqueous solution.

Derivative	f_{diffE0}	f_{EdiffD}	τ_{E0} (ns)	τ_D (ns)	τ_S (ns)	f_{EE0}	f_{ED}	f_{ES}	χ^2	f_{agg}
PyC4	0.30	0.34	44.3	51.3	3.5	0.00	0.01	0.34	1.03	0.01
PyC6	0.26	0.66	47.9	47.0	3.5	0.00	0.07	0.01	1.03	0.07
PyC8	0.34	0.58	46.8	47.5	3.5	0.00	0.00	0.08	1.05	0.00
PyC10	0.60	0.31	46.0	47.5	3.5	0.04	0.05	0.00	1.19	0.09
PyC12	0.51	0.40	45.8	45.8	3.5	0.02	0.02	0.06	1.04	0.03

Table S3.7. Parameters retrieved from the MFA of the monomer fluorescence decays of the PyCX-PAMAM-G0 dendrimers in 15 mM DTAB and 35 mM SDS aqueous solution.

Derivative	a_1	τ_1 (ns)	a_2	τ_2 (ns)	a_3	τ_3 (ns)	f_{Mfree}	τ_M	$\chi 2$
PyC4	0.30	4.95	0.61	15.60	0.05	55.48	0.04	132	1.07
PyC6	0.21	4.48	0.67	16.30	0.11	37.01	0.01	127	1.06
PyC8	0.20	5.04	0.51	20.98	0.27	42.05	0.03	127	1.20
PyC10	0.20	5.10	0.40	18.16	0.39	36.19	0.01	120	1.08
PyC12	0.16	4.46	0.38	15.25	0.42	37.96	0.03	120	1.12

Table S3.8. Parameters retrieved from the MFA of the excimer fluorescence decays of the PyCX-PAMAM-G0 dendrimers in 15 mM DTAB and 35 mM SDS aqueous solution.

Derivative	f_{diff}^{E0}	f_{Ediff}^{D}	τ_{E0} (ns)	τ_D (ns)	τ_S (ns)	f_{EE0}	f_{ED}	f_{ES}^{*}	χ^2	f_{agg}
PyC4	0.30	0.35	49.07	49.08	3.50	0.00	0.01	0	1.07	0.01
PyC6	0.55	0.37	48.30	48.31	3.50	0.01	0.04	0	1.06	0.05
PyC8	0.38	0.54	49.27	48.37	3.50	0.00	0.00	0	1.20	0.00
PyC10	0.67	0.29	50.24	48.46	3.50	0.02	0.01	0	1.08	0.02
PyC12	0.49	0.44	48.23	50.22	3.50	0.00	0.00	0	1.12	0.00

C] Equation used for the probability of finding two pyrenyl ends in a PyCX-PAMAM-G0 dendrimer within a distance r from each other

The PyCX-PAMAM-G0 dendrimers were parametrized according to Figure S3.1, where the parameters *a*, *b*, and *c* are the number of non-hydrogen atoms in the segments separating two pyrenyl groups and equal *X*, 7, and 4, respectively. Figure S3.1 indicates that one excited pyrene is separated from one ground-state pyrene by $2a + 2b + 1$ atoms and it is separated from two ground-state pyrenes by $2a + 2b + c$ atoms. Assuming that the internal segments separating every two pyrenyl labels obey Gaussian Statistics, the probability ($W(r)$) of finding one ground-state pyrene from one excited pyrene used to calculate the radial distribution function ($r^2 \times W(r)$) is given by Equation S3.3, where $\beta_1^2 = 3/(2\times(2a+2b+1)l^2)$ and $\beta_2^2 = 3/(2\times(2a+2b+c)l^2)$ and l is an average bond length.

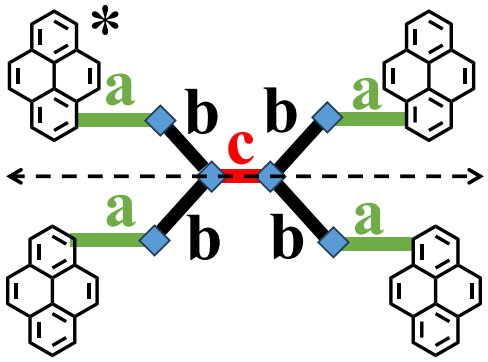


Figure S3.1. Parametrization of the PyCX-PAMAM-G0 dendrimers

$$W(r) = \frac{1}{3} \times \left[\left(\frac{\beta_1}{\sqrt{\pi}} \right)^3 e^{-\beta_1^2 r^2} + 2 \left(\frac{\beta_2}{\sqrt{\pi}} \right)^3 e^{-\beta_2^2 r^2} \right] \tag{S3.3}$$

Integration of the radial distribution function yields L_{Py}^2 given in Equation 3.4 in the main text.

Appendix C: S4-SI for Chapter 4

A] Materials, sample preparation, instruments, and analyzing methods

Materials: The synthesis and characterization by ^{1}H NMR and mass spectrometry of the PyCX-PAMAM-G0 samples with X = 4, 6, 8, 10, and 12 has been reported in earlier publications.[1-3] Omnipur® sodium dodecyl sulfate (SDS, >99%) and Sodium Chloride (99%) were purchased from Aldrich and used as received. Doubly distilled deionized water from Millipore Milli-RO 10 Plus and Milli-Q UF Plus (Bedford, MA) was used to prepare all aqueous solutions.

PyCX-PAMAM-G0 sample preparation: The procedure established in an earlier study was followed. The PyCX-PAMAM-G0 dendrimers and SDS were first suspended in chloroform, before evaporating the solvent under a gentle air stream resulting in a thin layer of white powder at the bottom of the round bottom flask. Upon rehydration with the appropriate amount of water, clear solutions of the PyCX-PAMAM-G0 samples were obtained in 50 mM SDS solutions. Since the 50 mM SDS concentration exceeded the 8 mM critical micelle concentration, SDS micelles formed that provided the hydrophobic environment required for the solvation of the 1-pyrenealkanoyl groups of the PyCX-PAMAM-G0 samples. Consequently, the solution exhibited well-defined absorption bands suggesting that the pyrenyl groups were well solvated. Furthermore, the pyrene excimer fluorescence decays showed a defined rise time as expected for excimer formation through diffusive encounters between solvated pyrenyl moieties. The NaCl concentration in the 50 mM SDS aqueous solution was adjusted from 0 to 100 mM and from 100 to 620 mM by adding a minimum volume of a 1 M or 5 M NaCl, respectively.

UV-Vis absorption measurements: To obtain a reasonable signal-to-noise ratio, the absorption spectra of dilute 0.3 × 10^{-6} M and 0.6 × 10^{-6} M PyCX-PAMAM-G0 aqueous solutions containing 50 mM SDS were measured using a 5.0 cm pathlength quartz cell on a Cary 100 UV-Visible spectrophotometer.

Steady-state fluorescence: The xenon arc-lamp of a HORIBA QM-400 spectrofluorometer was used to excite the PyCX-PAMAM-G0 at 344 nm. The fluorescence spectra of the PyCX-PAMAM-G0 solutions were acquired from 350 to 650 nm with a 1 nm slit width on the excitation and emission monochromators. Integration of the fluorescence spectra from 376 to 382 nm and from 500 to 530 nm yielded the fluorescence intensity of the pyrene monomer (I_M) and excimer (I_E), respectively. The I_E/I_M(SSF) ratio was obtained by dividing I_E by I_M, which was taken as a measure of the PEF efficiency for a given PyCX-PAMAM-G0 solution.

Time-resolved fluorescence: A FluoroHub time-resolved fluorometer from HORIBA was employed to obtain the pyrene monomer and excimer fluorescence decays of the PyCX-PAMAM-G0 aqueous solutions. The solutions were excited with a 336 nm DeltaDiode laser. Both pyrene monomer and excimer fluorescence decays had 20,000 counts at their decay maximum and were acquired at 379 and 510 nm over 1,024 channels with a time-per-channel of 0.44 and 0.87 ns and a 370 and 495 nm cut off filter, respectively. The cut off filters were inserted at the entrance of the emission monochromator to prevent stray light from reaching the photomultiplier tube detector. A triangular aluminium monolith was used for the instrument response function, which was obtained by setting the emission wavelength at the same 336 nm excitation wavelength.

Global model free analysis of the monomer and excimer fluorescence decays: The fluorescence emitted by pyrene-labeled macromolecules (PyLM) is due to three pyrene species, whose behavior is well-described by the MFA.[4] They are the species Py_{diff}*, Py_{free}*, and Py_{agg}*. Py_{diff}* describes those pyrenyl labels (Py_{diff}*) forming excimer by diffusive encounters. The species Py_{free}* represents pyrenyl labels that are not attached to the macromolecule and emit with their lifetime (τ_M). The species Py_{agg}* represents the two pyrene subspecies *E*0* and *D** that are well and poorly stacked with a ground-state pyrene label and emit with a shorter and longer lifetimes τ_{E0} and τ_D, respectively. The global MFA of the pyrene monomer and excimer fluorescence

decays yields the molar fractions f_{diff}, f_{free}, f_{E0}, and f_D of the pyrene species Py_{diff}*, Py_{free}*, $E0$*, and D*, respectively, with f_{agg} being equal to the sum $f_{E0} + f_D$ representing the aggregated pyrenes (Py_{agg}*).

The MFA acknowledges that any fluorescence decay can be fitted with a sum of exponentials. Consequently, the sum of exponentials shown in Equation S4.1 is used to fit the pyrene monomer fluorescence decays. The front part of Equation S4.1 describes PEF by diffusive encounters whereas the exponential with the longest lifetime τ_M represents the species Py_{free}*. Equation S4.2 was derived from the classic kinetic scheme for pyrene excimer formation and is used to the pyrene excimer fluorescence decays. The Marquardt-Levenberg algorithm[5] was used to optimize the parameters in Equations S1 and S2. These parameters were used to determine the molar fractions f_{diff} ($= f_{diffE0} + f_{diffD}$), f_{free}, and f_{agg} ($= f_{E0} + f_D$), which represent the molar fractions of the pyrene species, which form excimer by diffusion, do not form excimer, and are aggregated and form excimer by direct excitation.

$$[Py^*]_{(t)} = [Py^*_{diff}]_{(t=0)} \times \sum_{i=1}^{n} a_i \times \exp(-t/\tau_i) + [Py^*_{free}]_{(t=0)} \times \exp(-t/\tau_M) \tag{S4.1}$$

$$[E^*]_{(t)} = -[Py^*_{diff}]_{(t=0)} \times \sum_{i=1}^{n} a_i \frac{\frac{1}{\tau_i} - \frac{1}{\tau_M}}{\frac{1}{\tau_i} - \frac{1}{\tau_{E0}}} \exp(-t/\tau_i) + \left([E0^*]_{(t=0)} + [Py^*_{diff}]_{(t=0)} \times \sum_{i=1}^{n} a_i \frac{\frac{1}{\tau_i} - \frac{1}{\tau_M}}{\frac{1}{\tau_i} - \frac{1}{\tau_{E0}}} \right) \times \exp(-t/\tau_{E0})$$

$$-[Py^*_{diff}]_{(t=0)} \times \sum_{i=1}^{n} a_i \frac{\frac{1}{\tau_i} - \frac{1}{\tau_M}}{\frac{1}{\tau_i} - \frac{1}{\tau_D}} \exp(-t/\tau_i) + \left([D^*]_{(t=0)} + [Py^*_{diff}]_{(t=0)} \times \sum_{i=1}^{n} a_i \frac{\frac{1}{\tau_i} - \frac{1}{\tau_M}}{\frac{1}{\tau_i} - \frac{1}{\tau_D}} \right) \times \exp(-t/\tau_D)$$

$$+ [ES^*]_{(t=0)} \times \exp(-t/\tau_{ES}) \tag{S4.2}$$

The pre-exponential factors (a_i) and decay times (τ_i) obtained from the MFA of the fluorescence decays in the front part of Equation S4.1 were used to calculate the average lifetime $<\tau>$ with

Equation S4.3. $<\tau>$ could then be used to determine $<k>$ according to Equation S4.4.

$$<\tau>=\frac{\sum_{i=1}^{n} a_i \tau_i}{\sum_{i=1}^{n} a_i} \tag{S4.3}$$

$$<k>=\frac{1}{<\tau>}-\frac{1}{\tau_M} \tag{S4.4}$$

In the global MFA of the pyrene monomer and excimer fluorescence decays, the IRF was convoluted with Equations S1 and S2 and both convolution products were compared with the experimental decays after optimization of the MFA parameters according to the Marquardt-Levenberg algorithm.**Error! Bookmark not defined.** A fit was deemed satisfactory if the global χ^2 was smaller than 1.3 and the residuals and autocorrelation of the residuals were randomly distributed around zero.

B] UV-vis spectra of *PyCX-PAMAM-G0* in NSSA at various NaCl concentration.

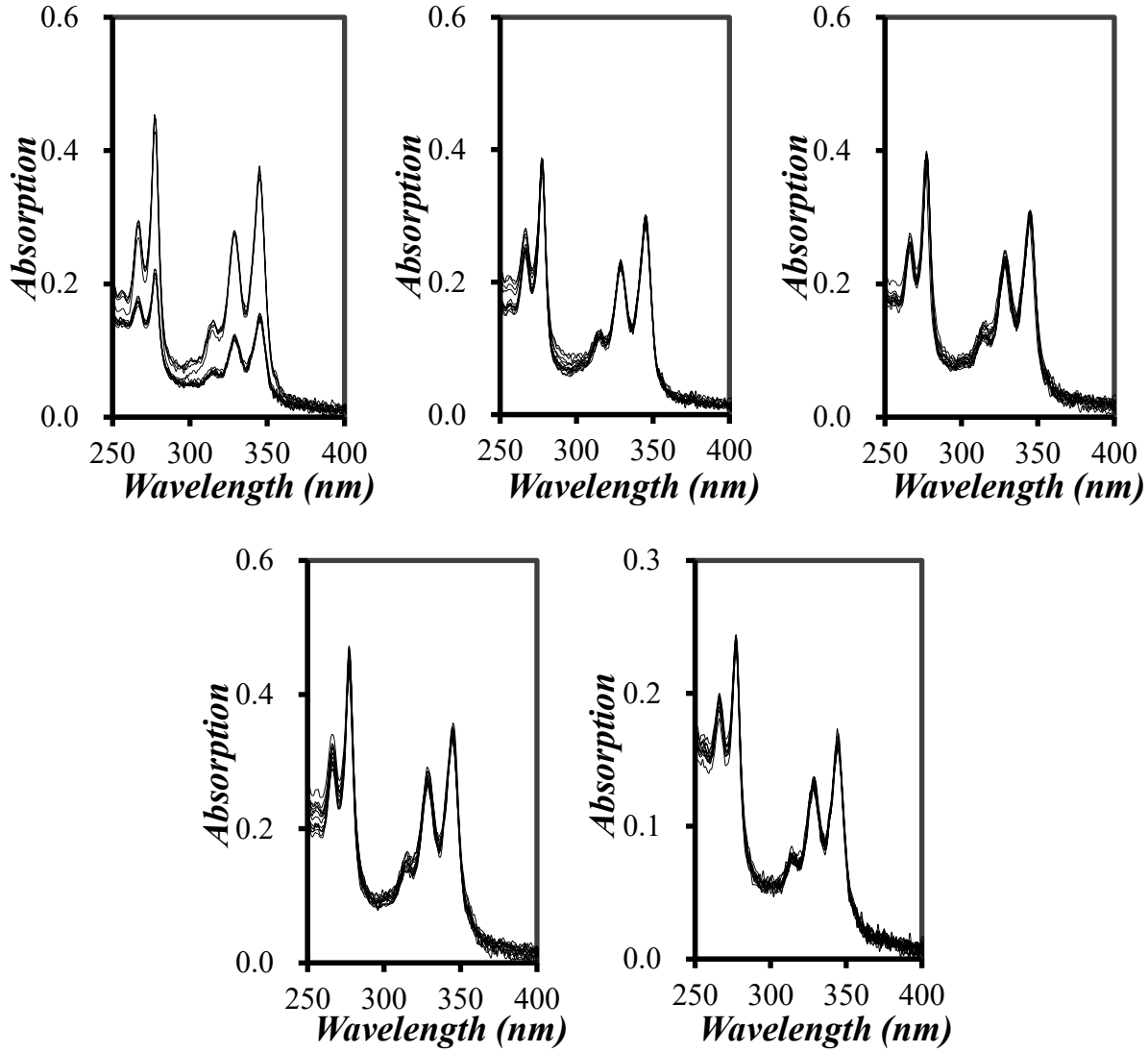


Figure S4.1. Baseline corrected UV-Vis absorption spectra of (top left) PyC4-PAMAM-G0, (top middle) PyC6-PAMAM-G0, (top right) PyC8-PAMAM-G0, (bottom left) PyC10-PAMAM-G0, and (bottom right) PyC12-PAMAM-G0 in 50 mM SDS aqueous solution with [NaCl] ranging from 0 to 620 mM. No significant absorption is observed at longer wavelength. The difference in absorption observed in top left figure is because the UV-vis experiment is conducted separately under 0-100mM and 200mM-620 mM range of [NaCl] with different PyC4-PAMAM-G0 concentrations. The different concentrations used in these experiments had no affect on their conformation and the fluorescence results.

C] Fluorescence spectra of the PyCX-PAMAM-G0 samples in 50 mM SDS aqueous solutions at various NaCl concentrations.

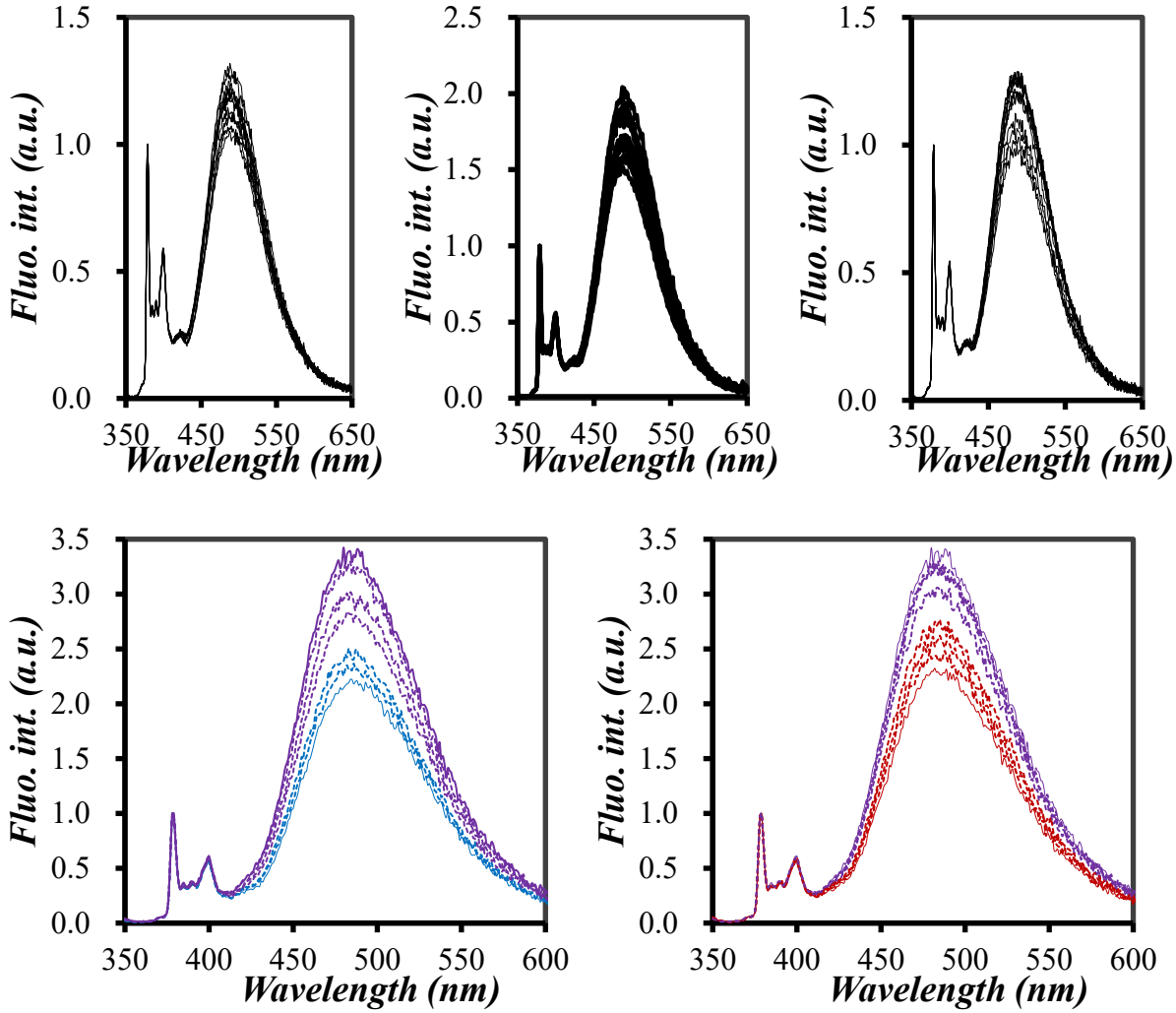


Figure S4.2. Fluorescence spectra of (top left) PyC4-PAMAM-G0, (top middle) PyC6-PAMAM-G0, and (top right) PyC8-PAMAM-G0 in 50 mM SDS aqueous solution with [NaCl] ranging from 0 to 620 mM showing a small variation with ionic strength, and fluorescence spectra of PyC10-PAMAM-G0 in 50 mM SDS aqueous solution with [NaCl] ranging from (bottom left) 0 to 200 mM showing a significant increase pyrene excimer fluorescence, and (bottom right) from 200 to 620 mM exhibiting an equivalent decrease in pyrene excimer fluorescence. The trends in Figures S4.2D and E resemble the ones obtained for PyC12-PAMAM-G0 presented in the main text and these variations in pyrene excimer fluorescence

were due to a similar conformational inversion.

D] Parameters obtained from the model free analysis (MFA) of the PyCX-PAMAM-G0 dendrimers

Table S4.1. Parameters retrieved from the MFA of the monomer fluorescence decays of the PyCX-PAMAM-G0 dendrimers in 50 mM SDS aqueous at various NaCl concentrations.

Linker	[NaCl] *(mM)*	a_1	τ_1 *(ns)*	a_2	τ_2 *(ns)*	a_3	τ_3 *(ns)*	f_{Mfree}	τ_M *(ns)*	χ^2
C4	0	0.34	5.33	0.50	11.68	0.06	32.05	0.102	132	1.06
	11	0.28	4.56	0.56	10.96	0.06	33.17	0.101		1.20
	20	0.36	5.20	0.45	11.91	0.09	25.29	0.103		1.13
	49	0.32	4.94	0.51	11.42	0.07	31.92	0.101		1.08
	93	0.29	5.19	0.48	11.56	0.12	25.53	0.108		1.17
	193	0.39	5.51	0.47	12.85	0.11	26.72	0.036		1.16
	284	0.34	5.60	0.49	13.39	0.13	26.60	0.040		1.19
	373	0.41	6.09	0.38	13.63	0.16	24.89	0.039		1.05
	458	0.25	5.03	0.50	12.61	0.20	25.16	0.042		1.20
	541	0.35	5.40	0.52	14.81	0.09	30.38	0.040		1.07
	566	0.32	5.31	0.51	14.63	0.14	28.18	0.041		1.22
	592	0.34	5.40	0.51	14.74	0.11	29.20	0.040		1.11
	618	0.31	5.68	0.50	14.74	0.14	28.01	0.044		1.10

Linker	[NaCl] *(mM)*	a_1	τ_1 *(ns)*	a_2	τ_2 *(ns)*	a_3	τ_3 *(ns)*	f_{Mfree}	τ_M *(ns)*	χ^2
C6	0	0.19	4.50	0.69	12.21	0.11	26.91	0.014	127	1.08
	10	0.23	5.27	0.65	12.45	0.11	26.97	0.014		1.10
	20	0.34	5.32	0.62	13.24	0.03	39.06	0.013		1.07
	48	0.27	5.31	0.65	13.66	0.07	32.97	0.017		1.15
	92	0.34	5.52	0.60	13.65	0.04	40.15	0.015		1.19
	198	0.18	3.89	0.72	12.73	0.09	31.56	0.011		1.15
	289	0.16	3.70	0.63	11.55	0.20	23.13	0.014		1.18
	376	0.19	3.79	0.71	12.31	0.09	29.23	0.013		1.19
	460	0.20	4.05	0.64	12.58	0.16	27.21	0.014		1.00
	542	0.26	5.44	0.60	13.96	0.13	27.92	0.015		1.10
	567	0.21	4.80	0.62	13.95	0.16	28.75	0.015		1.16
	593	0.25	5.59	0.56	14.14	0.17	26.30	0.016		1.27

	617	0.16	3.73	0.69	14.80	0.13	33.27	0.015		1.16

Linker	[NaCl] *(mM)*	a_1	τ_1 *(ns)*	a_2	τ_2 *(ns)*	a_3	τ_3 *(ns)*	f_{Mfree}	τ_M *(ns)*	χ^2
C8	0	0.26	5.367	0.57	15.26	0.13	33.33	0.036	127	1.19
	10	0.19	4.13	0.62	13.83	0.16	33.09	0.033		1.11
	19	0.19	3.657	0.65	13.03	0.13	32.18	0.034		1.18
	47	0.21	4.69	0.60	14.15	0.15	33.64	0.036		1.12
	92	0.26	3.86	0.56	13.36	0.14	30.85	0.036		1.13
	198	0.29	4.08	0.54	14.89	0.14	33.44	0.037		1.15
	288	0.21	3.10	0.53	12.24	0.22	29.42	0.040		1.07
	382	0.33	3.64	0.53	15.00	0.10	36.33	0.037		1.15
	461	0.23	2.86	0.50	12.47	0.23	30.33	0.041		1.14
	542	0.30	3.60	0.49	15.25	0.18	33.26	0.040		1.15
	570	0.25	3.79	0.57	16.21	0.14	39.97	0.038		1.20
	595	0.28	3.59	0.51	15.68	0.17	33.52	0.040		1.21
	621	0.24	4.13	0.55	16.74	0.17	37.77	0.041		1.20

Linker	[NaCl] *(mM)*	a_1	τ_1 *(ns)*	a_2	τ_2 *(ns)*	a_3	τ_3 *(ns)*	f_{Mfree}	τ_M *(ns)*	χ^2
C10	0	0.28	2.55	0.55	11.43	0.14	26.54	0.027	132	1.13
	11	0.36	2.51	0.54	11.27	0.07	31.55	0.025		1.14
	20	0.34	1.83	0.52	10.25	0.11	26.86	0.026		1.11
	48	0.39	2.08	0.49	9.96	0.09	26.78	0.028		1.19
	93	0.39	1.74	0.46	9.00	0.12	23.96	0.030		1.12
	193	0.38	1.39	0.34	6.28	0.20	15.52	0.072		1.01
	286	0.38	1.32	0.31	6.02	0.24	15.33	0.070		1.05
	375	0.37	1.86	0.34	6.78	0.22	17.05	0.076		1.18
	460	0.37	1.79	0.31	7.73	0.25	17.96	0.075		1.19
	542	0.36	2.29	0.35	10.07	0.22	20.84	0.075		1.15
	566	0.31	1.93	0.41	10.20	0.25	25.39	0.026		1.19
	591	0.32	2.35	0.44	11.55	0.22	27.14	0.027		1.15
	622	0.28	2.20	0.26	8.83	0.39	21.61	0.071		1.08

Linker	[NaCl] *(mM)*	a_1	τ_1 *(ns)*	a_2	τ_2 *(ns)*	a_3	τ_3 *(ns)*	f_{Mfree}	τ_M *(ns)*	χ^2
C12	0	0.32	2.98	0.49	11.95	0.12	35.32	0.065	127	1.19
	10	0.34	2.25	0.48	10.57	0.11	34.29	0.065		1.19
	20	0.36	1.67	0.44	9.34	0.13	30.30	0.069		1.05
	48	0.41	1.90	0.42	9.99	0.10	35.35	0.071		1.11
	94	0.45	2.28	0.38	10.72	0.09	34.52	0.080		1.07
	193	0.40	1.59	0.40	8.24	0.12	29.48	0.076		1.11
	284	0.44	2.16	0.39	9.62	0.09	33.86	0.078		1.11
	372	0.40	1.98	0.38	8.44	0.14	26.81	0.075		1.15
	459	0.40	2.16	0.41	9.82	0.11	32.39	0.070		1.10
	537	0.38	2.23	0.41	10.76	0.14	32.01	0.066		1.13
	562	0.34	2.31	0.42	9.90	0.17	30.70	0.064		1.13
	589	0.31	2.04	0.41	10.18	0.22	29.25	0.064		1.18
	615	0.35	2.65	0.40	11.86	0.18	31.26	0.062		1.13

Table S4.2. Parameters retrieved from the MFA of the excimer fluorescence decays of PyCX-PAMAM-G0 dendrimers in 50 mM SDS aqueous solution at various NaCl concentrations.

Linker	[NaCl] *(mM)*	$f_{EdiffE0}$	f_{EdiffD}	τ_{E0} *(ns)*	τ_D *(ns)*	τ_S *(ns)*	f_{EE0}	f_{ED}	f_{ES}^*	χ^2
C4	0	0.26	0.39	40.05	54.22	3.5	0.00	0.09	0.26	1.06
	11	0.33	0.33	43.21	55.40		0.00	0.04	0.29	1.20
	20	0.31	0.36	37.87	55.30		0.00	0.06	0.27	1.13
	49	0.30	0.38	44.70	53.57		0.00	0.01	0.31	1.08
	93	0.31	0.36	38.74	55.34		0.00	0.06	0.26	1.17
	193	0.26	0.34	44.90	56.20		0.00	0.01	0.39	1.16
	284	0.26	0.33	40.15	57.57		0.00	0.03	0.04	1.19
	373	0.26	0.33	43.65	56.87		0.00	0.01	0.40	1.05
	458	0.24	0.36	39.40	56.77		0.00	0.04	0.36	1.20
	541	0.33	0.27	57.02	44.14		0.01	0.00	0.38	1.07
	566	0.25	0.35	42.36	55.32		0.00	0.04	0.36	1.22
	592	0.25	0.36	42.26	56.37		0.00	0.01	0.38	1.11
	618	0.26	0.34	38.37	57.37		0.00	0.04	0.36	1.10

Linker	[NaCl] *(mM)*	$f_{EdiffE0}$	f_{EdiffD}	τ_{E0} *(ns)*	τ_D *(ns)*	τ_S *(ns)*	f_{EE0}	f_{ED}	f_{ES}^*	χ^2
C4	0	0.49	0.40	40.77	57.38	3.5	0.00	0.06	0.05	1.08
	10	0.23	0.64	35.00	52.01		0.00	0.12	0.00	1.10
	20	0.53	0.35	50.30	50.28		0.00	0.02	0.10	1.07
	48	0.47	0.41	41.10	55.88		0.01	0.08	0.04	1.15
	92	0.38	0.49	50.76	50.48		0.00	0.02	0.11	1.19
	198	0.32	0.58	43.45	52.18		0.00	0.06	0.04	1.15
	289	0.55	0.36	41.32	57.42		0.01	0.08	0.00	1.18
	376	0.39	0.52	47.38	52.06		0.00	0.06	0.04	1.19
	460	0.39	0.52	39.35	53.74		0.00	0.08	0.01	1.00
	542	0.41	0.49	50.20	50.12		0.01	0.06	0.04	1.10
	567	0.39	0.51	43.54	52.78		0.02	0.08	0.00	1.16
	593	0.36	0.54	49.77	51.22		0.00	0.06	0.04	1.27
	617	0.40	0.51	53.98	45.37		0.01	0.07	0.00	1.16

Linker	[NaCl] *(mM)*	$f_{EdiffE0}$	f_{EdiffD}	τ_{E0} *(ns)*	τ_D *(ns)*	τ_S *(ns)*	f_{EE0}	f_{ED}	f_{ES}^*	χ^2
C8	0	0.40	0.50	49.41	49.61	3.5	0.00	0.06	0.08	1.19
	10	0.56	0.32	51.79	42.88		0.00	0.07	0.05	1.11
	19	0.34	0.54	47.52	51.71		0.02	0.02	0.09	1.18
	47	0.39	0.47	52.10	46.15		0.05	0.07	0.01	1.12
	92	0.37	0.50	52.21	49.93		0.00	0.01	0.12	1.13
	198	0.36	0.48	50.62	50.72		0.00	0.06	0.10	1.15
	288	0.35	0.49	47.41	51.39		0.11	0.03	0.03	1.07
	382	0.37	0.47	51.08	51.07		0.00	0.04	0.12	1.15
	461	0.37	0.47	51.10	49.45		0.01	0.08	0.07	1.14
	542	0.34	0.51	50.86	50.91		0.00	0.02	0.13	1.15
	570	0.34	0.52	49.24	51.09		0.00	0.09	0.05	1.20
	595	0.30	0.56	50.10	52.16		0.00	0.01	0.13	1.21
	621	0.35	0.50	50.54	50.91		0.00	0.08	0.07	1.20

Linker	[NaCl] *(mM)*	$f_{EdiffE0}$	f_{EdiffD}	τ_{E0} *(ns)*	τ_D *(ns)*	τ_S *(ns)*	f_{EE0}	f_{ED}	f_{ES}^*	χ^2
C10	0	0.34	0.42	42.56	55.56	3.5	0.06	0.15	0.03	1.13
	11	0.17	0.57	43.24	53.50		0.01	0.19	0.06	1.14
	20	0.11	0.65	32.82	52.04		0.00	0.23	0.02	1.11
	48	0.27	0.45	43.50	55.44		0.08	0.14	0.07	1.19
	93	0.08	0.63	33.91	52.69		0.08	0.18	0.03	1.12
	193	0.05	0.64	48.82	51.35		0.06	0.25	0.00	1.01
	286	0.07	0.62	34.59	51.65		0.05	0.27	0.00	1.05
	375	0.11	0.54	46.08	52.24		0.10	0.25	0.00	1.18
	460	0.07	0.66	16.27	50.89		0.00	0.26	0.01	1.19
	542	0.21	0.51	50.75	51.63		0.09	0.19	0.00	1.15
	566	0.24	0.51	45.49	52.22		0.11	0.14	0.00	1.11
	591	0.31	0.54	49.64	49.70		0.02	0.10	0.03	1.05
	622	0.23	0.57	36.68	53.59		0.00	0.19	0.00	1.08

Linker	[NaCl] *(mM)*	$f_{EdiffE0}$	f_{EdiffD}	τ_{E0} *(ns)*	τ_D *(ns)*	τ_S *(ns)*	f_{EE0}	f_{ED}	f_{ES}^*	χ^2
C12	0	0.16	0.44	50.11	50.20	3.5	0.19	0.19	0.02	1.12
	10	0.12	0.45	51.18	51.07		0.22	0.17	0.04	1.13
	20	0.13	0.45	44.38	52.68		0.18	0.19	0.04	1.10
	48	0.09	0.43	50.77	50.39		0.22	0.21	0.05	1.14
	94	0.00	0.45	43.42	51.66		0.23	0.29	0.02	1.20
	193	0.02	0.42	46.67	51.45		0.30	0.26	0.00	1.11
	284	0.03	0.43	50.53	50.41		0.27	0.26	0.00	1.11
	372	0.07	0.45	49.63	49.60		0.25	0.21	0.02	1.15
	459	0.41	0.17	50.64	50.51		0.23	0.17	0.02	1.10
	537	0.20	0.44	50.06	50.01		0.18	0.16	0.02	1.13
	562	0.28	0.40	50.48	50.44		0.14	0.11	0.07	1.13
	589	0.48	0.21	49.43	51.42		0.23	0.05	0.02	1.18
	615	0.32	0.40	50.43	50.38		0.10	0.08	0.09	1.13

E] Equations used to determine the average end-to-end distance of the dendrimers

Equation S4.5 derived earlier[Error! Bookmark not defined.] was used to calculate the squared average end-to-end distance of the PyCX-PAMAM-G0 dendrimers with *a* (= *X*), *b* (= 7), and *c* (= 4) representing the number of carbon atoms in the linker connecting the pyrene moiety to the PAMAM-G0 dendrimer, the number of non-hydrogen atom in the aminoethyl propionamide building block of the PAMAM dendrimer, and the diaminoethylene core of the dendrimer, respectively.

$$L_{Py}^{2}(N)=\left(2a+\frac{\left[2-2^{N+2}+(N+1)\times 2^{N+3}\right]b+2^{N+1}c+2^{N+1}-1}{2^{N+2}-1}\right)\times l^{2} \qquad \text{(S4.5)}$$

Appendix C: S5-SI for Chapter 5

A] Global analysis of the monomer and excimer decays of PyCX-PAMAM-G0 using the model free analysis.

The fluorescence decays of the pyrene monomer and excimer acquired with the PyCX-PAMAM-G0 samples were fitted globally according to the MFA using Equations S1 and S2, respectively. The parameters in Equations S1 and S2 were optimized according to the Marquardt-Levenberg algorithm.[1] The MFA retrieved the parameters f_{diff} (= f_{diffE0} + f_{diffEL}), f_{free}, and f_{agg} (= f_{E0} + f_{EL}), which represent the molar fractions of the pyrene species, which form excimer by diffusion, are unreacted in the solution, and are aggregated forming excimer by direct excitation.

$$[Py^*]_{(t)} = [Py^*_{diff}]_{(t=0)} \times \sum_{i=1}^{n} a_i \times \exp(-t/\tau_i) + [Py^*_{free}]_{(t=0)} \times \exp(-t/\tau_M) \tag{S5.1}$$

$$[E^*]_{(t)} = -[Py^*_{diff}]_{(t=0)} \times \sum_{i=1}^{n} a_i \frac{\frac{1}{\tau_i} - \frac{1}{\tau_M}}{\frac{1}{\tau_i} - \frac{1}{\tau_{E0}}} \exp(-t/\tau_i) + \left([E0^*]_{(t=0)} + [Py^*_{diff}]_{(t=0)} \times \sum_{i=1}^{n} a_i \frac{\frac{1}{\tau_i} - \frac{1}{\tau_M}}{\frac{1}{\tau_i} - \frac{1}{\tau_{E0}}} \right) \times \exp(-t/\tau_{E0})$$

$$-[Py^*_{diff}]_{(t=0)} \times \sum_{i=1}^{n} a_i \frac{\frac{1}{\tau_i} - \frac{1}{\tau_M}}{\frac{1}{\tau_i} - \frac{1}{\tau_D}} \exp(-t/\tau_i) + \left([D^*]_{(t=0)} + [Py^*_{diff}]_{(t=0)} \times \sum_{i=1}^{n} a_i \frac{\frac{1}{\tau_i} - \frac{1}{\tau_M}}{\frac{1}{\tau_i} - \frac{1}{\tau_D}} \right) \times \exp(-t/\tau_D)$$

$$+[ES^*]_{(t=0)} \times \exp(-t/\tau_{ES}) \tag{S5.2}$$

B] Fluorescence spectra of pyrene in mixed micelles at 50 mM surfactant concentration.

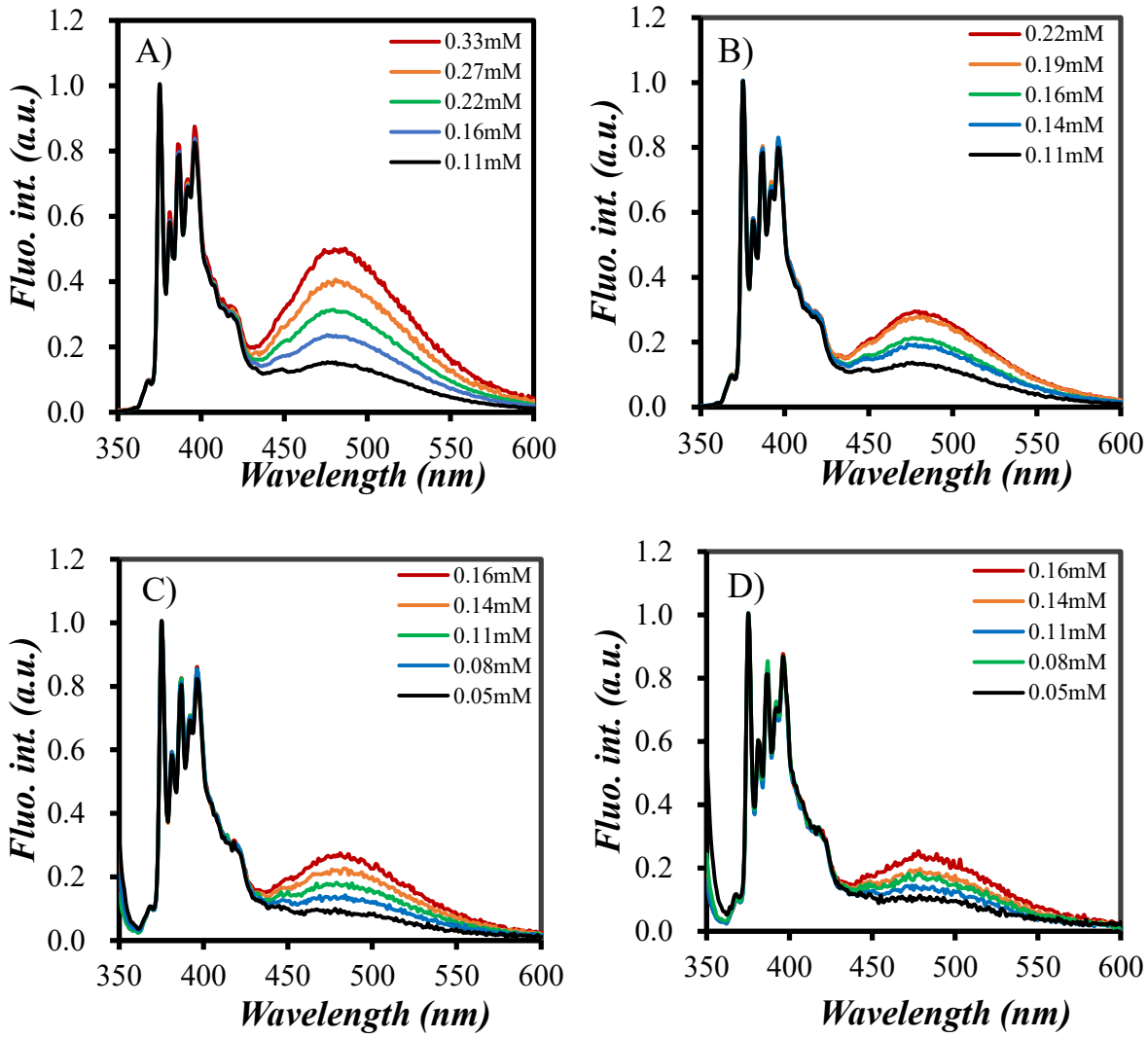


Figure S5.1. Fluorescence spectra of solutions with varying pyrene concentrations and with 40 mM SDS, 10 mM DTAB, and A)10, B) 20, C) 50, and D) 100 mM NaCl.

C] Fluorescence spectra of 0.45 μM pyrene in surfactant solution.

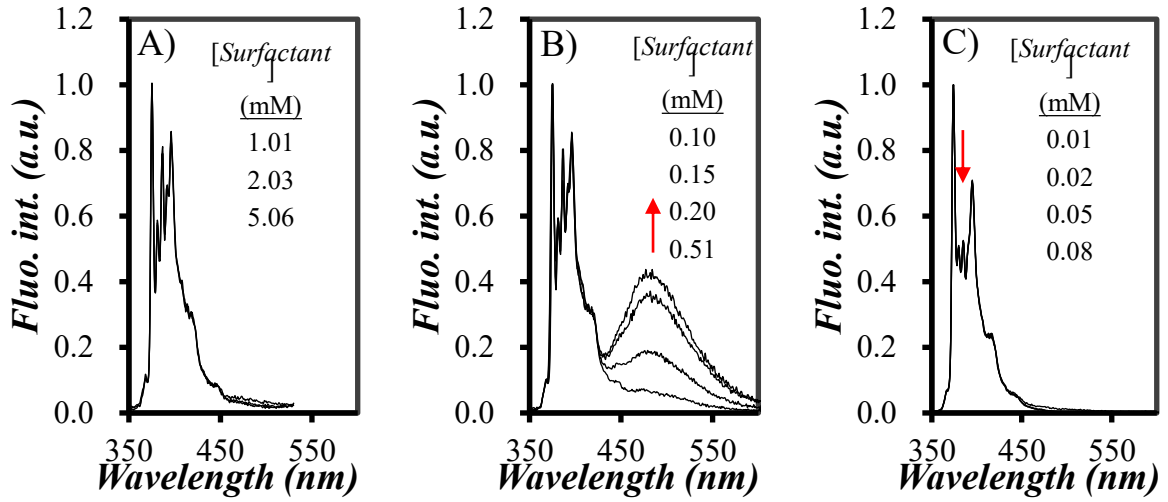


Figure S5.2. Fluorescence spectra of 0.45 μM pyrene and 10 mM NaCl in an aqueous solution of an 80:20 SDS:DTAB mixture with a total surfactant concentration ranging from A) 5.06 to 1.01 mM, B) 0.51 to 0.10 mM, and C) 0.08m to 0.01 mM.

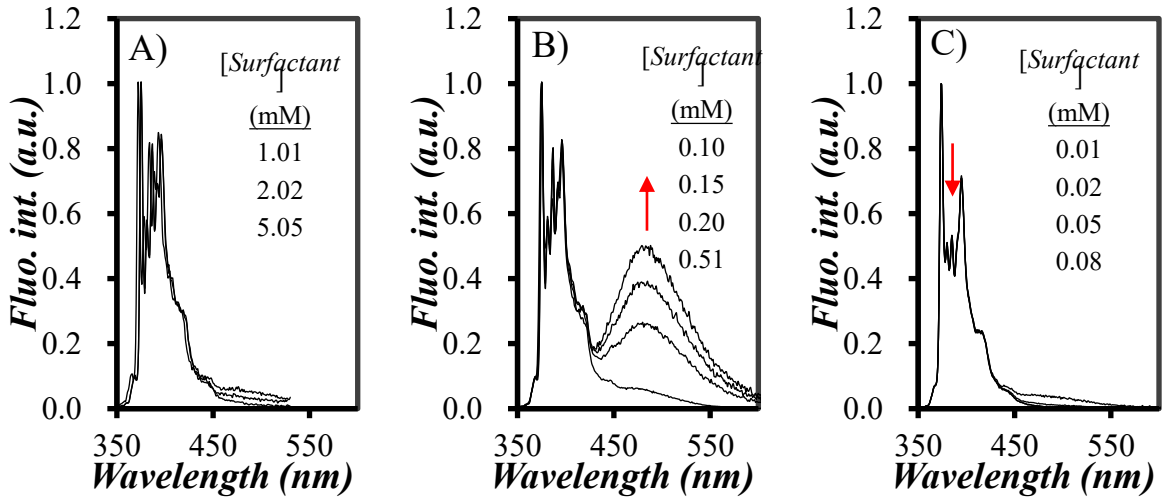


Figure S5.3. Fluorescence spectra of 0.45 μM pyrene and 20 mM NaCl in an aqueous solution of an 80:20 SDS:DTAB mixture with a total surfactant concentration ranging from A) 5.05 to 1.01 mM, B) 0.51 to 0.10 mM, and C) 0.08 to 0.01 mM.

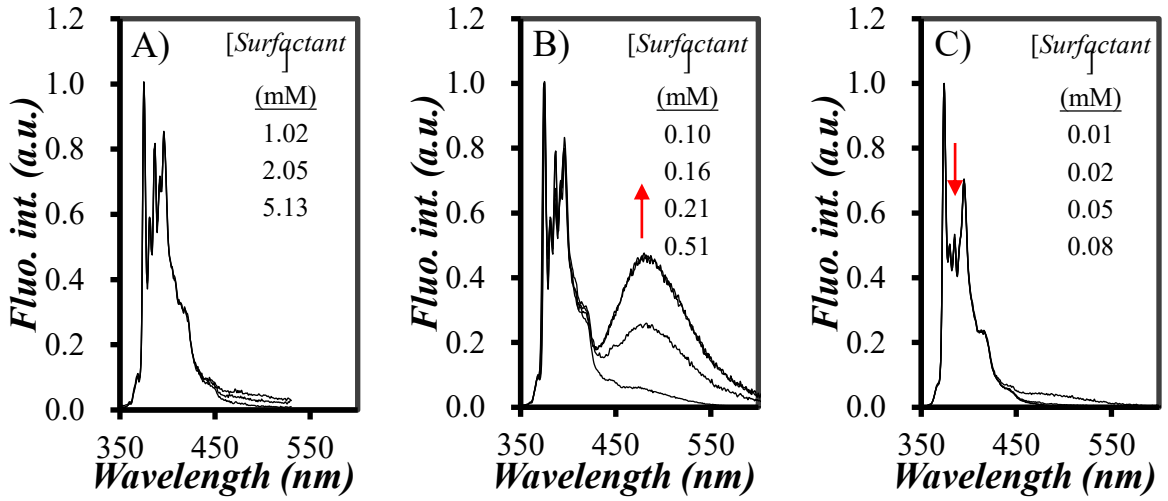


Figure S5.4. Fluorescence spectra of 0.45 μM pyrene and 50 mM NaCl in an aqueous solution of an 80:20 SDS:DTAB mixture with a total surfactant concentration ranging from A) 5.13 to 1.02 mM, B) 0.51 to 0.10 mM, and C) 0.08 to 0.01 mM.

D] Change in I_E/I_M(SSF) and I_1/I_3 with total surfactant concentration.

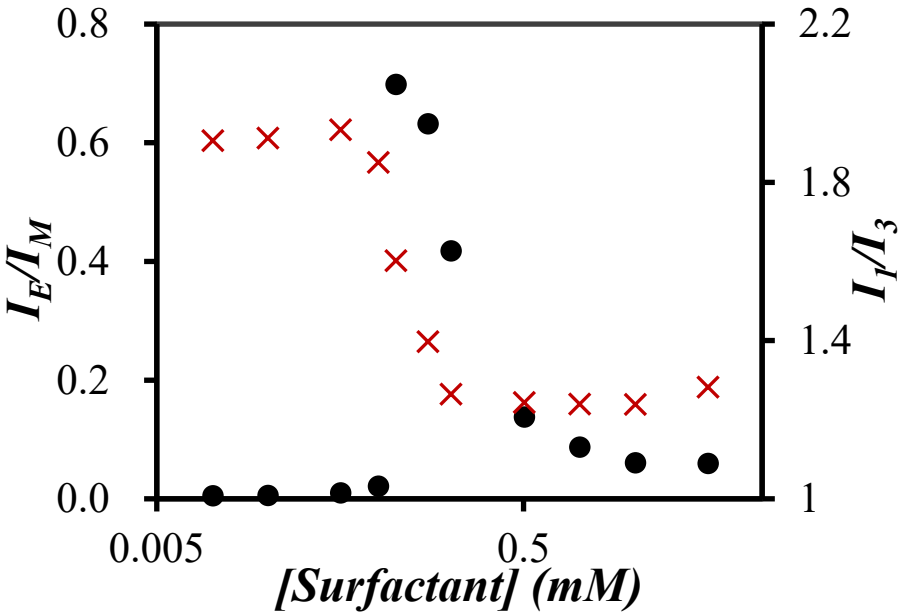


Figure S5.5. Plot of I_E/I_M(SSF) and I_1/I_3 obtained from the analysis of the fluorescence spectra of 0.45 μM pyrene in aqueous solution of an 80:20 SDS:DTAB mixture as a function of total surfactant concentration in the presence of 10 mM NaCl.

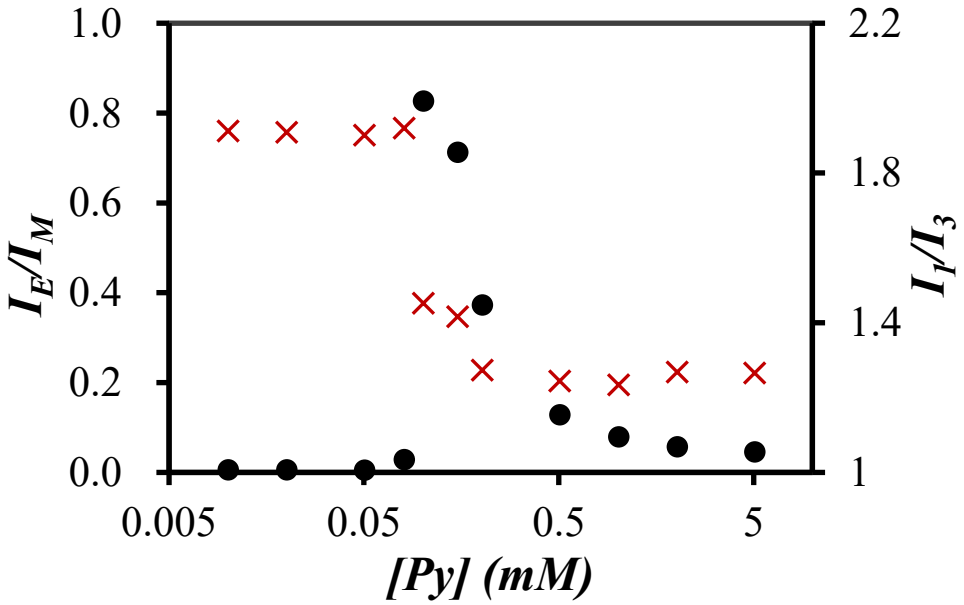


Figure S5.6. Plot of I_E/I_M(SSF) and I_1/I_3 obtained from the analysis of the fluorescence spectra of 0.45 μM pyrene in aqueous solution of an 80:20 SDS:DTAB mixture as a function of total surfactant concentration in the presence of 20 mM NaCl.

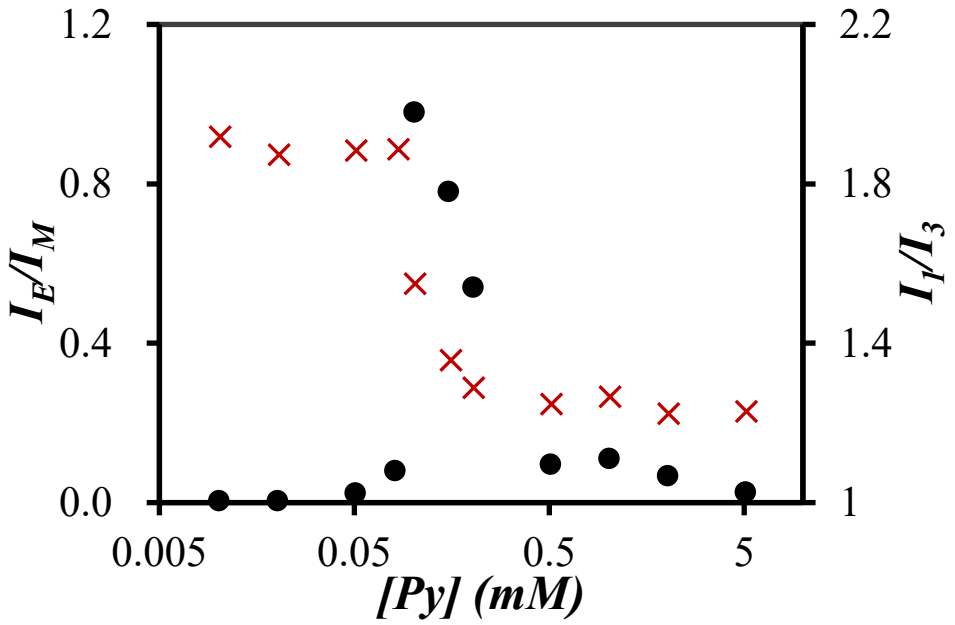


Figure S5.7. Plot of I_E/I_M(SSF) and I_1/I_3 obtained from the analysis of the fluorescence spectra of 0.45 μM pyrene in aqueous solution of an 80:20 SDS:DTAB mixture as a function of total surfactant concentration in the presence of 50 mM NaCl.

E] UV-vis spectra of PyCX-PAMAM-G0 in mixed micelles in the presence of NaCl.

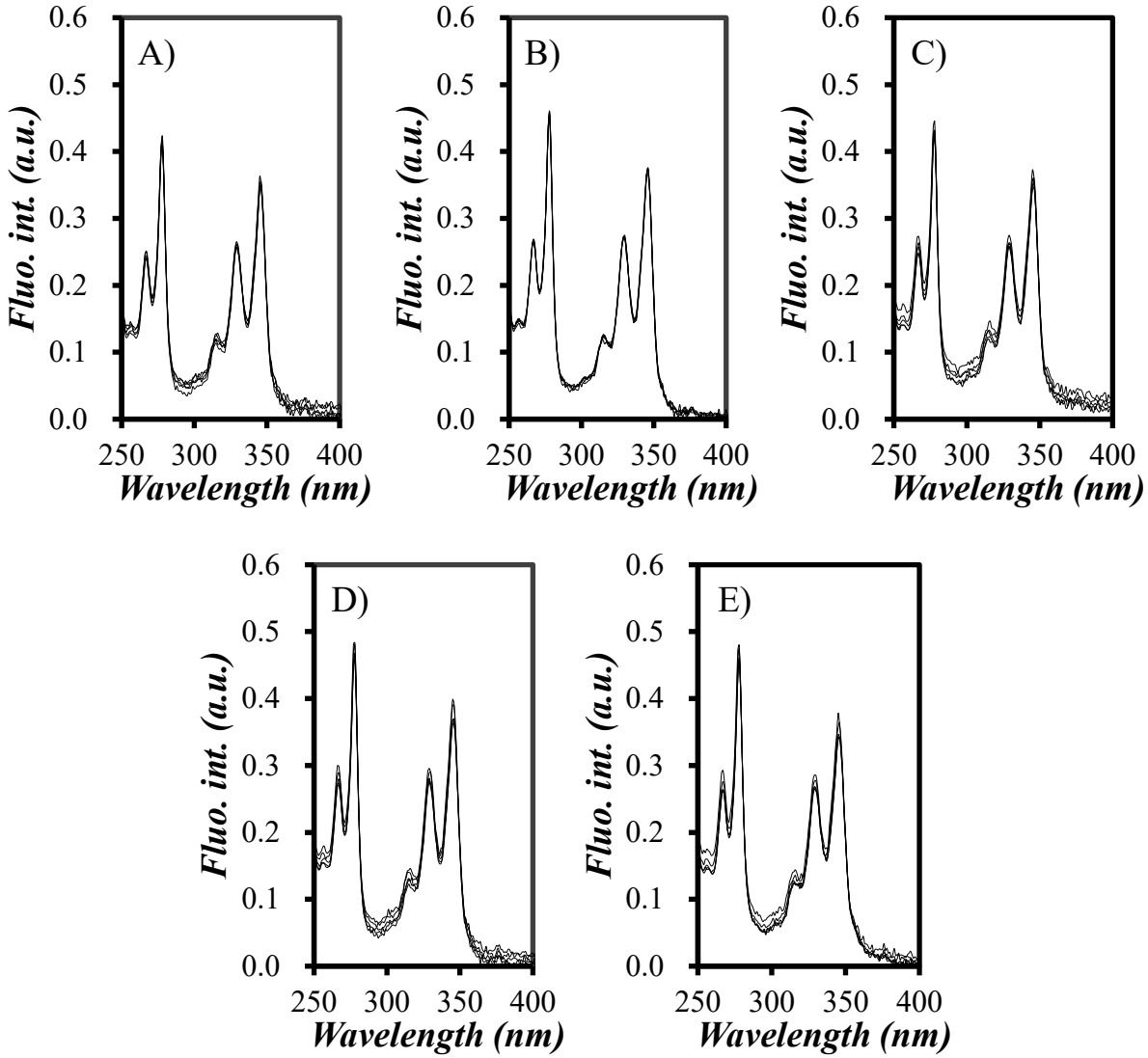


Figure S5.8. UV-vis spectra of about 1.6 μM A) PyC4-PAMAM-G0, B) PyC6-PAMAM-G0, C) PyC8-PAMAM-G0, D) PyC10-PAMAM-G0, and E) PyC12-PAMAM-G0 in aqueous solutions of an 80:20 SDS:DTAB mixture with a total surfactant concentration fixed at 50mM and a total NaCl concentration of 0mM, 10mM, 20mM, 50mM, and 100mM.

F] SSF spectra of PyCX-PAMAM-G0 in mixed micelles in the presence of NaCl

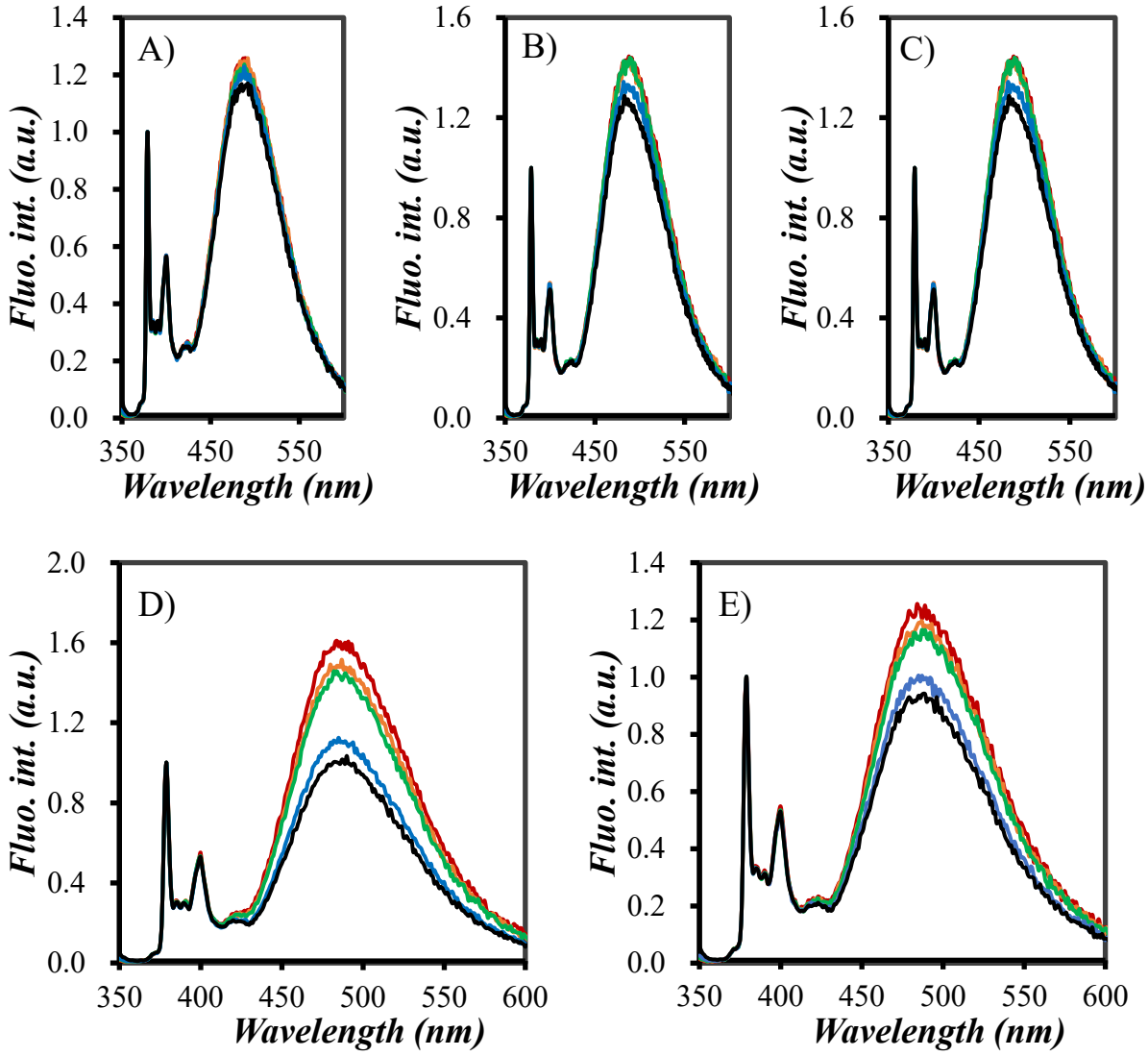


Figure S5.9. SSF spectra of about 1.6 μM A) PyC4-PAMAM-G0, B) PyC6-PAMAM-G0, C) PyC8-PAMAM-G0, D) PyC10-PAMAM-G0, and E) PyC12-PAMAM-G0 in aqueous solutions of an 80:20 SDS:DTAB mixture with a total surfactant concentration fixed at 50mM and a total NaCl concentration of (red) 0mM, (orange) 10mM, (green) 20mM, (blue) 50mM, and (black) 100mM.

G] Parameters obtained from the model free analysis (MFA) of molecular pyrene for N_{agg}(NSSA) measurements.

Table S5.1. Parameters retrieved from the MFA of the monomer fluorescence decays of molecular pyrene in 10 mM DTAB and 40 mM SDS aqueous solution in the presence of NaCl.

[NaCl] (mM)	[Py] (mM)	a_1	τ_1 (ns)	a_2	τ_2 (ns)	f_{Mfree}	τ_M (ns)	$\chi 2$
10	0.329	0.16	26.22	0.67	69.29	0.17	152.5	1.09
	0.274	0.10	25.64	0.66	72.19	0.23		1.12
	0.219	0.10	27.05	0.61	77.21	0.29		1.17
	0.164	0.06	28.02	0.53	81.77	0.41		1.21
	0.109	0.07	29.38	0.40	84.35	0.53		1.14
20	0.219	0.11	27.68	0.63	77.39	0.26		1.12
	0.192	0.12	29.41	0.59	81.65	0.30		1.11
	0.164	0.07	28.03	0.53	82.09	0.40		1.14
	0.138	0.08	31.14	0.48	85.34	0.44		1.19
	0.109	0.07	30.70	0.43	89.59	0.51		1.10
50	0.164	0.11	30.78	0.58	87.80	0.31		1.15
	0.137	0.07	29.26	0.53	87.59	0.40		1.15
	0.109	0.09	34.30	0.49	97.63	0.42		1.13
	0.081	0.07	32.84	0.39	97.27	0.54		1.11
	0.055	0.07	35.13	0.30	104.32	0.63		1.13
100	0.163	0.11	32.24	0.65	98.03	0.24		1.21
	0.136	0.09	32.90	0.63	100.14	0.28		1.23
	0.109	0.08	32.05	0.58	102.54	0.35		1.23
	0.082	0.08	34.00	0.53	107.90	0.39		1.19
	0.054	0.07	34.10	0.36	113.03	0.57		1.13

Table S5.2. Parameters retrieved from the MFA of the excimer fluorescence decays of molecular pyrene in 10 mM DTAB and 40 mM SDS aqueous solution in the presence of NaCl.

[NaCl] (mM)	[Py] (mM)	$f_{EdiffE0}$	f_{EdiffD}	τ_{E0} (ns)	τ_D (ns)	f_{EE0}	f_{ED}	χ^2
10	0.329	0.49	0.49	48.72	60.05	0.002	0.019	1.09
	0.274	0.48	0.50	45.11	45.22	0.006	0.006	1.12
	0.219	0.48	0.50	49.36	49.37	0.006	0.007	1.17
	0.164	0.49	0.50	48.07	48.11	0.005	0.007	1.21
	0.109	0.49	0.50	56.00	56.03	0.006	0.007	1.14
20	0.219	0.52	0.46	51.52	51.53	0.009	0.009	1.12
	0.192	0.53	0.45	51.55	51.48	0.012	0.007	1.11
	0.164	0.52	0.47	50.78	50.79	0.007	0.008	1.14
	0.138	0.52	0.46	50.68	50.58	0.012	0.006	1.19
	0.109	0.51	0.47	55.06	55.19	0.006	0.010	1.10
50	0.164	0.49	0.50	52.98	52.96	0.009	0.008	1.15
	0.137	0.49	0.49	50.90	50.91	0.008	0.008	1.15
	0.109	0.49	0.49	53.79	53.77	0.008	0.007	1.13
	0.081	0.50	0.48	56.04	56.05	0.008	0.008	1.11
	0.055	0.50	0.48	64.17	64.35	0.008	0.011	1.13
100	0.163	0.49	0.49	53.99	53.85	0.010	0.006	1.21
	0.136	0.51	0.47	54.64	51.69	0.008	0.008	1.23
	0.109	0.50	0.49	54.41	54.35	0.008	0.007	1.23
	0.082	0.50	0.48	58.20	58.18	0.008	0.007	1.19
	0.054	0.51	0.48	66.90	67.07	0.008	0.010	1.13

H] Parameters obtained from the model free analysis (MFA) of the PyCX-PAMAM-G0 dendrimers

Table S5.3. Parameters retrieved from the MFA of the monomer fluorescence decays of PyCX-PAMAM-G0 dendrimers in 10 mM DTAB and 40 mM SDS aqueous with NaCl.

[NaCl] *(mM)*	Derivative	a_1	τ_1 *(ns)*	a_2	τ_2 *(ns)*	a_3	τ_3 *(ns)*	f_{Mfree}	τ_M *(ns)*	$\chi 2$
10	**PyC4**	0.29	5.03	0.60	14.17	0.05	42.70	0.057	132	1.21
	PyC6	0.18	3.73	0.65	13.99	0.16	31.53	0.013	127	1.13
	PyC8	0.21	3.73	0.49	16.03	0.27	35.16	0.030	127	1.20
	PyC10	0.28	3.90	0.47	13.78	0.23	30.08	0.014	127	1.08
	PyC12	0.28	3.14	0.46	11.52	0.23	29.98	0.028	127	1.03
20	**PyC4**	0.31	5.74	0.57	15.27	0.06	47.62	0.055	132	1.14
	PyC6	0.17	3.07	0.61	13.16	0.21	27.73	0.013	127	1.10
	PyC8	0.17	3.37	0.47	15.54	0.32	35.72	0.033	127	1.18
	PyC10	0.29	3.36	0.50	14.02	0.20	31.06	0.012	127	1.19
	PyC12	0.24	2.88	0.46	11.12	0.27	31.41	0.030	127	1.10
50	**PyC4**	0.32	5.87	0.57	15.68	0.05	46.14	0.056	132	1.18
	PyC6	0.18	3.64	0.62	14.64	0.19	31.44	0.014	127	1.12
	PyC8	0.18	3.98	0.51	18.00	0.27	38.30	0.030	127	1.17
	PyC10	0.20	3.64	0.49	16.30	0.30	34.28	0.013	127	1.23
	PyC12	0.28	3.68	0.41	13.94	0.29	33.62	0.028	127	1.06
100	**PyC4**	0.29	5.94	0.58	15.86	0.07	40.93	0.058	132	1.14
	PyC6	0.19	3.88	0.63	15.50	0.16	32.56	0.012	127	1.18
	PyC8	0.19	5.13	0.47	20.02	0.31	38.79	0.035	127	1.14
	PyC10	0.20	3.47	0.47	17.19	0.32	34.45	0.012	127	1.19
	PyC12	0.26	3.70	0.41	14.55	0.30	35.73	0.028	127	1.07

Table S5.4. Parameters retrieved from the MFA of the excimer fluorescence decays of PyCX-PAMAM-G0 dendrimers in 10mM DTAB and 40 mM SDS aqueous solution with NaCl.

[NaCl] (mM)	*Derivative*	$f_{EdiffE0}$	f_{EdiffD}	τ_{E0} (ns)	τ_D (ns)	τ_S (ns)	f_{EE0}	f_{ED}	f_{ES}^*	χ^2
10	**PyC4**	0.28	0.36	49.65	49.66	3.50	0.000	0.014	0.348	1.21
	PyC6	0.27	0.65	48.11	48.20	3.50	0.000	0.072	0.005	1.08
	PyC8	0.43	0.49	48.21	48.17	3.50	0.000	0.003	0.077	1.20
	PyC10	0.43	0.45	51.59	44.10	3.50	0.064	0.055	0.000	1.08
	PyC12	0.44	0.46	47.88	47.90	3.50	0.019	0.036	0.046	1.03
20	**PyC4**	0.24	0.40	44.97	51.46	3.50	0.014	0.021	0.324	1.14
	PyC6	0.46	0.47	46.97	51.38	3.50	0.057	0.002	0.018	1.10
	PyC8	0.44	0.49	47.28	47.32	3.50	0.001	0.008	0.064	1.18
	PyC10	0.47	0.45	48.78	49.60	3.50	0.016	0.017	0.049	1.19
	PyC12	0.46	0.46	47.27	47.29	3.50	0.010	0.029	0.042	1.07
50	**PyC4**	0.29	0.36	49.62	49.63	3.50	0.000	0.015	0.335	1.18
	PyC6	0.28	0.65	48.36	48.59	3.50	0.046	0.000	0.025	1.12
	PyC8	0.41	0.52	48.55	48.42	3.50	0.000	0.006	0.068	1.17
	PyC10	0.45	0.47	48.35	46.14	3.50	0.056	0.018	0.000	1.23
	PyC12	0.43	0.50	47.31	48.16	3.50	0.000	0.014	0.060	1.06
100	**PyC4**	0.29	0.36	47.44	50.31	3.50	0.011	0.018	0.320	1.14
	PyC6	0.33	0.59	50.30	48.64	3.50	0.011	0.000	0.066	1.18
	PyC8	0.45	0.47	47.52	48.64	3.50	0.028	0.000	0.047	1.14
	PyC10	0.45	0.49	47.53	47.83	3.50	0.005	0.010	0.048	1.19
	PyC12	0.43	0.50	47.28	47.52	3.50	0.000	0.024	0.048	1.07

I] Equations used for the end-to-end distance of the dendrimers

Equation S5.3 was used to calculate the squared average end-to-end distance of the PyCX-PAMAM-G0 dendrimers with *a* (= *X*), *b* (= 7), and *c* (= 4) representing the number of carbon atoms in the linker connecting the pyrene moiety to the PAMAM-G0 dendrimer, the number of non-hydrogen atom in the aminoethyl propionamide building block of the PAMAM dendrimer, and the diaminoethylene core of the dendrimer, respectively.

$$L_{Py}^2(N) = \left(2a + \frac{\left[2 - 2^{N+2} + (N+1) \times 2^{N+3} \right] b + 2^{N+1} c + 2^{N+1} - 1}{2^{N+2} - 1} \right) \times l^2 \qquad \text{(S5.3)}$$